Summer 8-13-2019

DEVELOPMENT OF CHEMOKINE RECEPTOR 4 TARGETED MRI CONTRAST AGENT FOR THE PRECISION MRI IMAGING OF CANCER AND METASTASIS

Shanshan Tan

DEVELOPMENT OF CHEMOKINE RECEPTOR 4 TARGETED MRI CONTRAST AGENT FOR THE PRECISION MRI IMAGING OF CANCER AND METASTASIS

by

SHANSHAN TAN

Under the Direction of Jenny. J. Yang, PhD

ABSTRACT

Liver metastases are often observed with primary cancers, including uveal melanoma (UM), breast, ovarian, and colon cancer. Chemokine receptor 4 (CXCR4) is one of the major chemokine receptors that overexpressed by cancers due to its role in tumor growth, migration, and progression. Organs such as the liver, bone, and brain have an intrinsically high concentration of CXCR4 ligand, C-X-C motif chemokine ligand 12 (CXCL12). As a result, CXCR4 is also often expressed at metastases in these organs. There is an unmet medical need for noninvasively early detecting, staging, and monitoring the prognosis of liver cancers and metastases as well as probing tumor microenvironment for target therapy and drug. In this dissertation, we first report the elevated expression of CXCR4 in the UM patients' liver metastases and metastatic UM mouse

models and validate its role as an imaging biomarker for liver metastases. We then report our achievement in the development of a CXCR4-targeted MRI contrast agent, ProCA32.CXCR4, for sensitive detection of UM liver metastases using MRI. ProCA32.CXCR4 exhibits high relaxivities (r_1 = 30.9 mM^{-1} s^{-1}, r_2 = 43.2 mM^{-1} s^{-1}, 1.5 T; r_1 = 23.5 mM^{-1} s^{-1}, r_2 = 98.6 mM^{-1} s^{-1}, 7.0 T), strong CXCR4 binding affinity (K_d = 1.1 ± 0.2 μM), and the capability of CXCR4 molecular imaging in both metastatic and intrahepatic xenotransplantation UM mouse models. ProCA32.CXCR4 enables robust detection of UM metastases as small as 0.1 mm^2 in the liver. CXCR4 receptor blockage experiment proved the specific binding of ProCA32.CXCR4 to CXCR4. In addition, the application of ProCA32.CXCR4 in primary liver cancer detection and treatment effect monitoring are tested in hepatocellular carcinoma (HCC) mouse model. Except for gadolinium, we explored the possibility of manganese-based protein contrast agent and proved manganese-based ProCA exhibits high relaxivity and strong gadolinium binding affinity. We further designed and characterized ProCA32.RGD for integrin $\alpha_v\beta_3$ molecular imaging to reveal the tumor microenvironment. ProCA32.RGD targeted imaging was achieved in a 4T1 breast cancer mouse model. Further development of the biomarker targeted imaging agents is expected to have strong translation potential for early detection, surveillance, and treatment stratification of cancer and related diseases.

INDEX WORDS: MRI contrast agent, Gadolinium, Molecular imaging, CXCR4, Uveal melanoma, Metastasis, Early detection, HCC, Integrin $\alpha_v\beta_3$, Angiogenesis

DEVELOPMENT OF CHEMOKINE RECEPTOR 4 TARGETED MRI CONTRAST AGENT FOR THE PRECISION MRI IMAGING OF CANCER AND METASTASIS

by

SHANSHAN TAN

A Dissertation Submitted in Partial Fulfillment of the Requirements for the Degree of

Doctor of Philosophy

in the College of Arts and Sciences

Georgia State University

2019

DEVELOPMENT OF CHEMOKINE RECEPTOR 4 TARGETED MRI CONTRAST AGENT FOR THE PRECISION MRI IMAGING OF CANCER AND METASTASIS

by

SHANSHAN TAN

Committee Chair: Jenny. J. Yang

Committee: Hans Grossniklaus

Ming Luo

Phillip Zhe Sun

Maged Henary

Electronic Version Approved:

Office of Graduate Studies

College of Arts and Sciences

Georgia State University

July 2019

DEDICATION

Dedicated to my beloved parents and daughter. For their love, support, and sacrifices.

ACKNOWLEDGMENTS

After months of intensively writing, I would like to take the opportunity to thank all the people who helped and supported me through this journey as a finishing touch of my dissertation.

First of all, I would like to express my heartfelt gratitude to my Ph.D. advisor, Dr. Jenny. J Yang. She has been a great advisor and role model for me, her unconditional support and encouragement walk me through till today. Her hard-working, motivation, and passion for science is what I have been and will always look up to and learn from. She taught me the value of teamwork, communication, responsibility, and determination. Because of her training, I gained a variety of laboratory skills and critical-thinking, problem-solving mindset as a scientist that will be beneficial for my whole life.

I would like to thank my mentor, Dr. Shenghui Xue, who is a very patient and knowledgeable scientist. He trained me on all the essential techniques required for my research and continuously support my research regarding data processing, discussion, and manuscript preparation. I also would like to thank Dr. Fan Pu, who with Dr. Shenghui Xue trained me together on molecular cloning and protein expression, purification, and ELISA. I want to thank Dr. Jingjuan Qiao, another mentor of mine who works closely with me on the animal-related study. She trained me on immunohistochemistry staining, antibody purification, and helped with me every time of MRI experiments, etc.

I would like to thank all the previous and current MRI group members, Anvi Patel, Dr. Mani Salarian, Oluwatosin Y. Ibhagui for their great help and discussion regarding my research. I want to thank my mentee: Do Hyun Kong and Rogelio Rivera Ibarra for their hard work on ProCA32.RGD expression and purification. I would like to thank all previous and current Yang group members, including but not limited to Dr. Chen Zhang, Dr. Juan Zou, Dr. Xiaojuan Tan,

Rakshya Gorkhali, Cassie Miller, Xiaonan Deng, and Zongxiang Gui to be great colleagues and friends for me. I also want to express my deepest appreciation to Dr. Robert Wohlhueter, as a special lab member and sincere friend of mine, who helped me tremendously for scientific discussions.

The research in this dissertation is highly interdisciplinary and requires expertise in different fields. I would like also to express my gratitude for our collaborators: Drs. Hans Grossniklaus, Hua Yang for kindly providing us all the uveal melanoma-related animal models and guide us through all the pathological studies. Dr. David Lawson for great suggestions and discussion on CXCR4 related research. Drs. Zhi-ren Liu, Ravi Chakra Turaga, Ms. Malvika Sharma for providing HCC animal model and helpful discussion on the HCC project. Drs. Phillip Zhe Sun, Khan Hekmatyar and Yuguang Meng for MRI instrumentation support and data analysis.

Last but not least, I would like to thank my dissertation committee members: Drs. Hans Grossniklaus, Ming Luo, Phillip Sun, and Maged Henary, for kindly be my dissertation committee members and provide their scientific input and supporting my dissertation research.

TABLE OF CONTENTS

LIST OF TABLES

LIST OF FIGURES

LIST OF ABBREVIATION

ALT: alanine transaminase

ALP: alkaline phosphatase

AML: acute myeloid leukemia

AST: aspartate aminotransferase

AUC: area under curve

AFP: alpha-fetoprotein

BSA: bovine serum albumin

CAF: carcinoma-associated fibroblasts

CCR7: chemokine receptor 7

CHO cell: Chinese hamster ovary cell

CXCR4: chemokine receptor 4

CXCL12: C-X-C motif chemokine ligand 12

CT: computed tomography

ECM: extracellular matrix

DAPI: 4’,6-diamidino-2-phenylindole

DEN: diethylnitrosamine

DTPA: diethylenetriamine pentaacetate

ERK1/2: extracellular signal-regulated kinases 1/2

EGTA: ethylene glycol tetraacetic acid

ELISA: Enzyme-linked immunosorbent assay

FDG: fluorodeoxyglucose

FOV: field of view

FPLC: fast protein liquid chromatography

GBCA: gadolinium-based contrast agents

Gd-BOPTA: gadobenate dimeglumine

Gd-EOB-DTPA: gadoxetic acid

Gd-DTPA: Gadopentetic acid

GRPR: gastrin-releasing peptide receptor

GPCR: G protein-coupled cell surface receptors

HBSS: hank's balanced salt solution

HBV: hepatitis B

HCC: hepatocellular carcinoma

HCV: hepatitis C

HER2: Human epidermal growth factor receptor 2

HEPES: 4-(2-hydroxyethyl)-1-piperazineethanesulfonic acid

H&E: hematoxylin and eosin

HUVECs: human umbilical vein endothelial cells

ICP-OES: inductively coupled plasma optical emission spectrometry

IHC: immunohistochemistry

IP: intraperitoneal

IP_3: Inositol trisphosphate

IPTG: isopropyl β-D-1-thiogalactopyranoside

IRS: immune reactive score

LRET: luminescence resonance energy transfer

MALDI: matrix-assisted laser desorption/ionization

MRI: magnetic resonance imaging

MRS: magnetic resonance spectroscopy

MRT: mean residence time

MM: multiple myeloma

Mn-DPDP: mangafodipir trisodium

NMR: nuclear magnetic resonance

NSF: nephrogenic systemic fibrosis

OD: optical density

PBS: phosphate-buffered saline

PDGFR: platelet-derived growth factor receptor

PET: positron emission tomography

PEG: polyethylene glycol

PK: pharmacokinetics

ProCAs: protein-based Gd^{3+} MRI contrast agents

PSMA: prostate membrane antigen

PI3K: phosphoinositide 3-kinases

r_1: longitudinal relaxivity

r_2: transverse relaxivity

RIPA: radioimmunoprecipitation assay

SAR: structure-activity relationship

SCLC: small cell lung cancer

SDF-1: stromal-derived factor 1

SDS-PAGE: sodium dodecyl sulfate-polyacrylamide gel electrophoresis

SNR: signal noise ratio

SOC: standard of care

SPECT: single-photon emission computed tomography

T1: longitudinal relaxivity

T2: transverse relaxivity

TBST: TBS-Tween 20

TCEP: tris (2-carboxyethyl) phosphine hydrochloride

TME: tumor microenvironment

TE: echo time

TR: repetition time

UM: uveal melanoma

UV: Ultraviolet

VEGF: vascular endothelial growth factor

Vss: volume of distribution

τ_R: rotation correlation time

1 INTRODUCTION

1.1 Cancer as a metastatic disease

Cancer (Malignant Neoplasm) is a global public health issue and one of the leading causes of death in the United States. Caused by uncontrollable cell division and proliferation, cancer cells can invade locally (healthy tissues) and regionally (lymph nodes, tissue, and organs). Data from 2018 shows the estimated new cases of cancers in the United States is 1,735,350, and cancer causes about 609,640 patient deaths in the United States (1). Cancer is the second leading cause of death in all age groups after heart diseases (2).

Metastasis describes the invasion and colonization of tumor cells to tissues or organs that are not directly connected with the primary cancer sites. Metastasis is the top cause of cancer mortality and responsible for over 90 percent of cancer-related deaths. Most tumors metastasize through the bloodstream. The vasculature metastasis dissemination involves multiple stepwise processes that include local invasion, intravasation, subsistence in the circulation system, extravasation, and finally colonization. First, cancer cells locally infiltrate and invade adjacent tissue, and some of them break the basement membrane and leave primary tumor sites. Then, tumor cells separate from the primary tumor sites and enter into the vasculature system; this process called intravasation. After that, tumor cells migrate through vasculatures and find a way of extravasation and form metastases in new locations (3). Although metastasis is an inefficient process, it is still the primary cause of tumor-related death. Very few tumor cells can eventually survive all the steps and develop metastases. A lot of complicated factors contribute to this whole process: the initial mutation endows the tumor cells unlimited proliferation ability; the immune tolerance of tumor cells and the tumor cell successfully colonize and take over a new organ.

Organ-specific metastasis pattern is observed with various cancers, which means specific cancer has preferred sites of metastasis. Breast cancer usually metastasizes to the liver, bones, lungs, and brain. Colorectal and pancreatic cancer are more likely to metastasize to the liver and lungs. A large portion of prostate cancer goes to the bones, and uveal melanoma almost exclusively metastasizes to the liver (over 95%) (4). The reason for the organ-specific metastasis remains unknown. Potentially, the expression of genes in primary tumors might provide markers that facilitate the organ-specific metastasis.

The cellular mechanisms involved in metastasis are complicated. The factors of tumor cells include expression of the genes that alter cell adhesion in the primary site (5, 6), strategies to survival in the circulatory system (7, 8) and eventually colocalize secondary organ and forming new blood supply for further proliferation (9, 10). Also, tumor microenvironment significantly affects metastases progression. The various types of cells, such as cancer stem cells, immune-related cells, stroma cells, and fibroblasts consisted of the microenvironment facilitate and promote tumor progression (11). Understanding the mechanism of metastasis, monitoring the metastatic progression, and revealing the local anatomical and biological information of cancer metastases would be vitally crucial for tumor diagnosis, stratification of therapy and intervention.

As the improvement of the standard of care (SOC) during the past few decades, the cancer-related death rate has been decreasing, and most cancers with initial diagnoses of the localized disease have promising 5-year survival rates. However, for cancer patients with diagnoses of metastatic diseases, it is still an indication of the terminal disease stage. In some metastatic cancer, immunotherapy is proved to be able to improve the prognosis. For example, ipilimumab prolonged the overall survival of metastatic melanoma (12), and enzalutamide (an androgen-receptor-signaling pathway inhibitor) can significantly extend the survival of men with metastatic prostate

cancer (13). However, for the other types of cancer with metastases, such as breast cancer, gastric cancer, and pancreatic cancer, the survival rates remain unoptimistic (14-16).

1.1.1 Cancer diagnosis technology and early detection of cancer

The diagnosis of cancer is essential before, during, and after the cancer treatment. The common diagnostic tests include a review of health history, physical examinations, laboratory examinations, biopsy, imaging tests (ultrasound, CT, MRI, PET/CT), and endoscopy, etc. The major imaging modalities used in clinical settings are positron emission tomography (PET), single-photon emission computed tomography (SPECT) and magnetic resonance imaging (MRI) (17, 18). The modern technology allows genetic tests as well to provide more precise and further genetic information of cancer that could further benefit the cancer treatment.

Statistic evidence shows that the early detection of cancer can efficiently improve cancer prognosis. More than 90 percent of bowel cancer patients can survive the disease for more than five years if diagnosed at the earliest stage. The five-year survival rate of breast cancer patients diagnosed at the early stage is 90%; but for the women diagnosed at the most advanced stage, the five-year survival rate is 15%. For ovarian cancer, the five-year survival rate drastically dropped to 5% in patients diagnosed with the most advanced stage of the disease, compared to 90% of the five-year survival rate in patients diagnosed at the earliest stage (19).

The early detection and staging of cancer are critically important for the diagnosis and prognosis of cancer. The management of cancer becomes more precise and personalized, along with a better understanding of cancer pathophysiology. Cancer immunotherapy and targeted cancer therapy focus more on molecular and cellular levels than systemic levels. There are approved agents to target human epidermal growth factor receptor 2 (HER2) for breast cancer, epidermal growth factor receptor (EGFR) for non-small cell lung cancer (20, 21). Thus, knowing

the molecular information of tumor cells and microenvironment with non-invasive imaging assays becomes an unmet medical need which can be fulfilled by biomarker targeted molecular imaging. Our knowledge for cancer biomarkers and imaging capability is essential for the success of early detection.

1.2 Molecular imaging

"Molecular imaging is the *in vivo* visualization, characterization, and measurement of biological processes at the molecular and cellular levels (22)." On top of the present imaging assays, which rely on detecting the microscopical alteration of physiological status, molecular imaging enables more specific and quantitative assessment of disease status. Molecular imaging can non-invasively profiling the pathological characterizations of diseased tissues and enabling early detection, personalizing treatment stratifications, and following up the treatment effect. Histological analysis is the gold standard for analyzing the morphology and molecular signatures of tissues. However, the prominent disadvantage of histological analysis is the reliance on biopsy to collect tissue invasively and does not provide spatial information in the whole organ. The advances in molecular and cellular technology, the availability of different animal models and small animal scanners facilitate the development of molecular imaging. The rapid development of the molecular imaging field promises the possibility of assessing the pathological process on a molecular level with non-invasively imaging acquisitions.

The main deciding factors for molecular imaging, including biomarker, imaging sensitive instrumentation, and probes. Molecular imaging development is rooted in nuclear medicine, which has relatively higher sensitivity through the administration of radiolabeled tracers. Due to the limitation of sensitivity, the major imaging modality in molecular imaging is PET, SPET, and

Ultrasound. Recently, near IR fluorescence imaging probes have also been developed (23). For MRI, there is no targeted probe has been approved.

The definition of a biomarker is proposed to be "A characteristic that is objectively measured and evaluated as an indicator of normal biological processes, pathogenic processes, or pharmacologic responses to a therapeutic intervention." (24) Biomarkers are widely used in disease screening and diagnosing, cancer staging, stratification of treatments. Biomarkers, a parameter that considers the individual differences across the same disease, is crucial for cancer diagnosis, prognosis prediction, and treatment stratification. For instance, HER2 is found to be over-expressed and plays a vital role in breast cancer development. The HER2 status of breast cancer patients is related to the prognosis and guides the decision- making regarding the choice of using monoclonal antibody Trastuzumab (25, 26). Similarly, research of colorectal cancer shows that colorectal patients with KRAS wild type tumors can benefit from treatment with a combination of cetuximab and FOLFIRI when compared with FOLFIRI alone. Patients treated with cetuximab plus FOLFIRI showed a reduced risk of progression and metastasis (27). The selection of biomarker for cancer imaging is very challenging and requires careful validation of patient samples. This dissertation will address the validation of CXCR4 as a biomarker for the liver metastases. (Chapter 5)

1.3 Medical imaging modalities

PET imaging records the high-energy γ rays emitted from the subject. A neutron-deficient, positron emitted isotope was selected for labeling biomolecules as PET tracers. Positron emitted isotopes that were frequently used for developing PET tracers are ^{15}O, ^{13}N, ^{11}C, and ^{18}F (18). The PET radiotracers are made using either a cyclotron (28) or a generator. Fluorodeoxyglucose (FDG), an analog of glucose, is the most commonly used biologically active tracer for PET imaging.

^{18}FDG introduced to the subject, and the decay of ^{18}F generates positron (e^+) and an electron neutrino (v_e). After emission, the positron travels in the tissue and loses the energy until it annihilates with an electron and emits two annihilation gamma rays in opposite directions (29) (Figure 1.1). PET imaging has high sensitivity in the range of 10^{-11}–10^{-12} mole/L and with no depth limitation. As a result, PET imaging is a very robust imaging modality for clinical usage.

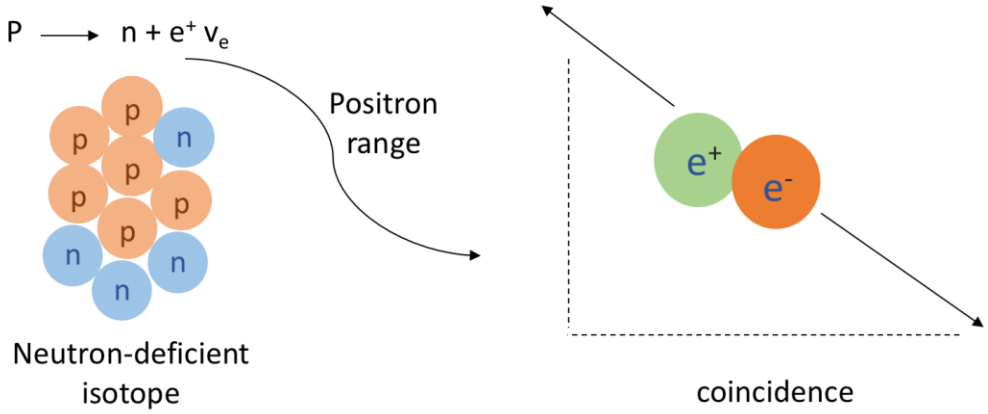

Figure 1.1 The principles of positron emission.
Positron emitted along with the decay of the neutron-deficient isotope, the detection of annihilation photons within the time window.

Single-photon emission computed tomography (SPECT) is less sensitive than PET imaging. However, SPECT has the advantage of allowing the usage of various isotopes with different energy γ-rays, which enables the simultaneous detection of multiple events at the same time.

Optical imaging as another approach to achieve molecular imaging has the advantage of being economical and has the potential of achieving multichannel imaging by using optical probes with different imaging spectra. Optical imaging, including bioluminescence imaging, fluorescence imaging, has the advantage of being detected at a very low level due to the background-free nature of the emitted light. The technical barrier of optical imaging is how to conquer the low light

transmission efficiency and detect the light emitted within the living subjects, especially for bigger animals.

Magnetic resonance imaging (MRI) obtains the three-dimensional imaging of the human body without radiation involvement and has been widely used in clinic settings. This technique has been rapidly developing, evolving, and deriving the different clinical applications due to its high resolution and sensitivity to soft tissues. MRI has the potential for molecular imaging due to its advantages of higher spatial resolution and non-radiation exposure. The sensitivity of current MRI contrast agents limits its applications in molecular imaging. This dissertation aims to develop novel biomarker targeted contrast agents to extent MRI application for molecular imaging.

1.4 Magnetic Resonance Imaging

1.4.1 Physics

The MRI technique builds on the basic principles of nuclear magnetic resonance and generates imaging information of the anatomy, function, and metabolism of tissues without causing ionizing irradiation. The nuclear magnetic resonance (NMR) phenomenon was described by Bloch and Purcell in 1946 (30, 31). Damadian proposed in 1971 that relaxation time for two solid malignant tumors, Walker sarcoma and Novikoff hepatoma are distinct from the healthy tissues (32). This discovery ignited the hope of distinguishing benign and malignant tissue using MRI. By detecting water relaxation in a strong magnetic field following a temporary pulse sequence, MRI provides the internal picture of tissues and organs for diagnosis.

Atoms with an odd number of protons and/or an odd number of neutrons exhibit the phenomenon of nuclear magnetic resonance because of the spin angular momentum they possess. Of the atoms exhibiting this phenomenon, such as ^{1}H, ^{31}P, and ^{23}Na, ^{1}H is the most abundant in the body and most practical for MRI imaging application. By applying a static magnetic field B_0,

all the ^{1}H spins will align with the direction of B_0 (*z*-direction) and produce a magnetization moment M. While the proton spins aligned in the *z*-direction interact with the radiofrequency field in the transverse direction, a torque will be induced, and the magnetization moment M will rotate away in a procession motion from its equilibrium position along with *z*-axis. M will eventually go back to the initial equilibrium position along with *z* after being excited by a radiofrequency field. In the process, the transverse component of M, M*xy* decays while the longitudinal component M*z* grows. Two parameters, T_1 and T_2, are introduced to characterize the return of different components of M. Introduced contrast agents alter the relaxation time constant and provide signal enhancement on imaging.

1.4.2 MRI contrast agents

Although MRI is a non-radiation, high-resolution imaging modality, the sensitivity of MRI is limited by the water background. To resolve this issue, MRI contrast agents have been applied to increase the contrast of imaging results by Lauterbur PC (33) for the first time in 1983. Since then, the MRI contrast agents have become an indispensable element of the MR imaging technique. Based on the bio-distribution preference of different contrast agents, they can be grouped to intravenous contrast agents, intravascular contrast agents, and hepatobiliary contrast agents such as gadobenate dimeglumine (Gd-BOPTA), gadoxetic acid (Gd-EOB-DTPA) and mangafodipir trisodium (Mn-DPDP). The gadolinium-based contrast agents are the most commonly used in medical applications since been first described as a potential NMR agent (34). Nine of these agents are commercialized for different imaging purposes.

MRI contrast between tissues in the image differentiates different tissues and local environment and reflects as the different intensity on MRI images. The MRI contrast arises from and is affected by multiple factors: proton density, innate T_1 and T_2 of tissue, perfusion, and

diffusion of local water molecules. The MRI contrast agents aim to alter the T_1 and T_2 of the tissue at their presence and enhance the contrast of images. All contrast agents shorten both T_1 and T_2. However, based on the predominant influence on T_1 or T_2, MRI contrast agents can be divided into T_1 contrast agents and T_2 contrast agents. More specifically, when a contrast agent alters longitudinal relaxation rate ($1/T_1$) and transverse relaxation rate ($1/T_2$) in a similar level, the contrast agents are T_1 weighted contrast agent, because the intrinsic faster T_2 of tissue contrasts enhance dominantly on T_1 in a percentage base (35). If a contrast agent alters transverse relaxation more predominantly than longitudinal relaxation, the contrast agent is a T_2 weighted contrast agent. The most commonly used MRI contrast agents, gadolinium-based contrast agents (GBCA), are T_1 contrast agents for the significant influence on T_1. There are very few exceptions of the application of GBCA that use the T_2 effect. The T_2 effect of gadolinium-based contrast agents reflects as darkening the signal on MRI images, and it only shows up when the contrast agent concentration is in mM range. For imaging purposes, the contrast agent concentration is usually much lower than one mM (36, 37). The T_2 effect of gadolinium contrast agents is limited by the increased risk of toxicity at a higher dosage.

Superparamagnetic iron oxide is T_2 weighted contrast agents because they affect the T_2 relaxation and show a darkening enhancement on T_2 weighted images (38). Transitional metal ion manganese (II) has five unpaired electrons that possess T_1 property and weak T_2 property, and attempts of using manganese-based contrast agents for enhancement have been made (33, 39, 40).

The gadolinium-based MRI contrast agents in clinical use are formulated with a chelator to protect the dissociation of free Gd^{3+}, which potentially causes toxicity (41). Due to the seven unpaired electrons, gadolinium possesses paramagnetic properties. Current GBCAs can be divided into linear and macrocyclic based on the structure of chelating ligands (42, 43). According to their

charges, they can be further divided into sub-categories of ionic and non-ionic ones. In general, macrocyclic contrast agents are more stable than the linear "open chain" ones, for the reason that the previous ones form a structure that cages the gadolinium ion. Ionic contrast agents are more stable than non-ionic ones for the stronger electrostatic interactions between Gd^{3+} and the donor groups (44, 45).

There are fundamental features that researchers are trying to look for in the design of gadolinium-based contrast agents, including high relaxivity, high stability, low toxicity, tissue specificity, or even biomarker specificity. Relaxivity (r_1 and r_2) is the capability of contrast agents shorten T_1 and T_2 and provides contrast enhancement on images. The higher relaxivity of contrast agents enables the same signal intensity by less concentration or increases the signal intensity by equivalent dosage. Developing MRI contrast agents with higher relaxivity increases the imaging sensitivity and reduces the contrast agent's toxicity potentially. High stability contrast agents are considerably safer. The linear contrast agents are less stable than macrocyclic contrast agents. Additionally, the majority of reported nephrogenic systemic fibrosis (NSF) cases were associated with the administration of the non-ionic, linear contrast agent Omniscan (46). Tissue specificity enables the contrast enhancement in a specific tissue and expands the application of the contrast agent. For example, the hepatocytes-specific contrast agents can be specifically uptake by hepatocytes and assist in the differentiating diagnosis of hepatocellular carcinoma. Biomarker-specific contrast agents that target specific biomarkers, especially cancer biomarkers, arise from the development of molecular imaging. Biomarker-targeted MRI contrast agents are expected to improve the understanding of diseases at a molecular level and help to make decisions regarding diagnosis and therapeutic stratification.

1.4.3 MRI contrast agents for molecular imaging

An important factor in achieving molecular imaging with MRI is to improve the relaxivity of contrast agents. MR imaging has lower sensitivity compared with nuclear medicine imaging approaches such as PET. As a result, MRI contrast agents must reach specific local concentrations to achieve imaging enhancement of biomarkers. The relaxation time of tissues is various. Taking tissue relaxation time measurement under 3.0 T as an example, the T_1 of gray matter is 1460 ± 33 ms (47), white matter is 840 ± 50 ms (48), the liver is 840 ± 50 ms (49). Assuming relaxation time of specific tissue is 1000 ms, in order to achieve an observable robust change (0.5 s^{-1}) on MR contrast enhancement with current gadolinium-based MRI contrast agents, a minimum concentration of 100 μM is required (calculation based on r_1 equal to 5 mM^{-1} s^{-1} and binding with biomolecule in a 1:1 stoichiometry) (35). Such a concentration of contrast agent cannot be achieved *in vivo* considering the biomarkers present in 10^{-6} -10^{-10} concentration in tissue (50) and the fast elimination of small molecule contrast agent.

Attempts have been made to achieve molecular MR imaging. One of the early approaches is to label monoclonal antibodies with Gd-DTPA. Matsumura A et al. use monoclonal antibodies against 9L glioma cells to conjugate Gd-DTPA and achieve tissue-specific enhancement of mouse brain tumors (51). Melanoma-specific enhancement was reported using monoclonal antibodies against melanoma conjugated with Gd-DTPA (52). Another example is the alphaVbeta3-targeted MRI contrast agent, which is reported to achieve molecular imaging through alphaVbeta3 and show the angiogenic 'hot spots' with magnetic resonance imaging (53). The robust enhancement of biomarkers requires higher relaxivity contrast agents with targeting capability.

Various factors attribute to the relaxivity of contrast agents. The rotational motion of contrast agents is decisive for the relaxivity. To achieve catalytical relax of bulky water, the

gadolinium should efficiently relax the water and the relaxed water can be exchanged quickly with the unrelaxed ones. For small molecules, the rotational rate is majorly decided by the relaxation efficiency. However, when the rotational motion becomes slower, the water exchange rate becomes a predominant factor. This phenomenon has been described with the relaxivity measurement of MS-325 and the analog MS-325-BMA. The relaxivity of both contrast agents in PBS buffer is similar. However, the relaxivity of MS-325 is significantly higher than MS-325-BMA in the human serum albumin solution (35). Once the agents were bound with human serum albumin, the rotational motion of both contrast agents slowed down, and the water exchange rate of MS-325-BMA is slower than MS-325 (54). One approach to improve the relaxivity of gadolinium contrast agents is to link multiple gadolinium in one molecule. This can improve the concentration of gadolinium in the target region and increase the contrast of images (55, 56). Another approach is to locate gadolinium in the center of the molecule and form more rigid local structures. In this case, the local motion of gadolinium is restricted and changes the factors governing the relaxivity to achieve significantly higher relaxivity (57, 58). Alternatively, the lipid platform for MRI contrast agents' construction and MRI has been reported to target the fibrin and detect thrombus *in vivo* (59, 60).

Hydration number *q* refers to the water molecule directly bound to the gadolinium in the inner coordination sphere. The water molecules in the second and outer coordination spheres contribute to the relaxivity as well. With more water molecules coordinating in the inner sphere, gadolinium contrast agents generate higher relaxivity (61). However, the tradeoff would be that the stability becomes less because the introduction of more coordination sites for the ligands decreases the thermodynamic stability of contrast agents.

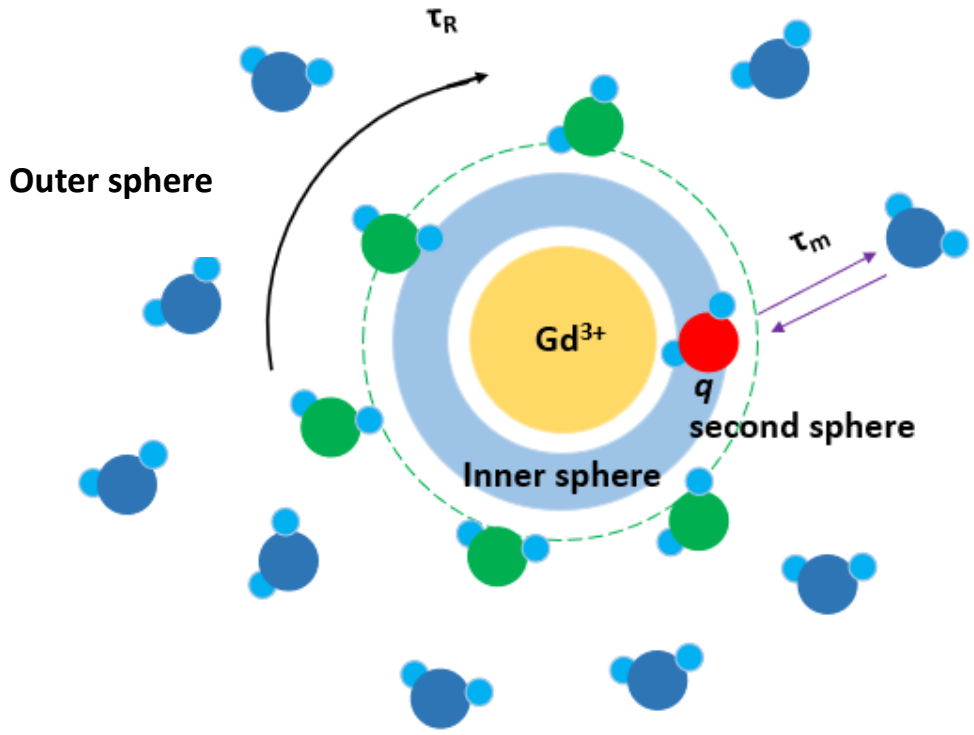

Figure 1.2 Physical parameters affect the relaxation of gadolinium-based MRI contrast agents.

1.4.4 Protein-based MRI contrast agents

Designing the MRI contrast agents with higher relaxivity need to consider multiple factors including hydration number *q*, second sphere and outer coordination sphere, rotational correlation time (τ_R), and water exchange rate. We designed a serious of protein-based Gd^{3+} MRI contrast agents (ProCAs) (62) which chelating the gadolinium (III) ion using the interaction between side chains of residues and gadolinium (III) ion, instead of linking the Gd-chelator with protein through covalent and noncovalent interaction. This allows optimizing the relaxivity related factors such as water number, rotational correlation time and second correlation sphere. We reported a novel MR contrast agent ProCA32 that has unprecedented liver imaging capability (63). ProCA32 is derived

from a parvalbumin scaffold with two gadolinium binding sites. ProCA32 possesses slower rotational correlation time (τ_R) than small molecules such as Gd-DTPA and exhibits a much higher relaxivity (both r_1 and r_2) when compared with current commercially available contrast agent. ProCA32 can image small metastases in millimeter-scale (63) whereas imaging capability of small chelator MR contrast agents usually limited to a centimeter scale. In addition, ProCAs allows the linkage of targeting moieties specific for biomarkers and achieve related biomarker molecular imaging. GRPR, PSMA, and HER2 specific imaging can be achieved by the administration of corresponding contrast agents (64-66).

An ideal protein-based MRI contrast agent should satisfy several criteria: high r_1 and r_2 relaxivity, strong Gd3+ binding affinity, low toxicity, high stability and solubility, suitable PK/PD properties, no interaction with other proteins, and low cost of production. This dissertation is focused on the development of CXCR4 targeted contrast agent, ProCA32.CXCR4. ProCA32.CXCR4 based on the ProCA32 structure and targeting CXCR4 with targeting moiety at the C terminus.

1.5 Chemokine receptor 4 (CXCR4)

The chemokines are a family of small, pro-inflammatory cytokines secreted by immune-related cells, which mediate chemotaxis of cells through the interaction with chemokine receptors. Interleukin 8 is the first chemokine been identified and characterized (67). Since then, more and more chemokines have been identified, until today, there are over 50 ligands identified in humans and mice (68). Chemokines are first appreciated as a chemoattractant for innate immune cells (69).

The chemokines achieve their biological roles by interaction with the chemokine receptors that expressed on the target cells. Chemokine receptors belong to the family of G protein-coupled

receptors (GPCR) that have seven transmembrane domains connected by three extra-membrane loops (70). Chemokine receptors can be divided into G-protein coupled chemokine receptors and atypical chemokine receptors based on their signaling (68). According to the positioning of the first two cysteines, chemokine receptors can be classified into four groups (CXC, CC, C, and CX3C) (71). Chemokine receptors were first appreciated as the mediators of leukocyte- trafficking in acute inflammation and then found to be involved in other biological processes such as T helper cell differentiation, angiogenesis, and co-entry of HIV. (72, 73)

Chemokine receptor 4 (CXCR4), also known as CD184 or "fusion", is the chemokine receptor for stromal-derived factor 1(SDF-1, renamed as CXCL12). Chemokine receptor 4 is a rhodopsin-like receptor encoded on chromosome 2. CXCR4 is widely expressed on many different types of cells such as leukocytes, progenitor, stem cells, endothelial, epithelial, and stromal cells. CXCL12 is the established natural ligand of CXCR4 since 1996 (74). In 2005, Burns et al. (75) reported chemokine receptor 7 (CCR7) is another receptor for CXCL12. CXCL12 is ubiquitously expressed in human tissue and has high expression levels in the liver, kidney, lungs, and bone marrow (76, 77). The CXCR4/CXCL12 axis mediates physiological and pathological processes such as cell migration, metastatic malignancy, vascularization, and organ homeostasis (78, 79). The biological effect of CXCR4 is achieved by binding the nature ligand CXCL12, to activate the downstream protein kinase to trigger the signaling pathway (Figure 1.3). Upon the activation of CXCR4 by interacting with CXCL12, the downstream signaling pathway is initiated by dissociation of βγ subunit and α subunit. A series of complex signal pathways transduction were achieved by activation of IP3 (Inositol triphosphate), ERK1/2 (extracellular signal-regulated kinases1/2), PI3K (phosphoinositide 3-kinases), JAK and calcium release to mediate a series of biological incidences including cell migration, proliferation, survival and gene transcription.

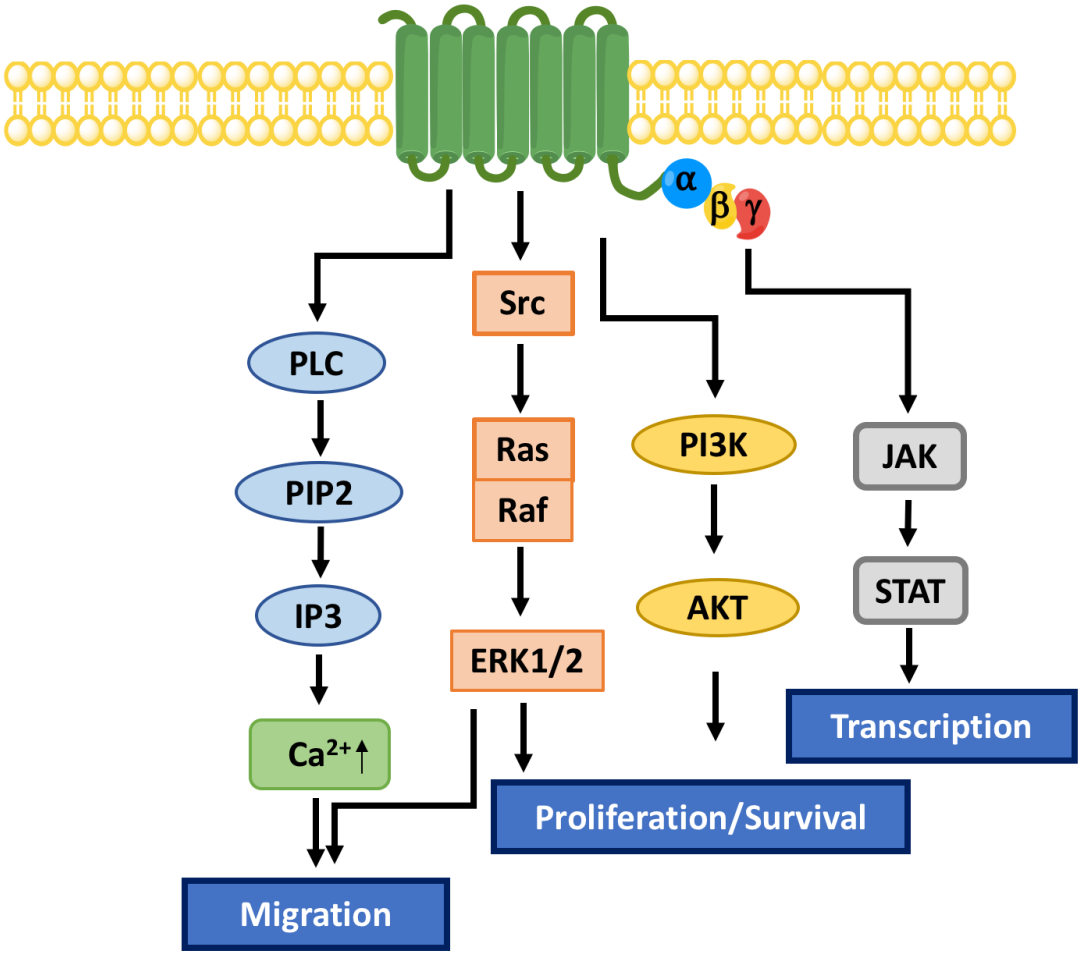

Figure 1.3 Chemokine receptor 4(CXCR4) mediated cellular pathways.

Chemokine receptor 4 has been found as co-receptor for HIV entry in 1996 (74). Since then, the focus of the CXCR4 study broadened from mere chemoattractant (80) to cell migration and cancer metastasis. CXCR4/CXCL12 axis regulates leukocytes trafficking (80), HIV infection (74), cell migration, and cancer metastasis (81). CXCR4 has a universal expression in different tissues and organs. Both the HPA and GTEx datasets showed that the RNA tissue category is expressed in all tissues that been studied (human protein atlas). It has a high expression level in immune-related tissues such as bone marrow, spleen, and lymph nodes (82). Functional CXCR4

protein is found on human epithelial cells (83, 84), endothelial cells (85), mast cells (86), and dendritic cells (87). CXCL12 chemoattracts cells that express CXCR4 along with the CXCL12 concentration gradients and play a pivotal role in a variety of physiological and pathological processes such as embryonic development, hematopoiesis, vascularization, inflammation, immune surveillance and cancer metastasis (79, 88). CXCR4 knockout mice exhibit hematopoietic and cardiac defects and fetal cerebellar development (89).

CXCR4 is the chemokine receptor that involves in the complex network of inflammation, wound healing, and cancer development. The network parallel with each other and well connected. As a result, CXCR4 participates and mediates various directional cell recruitment and triggers downstream signaling.

1.5.1 The significance of CXCR4 in cancer cells

Chemokine receptors are extensively expressed in the tumor cells and direct the tumor cells migration through the interaction with their ligands (90-92). CXCR4 is the major chemokine receptor expressed on tumor cells. CXCR4 was found to be expressed by over 23 types of cancer, including melanoma, breast cancer, and ovarian cancer (93). The expression levels are different between vary tumor types, primary tumor, and metastases and even different subpopulations of cells. The expression level of CXCR4 indicates cancer prognosis. Breast cancer is the most prevalent invasive cancer for women and comprises 16% of female cancer. Take breast cancer as an example; most breast tumor cells exhibit an elevated CXCR4 expression, whereas CXCR4 barely expressed in normal breast tissue. Xu et al. reported in 2013 that the overall survival and disease-free survival are negatively related to the CXCR4 expression level (94). Over 75% of triple-negative breast cancer patients have a high expression level of CXCR4 (95), and over-

expression of CXCR4 at primary tumor sites positively correlates the lymph mode metastasis and lower survival rates (96).

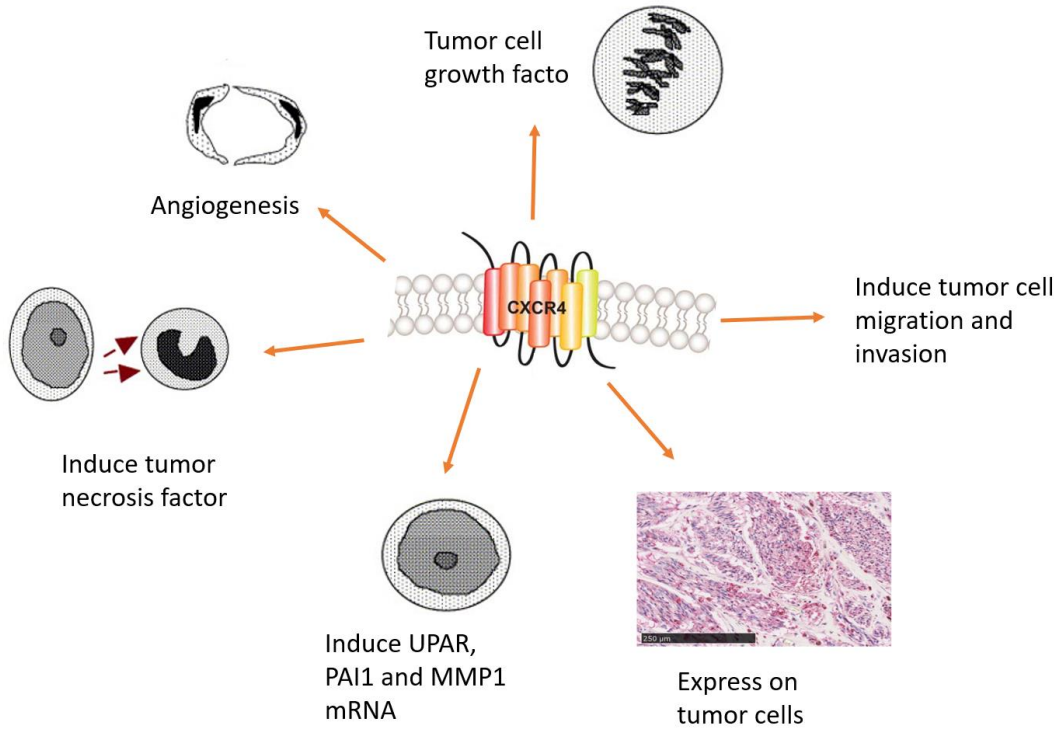

Figure 1.4 The roles of CXCR4 in cancer development.
Figure adapted from reference (90).

CXCR4 contributes to tumor immune suppression. One study shows that malignant human ovarian epithelial tumor cells have the high-level expression of stromal-derived factor-1and through the interaction with CXCR4, plasmacytoid DCs precursor chemotaxis, and adhesion/transmigration was activated. This protects plasmacytoid DCs precursor from tumor macrophage interleukin-10–induced apoptosis. (97) CXCR4 facilitates tumor growth. In human ovarian tumor cell line IGROV that has a high expression level of CXCR4, CXCL12 can stimulate cell growth *in vitro* (98).

CXCR4 expression levels vary from low to high in AML patients cells and is an independent prognostic marker in acute myelogenous leukemia (99). In multiple myeloma (MM), CXCR4 has been shown to involve in cancer homing and migration. The cancerous B-cells are attracted to bone marrow, where the stromal-cell secrets high level of CXCL12 (100). In acute myelogenous leukemia, the CXCR4/CXCL12 axis directs AML cells that express CXCR4 in the same fashion with directing normal hematopoietic stem cells migrate along with the CXCL12 gradient (101). Marrow stromal cells constitutively secrete CXCL12. Thus, the marrow niche provides a primary residual environment after chemotherapy. Specific aiming at mobilizing HSCs into the peripheral circulation, AMD 3100 as a potent, selective CXCR4 antagonist can antagonize CXCL12 binds to CXCR4 and interrupt the homing of AML cells to bone marrow stromal. By mobilization of AML cells into the peripheral circulation, AMD 3100 effectively sensitizing the AML cells to chemotherapy (101).

CXCR4/CXCL12 axis is found to be crucial for organ-specific metastasis, supported by the most common metastatic sites for CXCR4 positive cancer are those organs have high CXCL12 concentrations such as liver, lungs and bone marrow (102). Functional CXCR4 is expressed on breast tumor cells, breast tumor cells only metastasis to the organs and tissues strongly express the CXCR4 ligand, CXCL12, and the metastasis can be partially blocked by CXCR4 antibody (103). The majority of prostate cancer patients eventually develop metastases in the bone, which has a high CXCL12 level. It suggests that CXCR4/CXCL12 interaction plays an important role in prostate cancer metastasis (104). Therefore, the CXCR4 expression level is proposed to be a prognostic factor and therapeutic target for prostate cancer (105). The CXCL12 signaling study of human prostate cancer cell line-PC3 study by Fernandis, A.Z. proved that CXCL12 activates MEK/ERK signaling and NF-κB, which play an important role in cancerous cell survival (106).

CXCR4 inhibitors, including antibodies, peptides, and small molecules can reduce metastasis burden of prostate cancer cells in PCa mouse model studies (105, 107). CXCR4/CXCL12 axis also involved in regulating the metastasis in non-small cell lung cancer (108).

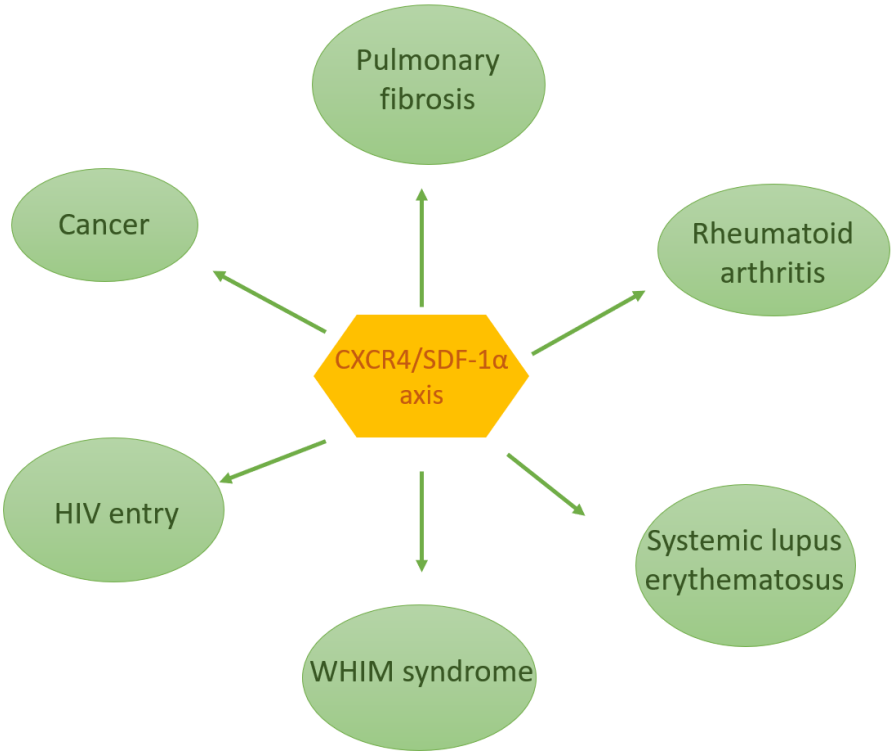

Figure 1.5 The role of CXCR4/SDF-1α axis in various diseases.
Figure adapted from reference (109).

1.5.2 CXCL12 in the cancer microenvironment

To date, numerous researches proved that tumor microenvironment (TME) provides habitat that favoring tumor proliferation, migration, and invasion. Carcinoma-associated fibroblasts (CAF) is one of the major cell types discovered in different tumors; CAF promotes tumorigenesis instead of suppressing tumor growth as normal fibroblasts do (110). CAF secret CXCL12 and stimulate breast cancer growth through the CXCL12 and CXCR4 interaction (111). CXCL12 promotes the expression of integrin and cancer cell adhesion in small cell lung cancer

(SCLC); α2, α4, α5 and β1 integrin mediates the adhesion of SCLC cells to fibronectin and collagen upon CXCL12 activation (112). A similar phenomenon is observed in prostate cancer PC3 study; CXCL12 treatment promotes the adhesion of PC3 cells to fibronectin (113).

Angiogenesis is another critical step for cancer progression; new forming vasculature guaranteed the nutrient supply for tumor growth. CXCL12 is proved to promote endothelial cell tube formation and angiogenesis (114, 115). *In vivo* study proved that the presence of CXCL12 is essential in blood vessel formation through a heme-oxygenase 1 dependent mechanism (116). Also, the CXCL12 level in plasma is related to bone marrow angiogenesis in multiple myeloma patients (117).

CXCL12 presented in the tumor microenvironment can also promote tumor cell proliferation and survival. In human glioblastoma cell lines study, CXCL12 treatment showed the ability to stimulate tumor cell growth; the CXCL12 dependent proliferation is correlated with phosphorylation and activation of pathways ERK (extracellular signal-regulated kinases) 1/2 and Ark (118).

1.5.3 CXCR4 as a therapeutic target

The critical role of the CXCR4-CXCL12 axis in various diseases and different stages of inflammation, cancers, and infectious diseases makes CXCR4 targeted therapy has strong translational potential. Intensive study on the structural biology of CXCR4 enriches the understanding of the CXCR4 structure and the interaction with ligands, including SDF-1 and other small molecules significantly. Wu et al. reported the crystal structure of CXCR4 in complex with IT1t, a small, drug-like, isothiourea derivative, and CVX15, a cyclic peptide characterized as CXCR4 inhibitor (Figure 1.6) (119).

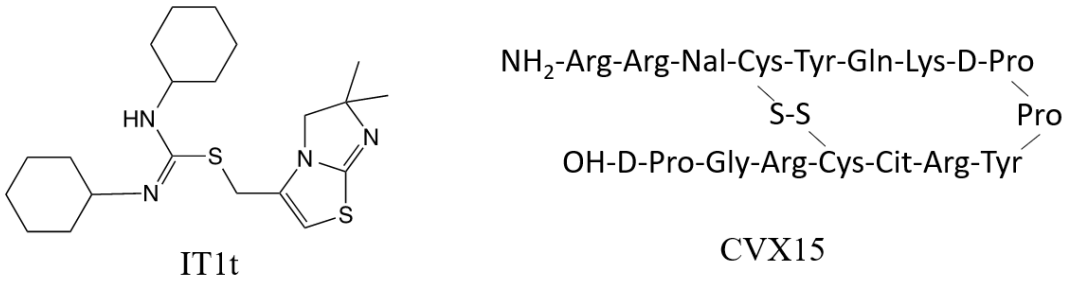

Figure 1.6 The chemical structure representation of CXCR4 antagonist IT1t and CVX15.

Massive attempts have been made on the development and optimization of the CXCR4 antagonists as anti-cancer and/or anti-HIV drugs. Overall, CXCR4 antagonists can be classified into peptide derivatives and small molecules. Cyclic peptide CVX15 and T140 can bind with CXCR4 and serve as a CXCR4 antagonist. Downsize of T140 to cyclopentapeptides and derivatives has successfully generated potent CXCR4 antagonists in cyclopentapeptide structures such as FC131 and FC122. FC131[cyclo(-D-Tyr-Arg-Arg-Nal-Gly-)] has the EC_{50} of 0.4 μM (120) and based on which a much more potent CXCR4 antagonist FC122 is synthesized with an EC_{50} of 88 nM (121).

Base on the cyclopentapeptides results, the SAR (structure-activity relationship) studies on cyclopentapeptide CXCR4 antagonists located the tripeptide motif L-/D-Arg1-Arg2-2-Nal3 as the minimal sequence for the antagonistic activity. A series of tripeptidomimetics of motif L-/D-Arg1-Arg2-2-Nal3 was synthesized and analyzed. Although no potent tripeptidomimetics were identified, the core structure still potentially be the bone structure for bulky CXCR4 antagonist development (122).

Another different approach of CXCR4 antagonist development based on the small molecules. Vitale et al. identified the phidianidine A (PHIA) as a new CXCR4 ligand through the

screening in a small marine natural product library available at ICB-CNR Institute (123). Truax et al. designed a series of tetrahydroisoquinoline analogs as CXCR4 antagonist with 3-650 nm potencies (124). AMD3100, brand name plerixafor, is a CXCR4 antagonist approved by the FDA in 2008 for the mobilization of hematopoietic stem cells (125). The effort has been made towards simplifying the AMD3100 structure to single cyclam connect to the aromatic structure by *p*-xylylenediamine linker (125). The computational approach to design the small molecule based on the SDF-1α interaction with CXCR4 has yield the small molecule CXCR4 ligands of μM scale potency (126).

1.5.4 CXCR4 molecular imaging

CXCR4, a chemokine receptor involves in numbers of the physio-pathological processes, has gained tremendous attention as a therapeutic target. Other than that, how to evaluate the CXCR4 expression non-invasively *in vivo* is the primary importance of monitoring and evaluate the treatment effects. However, current imaging techniques and agents are not able to assess CXCR4 expression. Hence, there is a critical unmet need for the development of CXCR4 specific imaging agent for molecular imaging purpose.

The important biological function and the potential role of the CXCR4/CXCL12 axis in the cancer development make CXCR4 targeting imaging and CXCR4 targeting therapy draw tremendous attention in the past decade. Developing CXCR4 specific imaging agent based on the research of CXCR4 antagonist development. By labeling the CXCR4 targeted small molecular or peptides with imaging agents is a basic approach for CXCR4 imaging agent development. T140 derivatives, FC131 derivatives, AMD 3100 derivatives, SDF-1α analogs, and CXCR4 targeting antibodies are all being used for CXCR4 contrast agent development (Figure 1.7). Among these, three classes of compounds are most extensively evaluated (127).

1. Bicyclams AMD3100 and AMD3465 with radiolabeling as PET or SPECT tracer.
2. Labeling of T140 peptide derivatives as PET, fluorescence tracer or hybrid tracer for multimodal imaging.
3. Labeling FC131 cyclic peptide derivatives for PET imaging.

^{64}Cu-AMD3100 (Figure 1.8 A) imaging capacity has been evaluated in the xenograft mouse model (128) and orthotopic and metastatic breast cancer mouse model (129). In the breast cancer mouse model, the tumor shows ^{64}Cu-AMD3100 uptake and the imaging effect can be blocked by unlabeled AMD3100 (129). The biodistribution study of ^{64}Cu-AMD3100 accumulation in liver, kidney, and immune-related organs and tissues such as bone marrow, spleen, and lymph nodes (130). [(99m)Tc] pertechnetate labeled AMD3100 (Figure 1.8 B) was used as a SPECT tracer to image the PC-3 bearing mouse model (131). It shows favorable CXCR4 binding and specific tumor affinity by CXCR4 targeting.

^{64}Cu-AMD3465 was investigated with glioblastoma models, the tumor-to-muscle and tumor-to-noise ratio are much higher than ^{64}Cu-AMD3100, suggesting the superior imaging capacity of ^{64}Cu-AMD3465 (132). However, a considerable amount of uptake in the liver and kidney were observed as well, although the liver and kidney have an intrinsic expression of CXCR4 that explains part of the uptake mediated by receptor. The non-specific liver and kidney of cyclams structure imaging agents still need to be further addressed.

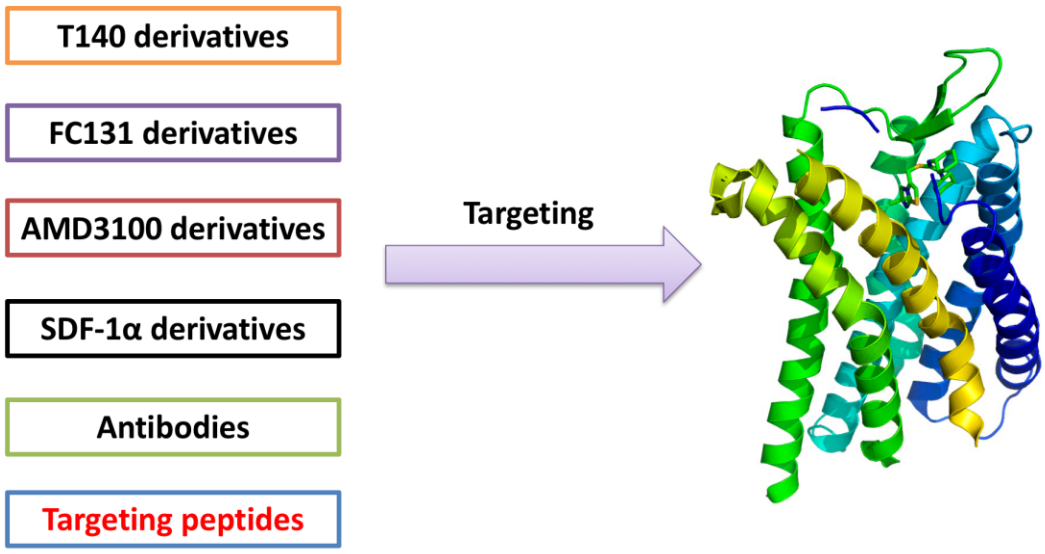

Figure 1.7 The targeting moieties for CXCR4 molecular imaging agents.
Targeting moieties including natural ligand of CXCR4, CXCL12 derivatives, CXCR4 antibodies, derivatives of CXCR4 antagonists and agonists were used for the current development of CXCR4 targeting imaging agent.

T140 peptide has a strong CXCR4 binding affinity; the T140 peptide derivatives have been labeled a series of radiometals as PET imaging tracer for CXCR4 molecular imaging. ^{68}Ga is suggested as a potential candidate for CXCR4 imaging for the favorable pharmacokinetics property and better tumor-to-muscle ratio (133). 4-^{18}F-T140 was proved to have low accumulation in the metabolic organs, including the liver and kidney (134). The biodistribution of 4-^{18}F-T140 is an advantage as opposed to AMD3100 based imaging for differentiating tumors in the metabolic organs with better signal-noise-ratio. Nishizawa K et al. reported the application of fluorescent CXCR4 antagonist TY14003 in superficial bladder cancer (135).

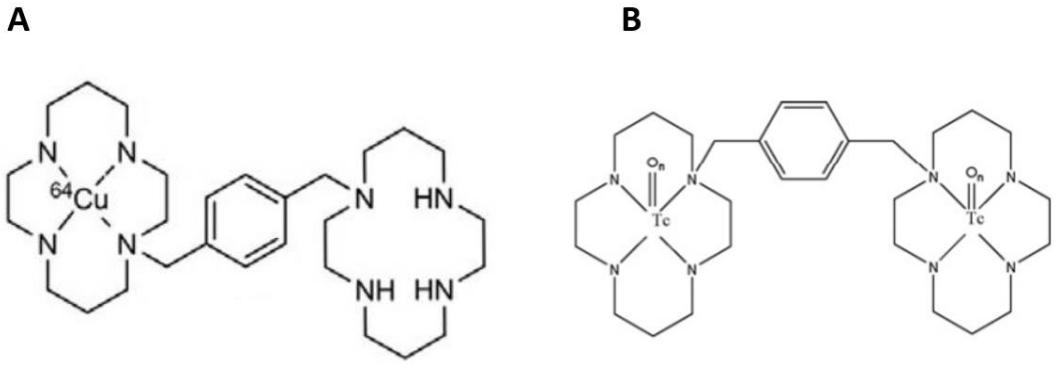

Figure 1.8 Structure of AMD3100 labeled CXCR4 imaging tracer.
A. ^{64}Cu labeled AMD3100 for PET imaging. B. [(99m)Tc]pertechnetate labeled AMD3100 for SPECT imaging.

F131 cyclic peptide derivatives show superiority as a PET tracer. ^{68}Ga-CPCR4-2 shows high stability and CXCR4 tumor specificity *in vivo*. In addition, it has very low accumulation in liver and kidney despite the renal clearance (136).

Tremendous effort has been made towards the development of CXCR4 specific imaging tracer. The majority of CXCR4 imaging tracers are nuclear medicine tracers. By labeled CXCR4 antagonist AMD3100 and the analogs, T140 peptide and derivatives, F131 cyclic peptide and derivatives, CXCR4 imaging have been achieved using PET, SPECT and fluorescence imaging. A good CXCR4 molecular imaging tracer is expected to have high tumor-to-muscle signal, low unspecific uptake, optimized pharmacokinetics property, and clearance. CXCR4 molecular imaging through MRI has not yet been reported. To develop the CXCR4 specific MRI contrast agent will fill the unmet need.

1.5.5 CXCR4 and uveal melanoma (UM)

Uveal melanoma (UM) is the most common primary intraocular malignancy in adults. Uveal melanoma almost exclusively metastasis to the liver (over 95%). Although it has progressively more early diagnosed but the prognosis still unrealistic cause the early metastasis.

The CXCR4/CXCL12 axis plays a crucial role in this process. First, the liver contains significant quantities of CXCL12, the natural ligand of CXCR4; it can attract CXCR4 positive cells. Moreover, cell-line based study of RT-PCT and flow cytometry (137) shows that all the primary uveal melanoma cell lines expressed CXCR4. Joseph Kim showed the CXCR4 expression in 89% (24 of 27) melanoma liver metastasis (138). A study by Bianca. D et al. on the Seventy formalin-fixed paraffin-embedded uveal melanoma patients' specimens shows the strong CXCR4 expression in the cytoplasm of uveal melanoma cells with an average immune reactive score (IRS) of 8.2 (139). Blocking the CXCR4-CXCL12 interaction with anti-CXCL12 antibody resulted in a reduction of chemotactic response, blocking CXCR4 expression by transfection of CXCR4 siRNA inhibited the invasive property of uveal melanoma (140). Besides, cross-talking between the CXCR4-CXCL12 axis and the VEGF (vascular endothelial growth factor) pathway were shown to benefit the tumor progression.

The patient tissue study detected CXCR4 protein of 41.4 percent cases (141). Blocking CXCR4 gene expression by transfection with CXCR4 siRNA inhibited invasive properties of uveal melanoma cells exposed to soluble factors produced by human livers (140).

The CXCR4-SDF1 axis plays an essential role in the organ-specific uveal melanoma metastasis. The CXCR4 expression level in primary melanoma is elevated, but the CXCR4 expression level in uveal melanoma is controversial, a cell line study conducted by H, Li discovered the primary melanoma cell lines express CXCR4 whereas metastasis cell lines showed the decreased expression level of CXCR4 (137).

1.5.6 CXCR4 and hepatocellular carcinoma (HCC)

Hepatocellular carcinoma (HCC) is the most common primary liver malignant disease with poor prognosis. HCC is associated with liver cirrhosis which caused by chronic inflammatory liver

diseases such as hepatitis B (HBV) and hepatitis C (HCV) infection, it also related to non-viral liver diseases including alcoholic fatty liver disease and non-alcoholic fatty liver diseases.

The role of CXCR4/SDF-1α in cancer is well recognized, and the intrinsic role of CXCR4 in HCC development is widely studied as well. One germen group evaluated the association of CXCR4 expression with HCC progression in both HCC cell lines and patient tissue study (142). They suggested the association of CXCR4 in HCC dissemination and played an important role in the tumor progression. In 2007, one immunohistochemical based patient tissue study located the CXCR4 overexpression in HCC sinusoidal endothelial cells when compared with none-HCC tissue, suggesting the CXCR4 expression mediated the neo-angiogenesis of HCC and can be a potential HCC treatment target (143). The same year, one study of mouse HCC cell lines with high and low metastases potential proved the relationship of CXCR4 and HCC metastasis again (144). Their main finding is CXCR4 has a significantly higher expression on the mouse hepatocarcinomatous cell lines with high potential of lymphatic metastasis (Hca-F) as opposed to the mouse HCC cell line with low potential of lymphatic metastasis (Hca-P). In addition, CXCR4 was found to correlate well with HCC patient bone metastasis, and the bone metastasis-free survival, which suggesting the CXCR4 expression as an independent risk factor for HCC (145). CXCR4 antagonist AMD3100 is used in combination with a broad kinase inhibitor—Sorafenib to prevent fibrosis in HCC (146).

Overall, CXCR4 expression in HCC consider as an independent risk factor and result in poor prognosis. The CXCR4 expression in HCC elevated and involved in neo-angiogenesis and metastasis. As a result, mapping and monitoring the CXCR4 level *in vivo* with non-invasive imaging assay has strong translational potential and improves the disease management as well as treatment.

1.6 Motivation and challenges of this research

The development of non-invasive imaging techniques and probes is pivotally important in improving the standard of care in cancer and cancer-related diseases. As the development in molecular cell biology, understanding about tumor etiology reach to an unprecedented level. Malignant diseases consist of various spectrum of molecular, cellular and systemic events and forming complex networks through chemokines chemokine receptors and cell signal pathways. Numerous cancer-related research and anti-tumor drug development have been done, and a lot more is undergoing. Assessment of cancer can no longer stay at a macroscopic level and satisfy the needs of researchers and clinicians.

Molecular imaging is a relatively new field; the development of molecular imaging techniques is an interdisciplinary subject. It has the potential to fulfill the needs in diagnosis, monitoring, and prognosis with a more detailed, microscopic, molecular level. The development of molecular imaging tracers and probes has the potential to facilitate the disease follow up in a personalized fashion tailored to individual patients. Molecular imaging that provides the local microenvironment information can guide the treatment stratification. Screening and assessing immune-related drugs more specific for individual targets of cancer required the assistant of molecular imaging as well.

Molecular imaging tracer is necessary for the achieving of molecular imaging. Molecular imaging is rooted in radiotracers owing to the intrinsic sensitivity of nuclear medicinal imaging modalities. F-18-FDG is widely used in clinical practice. Magnetic resonance imaging has the advantage of being non-radiation involved, with no depth limitation and 3D imaging in high resolution. Research has been concentrated in apply magnetic resonance spectroscopy, diffusion MRI, CEST MRI for molecular MRI.

The significance of the CXCR4/SDF-1α axis in cancer-related events is well recognized. CXCR4 plays roles in different types of cancers, different stages of cancers, and the overexpression of CXCR4 in tumor tissue sees as an independent risk factor leads to poor prognosis and higher metastasis potential. Therefore, the development of CXCR4 specific imaging agents is significant for cancer-related researches and pre-clinical, clinical cancer research. We devoted to developing new classes of protein-based MRI contrast agent platform for a series of cancer-related biomarkers including HER2, PSMA, GRPR, EGFR, CXCR4, and collagen. For better understanding of tumor microenvironments and identifying treatment targets. The platform technique of protein-based contrast agent is translational to different metals and different targeting labeling.

Challenges regarding this research are to develop specific biomarker targeted MRI contrast agent with enough sensitivity for the molecular imaging application. Relaxivity is an important factor to consider in the development of novel MR molecular imaging. Resolve the delivery of the imaging reagents is another challenge. We aim at delivering the MR imaging agents efficiently to the tumor region and optimized penetration for heterogeneity biomarkers detection. The cancer-related biomarker usually in a μM local range, to develop contrast agent with CXCR4 specific targeting capability and dynamic imaging capacity to enable the contrast agent specifically accumulates at targeting tissue and lesions and minimize the off-target binding is another challenge about this research.

Pharmacokinetics property of contrast agent is closely related to the imaging capacity and translational potential. Small molecules contrast agents possess short half-life and clearance to have a short time window for imaging. As blood pool agents, it would not be a big drawback. On the contrary, the shorter half-life will relatively reduce the risk of unwanted metal retention.

However, the *in vivo* targeting process is dynamic and influenced by blood flow, temperature, local tissue permeability, endocytosis. It is a very complicated process and might not be as time efficiency. We want to design contrast agents with suitable pharmacokinetic properties to enable the efficient *in vivo* delivery, binding and imaging, at the same time with proper clearance and less risk of metal toxicity caused by metal dissociation. To tune the pharmacokinetic property is a fine line and requires a great balance between imaging capacity and safety.

Simultaneous detection of multiple biomarkers that related to each other and reveal the spatial coregistration will take molecular imaging further. Owing to the platform technique of protein-based contrast agent is readily translational for different metal labeling. Once labeling with different paramagnetic metal ions, such as gadolinium, manganese, and dysprosium, ProCAs are expected to have different relaxivities. Once different metal ions labeled ProCAs attach to different targeting moieties, we expect to achieve simultaneous MR imaging of multi-biomarkers. To achieve so, the time of imaging acquisition, imaging acquisition sequence, higher spatial resolution, and the influence of innate tissue relaxivities. will be factors that have to take into consideration.

1.7 Overview of this dissertation

This dissertation consists of 10 chapters in total.

Chapter 1 is the introduction chapter and summarized the basic background information of this research. Including the cancer disease-related background, molecular imaging development, and approaches have been applied, and attempts have been made. Most of the molecular imaging research is done with nuclear medicine imaging, including PET, SPECT, and some multi-models imaging platform and tracers. Magnetic resonance imaging has the advantages of being non-radiation, non-invasive, and excellent spatial resolution. CXCR4 is an important chemokine

receptor in various cancer-related incidence. Developing CXCR4 targeted MRI contrast agents is expected to benefit cancer diagnosis, treatment monitoring, and prognosis.

Chapter 2 is the chapter of material and methods; it described the related experimental details of the experiments conducted in this research. All the material is used, and the method conducted is listed in detail in this chapter.

Chapter 3 is the chapter of CXCR4 targeted contrast agent design and production. Chapter 3 includes the rationale of design ProCA32.CXCR4, details of protein production and formulation and related results are described in this chapter.

Chapter 4 is the biophysical property study of ProCA32.CXCR4. Chapter 4 introduce the relaxivity, metal-binding capability, and selectivity, serum stability, transmetallation study of ProCA32.CXCR4.

Chapter 5 is the chapter of CXCR4 expression and detailed results of cell lines, animal models, patients' tissue.

Chapter 6 is the chapter summarizes the application of ProCA32.CXCR4 in cancer diagnosis, including uveal melanoma and ovarian cancer. Chapter 6 in detail documented the animal models, MRI scans, and histology correlation of pathology results with MRI results of mouse models.

Chapter 7 is the chapter regarding the application of ProCA32.CXCR4 in HCC diagnosis and treatment effect monitoring. Chapter 7 records detailed background information and related experimental results of ProCA32.CXCR4 in hepatocellular carcinoma.

Chapter 8 is a chapter regarding manganese-based contrast agent and multicolor MRI acquisition development. Including the initial result of Mn-ProCA32.CXCR4 relaxivities. Prediction of Mn-ProCA32.CXCR4 and Gd-ProCA32.CXCR4 concentration with relaxometer

and the potential application for multicolor MRI. Chapter 8 also includes the development of integrin $\alpha_v\beta_3$ targeted contrast agent ProCA32. RGD. The rationale of design integrin $\alpha_v\beta_3$ targeted contrast agent was documented. The initial characterization of ProCA32.RGD, including metal binding affinity, relaxivities, and integrin $\alpha_v\beta_3$ targeting capability were performed. ProCA32.RGD has been applied for breast cancer detection in a 4T1 mouse model.

Chapter 9 is the conclusion and significance of this dissertation research and summarized all the important scientific findings of this work and significance.

2 MATERIAL AND METHODS

2.1 CXCR4 expression study

2.1.1 Flow cytometry analysis

Flow cytometry was performed to quantify the expression of CXCR4. Cultured human uveal melanoma cells were dissociated with non-enzymatic cell dissociation solution (Sigma-Aldrich, St. Louis, MO). Cells were stained for 20 minutes at 4°C with APC mouse anti-human CD184 (clone 12G5) (BD Biosciences, San Jose, CA). Data acquisition was performed using a Becton Dickson Aria IIu FACS sorter (BD Biosciences, San Jose, CA). FlowJo software (Tree Star, Ashland, OR) was used for data analysis.

2.1.2 Immunohistochemical (IHC) analysis

UM patients' liver tissue and UM mouse model tissue were stained with CXCR4 antibody for IHC study. Briefly, tissue was fixed in 10% neutral buffered formalin and embedded in paraffin. The tissue blocks were then sliced with 5 μM thickness for staining. Paraffin-embedded sections were first deparaffinized and rehydrated. After rehydration, 1 part of 30% hydrogen peroxide and 9 parts of absolute methanol mixture was used to quench endogenous peroxidase

activity for 10 min, followed by washing with TBST for 3 times, each time for 5 min. Antigen retrieval was achieved by boiling in target retrieval solution (Agilent) for 20 min. Slides were then washed with TBST for 3 times, each time for 5 min, blocked in 5% bovine serum albumin (BSA, Thermo Fisher) in TBST for 2 h, and incubated with 1:300 dilution of primary antibody anti-CXCR4 antibody 12G5 (Abcam, ab189048) in TBST O/N at 4°C. The IHC staining was performed with a red chromogen kit following the corresponding protocol. Counter staining of the nucleus was performed with hematoxylin. A CXCR4 positive control (brain specimen) was processed with the same protocol. All cases of uveal melanoma (UM) hepatic metastases exhibited high expression levels of CXCR4, indicated by the brilliant red color staining.

2.2 ProCA32.CXCR4 expression, purification, and PEGylation

2.2.1 Protein design

ProCA32.CXCR4 is designed by linking a 21-mer targeting moiety to the C-terminus of ProCA32 with a flexible linker. The targeting moiety is derived from the N-terminus region of CXCR4 binding virus chemokine vMIP-II. The sequence of targeting moiety consists of 21 amino acid (LGASWHRPDKFCLGYQKRPLP) and including the key residues for CXCR4 interaction.

2.2.2 Expression

ProCA32.CXCR4 was expressed by *BL21 (DE3) pLysS* cell strain. Briefly, ProCA32.CXCR4 plasmid was transformed to *BL21 (DE3) pLysS* competent cells and a single colony was inoculated to 250 mL of 2.5% LB medium for small-scale culturing overnight at 37°C. The small-scale culture was then transferred to 1 L of 2.5% LB medium for large-scale culturing at 37°C and monitoring the optical density at 595 nm (OD_{595}). 0.5 mM isopropyl β-D-1-thiogalactopyranoside (IPTG) was used for induction protein expression when the OD_{595} reach

between 0.6 to 0.8. Protein was expressed at 37°C for 3 h after induction, and the temperature was adjusted to 25°C for overnight expression. Cell pellets were collected by centrifuging for 25 min at 7000 rpm.

2.2.3 Purification

Cell pellets collected from expression were suspended by Phosphate-buffered saline (PBS), in 1 g cell pellet to 10 mL PBS ratio and mixed thoroughly. Sonication is then used for breaking up the cell membrane and release cell content, cells were sonicated for 10 times, each time for 2 min, with 5 min intervals between each to avoid over-heat. The cell lysate was then pelleted down by centrifuging, and the supernatant was boiled for 10 min to remove impurities. The supernatant was incubated with 3% streptomycin overnight at 4°C to remove further impurities (i.e., DNA). After repeat centrifuging and boiling, the supernatant was placed in 10 mM HEPES (4-(2-hydroxyethyl)-1-piperazineethanesulfonic acid) buffer, pH 8.0 overnight at 4°C for dialysis. After dialysis, 40mM EGTA (ethylene glycol tetraacetic acid) was added into ProCA32.CXCR solution to chelate Ca^{2+} and other cations, and HiTrap Q HP anion exchange chromatography column (GE Healthcare) was used to finish purification.

2.2.4 Lysine PEGylation

Methoxy PEG Succinimidyl Carboxymethyl Ester reagent with the molecular weight of 2 kDa (JenKem Technology) was used for lysine PEGylation. ProCA32.CXCR4 was mixed with PEG reagent with a molar ratio of 1:5 and then shake at room temperature for 2 h or at 4°C for overnight. Excess non-reacted NHS-ester was quenched by 100 mM Tris buffer for 30 min at ambient temperature. The purification of the PEGylated protein sample was achieved by FPLC.

Polyacrylamide gel electrophoresis combined with coomassie-blue and iodine (I_2) staining was applied to test the PEGylation efficiency.

2.2.5 Cysteine PEGylation

Methoxy PEG maleimide (JenKem Technology) with a molecular weight of 2 kDa was used for cysteine PEGylation. A good protein concentration for PEGylation is between 1-10 mg/mL. 100x molar excess of Tris (2-carboxyethyl) phosphine hydrochloride (TCEP, Sigma-Aldrich) was added and reacted at room temperature for 20 minutes to reduce disulfide bond of ProCA32.CXCR4. Amicon concentrator was applied to remove the unreacted free TCEP. Maleimide PEG was mixed with reduced ProCA32.CXCR4 with a molar ratio of 1:1. The mixture was degassed with nitrogen, closed tightly, and reacted overnight at 4°C. MALDI (matrix-assisted laser desorption/ionization) Mass-spectrometry and coomassie-blue and iodine (I_2) staining were applied to analyze the PEGylation product.

2.3 Determination of *r*1 and *r*2 relaxivity values

To determine the relaxivity of ProCA32.CXCR4, different concentrations of ProCA32.CXCR4 from 0 μM (buffer only) to 100 μM were prepared in 50 mM HEPES, 100 mM NaCl, PH 7.2. The samples were incubated at 37°C for one hour before measurement. The relaxation times (T1 and T2) of different concentration of ProCA32.CXCR4 were measured by Bruker minispec relaxometer (60MHz) and the phantom was scanned by 7.0 T Bruker MRI scanner. Commercial GBCA such us Dotarem®, Magnevist®, Eovist® etc. were prepared with the same buffer and measured with same protocol. However, the concentration range was from 0 mM (buffer only) to 160 mM. Relaxivity values (r_1 and r_2) were calculated by the following equation.

$$r_i = \frac{\frac{1}{T_{i_{sample}}} - \frac{1}{T_{i_{buffer}}}}{[Gd^{3+}]_T}$$

Equation 2.1

Whereas the $T_{i_{sample}}$ is the relaxation time of contrast agent samples and the $T_{i_{buffer}}$ is the relaxation time of buffer only, $[Gd^{3+}]_T$ is the Total concentration of Gd^{3+}.

2.4 Metal-binding affinity and selectivity study

2.4.1 Determination of Tb^{3+} binding affinity of ProCA32.CXCR4

Fluorescence spectra were collected with QM1 fluorescence spectrophotometer (PTI) at room temperature. Tb^{3+}-tryptophan luminescence resonance energy transfer (LRET) emission spectrum (500 nm to 600 nm) was acquired following a 280 nm excitation. 30 μM of ProCA32.CXCR4 was added into DTPA chelator buffer (5 mM DTPA, 50 mM HEPES, 150 mM NaCl, pH 7.2) for titration. DTPA has a strong binding affinity to Tb^{3+} (K_d= 10^{-21} M, 25 °C). The "free" Tb^{3+} concentration can be calculated by:

$$[Tb^{3+}]_{free} = Kd_{Tb,DTPA} \times \frac{[Tb - DTPA]}{[DTPA]_{free}}$$

Equation 2.2

Whereas we assume the "free" Tb^{3+} is the portion triggered the LRET and cause fluorescence signal change, the Tb^{3+} binding affinity of ProCA32.CXCR4 can be calculated by the equation:

$$f = \frac{[Tb^{3+}]_{free}{}^{n}}{Kd_{Tb,ProCA32.CXCR4}{}^{n} + [Tb^{3+}]_{free}{}^{n}}$$

Equation 2.3

where *f* is the fractional LRET signal change followed each of titration points, n is the hill number.

2.4.2 Determination of Gd^{3+} binding affinity of ProCA32.CXCR4.

A competition method was applied to evaluate the Gd^{3+} binding affinity of ProCA32.CXCR4. 10 μM of ProCA32.CXRC4 and 20 μM Tb^{3+} were prepared in 5 mM DTPA (diethylenetriamine pentaacetate), 50 mM HEPES, 150 mM NaCl at pH 7.2, and incubated with different concentrations of Gd^{3+}, from 0 μM to 200 μM, at room temperature for overnight. By fitting the fluorescence signal decrease at 545 nm as the Gd^{3+} concentration increase, the apparent K_d of Gd^{3+} compete with terbium can be calculated by the equation:

$$f = \frac{\left([Tb]_T + [Gd]_T + K_{d_{app}}\right) - \sqrt{([Tb]_T + [Gd]_T + K_{d_{app}})^2 - 4 \times [Tb]_T \times [Gd]_T}}{2 \times [Tb]_T}$$

Equation 2.4

Where *f* is the fractional LRET signal change, $[Tb]_T$ is the total Tb^{3+} concentration, $[Gd]_T$ is the total Gd^{3+} concentration. K_{dapp} is the apparent dissociation constant of Gd^{3+} compete with Tb^{3+}.

The dissociation constant of Gd^{3+} binds to ProCA32.CXCR4 can be calculated by equation:

$$K_{d_{Gd,ProCA32.CXCR4}} = K_{d_{app}} \times \frac{K_{d_{Tb,ProCA32.CXCR4}}}{K_{d_{Tb,ProCA32.CXCR4}} + [Tb^{3+}]_T}$$

Equation 2.5

Where $K_{dTb,ProCA32.CXCR4}$ is the dissociation constant of Tb^{3+} binds to ProCA32.CXCR4, $[Tb^{3+}]_T$ is the total Tb^{3+} concentration.

2.4.3 Determination of Ca^{2+} binding affinity of ProCA32.CXCR4

The dissociation constant between ProCA32.CXCR4 and Ca^{2+} was determined by a similar assay that was developed by Tsien (147). 10 µM of ProCA32.CXCR4 was prepared in 5 mM EGTA (ethylene glycol tetraacetic acid), 50 mM HEPES, 150 mM NaCl at pH 7.2. Different concentration of Ca^{2+} was titrated into the system. Fluorescence change upon each titration was monitored by the emission spectrum of 200 nm to 300 nm followed by excitation of 280 nm, the concentration of free Ca^{2+} can be calculated by the equation:

$$[Ca^{2+}]_{free} = K_{d_{Ca,EGTA}} \times \frac{[Ca - EGTA]}{[EGTA]_{free}}$$

Equation 2.6

Where the dissociation constant of Ca^{2+} to EGTA ($K_{dCa,EGTA}$) is 1.51×10^{-7} M, The K_d of Ca^{2+} to ProCA32.CXCR4 ($K_{dCa,ProCA}$) can be determined by equation:

$$f = \frac{[Ca^{2+}]_{free}{}^{n}}{K_{d_{Ca,ProCA32.CXCR4}}{}^{n} + [Ca^{2+}]_{free}{}^{n}}$$

Equation 2.7

Where f is the fractional change of Tryptophan fluorescence intensity, $[Ca^{2+}]_{free}$ is the free Ca^{2+} concentration of each titration.

2.4.4 Determination of Zn^{2+} binding affinity of ProCA32.CXCR4.

The dissociation constant between Zn^{2+} and ProCA32.CXCR4 was determined by a modified fluorescence competition assay. In detail, 2 μM of Zn^{2+} and FluoZin™-1 (ThermoFisher) was prepared in 1:1 ratio, different concentrations of ProCA32.CXCR4 were titrated, fluorescence emission spectrum of 500 nm to 600 nm was acquired by 495 nm excitation, the apparent K_d of ProCA32.CXCR4 competes with Zn^{2+} can be calculated by the equation:

$$f = \frac{\left([Zn]_T + [ProCA32.CXCR4]_T + K_{d_{app}}\right) - \sqrt{([Zn]_T + [ProCA32.CXCR4]_T + K_{d_{app}})^2 - 4 \times [Zn]_T \times [ProCA32.CXCR4]_T}}{2 \times [Zn]_T}$$

Equation 2.8

Where $[Zn]_T$ is the total Zn^{2+} concentration and $[ProCA32.CXCR4]_T$ is the total ProCA32.CXCR4 concentration, K_{dapp} is the apparent dissociation constant. Knowing the dissociation constant of Zn^{2+} to Fluozin-1, the dissociation constant between Zn^{2+} and ProCA32.CXCR4 can be calculated by equation:

$$K_{d_{Zn,ProCA32.CXCR4}} = K_{d_{app}} \times \frac{K_{d_{Zn,Fluozin}}}{K_{d_{Zn,Fluozin}} + [Fluozin]_T}$$

Equation 2.9

Where K_{dapp} is the apparent dissociation constant of ProCA32.CXCR4 compete with Fluozin-1.

2.4.5 Determination of Mn^{2+} binding affinity of hProCA32.collagen1

The Mn^{2+} binding affinity of hProCA32.collagen1 was determined with a competition assay similar to Gd^{3+}-ProCA32.CXCR4 binding affinity determination. 10 μM of hProCA32.collagen1 was prepared with 20 μM of Tb^{3+} in 5 mM DTPA, 50 mM HEPES, 150 mM

NaCl at pH 7.2, different concentrations of Mn^{2+} (from 0 μM to 1000 μM) were then added into solution and incubate at ambient temperature for O/N. Fluorescence spectra of each sample are collected, and apparent K_d of Mn^{2+}-Tb^{3+} competition was fitted against the fractional fluorescence signal change at 545 nm by the equation:

$$f = \frac{\left([Tb]_T + [Mn]_T + K_{d_{app}}\right) - \sqrt{([Tb]_T + [Mn]_T + K_{d_{app}})^2 - 4 \times [Tb]_T \times [Mn]_T}}{2 \times [Tb]_T}$$

Equation 2.10

Whereas the f is the fractional fluorescence signal change, $[Tb]_T$ is the total Tb^{3+} concentration, $[Mn]_T$ is the total Mn^{2+} concentration and K_{dapp} is the apparent K_d of Mn^{2+}-Tb^{3+} competition.

By knowing the apparent K_d of Mn^{2+}-Tb^{3+} competition and the Tb^{3+} binding affinity of protein contrast agent, the disassociation constant of Mn^{2+} to contrast agent can be calculated by the equation:

$$K_{d_{Gd,ProCA32}} = K_{d_{app}} \times \frac{K_{d_{Tb,ProCA32}}}{K_{d_{Tb,ProCA32}} + [Tb^{3+}]_T}$$

Equation 2.11

2.5 Determination of the water coordination number of ProCA32.CXCR4

The water coordination number of ProCA32.CXCR4 was measured by terbium luminescence decay of ProCA32.CXCR4 – Tb^{3+} complex in H_2O and D_2O adapted from a reported assay (148). ProCA32.CXCR4 – Tb^{3+} complex was prepared in the H_2O and D_2O solution in 1:1 and 1:2 ratio. Tb^{3+} was excited by the xenon lamp at 265 nm and the terbium luminescence decay lifetime was collected at the emission of 545 nm. By fitting the decay curve with exponential decay, K_{H2O} and K_{D2O} can be obtained, ΔKobs is the difference between luminescence decay of

ProCA32.CXCR4 – Tb^{3+} complex in H_2O and D_2O. Standard curve of water number of different chelators are used to calculate the water number of ProCA32.CXCR4.

2.6 Cell culture

Melanoma cell lines, including B16LS9, Mel290, Mel270, 92.1, M20-09-196 were used in this study. The culture medium recipe is 500 mL RPMI 1640 1X with L-Glutamine with 10% fetal bovine serum (FBS), 12.5 mL Corning™ HEPES, 1 M solution (fisher scientific), 5 mL Corning™ Sodium Pyruvate 100mM Solution (fisher scientific), 5 mL Corning™ cellgro™ MEM Nonessential Amino Acid Solution (fisher scientific), 5 mL Corning™ MEM Vitamin Solution (fisher scientific) and 5 mL Penicillin-Streptomycin solution. All cells were thawed at 37°C and transferred to a 100 mm cell culture dish with 6 mL of medium. After reach over 90% of confluence, cells were washed by HBSS and suspended by 1 to 2 mL of 1% trypsin and centrifuged for 5 min at 1000 rpm. Then cells were passed to two 100 mm culture dish to keep culturing. Cells were frozen with a commercial freezing medium containing 10 % DMSO (dimethyl sulfoxide) for cryopreserving.

2.7 Cancer cell targeting study

2.7.1 Flow cytometry analysis

The flow cytometry was performed to quantify the expression of CXCR4. Cultured human uveal melanoma cells were dissociated with non-enzymatic cell dissociation solution (Sigma-Aldrich, St. Louis, MO). The cells were stained for 20 minutes at 4°C with APC mouse anti-human CD184 (clone 12G5) (BD Biosciences, San Jose, CA). Data acquisition was performed using a Becton Dickson Aria IIu FACS sorter (BD Biosciences, San Jose, CA). FlowJo software (Tree Star, Ashland, OR) was used for data analysis.

2.7.2 Immunofluorescence staining

2.7.2.1 NHS-fluorescein labeling protein

Fluorescein-5-EX N-hydroxysuccinimide ester (Sigma-Aldrich) was used to label ProCA32.CXCR4 and ProCA32. Protein solution concentrated between 1-10 mg/mL was prepared in 10 mM HEPES, pH 8.0 (Other non-amide-containing buffers at pH 7.0-9.0 may also be used). NHS-fluorescein was equilibrium to room temperature before reaction. 15 molar excess of NHS-fluorescein was mixed well with the protein solution and react at room temperature for 1 h. Non-reacted NHS-fluorescein was quenched by adding 100 mM Tris buffer. Protein was purified by gel filtration.

2.7.2.2 Immunofluorescence staining with melanoma cells to evaluate the CXCR4 binding affinity of ProCA32.CXCR4

Melanoma cell lines including B16SL9, Mel290, M20-09-196 were used for immunofluorescence staining. Melanoma cells were cultured until reaching 50-70% confluence and fixed on cover slides with 3.7% formaldehyde solution at 4°C. Fixed melanoma cells were incubated with 5μM NHS-fluorescein labeled ProCA32.CXCR4 (the control group was incubated with fluorescein-labeled ProCA32) for 1 h at 37 °C. The cells were washed thoroughly with TBS-Tween 20 (TBST) buffer. DAPI (4',6-diamidino-2-phenylindole, ThermoFisher) was used for nucleus staining, and the cells were imaged with Zeiss microscope. For colocalization study, after incubation with NHS-fluorescein labeled ProCA32.CXCR4, melanoma cells were then blocked with 5% BSA (prepared in TBST buffer) for 20 min at room temperature and incubated with 0.1% dilutions of primary antibody for CXCR4 (Abcam, ab189048) at 4 °C for overnight. After thoroughly washed with TBST buffer, melanoma cells were incubated with 0.1% dilutions of Goat anti-Mouse secondary antibody (Invitrogen, Alexa Fluor 555) for 60 min at room temperature.

DAPI (ThermoFisher) was applied to stain the nucleus, and slides were covered by coverslip and sealed. Colocalization analyses of red fluorescence (555 nm excitation) and green fluorescence (488 nm excitation) were done using Fiji's plugin coloc2.

2.7.2.3 Immunofluorescence staining of mouse tissue

The liver tissue of Mel290 mice was collected after injection of ProCA32.CXCR4 and ProCA32, and immunofluorescence staining was performed on collected liver tissues. 4 μM Cryosections of Mel290 mice livers were thawed at room temperature for 20 min and rehydrate the tissue sections with TBST. Tissue sections were surrounded with a hydrophobic barrier using Dako pen (Agilent) and blocked with 5% BSA for 60 min at room temperature then incubated with home-made ProCA32.CXCR4 and ProCA32 primary antibody (1:50 dilution) for 60 min at room temperature. After thoroughly washed with TBST, tissue slides were incubated with 0.1% dilution of Goat Anti-Rabbit secondary antibody (Invitrogen, Alexa Fluro-555) for 60 min at room temperature. DAPI (ThermoFisher) was then applied to stain the nucleus, and slides were covered and sealed.

2.7.3 Enzyme-linked immunosorbent assay (ELISA)

An indirect ELISA assay (Fig. 2.1) was used to quantify the CXCR4 targeting capability. Melanoma cells with CXCR4 expression were used to determine the ProCA32.CXCR4 targeting.

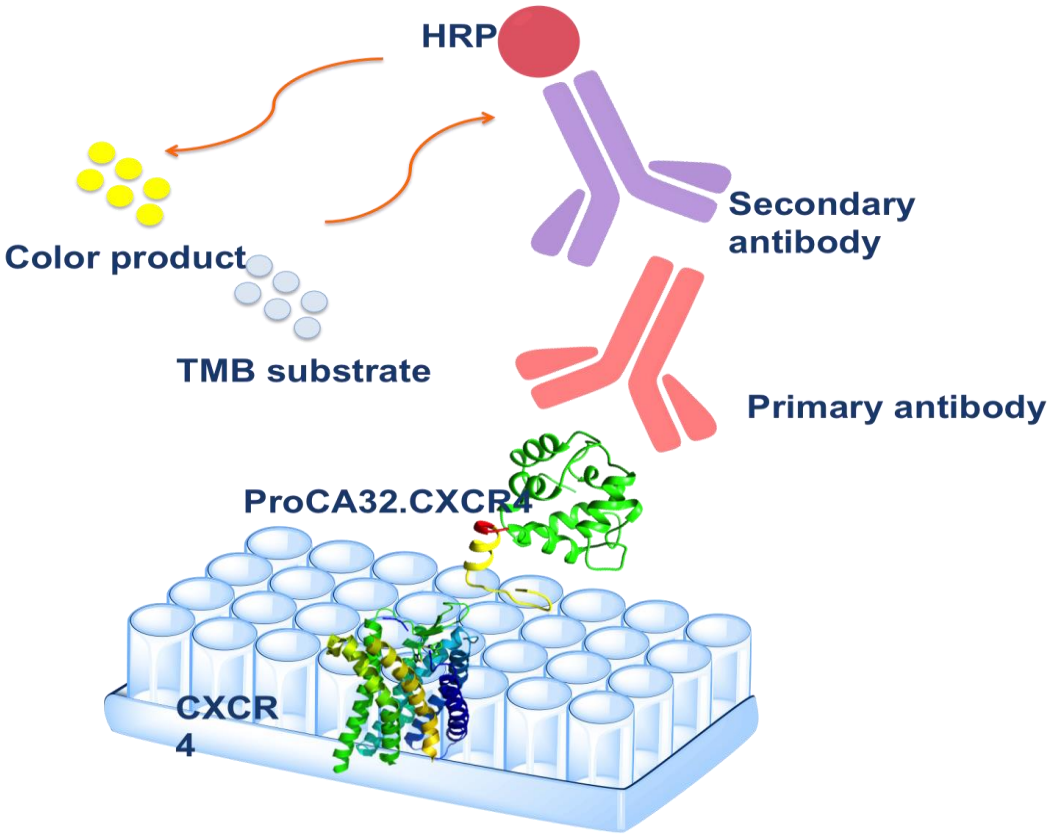

Figure 2. 1 Determing the CXCR4 binding affinity with indirect ELISA.

2.7.3.1 Preparation of cell lysate.

The cells were cultured in T-75 flasks until reach to about 90-95% confluence, and gently washed by HBSS before collected by plastic cell scraper. 1 ml of HBSS buffer was added into the flask, and cells were scraped from the flask. The mixture solution was transferred to a pre-cold tube and centrifuge at 8000 rpm for 10 min at 4C° to pellet down cells. The supernatant was gently decanted and 1 ml of RIPA buffer was added to lyse the cells for 1 h at 4C°. The mixture was then centrifuged at 12,000 rpm for 30 min at 4C° to remove the cell debris. The supernatant was collected as cell lysate, and the total protein concentration of cell lysate was measured by Bio-Rad assay.

2.7.3.2 Indirect ELISA

Melanoma 290 cell lysate in $NaHCO_3$ solution (pH 9.6) was incubated in 96-well plates overnight at 4 °C. The 96-well plates were washed thoroughly by TBST buffer and blocked by 5% BSA solution (prepared in TBST) for 60 min at room temperature. Different concentrations of ProCA32.CXCR4 (0 nM to 5000 nM, prepared in TBST) was added in different wells and incubated for one hour at room temperature. 0.1% ProCA32.CXCR4 antibody (self-generated polyclonal rabbit antibody) was added for 60 min incubation at room temperature. The secondary antibody, stabilized goat-anti-rabbit HRP-conjugated antibody (Pierce), was incubated for 45 min at room temperature. After washed with TBST, 100 µL of 1-Step™ Ultra TMB-ELISA Substrate Solution (ThermoFisher) was added into each well to visualize the color change. When a yellow gradient color was observed, 100 µL of 1 M H_2SO_4 was added into each well to terminate the reaction. The absorbance intensity at 450 nm wavelength was measured by FLUOstar OPTIMA plate reader, and data were plotted using GraphPad Prism 5.

2.7.4 MRI phantom scanning of ProCA32.CXCR4 incubated melanoma cells

CXCR4 expression cell lines are cultured according to the requirement. Cells are washed with PBS to remove serum and protein in the culture media. After that, cells were incubated with ProCA32.CXCR4 at 37°C for one hour. Wash the cells gently for three times with PBS buffer. Cells are collected with non-enzymatic cell dissociation solution and centrifuge with 1000 rpm for 5 minutes. Supernatant decanted gently to remove the PBS and gently resuspend the cells with PBS again. Repeat three times. Cell pellets are collected and transferred to the small tube for the phantom experiment to determine the relaxivities.

2.7.5 Cell attachment assay

The cells were cultured overnight under standard conditions. Next day, different cells (with appropriate cell numbers) were transferred to a new plate with wells that were coated with different proteins (indicated in the figures) with fresh medium. The cells were further cultured for 35 min in the CO_2 incubator at 37°C, upon incubation cells were washed three times gently. The attached cells were directly counted. In all attachment assays, the attachment is presented as a total number of cells attached to the plate per microscopic view field (calculated from the average of three view fields in each well in four wells).

2.8 Stability study of ProCA32.CXCR4

2.8.1 Serum stability

150 µL of 500 µM ProCA32.CXCR4 was mixed with 150 µL mouse serum and incubated at 37ºC for the serum stability study. 15 µL of samples were taken after 3 h, 4 h, 1 d, 2 d, 4 d, 6 d, 8 d, and 14 d of incubation. The samples were boiled for 10 min after being mixed with 2 µL of 1 M EGTA solution and SDS buffer and analyzed by western blot and Ponceau S staining flowing a standard procedure. Briefly, the mixture of protein sample and mouse serum taken from different time points at 37ºC incubation were prepared for the SDS-PAGE. Protein bands were transferred from the SDS-PAGE to nitrocellulose membrane. Ponceau S solution (Sigma-Aldrich) was used to stain the membrane from 5 min and rinse membrane 3-5 times in TBST buffer to achieve the desired staining results.

2.8.2 Transmetallation study

In order to characterize the resistance of the Gd^{3+}-ProCA32.CXCR4 complex to transmetallation by endogenous ions such as Zn^{2+}, a relaxometric transmetallation assessment was performed using a reported assay (149). Briefly, ProCA32.CXCR4 and other GBCA were mixed

with the same concentration of $ZnCl_2$ (2.5 mM) in pH 7.0 phosphate buffer. The final mixture contained 0.026 M KH_2PO_4, 0.041 M Na_2HPO_4, 2.5 mM Gd^{3+} complex, and 2.5 mM $ZnCl_2$. When transmetallation of Gd^{3+} by Zn^{2+} occurred, insoluble $GdPO_4$ formed and a decreased proton relaxation rate was observed. The longitudinal relaxation rate change of the mixture reflected the transmetallation process of Gd^{3+} by Zn^{2+} and the thermodynamic index was calculated by r_1 of the mixture after incubation at the present of Zn^{2+} over the initial r_1 of GBCA.

2.9 Animal study

2.9.1 Intrahepatic heterotopic xenotransplantation tumor model

10-wk-old female NU/NU mice (Jackson Laboratory, Bar Harbor, ME) were used to establish the intrahepatic heterotopic xenotransplantation tumor model. Mel290 cells were cultured and suspended in sterile PBS buffer. The mice were anesthetized with ketamine and xylazine mixture and placed to the supine position. A small incision was made along the right flank of the mouse. The liver was exposed with a small retractor. A 301/2-gauge needle was inserted into the liver until its point reached just below the liver sub capsule under a surgical microscope. Two million of Mel290 cells were inoculated in a volume of 20 ul PBS. The needle was then carefully removed at the same time that a sterile swab held the injection site. Formation of white cell bulla between hepatic parenchyma and the capsule was the criterion for successful injection. The incision was sutured with a 5-0 absorbable suture. After two to three weeks of Mel290 cell injection, melanoma tumor formed in the liver.

2.9.2 Intraocular melanoma mouse model with hepatic metastases

Human uveal melanoma M20-09-196 cells and 10-wk-old female NU/NU mice (Jackson Laboratory, Bar Harbor, ME) were used to generate the intraocular melanoma mouse model.

Subsequently, the mice with intraocular melanoma developed hepatic metastases. An aliquot of 10^6 uveal melanoma cells suspension in 2.5 μl PBS buffer was inoculated into the supra choroid space of the right eye of the nude mouse using a transcorneal technique. The mice were anesthetized with an intraperitoneal injection (IP) of ketamine and xylazine mixture. A tunnel was prepared from the limbus within the cornea, sclera and ciliary body to the choroid with a 301/2-gauge needle under a surgical microscope. The tip of a 10 μl glass syringe with a 31-gauge / 45-degree point metal needle (Hamilton, Reno, NV) was used to introduce cell suspension into the supra choroid space through the needle track. The eyes were enucleated after two weeks of inoculation. Metastases in liver formed after 8-12 months of tumor cells inoculation.

2.9.3 SKOV3 Orthotropic Human Ovarian Cancer Xenograft Model

SKOV3 orthotopic human ovarian cancer xenograft mouse model was developed by Dr. Lily Yang with the following procedure (150). SKOV3 ovarian cancer cells were cultured in McCoy 5A medium with 10 % fetal bovine serum and 1 % penicillin and streptomycin. SKOV3 cells were collected when the confluence reaches 80 % and suspended in sterile PBS buffer. Mice were anesthetized by injecting a mixture of 95 mg/kg ketamine hydrochloride and 5 mg/kg xylazine of body weight in sterile saline intramuscularly. Right ovary of mice was exposed by abdominal incision. At least 5×10^4 cells in 20 μL PBS were injected orthotopically into the ovarian bursa of each mouse. Close the abdominal incision after injection and monitor the mice until completely awake.

2.9.4 DEN induced HCC mouse model

Equal number of male and female mice with C57BL/6 genetic background were used for developing DEN induced HCC mouse model. Diethylnitrosamine (DEN, Sigma–Aldrich N0756) was dissolved in sterile saline. 14-day-old mice were treated with a single dose of

Diethylnitrosamine (DEN, Sigma–Aldrich N0756) at a dose of 25 mg/kg body weight by IP injection. Mice in one randomly pre-assigned group were euthanized 11 months after DEN administration for histological and biochemical analyses. The livers were removed and weighted right after euthanasia, the numbers of visible tumors on the liver surface were counted macroscopically. The largest lobes were fixed in formalin and embedded in paraffin. Sections were stained with hematoxylin and eosin and examined microscopically. Doxorubicin treatment: Doxorubicin hydrochloride salt was dissolved in sterile DD water. Mice received doxorubicin (3 mg/kg) bi-weekly for 4 weeks. The mice were then analyzed for MRI screening and euthanized for pathological analyses.

2.9.5 4T1 breast tumor mouse model

Luciferase stable transfected 4T1 breast cancer cells were cultured in RPMI-1640 medium supplemented with 10 % FBS and 1 % penicillin and streptomycin until confluence reach 80 %. Cells were detached by trypsin and suspended in sterile PBS. 5×10^4 cells were orthotopically injected to the mammary pad of mice. The orthotopic breast tumors will form around 2 weeks, and lung metastases will form around 3 - 4 weeks.

2.9.6 Subcutaneous UM murine model

Ten-week-old female NU/NU mice were used for the subcutaneous UM murine model. Aliquots of $2*10^6$ Mel 290 cells were suspended in 50 µL of PBS buffer mixed with 50 µL of Matrigel Matrix (Corning Life Science) and injected subcutaneously both on the right and left side of the back of NU/NU mice. After six weeks, subcutaneous tumors of 60-120 mm^3 in volume were formed.

2.10 MRI scan

M20-09-196 mice and HCC mice were all scanned with a 7.0 T Agilent MRI scanner at the University of Georgia. Mice were anesthetized by breathing in isoflurane through isoflurane vaporizer. The respiration rates of animals were monitored throughout the MRI scanning and controlled to be 70-80 times per minute. T_1 weighted images, T_2 weighted images were collected by spin-echo and fast spin-echo sequence before and after one bolus injection of 0.025 mmol/kg ProCA32.CXCR4 at 3 h, 24h, 48h. T_1 map and T_2 map were also collected at the same time points. T_1 map was collected by the fast spin-echo protocol. The parameters of acquisition: TR, 5000 ms; ESP, 8.17 ms; 8 inversion times cover from 0.01 ms to 1.5 ms with the same interval in between; FOV, 3.5 cm × 3.5 cm by a matrix of 512 × 512; thickness, 1 mm with no gap. The parameters of T_2 map acquisition: TR, 2000 ms; TE, 8 ms to 96 ms with 8 ms interval in between; FOV, 3.5 cm × 3.5 cm by a matrix of 512 × 512; thickness, 1 mm with no gap. Control mice were injected with one bolus same dosage of ProCA32 and imaged at the same time points with the same parameters. The parameters of spin-echo sequence: TR, 500 ms; TE, 14.89 ms; FOV, 3.5 cm × 3.5 cm by a matrix of 512 × 512; thickness, 1 mm with no gap. The parameters of fast spin-echo sequence: TR/ESP, 4000 ms/ 10 ms; FOV, 3.5 cm × 3.5 cm by a matrix of 512 × 512; thickness, 1 mm with no gap.

M290 mice MR images were all collected on a 4.7 T small-bore Varian MR scanner at Emory University. Mice were anesthetized follow a similar procedure and T1 weighted images were collected before and after one bolus injection of 0.025 mmol/kg ProCA32.CXCR4 at 12 min, 50 min, 3 h, 22 h, 46 h by gradient echo sequence. The parameters of gradient echo sequence: TR/TE, 140 ms/11 ms; FOV, 4 cm × 4 cm by a matrix of 512 × 512. MR images are processed and analyzed by Fiji and MRIcron.

MRI results of blocking experiment were acquired with the 7.0 T Bruker MRI scanner at Yerkes National Primate Research Center. Subcutaneous UM mice were anesthetized follow a similar procedure as detailed above, and T1 weighted images were collected before and after one bolus injection of 0.025 mmol/kg Cys-ProCA32.CXCR4 or Lys-ProCA32 at 3 h, 24 h, and 48 h. Blocking group mice received i.v. injections of 0.025 mmol/kg CXCR4 blocking reagent 24 h and 12 h prior to the injection of Cys-ProCA32.CXCR4. The parameters of the RARE sequence were: TR/TE, 560 ms/11 ms; FOV, 3.5 cm × 3.5 cm by a matrix of 256 × 256. MRI data were processed and analyzed by Fiji and MRIcron.

2.11 Organ distribution, toxicity, and pharmacokinetics study of ProCA32.CXCR4

2.11.1 Organ distribution study.

ICP-OES was used to analyze the Gd^{3+} distribution in different mouse organs after injection of ProCA32.CXCR4. Healthy CD-1 mice were injected with 0.025 mmol/kg bolus dosage of ProCA32.CXCR4. Animals were euthanized 46 h and 7 days after receiving an injection of ProCA32.CXCR4. Organs including heart, liver, spleen, kidney, brain, muscle, and skin were subsequently collected and used for ICP-OES analysis. Tissues (0.1–0.5 g) of each organ were dissolved overnight in 1 mL of 67-69% nitric acid, Optima^{TM} (Fisher Chemical). Undissolved solid particles were removed by filtration, and the supernatant was retained for Gd^{3+} content analysis by ICP-OES.

2.11.2 Toxicity study of ProCA32.CXCR4

ProCA32.CXCR4 acute toxicity was tested by a bolus injection of 100 μL, 7 mmol ProCA32.CXCR4 to 10-week-old healthy CD-1 mice. ProCA32.CXCR4 with two different PEGylation (Cys-ProCA32.CXCR4 and Lys-ProCA32.CXCR4) were tested, respectively. For

each experiment group, n = 3, the control group are mice with saline injection. Mice were observed every eight hours post-injection, then euthanized after five days. Terminal blood was collected by cardiac puncture, and serum was transferred immediately to micro-centrifuge tubes. Plasma was separated from blood cells by centrifugation at 14,000 rpm, 4°C for 10 min. Serum samples were used for blood biochemistry tests and kidney function tests to measure ALT, AST, and electrolyte levels. Tissues including heart, muscle, liver, spleen, kidney, tail, and brain, were collected for analysis of gadolinium distribution, using ICP-OES.

2.11.3 Pharmacokinetic study

Female CD-1 mice (8–10 weeks old) were used to determine the pharmacokinetic parameters of ProCA32.CXCR4. ProCA32.CXCR4 (100 μL, 0.025mmol/kg) was administered through tail vein IV injection. The blood samples were collected at various time points using saphenous vein up to seven days using a sparse sampling design (3–6 animals per time point). Immediately following blood sample collection, samples were stored on ice, serum was obtained through centrifugation, and Gd^{3+} concentration was determined using ICP-OES. Pharmacokinetic parameters were calculated using the non-compartmental analysis tool of Phoenix WinNonlin software. The areas under the concentration-time curve (AUClast and AUCinf) were calculated using a linear trapezoidal rule. The clearance and volume of distribution (Vss) were estimated following IV dose administration. The elimination rate constant value (k) was obtained by linear regression of the log-linear terminal phase of the concentration-time profile using at least three declining concentrations in terminal phase with a correlation coefficient of >0.8. The terminal half-life value (T1/2) was calculated using the equation 0.693/k.

3 DESIGN, EXPRESSION, PURIFICATION, AND PEGYLATION OF PROCA32.CXCR4

3.1 Introduction

CXCR4 is found to be expressed in over 23 different kinds of tumors and closely related to cancer progression and development of metastases. Chemokine receptor 4 (CXCR4) plays a crucial role in cell migration and cancer metastasis to several organs such as liver, bone marrow, and lung that have the intrinsically high concentration of its natural ligand CXCL12 (140, 151, 152). (Figure 3.1). CXCR4 has gained tremendous attention over the past few decades for its widely up-regulation in various types of cancers. It is now gradually becoming a novel molecule target for anti-cancer diagnosis and treatment. A CXCR4 antagonist, Plerixafor (Mozobil®, AMD3100), is approved by the FDA for stem cell mobilization. Another ongoing study is focused on the effect of another CXCR4 antagonist, X4P-001, on T-cell infiltration in human metastatic melanoma. The importance of CXCR4 in cancer-related incidence is the motivation of achieving CXCR4 targeted imaging for cancer.

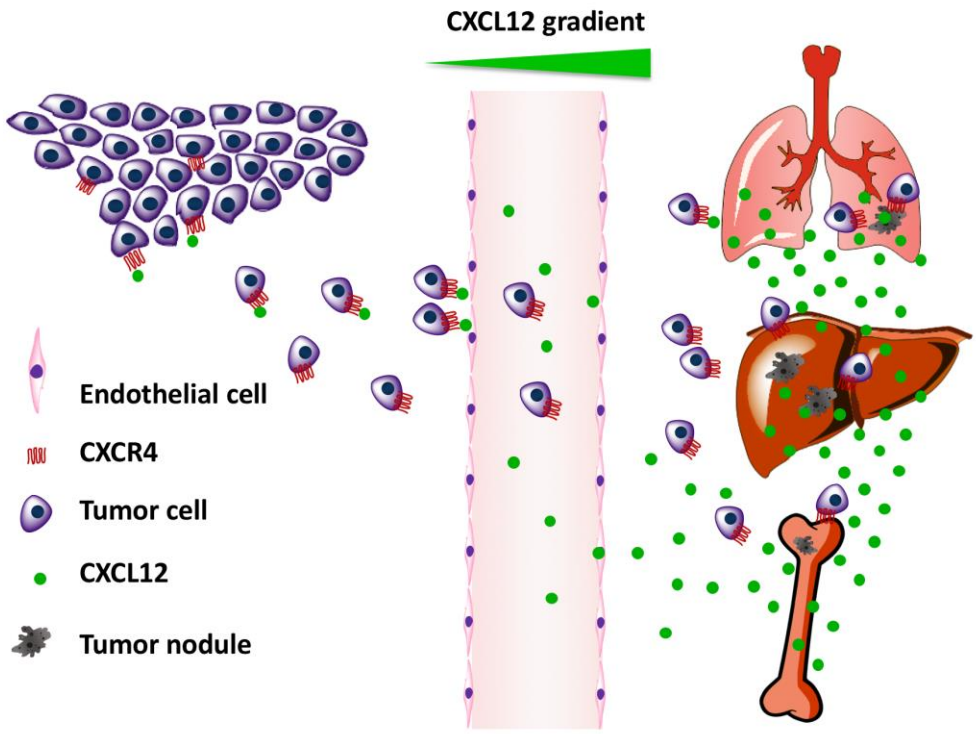

Figure 3.1 Cancers metastasize through the CXCR4-CXCL12 gradient in an organ-specific pattern.
Tumor cells that express CXCR4 metastasize through CXCR4-CXCL12 interaction to specific organs that have intrinsically high concentration of CXCL12 such as the lung, liver and bone.

vMIP-II, a viral chemokine encoded by human herpesvirus 8, displays diverse interactions with both CC and CXCR4 (153-155). vMIP-II interacts with CXCR4 as an antagonist and inhibits the Th1-associated inflammation. Due to these properties of vMIP-II, it is a potential candidate for anti-inflammatory and anti-HIV drugs. A crystal structure of CXCR4 and vMIP-II complex reveals the interaction of vMIP-II to CXCR4 is through the N-terminus and N-loop of vMIP-II (156). The central residues that participate in the interaction are mainly in the N-terminus. It supported by the study of synthesis peptides with the N-terminus sequence of vMIP-II, the peptide contains the amino acid sequence of residues 1- 21 of vMIP-II (LGASWHRPDKCCLGYQKRPLP), displays appreciable CXCR4 binding affinity (IC_{50} = 190 nM) when compared with the vMIP-II (IC_{50} = 14.8 nM) (157).

MRI imaging is widely used in clinical practice, and MRI contrast agent development can efficiently improve the sensitivity of MRI. As stated in chapter 1, the current contrast agents in clinical usage are not sensitive enough to achieve molecular imaging. Based on the platform of ProCA32, after careful review of the CXCR4 targeting moieties, we designed the CXCR4 specific targeting contrast agent, namely, ProCA32.CXCR4. ProCA32.CXCR4 was designed based on the platform of protein-based contrast agent ProCA32. ProCA32 was developed by previous lab member Dr. Xue, which contains two Gd^{3+} binding sites. By linking the CXCR4 targeting moiety to the C terminus of ProCA32 with a flexible linker, we designed ProCA32.CXCR4 as the CXCR4 targeted MRI contrast agent for CXCR4 specific molecular imaging with MRI (Figure 3.2). Based on the complex X-ray structure of CXCR4 and vMIP-II, we designed the CXCR4 targeting moiety, included key CXCR4 interaction residues from vMIP-II, that reach into the binding pocket and interact with key residues D262, D97, S285, and E288 of CXCR4 in both chemokine recognition sites 1 and (Figure 3.4) (156).

ProCA32.CXCR4 was bacterially expressed and purified following a previously reported protocol (63). One cysteine is introduced for site-specific PEGylation through thiol group with maleimide PEG reagent. The post-expression modification was done through NHS-ester PEGylation or maleimide PEGylation verified by coomassie blue staining, and iodine (I_2) staining.

```
Rat_ProCA32          1 MSMTDLLSAEDIKKAIGAFTAADSFDHKKFFQMVGLKKKSADDVKKVFHI     50
Rat_ProCA32.CXCR4    1 MSMTDLLSAEDIKKAIGAFTAADSFDHKKFFQMVGLKKKSADDVKKVFHI     50

Rat_ProCA32          51 LDKDKDGFIEEDELGSILKGFSSDARDLSAKETKTLMAAGDKDGDGKIGV    100
Rat_ProCA32.CXCR4    51 LDKDKDGFIEEDELGSILKGFSSDARDLSAKETKTLMAAGDKDGDGKIGV    100

Rat_ProCA32          101 EEWSTLVAES-----------------------    110
Rat_ProCA32.CXCR4    101 EEWSTLVAESGGGLGASWHRPDKACLGYQKRPLP    134
```

Figure 3.2 Sequence alignment of Rat_ProCA32 and Rat_ProCA32.CXCR4.

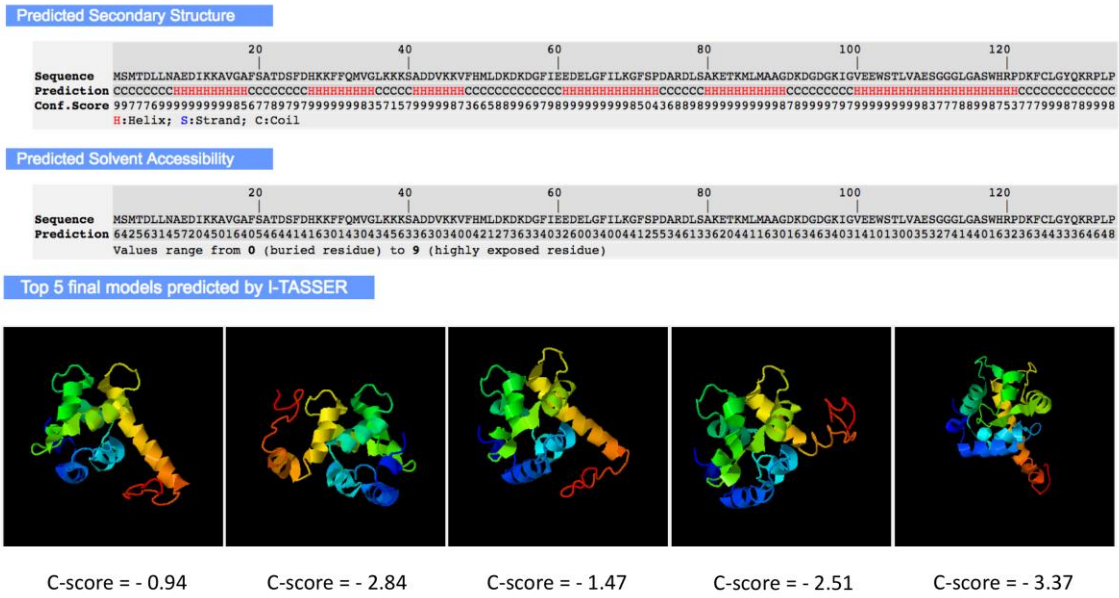

Figure 3.3 Predicted secondary structure, solvent accessibility, and models of ProCA32.CXCR4.

Prediction of secondary structure, solvent accessibility and final models of ProCA32.CXCR4 using I-TASSER (158). C-score is the confidence of protein model predicted by I-TASSER, which is typically in the range of [-5,2], where the higher value of C-score corresponding higher confidence of the prediction.

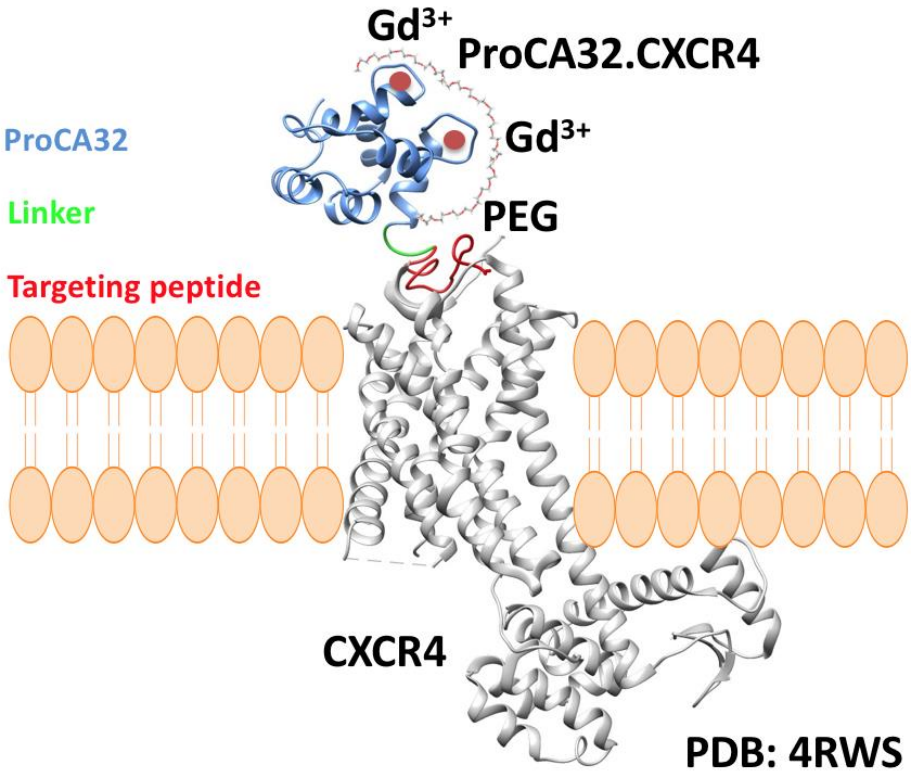

Figure 3.4 Model structure of the ProCA32.CXCR4 interacting with CXCR4.
ProCA32.CXCR4 contains two Gd^{3+} binding sites, the C terminus of ProCA32.CXCR4 is the CXCR4 targeting moiety which can interact with CXCR4 by residue-residue interaction and electrostatic interaction.

3.2 Results

3.2.1 Expression, purification of ProCA32.CXCR4

ProCA32.CXCR4 was expressed by cell strain BL21(DE3) pLysS with 0.5 mM IPTG induction followed by a protocol described in chapter 2. The expression of ProCA32.CXCR4 consists of small-scale culture and large-scale expression. Ampicillin resistant agar plates were used for transformation of ProCA32.CXCR4 plasmid. A single colony was inoculated in 250 ml LB media with 0.1% ampicillin for small scale culture overnight at 37 °C. The second day, small scale culture LB media were transferred to 1-liter LB media with 0.1% ampicillin for large scale

expression at 37°C. Measure the OD_{595} of the LB media to ensure large-scale culturing starts from OD_{595} around 0.1. Observing the OD_{595} change along with time and add 0.5 mM IPTG when culture solution OD_{595} reach between 0.6-0.8. After adding IPTG for inducing expression, keep the culturing temperature at 37 °C for three hours, and reduce the temperature to 25°C for overnight expression. Different conditions for expression have been tested: 28°C culturing for 4 hours after IPTG induction generated comparable yield with 25°C overnight expression.

The expression of ProCA32.CXCR4 is confirmed by Coomassie blue staining of SDS-PAGE (Figure 3.5 A). Molecular weighted of ProCA32.CXCR4 is 14.3 kDa and after induction cell pellet clearly shows thicker band of protein around 14.3 kDa. The yield of ProCA32.CXCR4 expression is calculated to be in a range of 60 to 100 mg/L LB media, varies by the batch of expression.

Purification of ProCA32.CXCR4 followed by a series of steps including sonication, boiling, dialysis, and FPLC (fast protein liquid chromatography). Cell pellet from expression LB media was collected by centrifuging at 8000 rpm. The cell pellet was resuspended in PBS buffer in a ratio of 1:10, more specific, 1 gram of cell pellet resuspended in 10 ml PBS buffer. Sonication was applied to break cell structure and release the expressed protein. Sonication was carried out 10 times in total, every time for 1 minute and with a 10 minutes interval in-between for cooling down the solution. After sonication, the solution should become semitransparent and with good consistency. Pellet down the solution with centrifuge and boiled the supernatant to further remove the impurities. 3% streptomycin was used to sediment the DNA for overnight. Followed by which the solution is pellet down with centrifuge and boiled again and dialysis with 10 mM HEPES

buffer for overnight. After dialysis, the solution was centrifuged and pellet down, 40 mM EGTA was added for incubation for 48 hours, and the sample is ready for FPLC.

Ion exchange column was utilized to purify ProCA32.CXCR4 after sonication and boiling. Fractions eluted from different peaks of FPLC spectra were collected separately, SDS-PAGE was applied to verify the components of each elution from corresponding peaks (Figure 3.5 B, Figure 3.6 B). As shown in the purification SDS-PAGE (Figure 3.6 B), protein sample eluted from peak 2, peak 3, and peak 4 were proved to be ProCA32.CXCR4 (MW = 14.3 kDa) and in the presence of both monomer and dimer form. As shown in Figure 3.5, a large percentage of the ProCA32.CXCR4 present in the monomer form.

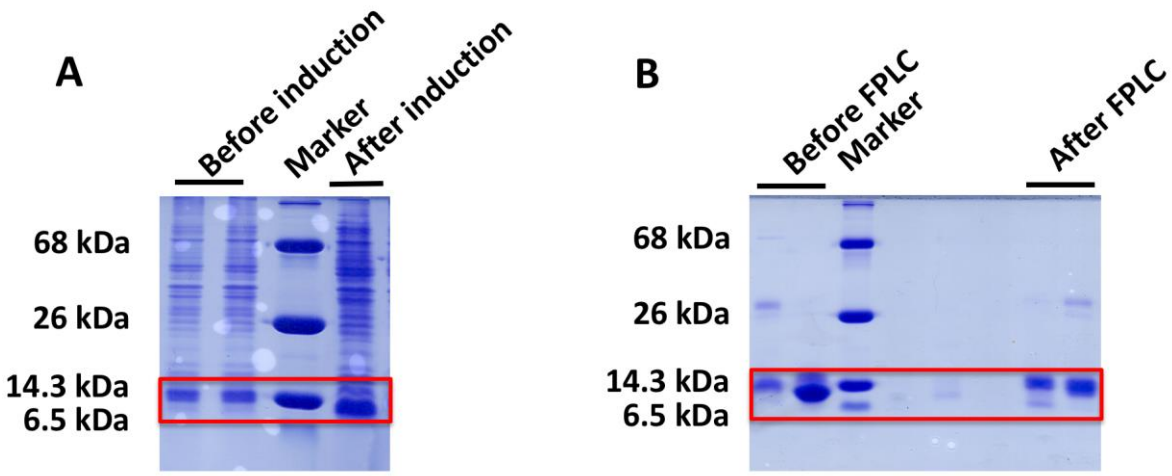

Figure 3.5 Expression and purification SDS-PAGE of ProCA32.CXCR4.
(**A**) Coomassie blue staining of BL21(DE3) pLysS cell pellets before and after IPTG induction. Cell pellets after IPTG induction show significantly thicker protein band around 14.3 kDa. (**B**) Coomassie blue staining of SDS-PAGE of samples collected before FPLC and after FPLC. After FPLC purification, only the ProCA32.CXCR4 showed in the SDS-PAGE, in both monomer and dimer form.

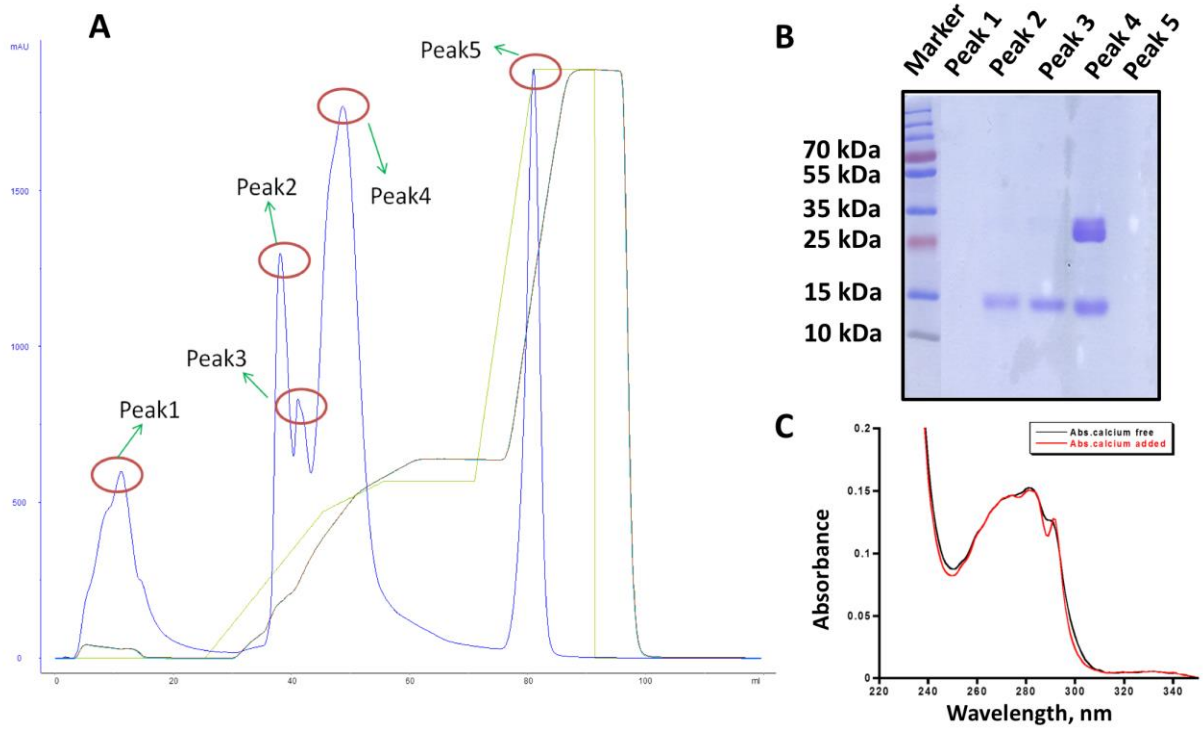

Figure 3.6 Purification of ProCA32.CXCR4.

(**A**) FPLC absorbance spectrum of ProCA32.CXCR4 purification. Peak 1 fractions are unbounded protein; peak 2 fractions represented the Ca^{2+} bound form of ProCA32.CXCR4, fractions from peak 4 are the Ca^{2+} free form of ProCA32.CXCR4, fractions eluted from peak 3 are the mixture of Ca^{2+} loaded and Ca^{2+} free form of ProCA32.CXCR4. Peak 5 fractions are the DNA impurity. (**B**) SDS-PAGE coomassie blue staining of fractions eluted from FPLC. Protein bands showed on peak 2, peak 3, and peak 4 elution fractions. (**C**) The UV absorbance of protein sample collected from FPLC peak 4. The red curve shows the absorbance spectrum of Ca^{2+} bound ProCA32.CXR4. The black curve shows the Ca^{2+} free ProCA32.CXCR4. The UV spectrum of Ca^{2+} binding form ProCA32.CXCR4 show a hump at 295 nm.

3.2.2 PEGylation of ProCA32.CXCR4

ProCA32.CXCR4 was PEGylated after expression for post-expression modification to further optimize solubility, stability, and pharmacokinetic properties. Site-specific PEGylation including cysteine specific PEGylation through thiol group with maleimide group of the PEGylation reagent and lysine-specific PEGylation through amide group on the lysine side chain with NHS ester from the PEG reagent (Figure 3.7).

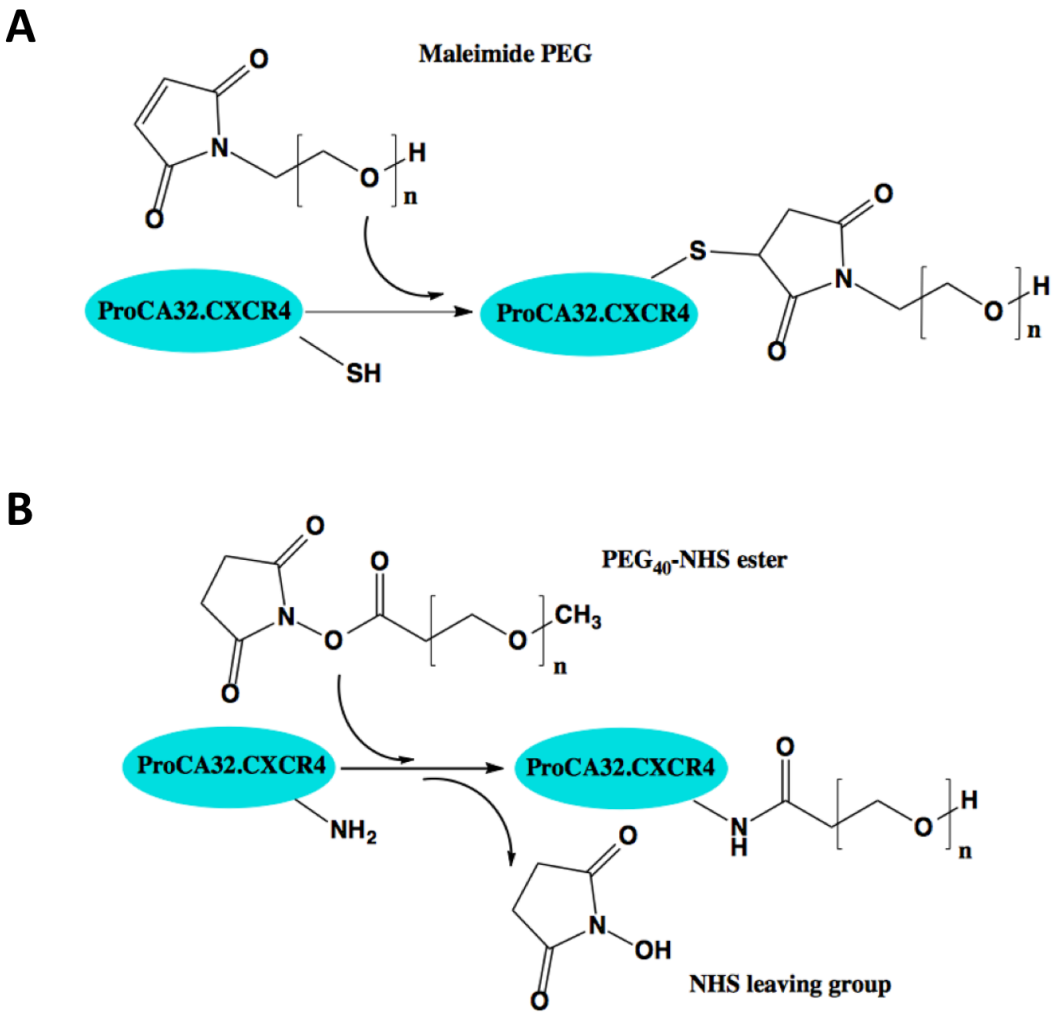

Figure 3.7 Illustration of PEGylation.
(**A**) Reaction mechanism of site-specific maleimide PEGylation (Cys-PEGylation). The maleimide group of polyethylene glycol (PEG) specifically react with the thiol group from cysteine. (**B**) Reaction mechanism of NHS ester-PEGylation (Lys-PEGylation). The NHS ester group of PEG agent react with the amine group from lysine side chain.

PEGylation of both lysine-specific and cysteine specific were carried out in an oxygen-free system with degassing the solution by flushing nitrogen. Cysteine specific PEGylation requires a reduced environment to break the disulfide bond and expose the thiol group. Reducing reagent TCEP (tris (2-carboxyethyl) phosphine hydrochloride) was used to reduce the disulfide bond

before cysteine PEGylation. During PEGylation, the falcon tube was wrapped with aluminum foil to avoid light and generation of radical.

Lysine PEGylation product contains ProCA32.CXCR4 with different PEGylation sites. Coomassie blue staining and iodine staining of SDS-PAGE shows multiples bands for the Lysine PEGylation products (Figure 3.8). Cysteine PEGylation generates the homogenous PEGylation product with only one site been PEGylated, the Coomassie blue staining and iodine staining of cysteine PEGylation product shows only two bands, one for the non-reacted ProCA32.CXCR4 and the upper one is ProCA32.CXCR4 with one cysteine PEGylated (Figure 3.8).

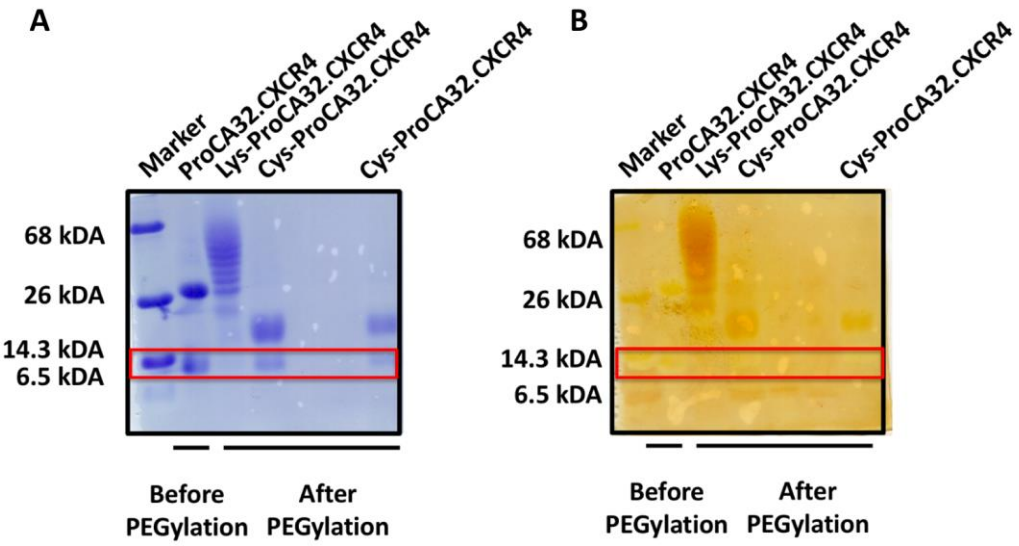

Figure 3.8 PEGylation SDS-PAGE of ProCA32.CXCR4.
(**A**) Coomassie blue staining of ProCA32.CXCR4 before and after PEGylation. ProCA32.CXC4R form in monomer and dimer before PEGylation, as indicated by the two bands on SDS-PAGE. Cys-PEGylation product of ProCA32.CXCR4 composed non-PEGylated ProCA32.CXCR4 and Cys-ProCA32.CXCR4, indicated by two bands on SDS-PAGE. Multiple protein bands of Lys-ProCA32.CXCR4 product represents Lys-ProCA32.CXCR4 with a various number of PEGylation sites. (**B**) Iodine (I_2) staining of ProCA32.CXCR4 before and after PEGylation. Iodine staining shows PEG as brown color on an SDS-PAGE gel, indicate the positions of PEG and PEGylated ProCA32.CXCR4.

3.3 Conclusion and discussion

ProCA32.CXCR4 expression, purification, and PEGylation are critically important for the generation of CXCR4 specific contrast agent. We aim at producing ProCA32.CXCR4 in an economical and time-efficient fashion and the protocol allows for the translational usage for large scale production meet industrial standards.

ProCA32.CXCR4 is bacterially expressed and purified in a relatively simple steps protocol. The yield of expression is good (60-100 mg/L LB) by optimizing expression procedures. The protein yield exhibit best if follow three hours after induction expression at 37°C and decrease the expression temperature to 25°C for overnight expression. ProCA32.CXCR4 is heat resistant and structurally stable at boiling temperature. This property enables the purification of ProCA32.CXCR4 from a lot of the impurity proteins efficiently. FPLC can further separate ProCA32.CXCR4 from remaining impurities and separate the metal (Ca^{2+}) free form of ProCA32.CXCR4 with metal (Ca^{2+}) loaded for gadolinium loading formulation. EGTA incubation is a critical step for chelating metal ions, majorly Ca^{2+}. 48 hours incubation with EGTA of the ProCA32.CXCR4 before FPLC efficiently remove the preloaded metal ions and yield more Ca^{2+} free ProCA32.CXCR4. Longer incubation time is tested as well, no significant difference of Ca^{2+} free ProCA32.CXCR4 and Ca^{2+} loaded ProCA32.CXCR4 ratio was observed from longer incubation time samples.

PEGylation of ProCA32.CXCR4 has successfully achieved by both cysteine PEGylation and lysine PEGylation. After PEGylation, the solubility and stability of ProCA32.CXCR4 is much improved and allow for the storage of ProCA32.CXCR4 at higher concentration and longer shelf life. Lysine PEGylation increases the molecular weight of ProCA32.CXCR4 by 4-5 sites PEGylation on average, which increase the molecular weight by 10 kDa to 30 kDa varies by the

length of PEG reagents being used. Lysine PEGylated ProCA32.CXCR4 potentially has longer *in vivo* circulation half-life because of the larger molecular weight. Cysteine PEGylation is more ideal in the sense that it generates homogenous PEGylation product. The efficiency of cysteine PEGylation is slightly lower than lysine PEGylation, which means more reagents might be wasted during cysteine PEGylation procedure. There are several steps worth noting in the PEGylation: protein solution should be properly degassed to remove the oxygen; protein sample tube should be properly wrapped by aluminum foil to avoid exposure to light.

pH is an essential factor for the PEGylation, maintaining a pH neutral environment improves the efficiency and percentage of PEGylation. Avoid radical is another factor in successfully PEGylation; it is recommended to thoroughly degas the solution and avoid light by wrapping with aluminum foil. Different PEGylation approaches, including N terminal amide PEGylation and different sizes of PEGylation reagents, can be tested for further optimization of PEGylation protocol.

3.4 Summary

The expression, purification, and PEGylation of ProCA32.CXCR4 was achieved based on a previously reported protocol of ProCA32 with minor modification to improve the yield, quantity of metal free form of ProCA32.CXCR4 for later gadolinium loading. Different PEGylation was tested to optimize the solubility, stability and pharmacokinetic property of ProCA32.CXCR4. Lysine specific PEGylation is more efficient in terms of percentage of PEGylated ProCA32.CXCR4 over the total amount when compare with cysteine PEGylation. Cysteine specific PEGylation has the advantage of generating homogenous PEGylation for industrial production standard.

4 BIOPHYSICS STUDY OF PROCA32.CXCR4

4.1 Introduction

Since the FDA approval of gadopentetate dimeglumine (Magnevist®; Bayer HealthCare Pharmaceuticals) in 1988, Gd^{3+}-based contrast agents (GBCAs) have been widely used for clinical MR imaging. GBCAs was considered to safe until the first nephrogenic systemic fibrosis (NSF) been identified in 1997 (159-161). NSF was thought to be a disease only involve skin symptoms, and the original name was Nephrogenic Fibrosing Dermopathy (NFD) (160). More and more in-depth study of NSF makes researchers realized that it is a systemic disease that involves multiple organs and tissues and happened mostly in the patients with a history of dialysis because of chronic renal diseases. In some cases, NSF patients progress rapidly and lead to severe physical disability and deaths (162). P. Marckmann and colleagues proposed the causative role of gadodiamide application in the development of NSF. Since then, NSF has been identified as the side effect of gadolinium-based contrast agents, especially in the patients with compromised renal function. Moreover, the standard and dosage of gadolinium-based contrast agents' application have been modified, and the patients' renal function listed as a factor that taken into consideration. No standard treatment was established for NSF, and some cases showed kidney transplantation and extracorporeal photopheresis could help to treat the disease (163).

The confidence of GBCAs was reestablished since more stable gadolinium-based contrast agents being used, and the usage of GBCA in patients with renal malfunction was limited. More recent data demonstrated that, in patients with the history of GBCA administration, gadolinium accumulate in tissues including brain, bone, and kidneys regardless of patients' renal function status. Repeatedly exposure to gadolinium increases the risk of gadolinium accumulation. (164, 165). The brain deposition of gadolinium was first identified because the signal increase of

dentate nuclei (DN) in unenhanced T_1 weighted MR images of patients with normal renal function, and this enhancement was associated with exposure to gadolinium-based contrast agents (166, 167). Since then gadolinium-based contrast agent was accepted as the primary etiology of brain tissue deposition.

We have carefully considered these factors in the design of ProCA32.CXCR4 for clinical translational purpose. The Gd^{3+} binding sites of ProCA32.CXCR4 was well designed to balance Gd^{3+} binding for safety, and water accessibility for relaxivities. ProCA32.CXCR4 was shown to have unprecedented gadolinium kinetic and thermodynamic stability. The Log (K_{Gd}) of ProCA32.CXCR4 is 21.89. Metal selectivities of ProCA32.CXCR4 for Gd^{3+} over Zn^{2+} and Ca^{2+} are 10^6-10^{12} times greater than approved contrast agents, Dotarem and ProHance. The inertness of ProCA32.CXCR4 in the presence of Zn^{2+} verified its strong stability against transmetallation. Moreover, the improved relaxivity of ProCA32.CXCR4 enabled excellent contrast enhancement in vivo with only one-quarter of gadolinium dosage compared with other GBCAs. No trace of gadolinium was detected in mice brain after ProCA32.CXCR4 administration and we have also not observed any acute toxicity and tissue/organ toxicity. Collectively, strong Gd^{3+} binding affinity, excellent metal selectivity, inertness against transmetalation and less injection dosage makes ProCA32.CXCR4 has an excellent safety profile.

4.1.1 Gadolinium toxicity and deposition

All clinical approved GBCAs are considered to be safe when administrating in a lower dosage (0.1 to 0.3 mmol/kg) in the patients without renal insufficiency (46). Gadolinium is a rare earth element and belongs to the lanthanide family. The free Gd^{3+} is toxic for humans, and the chelated form will be far less toxic since it can eliminate from kidney before dissociating from chelator. As a result, the toxicity of gadolinium-based contrast agent is considered to positively

related to the stability of gadolinium-chelator complex. The free gadolinium deposited in tissues including brain, bone, and kidney as well as other lanthanide family metal ions. In the insufficient renal function patients, the half-life of GBCAs elimination is significantly prolonged than the patients with normal renal function, which allows more time for free Gd^{3+} being dissociated from chelator. It is one of the reasons that most of the reported NSF patients was administrated with nonionic linear GBCA gadodiamide (Omniscan) (168).

The GBCAs can be classified into two categories according to their chemical structure, linear and macrocyclic. The linear ones have an open-chain structure that is not fully closed where the macrocyclic ones are caged in the chelator by the ligands. The etiology of NSF is considered primarily to be free Gd^{3+} release from the chelator complex, and this process is related to two factors: kinetic stability and thermodynamic stability (Table 4.1). Kinetic stability of GBCAs defined by the dissociation rate of Gd^{3+} from the gadolinium complex, thermodynamic stability of GBCAs characterized by the energy that requires for the dissociation of Gd^{3+} from chelator complex to happen. As a result, GBCAs with higher kinetic stability and thermodynamic stability will less readily to release Gd^{3+}. Notably, the description of kinetic stability and thermodynamic stability are under pH 1.

According to the stability under physiological condition, Frenzel et al. described the GBCAs into three different stability classes: macrocyclic, linear ionic, and linear nonionic (45). The macrocyclic GBCAs are most stable under physiological conditions (incubation with human serum at 37 °C, pH 7.4), the Gd^{3+} release rate after 15 days incubation is less than 0.1 %, and the initial Gd^{3+} release rate is less than 0.007 %/d. On the contrary, the release of Gd^{3+} rate of linear GBCAs are way faster than predicted value by the conditional stability constant, and nonionic linear GBCAs are about 10 times faster than the ionic linear GBCAs. Also, the elevated phosphate

level of human serum facilitates the release of Gd^{3+}. These results suggesting evaluation of GBCAs under physiological condition will be more clinically relevant, and the thermodynamic stability under physiological condition (pH 7.4) is termed conditional stability constant (45).

Table 4.1 A summary of chemical structure and stability of clinic contrast agents. Table adapted from reference (46).

Contrast agent	Trade name	Chemical structure	Concentration (mmol/ml)	Thermodynamic stability constant	Conditional stability constant	Elimination pathway
Gadodiamide	Omniscan	Linear nonionic	0.5	16.8	14.9	Renal
Gadoversetamide	OptiMARK	Linear nonionic	0.5	16.6	15	Renal
Gadopentetate dimeglumine	Magnevist		0.5	22.1	17.7	Renal
Gadobenate dimeglumine	MultiHance	Linear ionic	0.5	22.6	18.4	93 % Renal 3 % Biliary
Gadoxetic acid disodium	Primovist	Linear ionic	0.25	23.5	N/A	50 % Renal 50 % Biliary
Gadofosveset trisodium	Vasovist	Linear ionic	0.25	22	N/A	91 % Renal 9 % Biliary
Gadoteridol	ProHance	Macrocyclic nonionic	0.5	22.8	17.1	Renal
Gadobutrol	Gadavist	Macrocyclic nonionic	0.5	21.8	N/A	Renal
Gadoterate meglumine	Dotarem	Macrocyclic ionic	0.5	25.4	19	Renal

4.1.2 Metal selectivity and stability of ProCA32.CXCR4

Two major goals are wanted to achieve in the design of ProCA32.CXCR4. First, optimized stability is desired for safety consideration. Secondly, sufficient water access and the exchange rate is crucial for maximizing relaxivities of ProCA32.CXCR4. By modifying the calcium-binding pocket of parvalbumin, we designed binding pockets for gadolinium with ideal ligand coordination. The similar radius of calcium and gadolinium facilitates the gadolinium fit in the binding pockets, and the 3-positive charge of gadolinium ion results in the stronger coordination of gadolinium in the binding pockets than calcium. The thermodynamic stability of ProCA32.CXCR4 is accessed under physiological condition (human serum incubation at 37 °C, pH 7.4) and the binding affinity (defined by the dissociation constant) of ProCA32.CXCR4 with

different metallic ions including terbium, gadolinium, calcium, and zinc are evaluated under the physiological condition as well.

4.1.3 Pharmacokinetics and toxicity study

Pharmacokinetics, abbreviated as PK, described what the body does to a drug. Pharmacokinetic includes the studies the absorption, distribution, metabolism and elimination of substances. Four fundamental parameters, including volume of distribution, half-life, bioavailability, and excretion, provide the basis of understanding pharmacokinetic properties of a drug (169). Pharmacokinetics parameters are closely related to each other. When a substance has faster clearance, it will show shorter half-life, higher clearance, and lower exposure, otherwise, it shows more prolonged blood circulation, lower clearance, and higher exposure. The study of pharmacokinetics property of a drug predicts the *in vivo* behavior of a drug and helps to decide the dosage to improve therapeutic effects and minimize side effects (170) .

Volume of distribution described by the amount of drug in the body over the concentration of drug in the plasma or blood. In fact, lots of drugs exhibit volume of distribution larger than the volume of the plasma or blood, because of the volume of distribution is an apparent volume pool requires for the drug distributed evenly throughout the body. Drugs with good tissue penetration can be distributed to the organs faster and only leave a small amount of drug in the plasma or blood. The distribution of a drug depends on the patients' factors and the chemical properties of the drug. The binding of the drug to the blood cells, plasma protein, and tissue are deciding factors for the distribution as well.

Half-life measures the time requires for the concentration of a drug reduce 50%. Half-life defined by both changes of volume of distribution and clearance. It provides a way to estimate the distribution of drug reach a steady state.

The bioavailability defined by the amount of intact drug reaches to the sites of actions, or the systemic circulation. By definition, a drug's bioavailability will be 100% right after administration if it administrated intravenously. The bioavailability of drug decreases when administrated through other routes.

To study the pharmacokinetic properties of ProCA32.CXCR4 provide a better understanding of dosage, imaging time window, specific organ distribution, and toxicity. As for the translational application for human patients. We study the distribution of ProCA32.CXCR4 in different organs, including the liver, kidney, spleen, heart, muscle by analyzing the gadolinium content with ICP-OES and pharmacokinetics profile of ProCA32.CXCR4 was analyzed by the change gadolinium concentration in whole blood followed the administration of ProCA32.CXCR4 along with time. Toxicity evaluated by the clinical pathology profile of mice followed by ProCA32.CXCR4 injection and organ toxicity were evaluated by the H & E staining of mouse tissue including

4.2 Results

4.2.1 Relaxivity study of ProCA32.CXCR4

Relaxivity is a crucial property of MRI contrast agent; the major goal of this study is to design a novel contrast agent with improved relaxivities to enable molecular imaging using MRI. The relaxivities of ProCA32.CXCR4 is evaluated at 1.4 T and 7.0 T respectively because higher field application will allow higher resolution imaging and is the future direction of MRI. Also, we have noticed that the relaxivities vary with different PEGylation. The relaxivities (both r_1 and r_2)

of non-PEGylated ProCA32.CXCR4, lysine PEGylated ProCA32.CXCR4 (Lys-ProCA32.CXCR4) and cysteine PEGylated ProCA32.CXCR4 (Cys-ProCA32.CXCR4) were evaluated, respectively.

ProCA32.CXCR4 has two gadolinium binding sites. It raises the question of what the best loading ratio of ProA32.CXCR4 and gadolinium are to achieve the optimized relaxivities per particle and relaxivities per gadolinium. One experiment was carried out for this study by setting the concentration of gadolinium as 50 μM in buffer solution, different concentration of ProCA32.CXCR4 (range from 0 μM to 100 μM) were titrated in, and both r_1 and r_2 values were measured at different loading ratio. The result shows that the best relaxivities per gadolinium are achieved when loading with ProCA32.CXCR4 in 2:1 ratio (Figure 4.1 A, B). When the ProCA32.CXCR4 concentration increase form 0 μM to 25 μM, the relaxivities increase as the ProCA32.CXCR4 concentration increase. When the ProCA32.CXCR4 concentration increase from 25 μM to 100 μM, the relaxivities (both r_1 and r_2) decrease as the ProCA32.CXCR4 concentration increase (Figure 4.1 A, B). The relaxivities of per gadolinium are only half the value when loading gadolinium with ProCA32.CXCR4 in 1:1 ratio when compared with load gadolinium with ProCA32.CXCR4 in 2:1 ratio (Figure 4.1 C, D). The relaxivities of non-PEGylated ProCA32.CXCR4, cysteine PEGylated ProCA32.CXCR4 and lysine PEGylated ProCA32.CXCR4 exhibited no difference with each other (Figure 4.1 C, D). Further relaxivities studies are carried out under the loading ratio of ProCA32.CXCR4 to gadolinium at 1:2 unless otherwise stated.

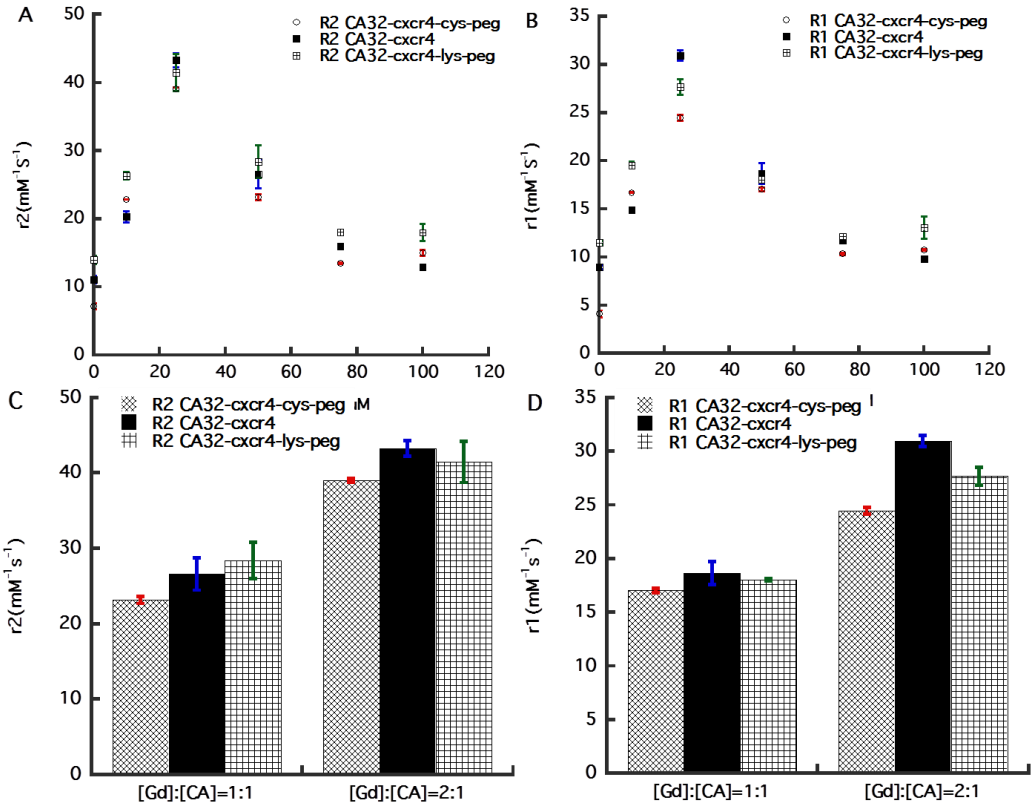

Figure 4.1 Relaxivities comparison of different PEGylation of ProCA32.CXCR4.
(**A**) The r_2 relaxivity of 50 µM Gd^{3+} loaded with different concentration of non-PEGylated ProCA32.CXCR4, cysteine PEGylated ProCA32.CXCR4 and lysine PEGylated ProCA32.CXCR4. (**B**) The r_1 relaxivity of 50 µM Gd^{3+} loaded with different concentration of ProCA32.CXCR4, ProCA32.CXCR4-Cys and ProCA32.CXCR4-Lys (**C**) Comparison of r_2 of different PEGylation of ProCA32.CXCR4 loaded with gadolinium in 1:1 and 1:2 ratio. (**D**) r_1 Comparison of different PEGylation of ProCA32.CXCR4 loaded with gadolinium in 1:1 and 1:2 ratio. Measurements are done at 1.4 T in 50 mM HEPES, 100 mM NaCl at pH 7.2, 37°C.

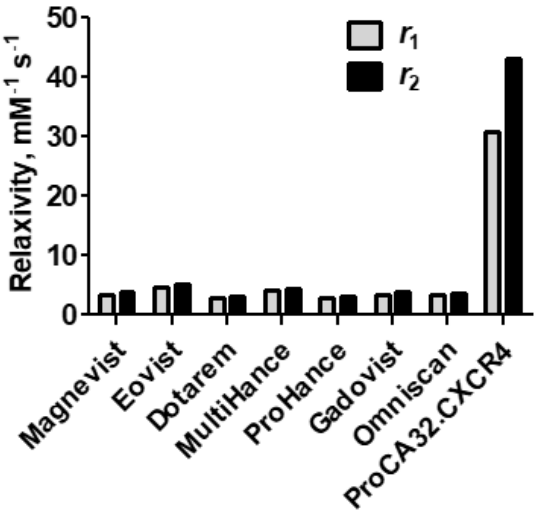

Figure 4.2 Relaxivities study of ProCA32.CXCR4 and comparison with clinic GBCAs. Comparison of ProCA32.CXCR4 relaxivities with commercial GBCAs. Measurements are done under 1.4 T magnetic field.

The per gadolinium r_1 and r_2 values of ProCA32.CXCR4 were 30.9 $mM^{-1} s^{-1}$ and 40.2 $mM^{-1} s^{-1}$, respectively, at 1.4 T (Figure 4.3 A). Both r_1 and r_2 relaxivity values were 8 to 10 times greater than the clinically-approved Gd^{3+}-based contrast agents (GBCA) (Figure 4.2 and Table 4.2). Also, ProCA32.CXCR4 exhibited good relaxivities at higher magnetic field 7.0 T as well (Figure 4.3 B), the r_1 and r_2 relaxivity values of non-PEGylated ProCA32.CXCR4 were 17.4 $mM^{-1}S^{-1}$ and 88.7 $mM^{-1}S^{-1}$, respectively. Interestingly, the relaxivities of the non-PEGylated form of ProCA32.CXCR4, lysine-PEGylated ProCA32.CXCR4 (Lys-ProCA32.CXCR4), and cysteine-PEGylated ProCA32.CXCR4 (Cys-ProCA32.CXCR4) did not exhibit significant differences (Figure 4.1 C, D and Table 4.2). The r_1 and r_2 relaxivities of ProCA32.CXCR4 are largely retained after PEGylation. Overall, ProCA32.CXCR4 exhibited significantly improved r_1 and r_2 relaxivities when compared with clinical gadolinium-based contrast agents at both 1.4 T and 7.0 T. The unique dual relaxation properties are essential for achieving early detection of small size tumor lesions in early stages using MRI.

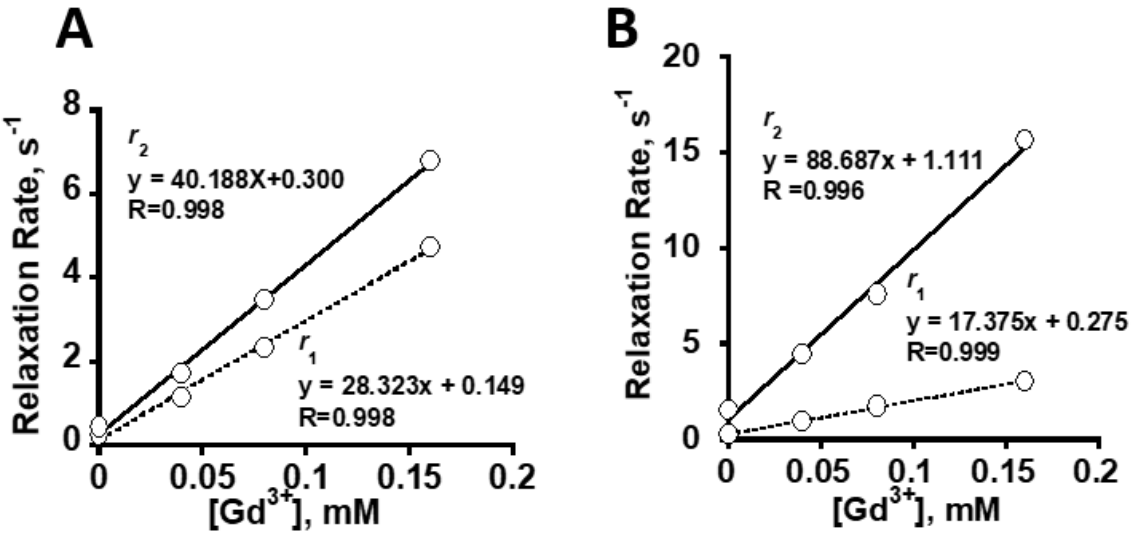

Figure 4.3 Determine Relaxivities of ProCA32.CXCR4 at different magnetic fields.
(**A**) Relaxivity assessment of ProCA32.CXCR4 with 60 MHz relaxometer. At 1.4 T, r_1 of ProCA32.CXCR4 is 28.3 mM^{-1} s^{-1}, r_2 of ProCA32.CXCR4 is 40.2 mM^{-1} s^{-1}. (**B**) Relaxivity assessment of ProCA32.CXCR4 with 7.0 T MR scanner. r_1 of ProCA32.CXCR4 is 17.4 mM^{-1} s^{-1}, r_2 of ProCA32.CXCR4 is 88.7 mM^{-1} s^{-1}.

Table 4.2 Relaxivities of investigated contrast agents at the different magnetic fields.

Relaxivities of investigated contrast agents in 10 Mm HEPES buffer at 37 ºC				
Contrast agent	*r*1 (1.5 T)	*r*2 (1.5 T)	*r*1 (7 T)	*r*2 (7 T)
Dotarem®	3.0 ± 0.2	3.3 ± 0.4	2.8 ± 0.4	5.3 ± 0.5
Magnevist®	3.1 ± 0.4	3.3 ± 0.2	3.1 ± 0.4	6.7 ± 0.4
Eovist®	4.3 ± 0.5	5.4 ± 0.4	4.9 ± 0.1	7.8 ± 0.7
ProHance®	3.4 ± 0.6	3.3 ± 0.4	3.4 ± 0.1	8.3 ± 0.6
ProCA32.CXCR4	30.9 ± 0.5	43.2 ± 1.0	23.5 ± 1.2	98.6 ± 3.2
Lys-ProCA32.CXCR4	27.6 ± 0.9	41.4 ± 2.7	20.3 ± 1.1	93.7 ± 4.2
Cys-ProCA32.CXCR4	28.3 ± 0.6	40.2 ± 0.3	17.4 ± 0.7	88.7 ± 3.1

* Relaxivity values in mM^{-1} s^{-1}

4.2.2 Metal-binding and metal selectivity study of ProCA32.CXCR4

4.2.2.1 Determine the Tb^{3+} binding affinity of ProCA32.CXCR4

In the process of designing new generation MRI contrast agent, improving the sensitivity (relaxivity) is primarily essential. Water proton relaxation by gadolinium (III) occurs via a dipolar mechanism and has a $1/r^6$ dependence on the distance between the ion and the nucleus. Because of this, it is critical to have one or more exchangeable waters in the inner- coordination sphere. Water exchange in and out of the first coordination sphere should be fast. Two major factors contribute to increasing the relaxation rate of bulk solvent: the paramagnetic ion should efficiently relax the water that accesses it, and the relaxed water should exchange rapidly with the bulk water.

ProCA32.CXCR4 has a wide metal binding pocket which allows more accessibility for the water molecules and faster bulk water exchange rate. In comparison with commercial MRI contrast agent such as Gd (DTPA), ProCA32.CXCR4 has more rigidity in molecular structure and slower in rotational speed, which leads to a higher relaxivity. For gadolinium (III) based contrast agents, high gadolinium (III) binding affinity is required for safety concern. To determine the gadolinium binding affinity can address this issue.

Gadolinium (III) has no fluorescent property. Therefore, an indirect method first was developed for gadolinium binding affinity measurement. Terbium has the similar element radius and carries the same charge with gadolinium. In addition, terbium has fluorescence property and can be excited with 330 nm wavelength light. One tryptophan was introduced close to the metal-binding sites to enable the luminescence resonance energy transfer (LRET). Fluorescence spectrum of terbium bond ProCA32.CXCR4 was collected (Figure 4.5 A). The terbium-ProCA32.CXCR4 complex fluorescence spectrum shows a peak at 545nm when excited with 280

nm wavelength light. The intensity is increasing in 545 nm indicating Tb^{3+} bound ProCA32.CXCR4 concentration increase. By fitting the intensity increase at 545 nm, dissociation constant of Tb^{3+} bound with CXCR4 can be calculated from the fractional signal intensity change corresponding to the "free terbium" concentration.

Calibration of Tb^{3+} can be achieved by either ICP-OES or complexometric titration. ICP-OES determined the ion concentration by intensity- concentration correlation defined by standard curve. Complexometric titration is the titration of the metal ion with the ligand that readily to form a complex with the metal ion. Xylenol orange was used as a metal indicator for complexometric titration of Tb^{3+} solution with DTPA buffer with known DTPA concentration. Once the titration reaches the endpoint, xylenol orange turns from violet to yellow color; this colorimetric change can also be detected more precisely by UV spectroscopy (Figure 4.4). Tb^{3+} solution concentration can be calculated with the equation

$$C_{Tb} \times V_{Tb} = C_{DTPA} \times V_{DTPA} \qquad \text{Equation 4.1}$$

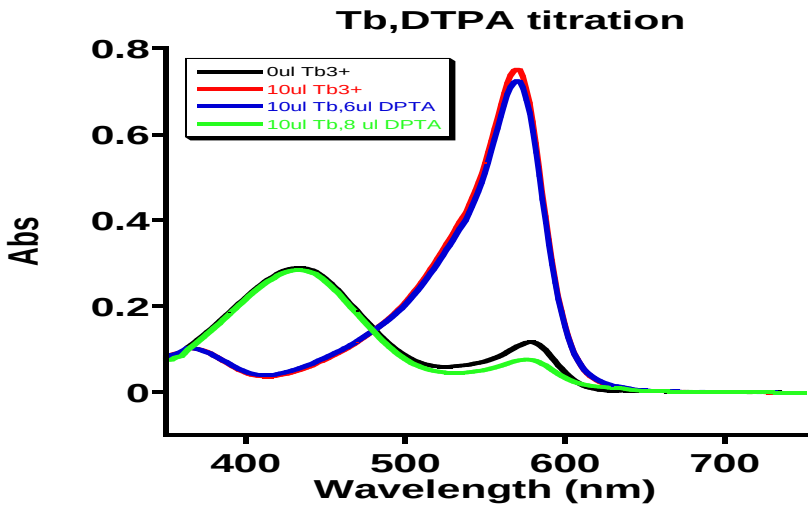

Figure 4.4 The UV spectrum of Tb^{3+}-DTPA titration in xylenol orange buffer.

The Tb^{3+} binding-affinity of ProCA32.CXCR4 is expected to be strong, and a DTPA buffer system was applied to control the free terbium concentration. DTPA chelator buffer contains 5 mM DTPA, 50 mM HEPES, 150 mM NaCl, and in pH 7.2. The dissociation constant of DTPA with Tb^{3+} is 10^{-21} M at 25 °C. The "free" Tb^{3+} concentration can be calculated by Equation 2.2.

Free Tb^{3+} has weaker 545nm emission peak when excited with 280 nm UV, a control group without ProCA32.CXCR4 was paralleled measured for signal subtraction. The intensity difference between the control sample and ProCA32.CXCR4 titration sample represents the signal intensity triggered by Tb^{3+} binding to the ProCA32.CXCR4. By fitting the free Tb^{3+} concentration and the corresponding fractional fluorescence intensity change with Equation 2.3, the K_d value of Tb^{3+} bound with ProCA32.CXCR4 is $3.38e^{-22}$ (Figure 4.5).

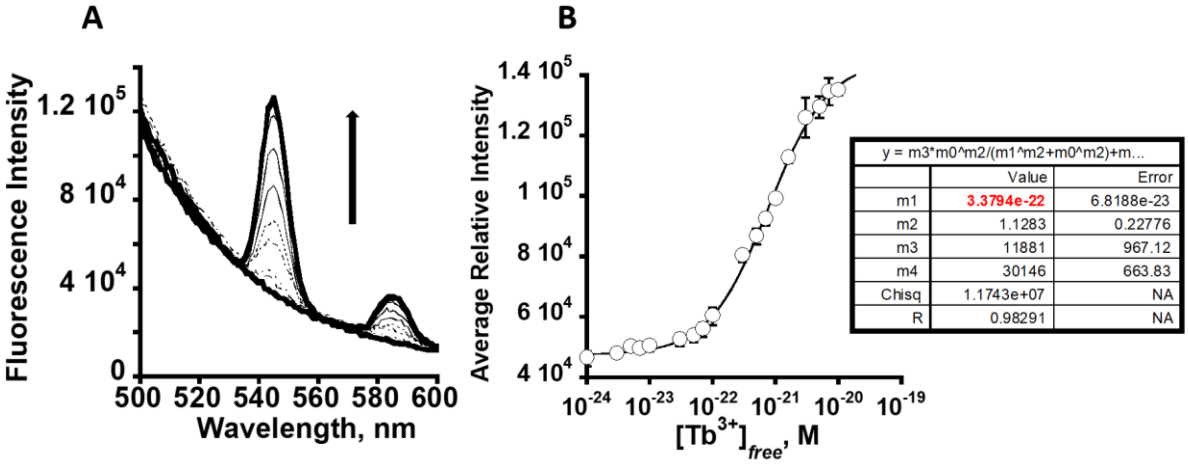

Figure 4.5 Determination of K_d value of Tb^{3+} binding affinity with ProCA32.CXCR4. Dissociation constant of Tb^{3+} with ProCA32.CXCR4 determined with DTPA-Tb^{3+} buffer system (5 mM DTPA, 50 mM HEPES, 150 mM NaCl, pH 7.2), K_d=3.38e-22 M. Data fitted with Hill equation.

4.2.2.2 Determine the Gd^{3+} binding affinity of ProCA32.CXCR4

The binding affinity of Gd^{3+} bound with ProCA32.CXCR4 determines the stability of gadolinium association with ProCA32.CXCR4 and the safety profile of ProCA32.CXCR4 for *in vivo* application. The Gd^{3+} binding affinity of ProCA32.CXCR4 is determined with DTPA buffer system and competitional titration with Tb^{3+}. Gd^{3+} and Tb^{3+} have the same charge and expected to possess a similar binding affinity to ProCA32.CXCR4.

In order to determine the Gd^{3+} binding affinity of ProCA32.CXCR4. 10 μM of ProCA32.CXRC4 and 20 μM Tb^{3+} were prepared in 5 mM DTPA, 50 mM HEPES, 150 mM NaCl at pH 7.2. Different concentrations of Gd^{3+}, from 0 μM to 200 μM, were incubated with Tb^{3+} loaded ProCA32.CXCR4 at room temperature for overnight. Fluorescence signal intensity of LRET between Tb^{3+} and ProCA32.CXCR4 decreases along with the Gd^{3+} concentration increases (Figure 4.6 A). By fitting the signal decrease with Equation 2.4, the apparent K_d of Gd^{3+}-Tb^{3+}competition was calculated (Figure 4.6 B).

Tb^{3+}-ProCA32.CXCR4 binding affinity and apparent K_d of Tb^{3+}- Tb^{3+} competition was obtained by fluorescence titration, Gd^{3+}- ProCA32.CXCR4 binding affinity is $1.2e10^{-22}$, calculated by Equation 2.5.

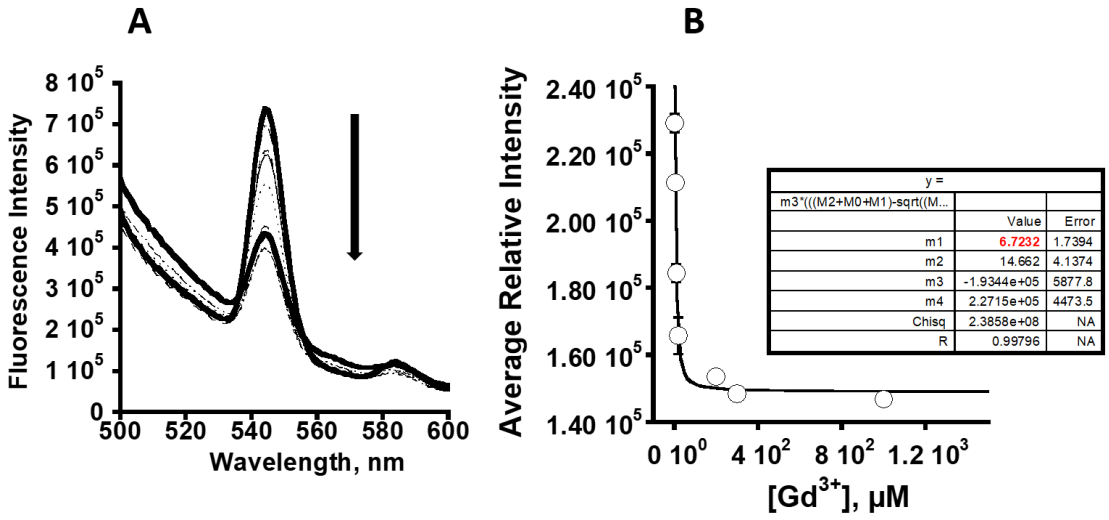

Figure 4.6 Determination of Gd^{3+} binding affinity of ProCA32.CXCR4.
The Gd^{3+} binding affinity of ProCA32.CXCR4 is determined in DTPA buffer system (5 mM DTPA, 50 mM HEPES, 150 mM NaCl, pH 7.2) by competing Tb^{3+} loaded ProCA32.CXCR4 with different concentration of Gd^{3+} and fit the fluorescence signal decrease at 545 nm with one to one binding. The K_d of Gd^{3+} -ProCA32.CXCR4 binding is 3.38e-22 M.

4.2.2.3 Determine Ca^{2+} binding affinity of ProCA32.CXCR4

Assessment of Ca^{2+} binding affinity of ProCA32.CXCR4 is important. ProCA32 is based on the scaffold protein parvalbumin, which is a calcium-binding protein. The gadolinium binding pockets of ProCA32.CXCR4 are modified calcium-binding sites. For *in vivo* application, one challenge is to improve the metal selectivity of ProCA32.CXCR4. The physiologically present metal ions such as Ca^{2+} and Zn^{2+} are competitors for Gd^{3+} and result in Gd^{3+} dissociation. The Ca^{2+} binding affinity of ProCA32.CXCR4 was determined by a fluorescence spectroscopy titration. A chelator buffer system contains 50 mM HEPES, 150 mM NaCl, and 5 mM EGTA at pH=7.2 was applied. 10 µM final concentration of ProCA32.CXCR4 was used for calcium titration. Different concentrations of calcium chloride ($CaCl_2$) were added into the buffer system, and the free calcium that dissociated from the EGTA buffer system is assumed binds to ProCA32.CXCR4 metal

binding pockets. The “free” calcium concentration was calculated using Equation 2.6 (Roger Tsien):

The fluorescence emission spectra record the wavelength from 300 nm to 400 nm followed by excitation of 280 nm. The fluorescence intensity changes at 310 nm corresponding to each titration point were used to calculate the dissociation constant of Ca^{2+} bind to ProCA32.CXCR4 using Equation 2.7, Ca^{2+} binding affinity of ProCA32.CXCR4 is 1.3 ± 0.1 e^{-8} M by hill equation fitting (Figure 4.7 B).

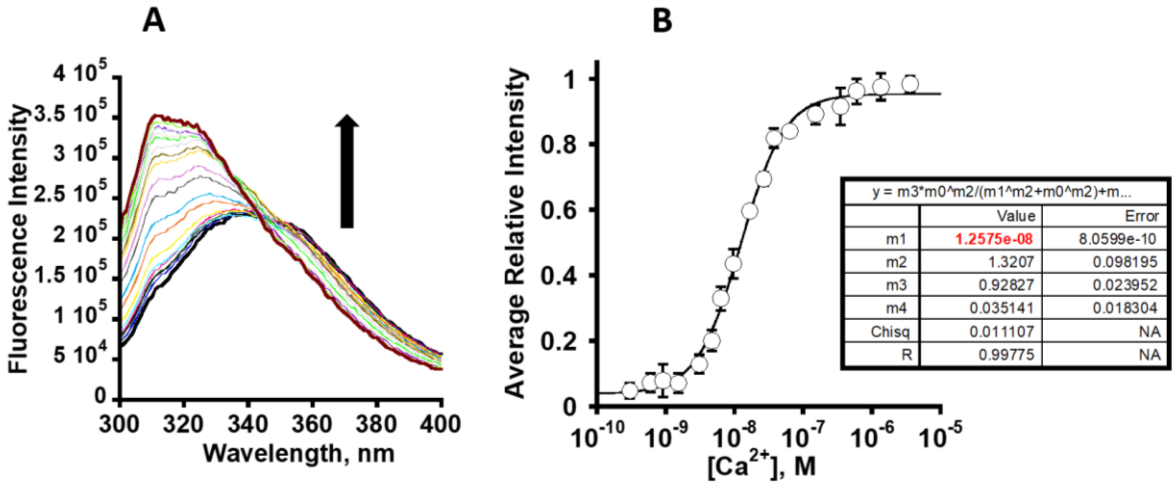

Figure 4.7 Determine the Ca^{2+} binding affinity of ProCA32.CXCR4.
The Ca^{2+} binding affinity of ProCA32.CXCR4 is determined in EGTA chelator buffer (50 mM HEPES, 150 mM NaCl, and 5 mM EGTA at pH=7.2). (**A**) Fluorescence spectra blue shift, and the intensity increases as the $CaCl_2$ titrated to the solution. (**B**) Fitting of the fluorescence intensity change in 520 nm along with an increase in Ca^{2+} concentration. The Ca^{2+} binding affinity of ProCA32.CXCR4 is 1.3±0.1 e-8 M. Data fitted by Hill equation.

ProCA32.CXCR4 has two metal-binding sites and cooperative bindings between the binding sites. Hill equation describes the cooperative binding assuming fixed cooperativity and denoted by Hill number *n*. When $n > 1$, means the whole system exhibits positive cooperativity,

when $n < 1$, the whole system exhibits negative cooperativity. Hill equation assumes the multiple binding sites possess same binding affinity.

In order to address the Ca^{2+} binding affinity of two binding sites, Adair equation hypothesized binding affinity depend on the ligand saturation instead of being a fixed parameter. It describes the binding affinity of each site more individually by an apparent macroscopic association constant *Ki*. By fitting the "free" Ca^{2+} concentration versus the fluorescence intensity change with Adair equation, K_d of Ca^{2+} binding affinity of two binding sites is 1.0 × e10^8 M and 6.7e × 10^7 M respectively (Figure 4.8).

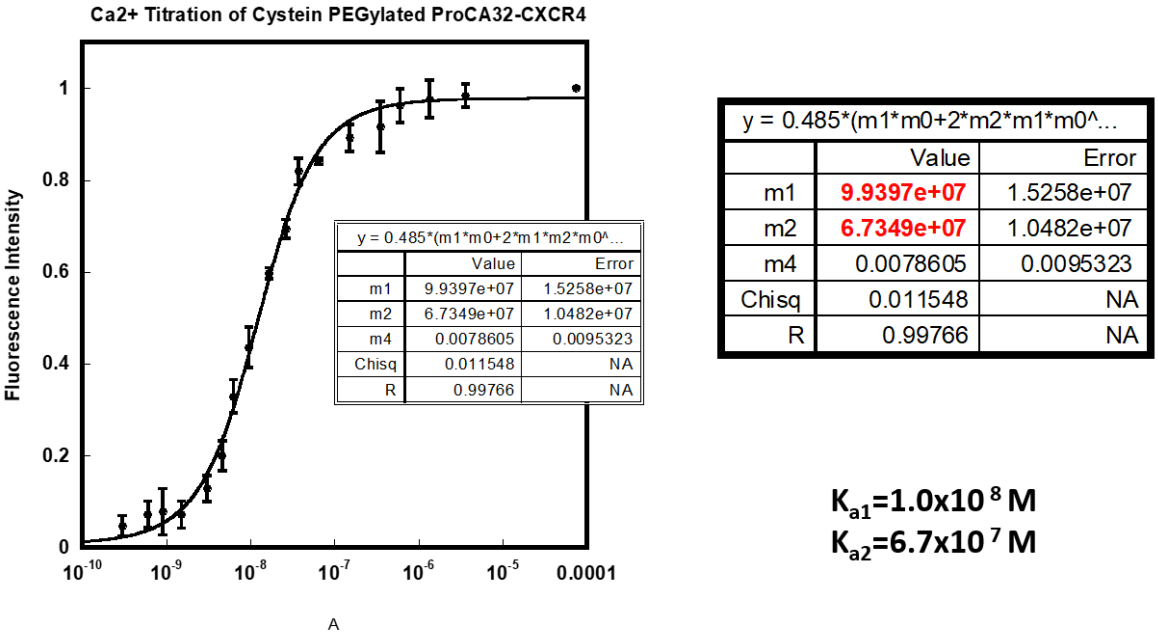

Figure 4.8 The Ca^{2+} binding affinity of ProCA32.CXCR4 Fitted with Adair equation. The Ca^{2+} binding affinity of ProCA32.CXCR4 is determined in EGTA chelator buffer (50 mM HEPES, 150 mM NaCl, and 5 mM EGTA at pH=7.2) and fitted with Adair equation to determine the Ca^{2+} binding affinity of each metal-binding sites. The K_d of Ca^{2+}-ProCA32.CXCR4 bindings are 1.0 e10^8 M and 6.7 e10^7 M, respectively.

4.2.2.4 Determine the Zn^{2+} binding affinity of ProCA32.CXCR4

The Zn^{2+} binding affinity of ProCA32.CXCR4 was determined by a competitional binding assay.1 μM of $ZnCl_2$ and 4 μM of Fluozin-1 were added in 50 mM HEPES, 150 mM NaCl, at pH 7.2 for titration. Different concentrations of ProCA32.CXCR4 from 0 μM to 80 μM were added to compete with Fluozin-1 for Zn^{2+} binding. Fluorescence spectra cover wavelength 500 nm to 600 nm were recorded following each titration. Fluorescence signal intensity changes at 510 nm were fitted with one to one binding and apparent K_d of ProCA32.CXCR4 competition with Fluozin-1 is acquired (Figure 4.9).

Dissociation constant of Fluozin-1 bound to Zn^{2+} is known to be 8 μM. The K_d between ProCA32.CXCR4 and Zn^{2+} were calculated with Equation 2.9 to be 1.6 ± 0.3 e^{-8}.

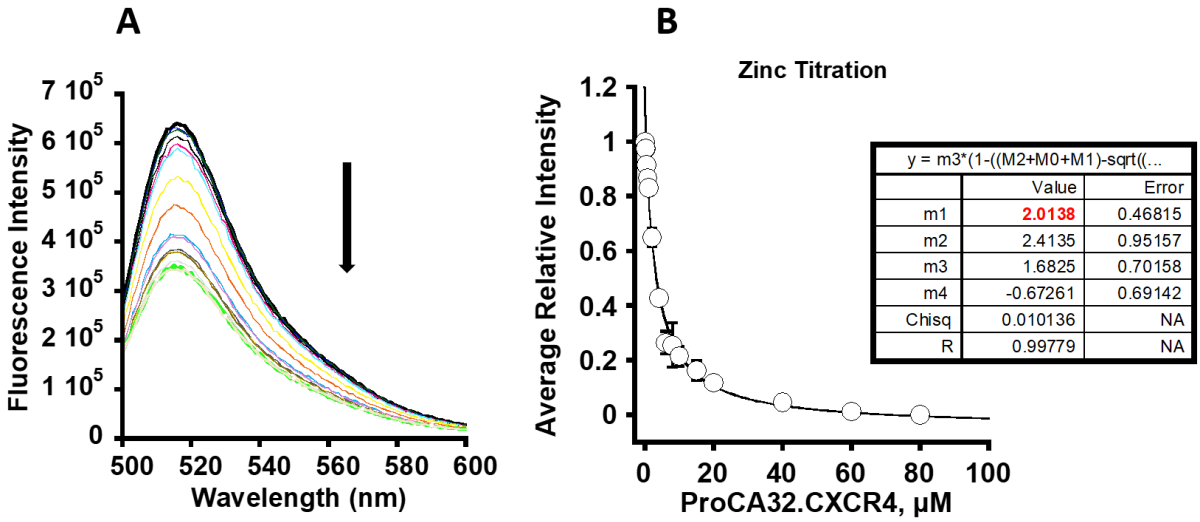

Figure 4.9 Determine the Zn^{2+} binding affinity of ProCA32.CXCR4.
The Zn^{2+} binding affinity of ProCA32.CXCR4 is determined by competition assay. (**A**) By competing binding of Fluozin-1 to Zn^{2+} with ProCA32.CXCR4, fluorescence intensity decreases. (**B**) Fitting the fluorescence intensity decrease at 510 nm along with ProCA32.CXCR4 concentration increase, apparent Kd of ProCA32.CXCR4-Fluozin-1 competition is 2.01 μM.

4.2.3 Determine water number (q) of ProCA32.CXCR4

Water number *q* of ProCA32.CXCR4 is a key factor affecting the relaxivities of contrast agents. The water number of ProCA32.CXCR4 is measured by a lifetime of terbium luminescence decay with ProCA32.CXCR4: Tb^{3+} loading ratio of 1:1 and 1:2 respectively (Figure 4.12). There are two components of terbium luminescence decay: radiative decay (Γ) and non-radiative decay (K). Many factors contribute to non-radiative decay, such as quenching, energy transfer, and molecular collation. Water number is an important factor influent non-radiative decay. By replacement of H_2O molecule with D_2O, the water number contribution to the terbium luminescence decay is eliminated because D_2O does not cause luminescence decay. By this way, the difference between terbium lifetime (Δk_{obs}) of ProCA32.CXCR4 prepared in H_2O and D_2O respectively reflect the water number of ProCA32.CXCR4.

The correlation of water number and Δk_{obs} is established by the water number of other chelators and their Δk_{obs}, respectively (Figure 4.11). Water number standard curve was determined by fluorescence lifetime of other chelators: DTPA, EDTA, and NTA. The water number of DTPA, EDTA, NTA, and aqua is determined by X-ray powder diffraction by reported literature (171). The water number of ProCA32.CXCR4 are 0.5 and 0.64 respectively with 1:2 and 1:1 ProCA32.CXCR4 and Tb^{3+} loading ratio. The water number of ProCA32.CXCR4 is consistent with ProCA32-P40.

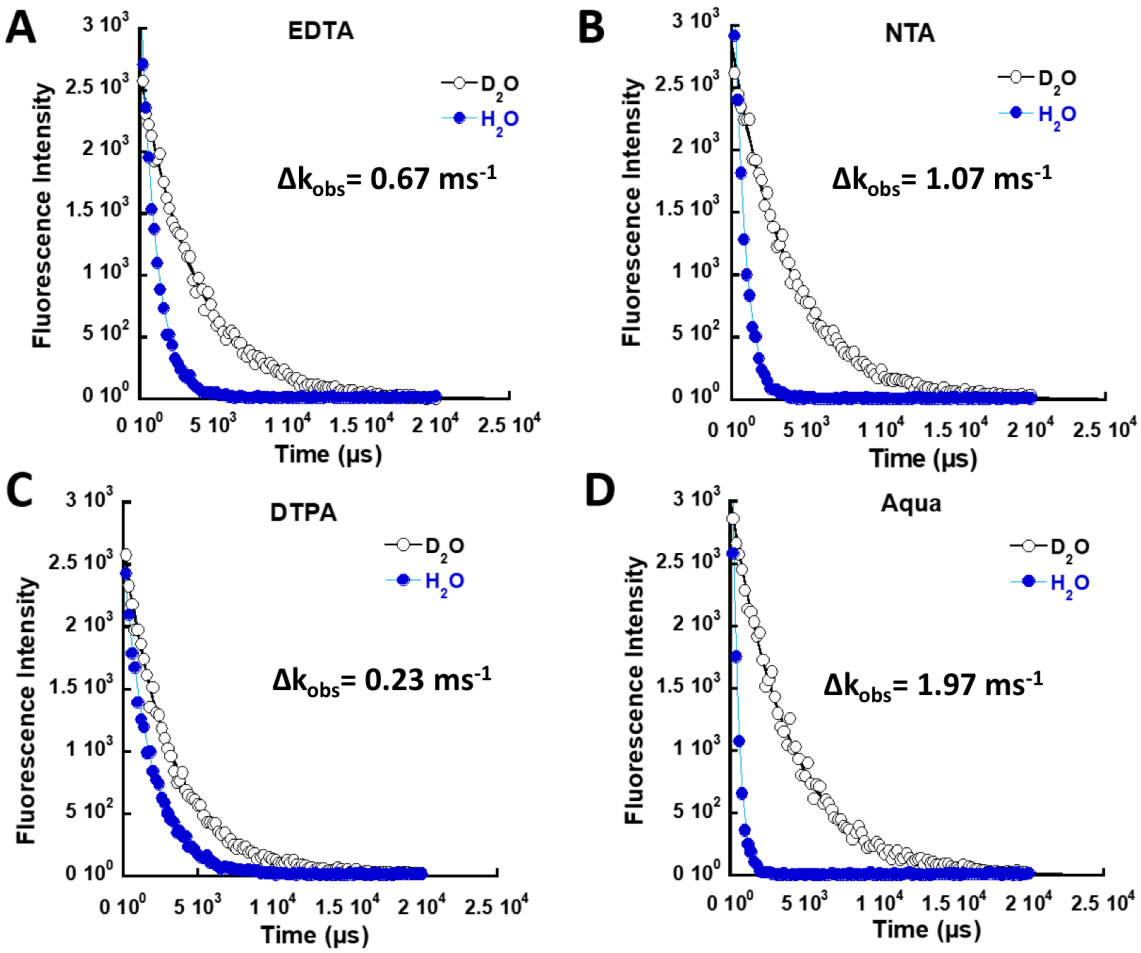

Figure 4.10 Fluorescence lifetime of different chelators and the corresponding Δk_{obs}. The fluorescence lifetime of different chelators including EDTA, NTA, DTPA and aqua. The corresponding lifetime difference of EDTA, NTA, DTPA, and aqua are 0.67 ms^{-1}, 1.07 ms^{-1}, 0.23 ms^{-1} and 1.97 ms^{-1}.

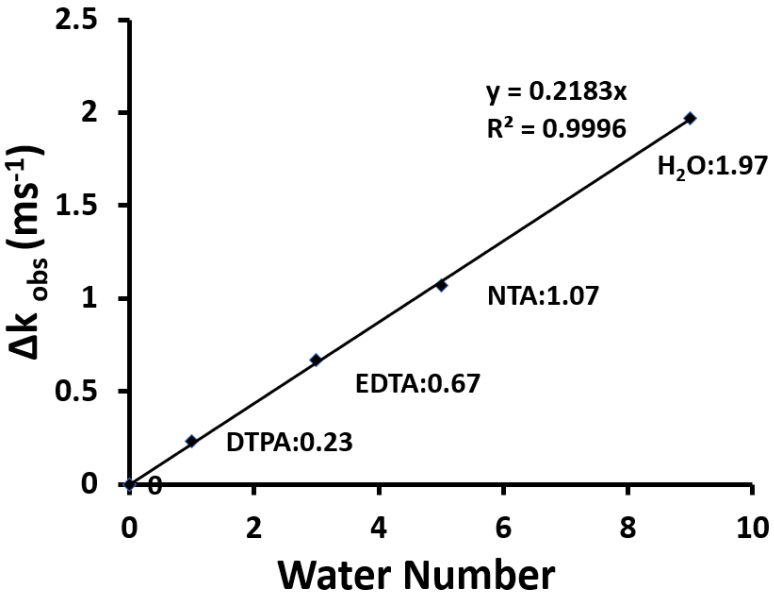

Figure 4.11 Standard curve of water number of different chelators versus Δk_{obs}.

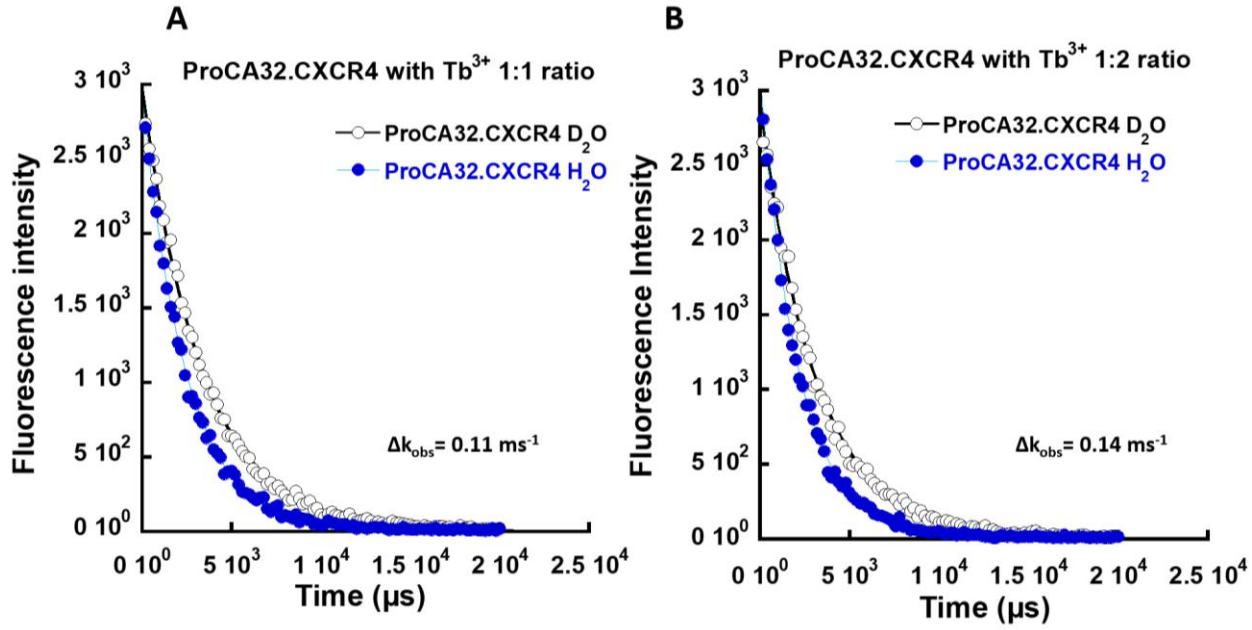

Figure 4.12 Determine water number of ProCA32.CXCR4 with different loading ratio with Tb^{3+}.

Δk_{obs} of ProCA32.CXCR4 is determined by ProCA32.CXCR4 load with Tb^{3+} in 1:1 and 1:2 ratio. (**A**) Δk_{obs} of ProCA32.CXCR4 when loaded with Tb^{3+} in 1:1 ratio is 0.11 ms^{-1}. (**B**) Δk_{obs} of ProCA32.CXCR4 when loaded with Tb^{3+} in 1:2 ratio is 0.14 ms^{-1}

4.2.4 Serum stability study of ProCA32.CXCR4

Serum stability of ProCA32.CXCR4 describes the capability of ProCA32.CXCR4 to stay structurally intact under physiological conditions. Serum stability study of ProCA32.CXCR4 carried out by incubating 150 µL of 500 µM ProCA32.CXCR4 with 150 µL of mouse serum at 37°C for up to 14 days. 15 µL of the mixed sample was taken at 0 hours, 3 hours, 4 hours, 1 day, 2 days, 4 days, 6 days, 8 days, and 14 days after incubation. 300 µL of mouse serum without adding ProCA32.CXCR4 was served as control. Samples collected from different time points were analyzed by gel electrophoresis and ponceau red staining of the nitrocellulose membrane. ProCA32.CXCR4 is stable up to 14 days when incubated with mouse serum under 37°C (Figure 4.13), whereas the mouse serum protein started to degrade at 4 hours after incubation at 37°C (Figure 4.14). ProCA32.CXCR4 can stay structurally stable under physiological conditions, and the serum stability guaranteed the *in vivo* application of ProCA32.CXCR4.

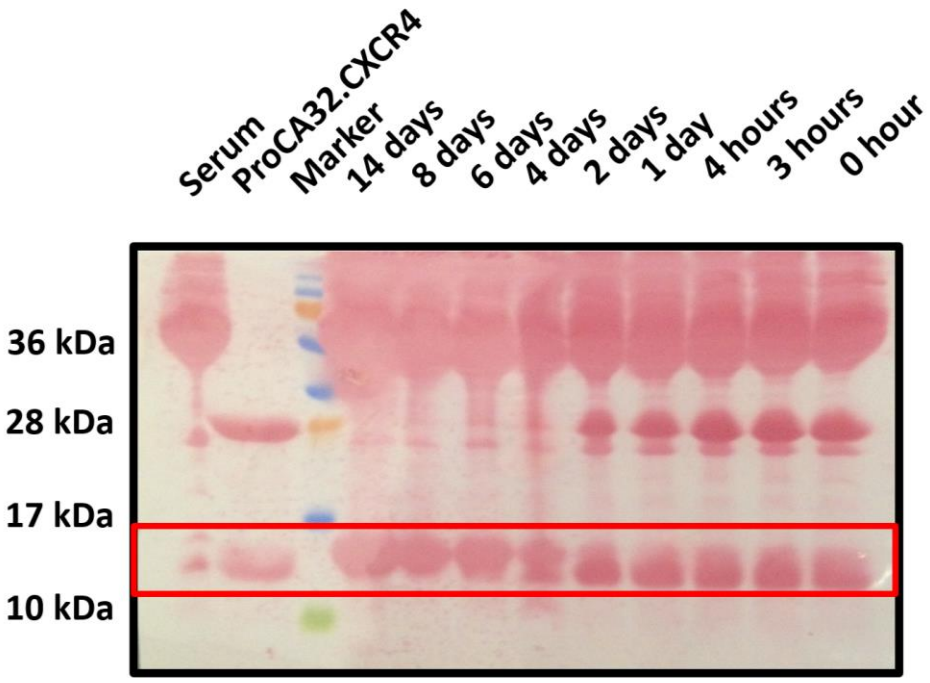

Figure 4.13 Serum stability study of ProCA32.CXCR4
ProCA32.CXCR4 is stable in mouse serum at 37°C for up to 14 days. Ponceau red staining of nitrocellulose membrane with gel transfer shows the ProCA32.CXCR protein bands (highlighted by red frame) is intact up to 14 days when incubated with mouse serum at 37°C.

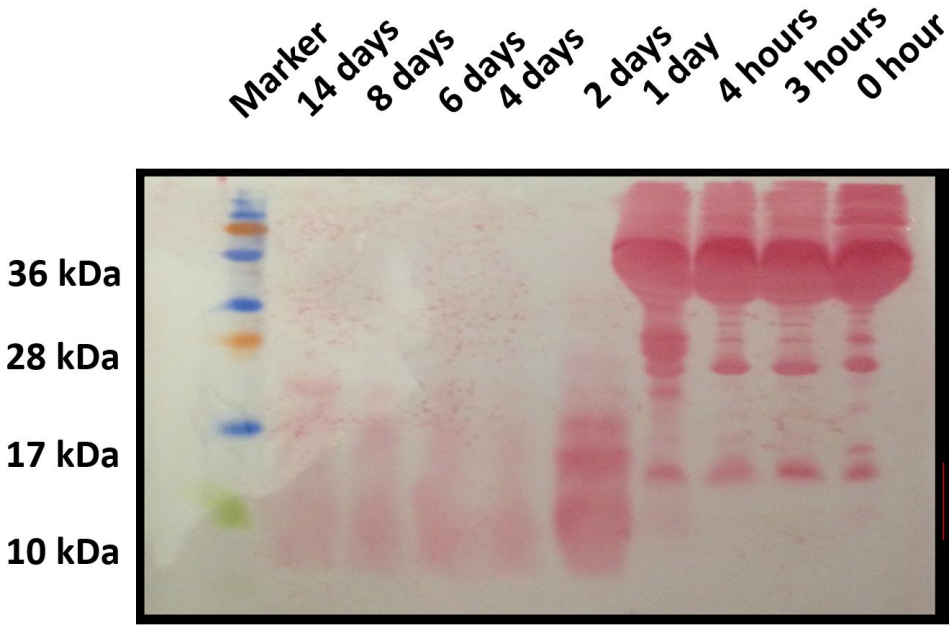

Figure 4.14 Ponceau red staining of mouse serum incubates at 37°C for up to 14 days.

4.2.5 Transmetallation study of ProCA32.CXCR4

The kinetic inertness of gadolinium complex regarding the transmetallation process from physiological ions is an important factor to evaluate the suitability of such gadolinium complex as an MRI contrast agent. A relaxometric transmetallation assessment was performed to characterize the kinetic inertness of the Gd^{3+}-ProCA32.CXCR4 complex to transmetallation process in the presence of Zn^{2+}. ProCA32.CXCR4 is mixed with the same concentration of $ZnCl_2$ (2.5 mM) in pH 7.0 phosphate buffer. The final mixture contained 0.026 M KH_2PO_4, 0.041 M Na_2HPO_4, 2.5 mM Gd^{3+} complex, and 2.5 mM $ZnCl_2$. When transmetallation of Gd^{3+} by Zn^{2+} occurred, insoluble $GdPO_4$ formed, and a decrease in longitudinal relaxation rate was observed. The longitudinal relaxation rate change of the mixture along with time reflected the transmetallation process of Gd^{3+} by Zn^{2+}. The thermodynamic index was calculated by r_1 of the mixture after incubation at the

present of Zn^{2+} over the initial r_1. Transmetallation of other GBCAs is measured following the same protocol as a comparison.

The transmetallation study (Figure 4.15) indicated that ProCA32.CXCR4 complex with Gd^{3+} has the highest stability in the presence of Zn^{2+}, with a higher thermodynamic index ($R_1(t)$ = 4320 min/ $R_0(t)$= 0 min) of 0.958, over Gadovist (0.952), ProHance (0.926), and Dotarem (0.932) (Table 4.3). Other linear reagents such as Magnevist® (gadopentetate) and Eovist® (gadoxetate) cannot protect Gd^{3+} well against transmetallation by Zn^{2+}, and relaxivity measurements of those contrast agents were significantly reduced when incubated in the presence of Zn^{2+} (Table 4.3).

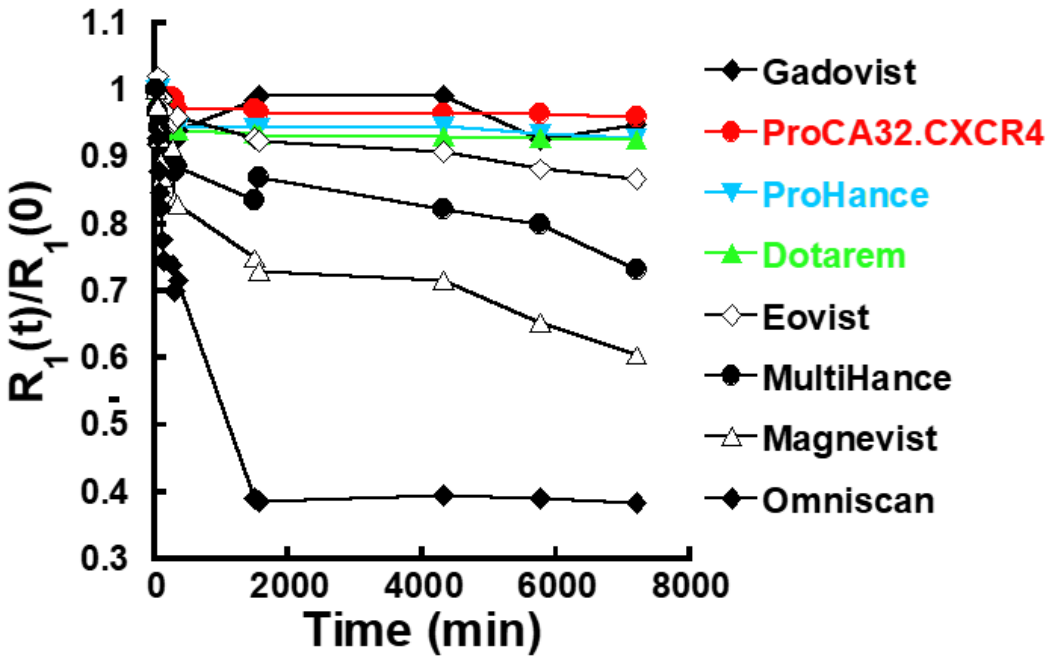

Figure 4.15 Transmetallation study of ProCA32.CXCR4 and other GBCAs.
Transmetallation study of ProCA32.CXCR4 and other GBCAs are carried out with a relaxometric assay. Thermodynamic index ($R_1(t)$ = 4320 min/ $R_0(t)$= 0 min) represents the preserve of longitudinal relaxivity at the presence of Zn^{2+}. ProCA32.CXCR4, ProHance, and Dotarem show higher kinetic inertness than other GBCAs such as MultiHance, Magnevist, and Omniscan.

Table 4.3 Thermodynamic index of ProCA32.CXCR4 and other GBCAs at 72 hours incubation with a Zn^{2+}-containing phosphate buffer.

Contrast Agent	*Thermodynamic Index (R_1t = 4320 min/R_0t = 0 min)
ProCA32.CXCR4	0.958
Gadovist	0.952
ProHance	0.926
Dotarem	0.932
Eovist	0.907
MultiHance	0.821
Magnevist	0.716
Omniscan	0.394

4.2.6 Biodistribution study of ProCA32.CXCR4

Biodistribution study of ProCA32.CXCR4 aims to assess the amount of ProCA32.CXCR4 distributed to different organs after a specific time of ProCA32.CXCR4 injection. ICP-OES was used to analyze the gadolinium content of different organs, and tissues follow different dosages of ProCA32.CXCR4.

The distribution of Cys-ProCA32.CXCR4 to organs including liver, spleen, heart, and kidney were analyzed following the injection of imaging dosage (100 µL of 5 mM Cys-ProCA32.CXCR4). Gadolinium concentration (µM/g), percentage injection dosage per gram tissue (%ID/g), and percentage injection dosage per organ (%ID/organ is calculated). Mice injected with Cys-ProCA32.CXRC4 were euthanized 50 minutes, 3 hours, 25 hours, and 30 hours after above described dosage of Cys-ProCA32.CXCR4.

A standard curve is made of ICP-OES measurement of different known concentration of gadolinium solution versus intensity (Figure 4.16). Different tissues, including liver, spleen, heart, and kidney, were weighted and dissolved in concentrated nitric acid and filtered before ICP-OES analysis. The concentration of gadolinium in tissue solutions was calculated by the standard curve and intensity.

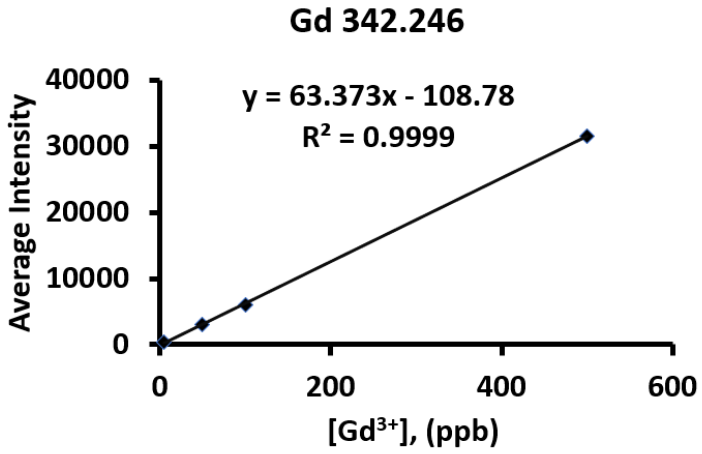

Figure 4.16 Standard curve of gadolinium intensity.

The analysis of gadolinium concentration in different organs at different time points (50 minutes, 3 hours, 25 hours, and 30 hours) followed Cys-ProCA32.CXCR4 are listed below (

Table 4.4 to

Table 4.7, Figure 4.17 to Figure 4.20). Results show that Cys-ProCA32.CXCR4 has high liver affinity, the percentage injection dosage in liver account for 17.65 % of total injection after 50 minutes of injection. The gadolinium concentration in the liver keeps increase up to 25 hours

after injection. At 25 hours after injection, the amount of gadolinium in the liver account for 66.64 % of total injection dosage.

Table 4.4 The concentration of gadolinium in the liver at different time points follow the injection of Cys-ProCA32.CXCR4.

Liver	$[Gd^{3+}]$,μm/g	%ID/g organ	%ID/organ
50 min	0.12	12.09	17.66
3 h	0.30	29.67	43.32
25 h	0.46	45.65	66.64
30 h	0.36	36.16	52.79

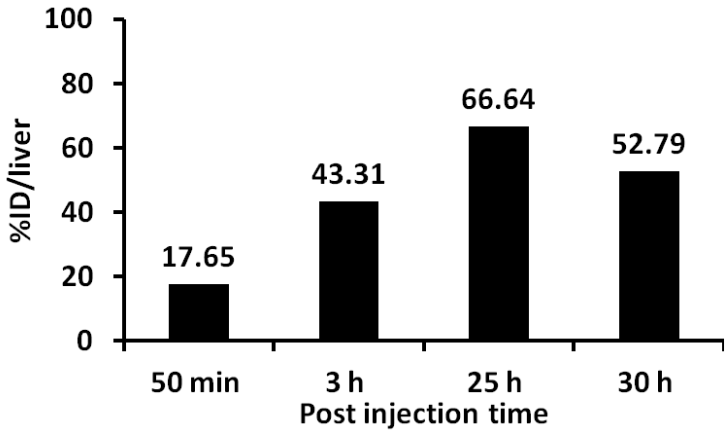

Figure 4.17 Percentage injection dosage of gadolinium in the liver.
Biodistribution of gadolinium (characterized by percentage injection dosage in the liver) after 50 minutes, 3 hours, 25 hours, and 30 hours injection of ProCA32.CXCR4.

The gadolinium has the second-highest gadolinium distribution is spleen. However, it is significantly lower than the liver. At the peak time point (25 hours), 8.32 % of the total injection

dosage of Cys-ProCA32.CXCR4 goes to the spleen. Cys-ProCA32.CXCR4 barely distributed to the kidney and heart.

Table 4.5 Gadolinium concentration in the kidney at different time points followed the injection of Cys-ProCA32.CXCR4.

Kidney	$[Gd^{3+}]$,μm/g	%ID/g organ	%ID/organ
50 min	0.03	3.40	1.33
3 h	0.03	2.78	1.08
25 h	0.05	5.36	2.09
30 h	0.04	4.01	1.56

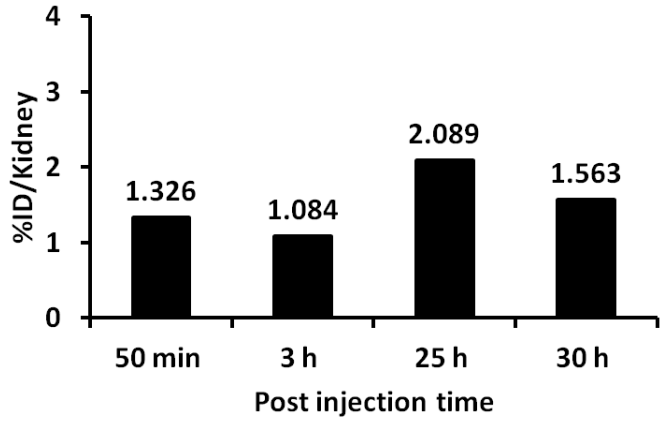

Figure 4.18 Gadolinium distribution in the kidney.
Biodistribution of gadolinium (characterized by percentage injection dosage) in kidney after 50 minutes, 3 hours, 25 hours, and 30 hours injection of ProCA32.CXCR4.

Table 4.6 Gadolinium concentration in the spleen at different time points followed the injection of Cys-ProCA32.CXCR4.

Spleen	$[Gd^{3+}]$,µm/g	%ID/g organ	%ID/organ
50 min	0.08	7.55	1.28
25 h	0.49	48.97	8.32
30 h	0.32	31.51	5.36

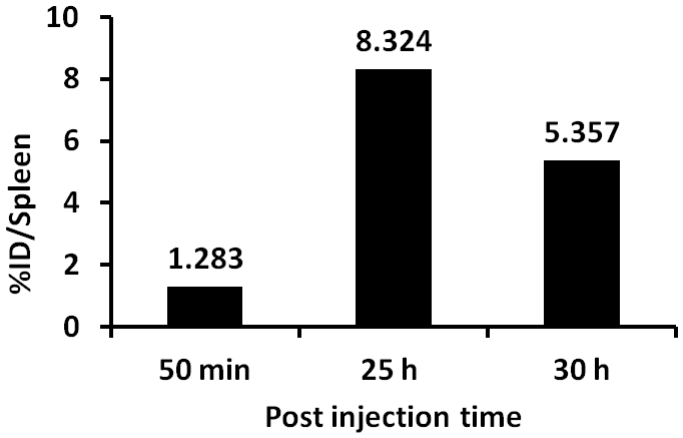

Figure 4.19 Gadolinium distribution in the spleen.
Gadolinium concentration (characterized by percentage injection dosage) in spleen after 50 minutes, 3 hours, 25 hours, and 30 hours injection of ProCA32.CXCR4.

Table 4.7 Gadolinium concentration in the heart at different time points followed by the injection of Cys-ProCA32.CXCR4.

Heart	$[Gd^{3+}]$, µm/g	%ID/g organ	%ID/organ
50 min	0.02	1.78	0.30
25 h	0.01	0.66	0.11
30 h	0.00	0.34	0.06

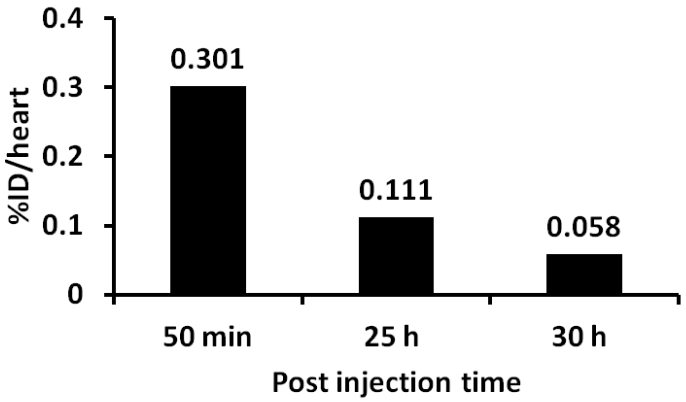

Figure 4.20 Gadolinium concentration in the heart.
Gadolinium concentration (characterized by percentage injection dosage) in the heart after 50 minutes, 3 hours, 25 hours, and 30 hours injection of ProCA32.CXCR4.

Biodistribution of gadolinium in different organs after 5 days injection of different PEGylation of ProCA32.CXCR4 was analyzed to compare the influence of PEGylation on biodistribution and the gadolinium retention after a more extended time. The gadolinium concentration in the liver of the mouse with Cys-ProCA32.CXCR4 injection at 5 days further decreases than 30 hours, the other organs including heart, spleen, and kidney as well. Interestingly, compared with Cys-ProCA32.CXCR4, Lys-ProCA32.CXCR4 exhibited higher gadolinium retention; it might be a result of Lys-ProCA32.CXCR4 has multiple PEGylation sites and a longer

half-life. The result suggests Lys-ProCA32.CXCR4 has longer time window for imaging than Cys-ProCA32.CXCR4 and could require less dosage when compared with Cys-ProCA32.CXCR4.

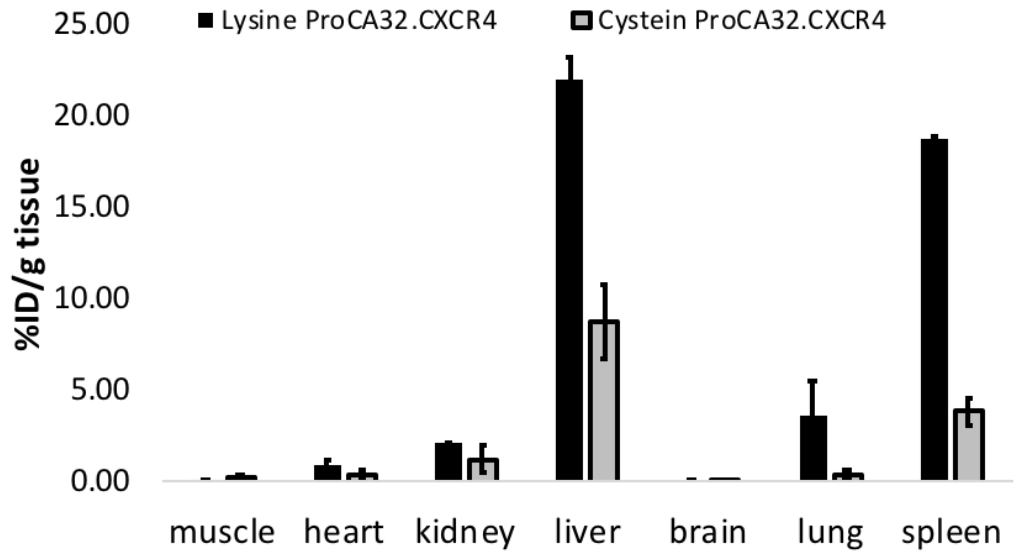

Figure 4.21 Gadolinium bio-distribution after 5 days injection of ProCA32.CXCR4 with different PEGylation.

The liver and spleen are the organs most retain gadolinium, followed by lung, kidney, muscle, and brain has almost no distribution.

4.2.7 Pharmacokinetics study of ProCA32.CXCR4.

Detailed pharmacokinetics study showed ProCA32.CXCR4 has good exposure and bioavailability, $AUC_{0\text{-}72h}$ of ProCA32.CXCR4 was 113.20 μg·h/mL (Table 4.8), larger than ProCA32-P40 (33.77 μg·h/mL). Because of ProCA32.CXCR4 is CXCR4 targeted contrast agent and expected to have higher tissue affinity caused by CXCR4 targeting. The clearance of ProCA32.CXCR4 was 0.31 mL/min/kg, slightly less than Eovist (0.4 mL/min/kg). ProCA32.CXCR4 had a half-time of 9.19 h, with a mean residence time (MRT) of 19.58 h.

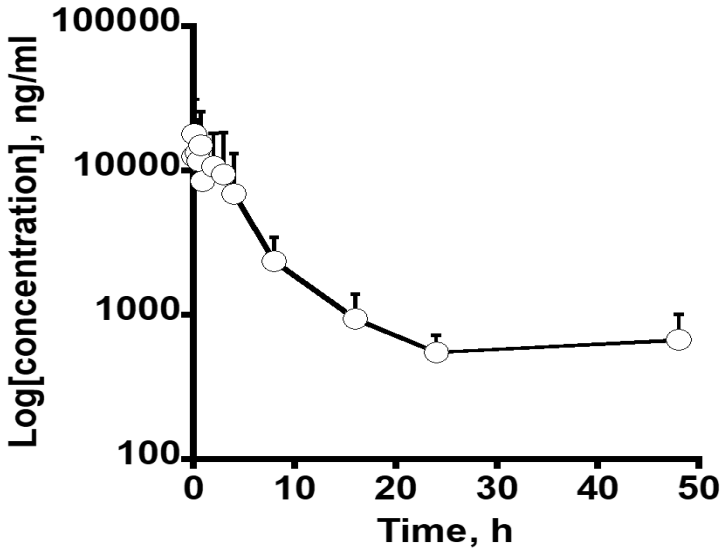

Figure 4.22 Pharmacokinetics curve of ProCA32.CXCR4.

Table 4.8 Pharmacokinetics parameters of ProCA32.CXCR4 and comparison with Eovist and ProCA32-P40.

Contrast Agent	Eovist	ProCA32-P40	ProCA32.CXCR4
$t_{1/2\beta}$ (h)	0.2	8.09	9.19
V_c (L/kg)	N/A	0.20	1.38
V_{ss} (L/kg)	0.21	0.76	1.96
CL (mL/min/kg)	0.4	0.11	0.31
MRT (h)	N/A	13.90	19.58
$AUC_{0\text{-}72h}$ (μg·h/mL blood)	N/A	30.77	113.20

4.2.8 Toxicity study of ProCA32.CXCR4

In the toxicity study, ProCA32.CXCR4 with cysteine PEGylation and lysine PEGylation were tested respectively. The acute toxicity was tested by a bolus injection of 100 μL, 5 mM ProCA32.CXCR4 to 10-week-old healthy CD1 strain mice. Each group contains 3 animals, control group with saline injection. Mouse blood collected through a terminal collection by cardiac puncture. Serum was collected as previously described in the material and methods section. Alanine transaminase (ALT), aspartate aminotransferase (AST), alkaline phosphatase (ALP), albumin, and bilirubin levels in blood serum were tested to evaluate ProCA32.CXCR4 acute toxicity. Alanine transaminase (ALT) is used to metabolize protein in the body. If the liver is damaged or not functioning properly, ALT is released into the blood. This causes the ALT level to increase. An elevated level of ALT indicates liver damage. Aspartate aminotransferase (AST) is an enzyme found in several different tissues and organs, including the heart, liver, and muscles. Since AST are not exclusively located in the liver, it usually assists the diagnosis of liver damage together with ALT. An elevated AST level indicates liver or muscle damage. Alkaline phosphatase (ALP) is an enzyme found in bones, bile ducts, and liver. High level of ALP is an indication for liver damage, blockage of the bile ducts, or bone diseases. Children and adolescents may have elevated levels of ALP because of bone development. Albumin is the main protein generated by the liver. It has many important biological functions. Albumin test measures the ability of the liver to produce albumin. A decrease in albumin level is an indication of abnormal liver function. Bilirubin is generated in the breakdown process of red blood cells. Bilirubin passes through the liver before excreted through bile ducts. Damaged livers cannot efficiently process bilirubin, which leads to the abnormally elevated level of bilirubin in the blood.

Pathology profile of mice with the injection of ProCA32.CXCR4 is listed in Table 4.9. ALP, ALT levels of mice with the injection of the cysteine PEGylated ProCA32.CXCR4 and lysine PEGylated ProCA32.CXCR4 are comparable with the results from control mice. AST levels show slightly increase when compared with control mice. It could be caused by the *in vitro* hemolysis during the serum sample preparation, which needs to be further verified by repeat the toxicity result: Albumin, total bilirubin, bilirubin-conjugated, and bilirubin-unconjugated levels in ProCA32.CXCR4 injected mice has no significant difference when compared with control mice.

Mice tissues, including brain, muscle, kidney, lung, heart, liver, and spleen, were collected and fixed by formalin and embedded by paraffin. Tissues are sliced to 5 μM thickness sections and stained with H&E staining (Figure 4.23). H&E staining of tissues from mice after seven days and fourteen days after injection of ProCA32.CXCR4 shows no difference with healthy tissues. Pathology profile analysis of ProCA32.CXCR4 combined with H&E staining of mice tissues suggesting the ProCA32.CXCR4 exhibit no acute toxicity in the mouse study.

Table 4.9 Clinical pathology profile of mice with the injection of ProCA32.CXCR4.
Mouse serum samples collected 2 days after injection of saline (control, n = 3) or 0.025 mmol/kg of Lys-ProCA32.CXCR4/Cys-ProCA32.CXCR4 (n = 3) were used for pathology profiling. Data are expressed as mean ± SD.

Analyte	Control	Lys-ProCA32.CXCR4	Cys-ProCA32.CXCR4
Cholesterol, mg/dL	98.3 ± 20.1	109.7 ± 26.4	110.3 ± 12.7
Glucose, mg/dL	283.0 ± 45.6	253.7 ± 92.0	282.0 ± 81.1
Calcium, mg/dL	11.0 ± 0.5	7.6 ± 2.1	9.4 ± 0.5
Phosphorus, mg/dL	12.8 ± 1.5	13.7 ± 3.0	13.8 ± 3.5
Chloride, mmol/L	110.1 ± 5.1	104.7 ± 4.2	109.2 ± 7.3
Potassium, mmol/L	12.6 ± 0.7	10.4 ± 0.9	15.7 ± 3.3
Sodium, mmol/L	149.2 ± 4.7	144.0 ± 5.6	141.5 ± 2.5
Creatinine, mg/dL	0.2 ± 0.1	0.4 ± 0.3	0.6 ± 0.5
Albumin, g/dL	3.0 ± 0.3	2.9 ± 0.5	3.1 ± 0.3
Total Bilirubin, mg/dL	0.2 ± 0.2	0.4 ± 0.3	0.3 ± 0.2
ALP(U/L)	85.7 ± 13.3	52.3 ± 18.6	46.3 ± 18.9
ALT(U/L)	36.0 ± 7.9	74 ± 9.2	118.0 ± 31.7

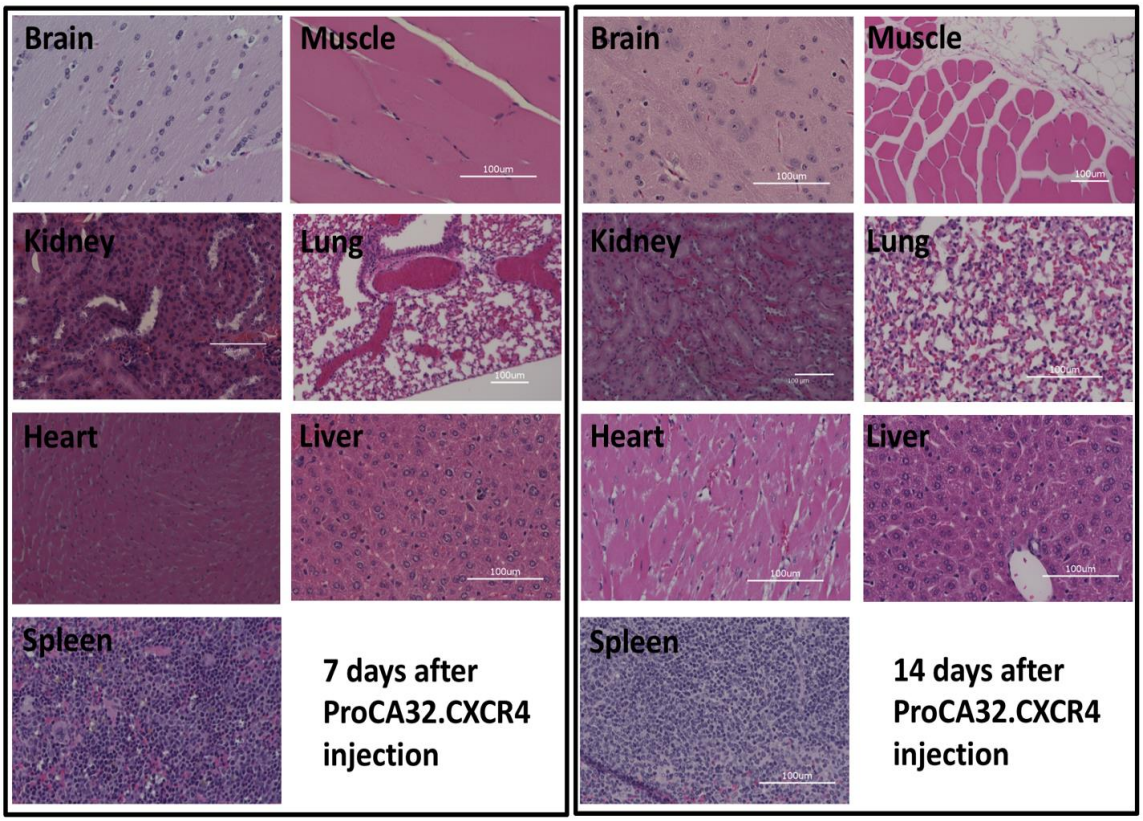

Figure 4.23 H&E staining of mice tissues collected 7 and 14 days after injection of ProCA32.CXCR4.

Mice (n=3) organs, including brain, kidney, heart, spleen, muscle, lung, and liver, were collected 7 and 14 days after injection of 0.025 mmol/kg ProCA32.CXCR4. No obvious tissue damage occurred in the mouse organs.

4.3 Conclusion and discussion

The biophysics properties including relaxivities, metal binding affinities, water number, inertness to transmetallation process were well defined and characterized. ProCA32.CXCR4 shows both high longitudinal and transverse relaxivities, at the lower and higher magnetic field. The r_1 and r_2 values per gadolinium for ProCA32.CXCR4 are 30.9 $mM^{-1}\,s^{-1}$ and 40.2 $mM^{-1}\,s^{-1}$, respectively, at 1.4 T. At 7.0 T magnetic field, the r_1 and r_2 of ProCA32.CXCR are 17.4 $mM^{-1}\,s^{-1}$, 88.7 $mM^{-1}\,s^{-1}$, respectively. The relaxivities will be doubled if calculated as per ProCA32.CXCR4 particle relaxivities since ProCA32.CXCR4 has two gadolinium binding sites. PEGylation has no

significant influence on relaxivities. ProCA32.CXCR4 with different PEGylation and non-PEGylation exhibit no significant difference in relaxivities. The relaxivities of ProCA32.CXCR4 are significantly improved in comparison with other GBCAs and enable more sensitive MR imaging.

The best loading ratio of ProCA32.CXCR4 with gadolinium to achieve the optimized relaxivities is 1:2 when setting the concentration of gadolinium and increase the concertation of ProCA32.CXCR4, the relaxivities of ProCA32.CXCR4 – Gd^{3+} complex first increase and then decrease. Relaxivity values reach to the highest when the concentration of ProCA32.CXCR4 : Gd^{3+} equals to 1:2. It can be explained by the two Gd^{3+} binding sites of ProCA32.CXCR4 have different gadolinium binding affinity which caused by a difference in metal coordination. Fitting Ca^{2+} binding curve of ProCA32.CXCR4 with Adair equation also validated that two metal-binding sites of ProCA32.CXCR4 possess different metal binding affinities. Water number measurement of ProCA32.CXCR4 by terbium fluorescence lifetime shows that ProCA32.CXCR4-Tb^{3+} complex (ProCA32.CXCR4: Tb^{3+} =1:2) has water number of 0.5. The water number measurement validated the inequivalence of two metal-binding sites in coordination. The two binding sites of ProCA32.CXCR4 only possess one water, one metal-binding site coordinates metal through water molecule while the other binding site does not. When the concentration of gadolinium is fixed, ProCA32.CXCR4 concentration increases, the Gd^{3+} initially saturated two binding sites, so an increase in relaxivities are observed. When the concentration of ProCA32.CXCR4 reaches the half concentration of gadolinium, highest relaxivities are observed because theoretically, all Gd^{3+} can bind to ProCA32.CXCR4. When keep increasing the ProCA32.CXCR4 concentration after that point, more Gd^{3+} starts to go to the binding site with higher affinity. As a result, a decrease in

relaxivities is observed because the binding site with higher affinity does not coordinate Gd^{3+} through a water molecule.

The relaxivities of Mn^{2+} based ProCA32.CXCR4 have been assessed under both lower and higher magnetic field. Mn-ProCA32.CXCR4 has superb relaxivities at both 1.4 T and 7.0 T.

ProCA32.CXCR4 has a comparable binding affinity with Gd^{3+} when compared with small chelator based GBCAs. However, ProCA32.CXCR4 metal selectivity over physiologically present metal ions such as Zn^{2+} and Ca^{2+} are much better than other GBCAs. ProCA32.CXCR4 inert to metal transmetallation at the presence of Zn^{2+} and possess high kinetic stability. Serum stability shows ProCA32.CXCR4 is stable in serum at 37 °C incubation up to 14 days. No degradation was observed.

Pharmacokinetics study shows ProCA32.CXCR4 has good exposure and relatively fast clearance. The volume of distribution of ProCA32.CXCR4 is three times higher than non-targeted ProCA32, which is the evidence that ProCA32.CXCR4 has better tissue distribution result from CXCR4 targeting.

ProCA32.CXCR4 majorly distributed to the liver after intravenous administration. The percentage injection dosage of each organ shows that liver retains the majority amount of ProCA32.CXCR4, followed by the spleen. Kidney and heart have a very small amount of ProCA32.CXCR4 distributed.

The toxicity of ProCA32.CXCR4 is described by pathology profile analysis of mouse serum and H&E staining of mouse tissues, including brain, muscle, kidney, lung, heart, liver, and spleen. No abnormality of mouse serum pathology profile was identified and H&E staining of tissues of the mouse with ProCA32.CXCR4 injection have no significant difference in comparison with normal mouse tissues. ProCA32.CXCR4 exhibited no acute toxicity according to the results.

4.4 Summary

CXCR4 targeted contrast agent ProCA32.CXCR4 is expressed and purified with high yield as described in chapter 3. In chapter 4, biophysics properties and pharmacokinetic properties and toxicity of ProCA32.CXCR4 are well characterized.

ProCA32.CXCR4 has both high longitudinal relaxivity and transverse relaxivity in the lower and higher magnetic field. r_1 value of ProCA32.CXCR4 is lower at 7.0 T as opposed to the value in 1.4 T. r_2 value of ProCA32.CXCR4 is higher at 7.0 T as opposed to the value in 1.4 T. Both cysteine PEGylation and lysine PEGylation largely retains the relaxivities of ProCA32.CXCR4. ProCA32.CXCR4 has much-improved relaxivities than other GBCAs and enable the application in molecular imaging. ProCA32.CXCR4 has comparable Gd^{3+} binding affinity with small chelator based GBCAs but better metal selectivity over physiologically present metal ions like Ca^{2+} and Zn^{2+}. The binding affinity to different metal ions is summarized in Table 4.10. Mn-ProCA32.CXCR4 has better relaxivities than Gd-ProCA32.CXCR4; especially the r_2 value of Mn-ProCA32.CXCR4 (Table 4.11).

Table 4.10 Summary of the metal-binding affinity of ProCA32.CXCR4.

Contrast agent	Cys-ProCA32.CXCR4	ProCA32.CXCR4	Lys-ProCA32.CXCR4
K_d (Ca^{2+}) (M)	$1.4 \pm 0.2 \times 10^{-8}$	$1.3 \pm 0.1 \times 10^{-8}$	$2.3 \pm 0.4 \times 10^{-8}$
K_d (Zn^{2+}) (M)	$7.8 \pm 2 \times 10^{-5}$	$1.6 \pm 0.3 \times 10^{-6}$	$1.9 \pm 0.1 \times 10^{-6}$
K_d (Tb^{3+}) (M)	$6.5 \pm 0.2 \times 10^{-22}$	$4.6 \pm 1.3 \times 10^{-22}$	$7.3 \pm 0.4 \times 10^{-22}$
K_d (Gd^{3+}) (M)	$1.1 \pm 0.1 \times 10^{-22}$	$1.3 \pm 0.2 \times 10^{-22}$	$1.4 \pm 0.1 \times 10^{-22}$

Table 4.11 Summary of relaxivities of Gd-ProCA32.CXCR4 and Mn-ProCA32.CXCR4.

Contrast agent	r1, 1.5 T ($mM^{-1}s^{-1}$)	r2, 1.5 T ($mM^{-1}s^{-1}$)	r1, 7 T ($mM^{-1}s^{-1}$)	r1, 7 T ($mM^{-1}s^{-1}$)
Gd-ProCA32.CXCR4	32.0	44.8	10.8	11.9
Mn-ProCA32.CXCR4	60.0	133.2	49.7	142.8

ProCA32.CXCR4 has superior metal selectivity for Gd^{3+} over Zn^{2+} ($\log(K_{Gd}/K_{Zn})$ =16.1) (Table 4.12) that is 10^{11} to 10^{12} order of magnitude higher than small chelator contrast agents. For other physiological metal ions such as Ca^{2+}, ProCA32.CXCR4 also exhibited better metal selectivity than small chelator GBCA, such as Dotarem® (gadoterate meglumine) and ProHance® (Gadoteridol) (Table 4.12).

Table 4.12 Metal (Zn^{2+}, Ca^{2+}, Gd^{3+}, and Tb^{3+}) binding affinity and metal selectivity of ProCA32.CXCR4 and comparison with clinical contrast agents.

Contrast Agent	Log (K_{Tb})	Log (K_{Gd})	Log (K_{Ca})	Log (K_{Zn})	Log (K_{Gd}/K_{Ca})	Log (K_{Gd}/K_{Zn})
Magnevist®	22	22.46	10.75	18.6	12.24	4.13
Eovist®	N/A	23.6	11.82	18.78	12.22	5.18
Dotarem®	N/A	24.7	17.23	21.05	7.46	3.65
MultiHance®	N/A	21.91	N/A	17.04	N/A	4.87
ProHance®	N/A	23.8	14.83	19.37	10.07	4.37
PEG-ProCA32	21.08	22.44	9.55	8.77	13.1	14.3
ProCA32.CXCR4	21.34	21.89	7.89	7.80	14.0	16.1
Lys-PEG-ProCA32.CXCR4	21.11	21.92	7.85	7.89	13.9	16.0
Cys-PEG-ProCA32.CXCR4	21.19	21.96	8.02	7.11	14.1	15.7

ProCA32.CXCR4 has good serum stability and stay intact in serum up to 14 days. ProCA32.CXCR4 inert to the transmetallation process and exhibit good kinetic stability. Pharmacokinetics profile shows ProCA32.CXCR4 has good exposure when compared with non-targeted contrast agent ProCA32. ProCA32.CXCR4 demonstrates no acute toxicity.

Since the FDA approval of gadopentetate dimeglumine (Magnevist®; Bayer HealthCare Pharmaceuticals) in 1988, Gd^{3+}-based contrast agents (GBCAs) have been widely used for clinical MR imaging. However, nephrogenic systemic fibrosis (NSF) and gadolinium brain deposition in patients and animals associated with GBCAs administration raised the concern of gadolinium toxicity (164, 165, 172). We have carefully considered these factors in the design of

ProCA32.CXCR4 for clinical translational purpose. The Gd^{3+} binding sites of ProCA32.CXCR4 were well designed to balance Gd^{3+} binding for safety, and water accessibility for relaxivities. ProCA32.CXCR4 was shown to have unprecedented gadolinium kinetic and thermodynamic stability. The Log (K_{Gd}) of ProCA32.CXCR4 is 21.89. Metal selectivities of ProCA32.CXCR4 for Gd^{3+} over Zn^{2+} and Ca^{2+} are 10^6-10^{12} times greater than approved contrast agents, Dotarem and ProHance. The inertness of ProCA32.CXCR4 in the presence of Zn^{2+} verified its strong stability against transmetallation. Moreover, the improved relaxivity of ProCA32.CXCR4 enabled excellent contrast enhancement *in vivo* with only one-quarter of gadolinium dosage compared with other GBCAs. No trace of gadolinium was detected in mice brain after ProCA32.CXCR4 administration and we have also not observed any acute toxicity and tissue/organ toxicity. Collectively, strong Gd^{3+} binding affinity, excellent metal selectivity, inertness against transmetalation and less injection dosage makes ProCA32.CXCR4 has an excellent safety profile.

In summary, ProCA32.CXCR4 has high relaxivity, good stability, good pharmacokinetic profile, and low toxicity and makes an ideal candidate for CXCR4 specific MR imaging with translational potential for clinical applications.

5 VALIDATION OF CXCR4 AS A BIOMARKER FOR LIVER METASTASIS AND TARGETING ANALYSIS OF PROCA32.CXCR4

5.1 Introduction

Chemokine receptor 4 is by far the most widely expressed chemokine receptor in various cancers, over 23 different types of cancer cells showed elevated CXCR4 expression levels (93). CXCR4/SDF-1α axis mediates the organ-specific metastasis (173). CXCR4 ligand SDF-1α has high expression in the organs, including lung, liver, and bone marrow that represented common metastasis destinations in breast cancer and pancreatic cancer (103, 174).

Uveal melanoma (UM) has the specific liver metastases tendency; approximately 50 % of uveal melanoma patients will eventually develop liver metastases (175). In the patients that develop metastases, 93 % metastasizing to the liver (176). The involvement of liver metastases is a sign of poor prognosis and leading to deaths because of the lack of effective treatment. The liver-specific metastases of uveal melanoma raise the interest of studying the CXCR4 expression level in uveal melanoma cells. CXCR4 expression levels on primary eye uveal melanoma, and uveal melanoma metastases were reported. H, Li et al. reported the differentiation CXCR4 expression level on primary uveal melanoma cell lines and metastatic uveal melanoma cell lines (137), the primary uveal melanoma cell lines express CXCR4 whereas the metastatic uveal melanoma cell lines express little or no CXCR4. An immunohistochemistry study on UM patient tissues shows the positive IHC staining of CXCR4 in both primary UM tissues and metastatic UM tissues (177). Another study based on UM patient tissues reported the CCR7 expression in uveal melanoma is a risk factor for poor prognosis, whereas the CXCR4 expression has no clinical relevance (178). H. Grossniklaus et al. reported CXCR4 generally expressed by uveal melanoma cell lines and CXCR4 antagonist downregulated the formation of hepatic micrometastases in mouse model study (179).

The CXCR4 expression in UM is controversial and not conclusive. However, the uveal melanoma liver metastasis pattern indicating the relevancy of CXCR4 expression and liver metastases formation in uveal melanoma patients. Blocking CXCR4 expression by siRNA transfection in UM cells resulted in inhibition of chemotactic responses as well as invasiveness of UM cells (180). Therefore, the CXCR4 can be a potential biomarker and predicting factor for uveal melanoma. We aim to evaluate the CXCR4 expression level with uveal melanoma cell lines, UM patient tissues, and UM mouse models and establish the understanding of CXCR4 expression in UM development.

Ovarian carcinoma is a common gynecologic malignancy and one of the leading causes of cancer deaths in women, in which epithelial ovarian cancer is the most common pathology subtype. Region-based studies showed that ovarian cancer has the trend of decreasing age of diagnosis and increasing in incidence rate (181, 182). Survival of ovarian cancers has improved owing to surgery management and chemotherapy, but the overall prognosis remains dismal. Therefore, new therapeutic targets and approaches require ovarian cancers.

CXCR4 and CXCL12 are found to be highly expressed in ovarian cancers whereas there is no or minimum expression of CXCR4 in healthy ovarian tissue (98, 183), and anti CXCR4 therapy has proved to be effective in ovarian cancer (184). It makes CXCR4 a promising therapeutic and diagnostic target for ovarian cancer. The overexpression of CXCR4 is recommended as an independent risk factor of bad prognosis and resistance for chemotherapy (183, 185). Imaging of ovarian cancer and metastases is critically important for cancer management. CXCR4 targeted imaging agent will be beneficial for the detection of ovarian cancer and metastases and differentiate the chemo sensitive type to stratify therapy.

5.2 Results

5.2.1 Cell lines selection

Human uveal melanoma Mel290, Mel270, 02-1486, OMM1, OMM2.3, OMM2.5, 92.1, OCM1 cells, and mouse uveal melanoma Queens, B10BR11.1 cell is selected for CXCR4 expression analysis using flow cytometry.

5.2.2 Evaluate the CXCR4 expression level of melanoma cells

Flow cytometry was used for screening and evaluating the CXCR4 expression level across different melanoma cell lines. In the melanoma cell lines been studied, all of them has CXCR4

expression. In Mel290 and M20-09-196), over 90% of cell populations from exhibited CXCR4 over-expression (Figure 5.1, Figure 5.2).

CXCR4 expression in uveal melanoma also evaluated with immunofluorescence staining of CXCR4. Human uveal melanoma cell OMM2.3 and mouse melanoma cell B16LS9 showed CXCR4 expression, indicated by green fluorescence in Figure 5.3. CXCR4 expression was observed in the cytoplasm and cell membrane.

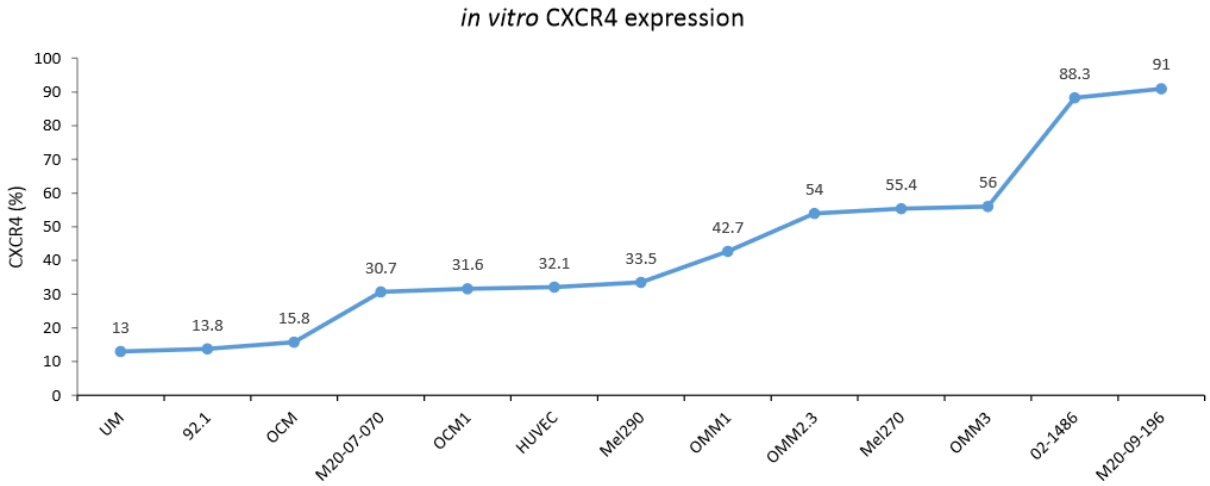

Figure 5.1 CXCR4 is expressed by uveal melanoma cell lines.
Metastatic UM cell lines have elevated CXCR4 expression. FACS result shows generally elevated CXCR4 expression across the different UM cell lines.

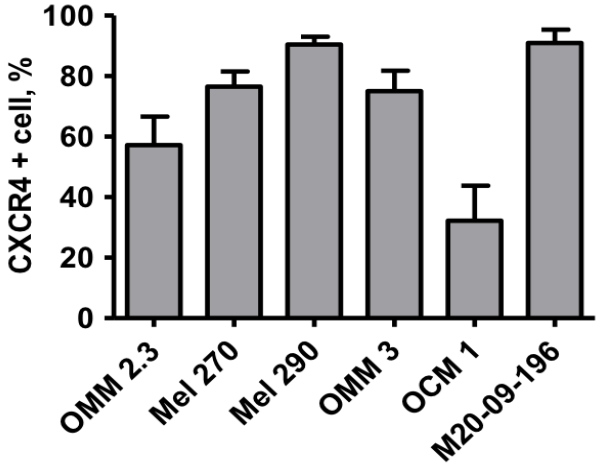

Figure 5.2 CXCR4 expression in uveal melanoma cell lines.

Metastatic UM cell lines have elevated CXCR4 expression. FACS results show generally elevated CXCR4 expression across the different UM cell lines, especially in Mel 290, Mel 270, and M20-09-196, in which over 80% of cell counts were CXCR4 positive, measurements of each cell line are triplicate.

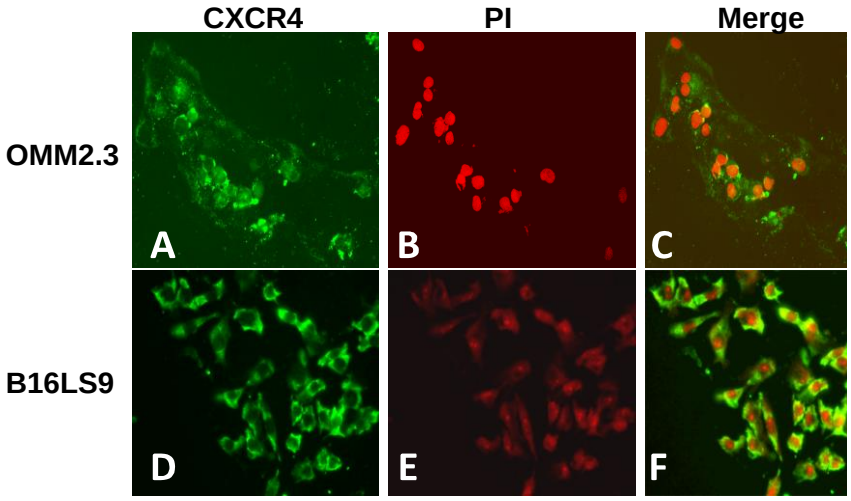

Figure 5.3 CXCR4 expression in human and mice melanoma cell.
Data from Dr. Hua Yang.

5.2.3 In vivo CXCR4 expression study

Flow cytometry analysis and immunofluorescence staining of CXCR4 with uveal melanoma show CXCR4 overly expressed across different uveal melanoma cell lines. Owing to the possibility of discrepancy in cell lines and the *in vivo* expression of CXCR4, metastatic uveal melanoma mouse models and uveal melanoma patient tissues are analyzed by immunohistochemical staining of CXCR4 to further investigated the CXCR4 expression *in vivo*.

UM patients' liver tissue with metastases were stained with CXCR4 antibody for IHC study. A CXCR4 positive control (brain specimen) was processed with the same protocol. 73% of uveal melanoma (UM) hepatic metastases (8 out of 11 cases) exhibited high expression levels of CXCR4, indicated by the brilliant red color staining (Figure 5.4). Patient information see table

Table 5.1 Patient information of melanoma liver metastasis cases.

Patient #	Age	Primary Melanoma
1	58	Leg, left
2	32	Chest
3	66	Scalp
4	59	"Side" (Neck), left
5	49	Back
6	61	Ocular, left-sided
7	37	Back
8	66	Ocular (Choroidal), left
9	59	Back
10	47	Shoulder, Right
11	64	Uveal, left

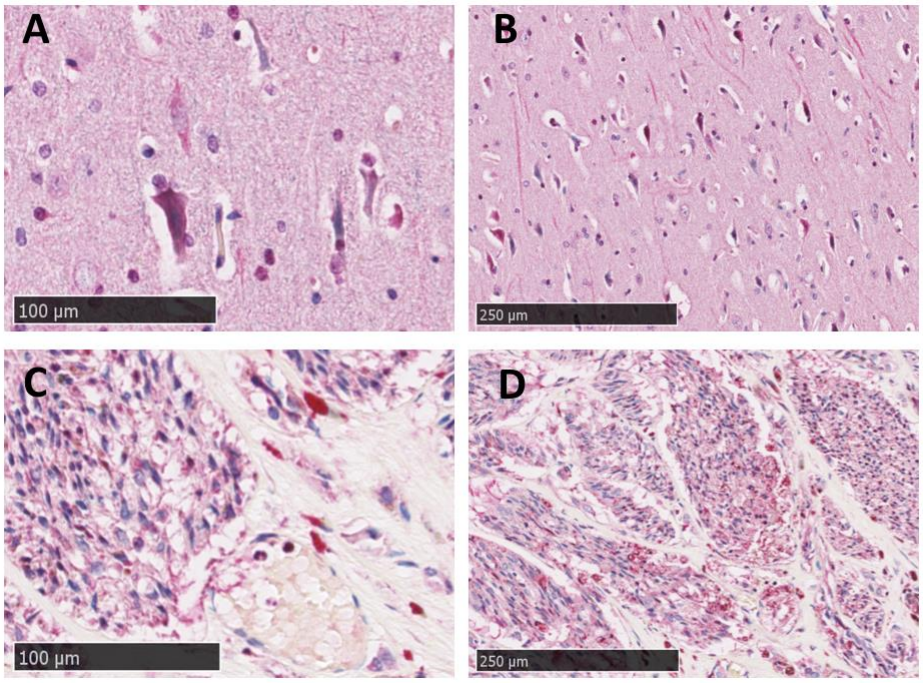

Figure 5.4 CXCR4 immunohistochemical staining of uveal melanoma liver metastases and brain tissue as the positive control.
(**A**), (**B**) CXCR4 immunohistochemical staining of brain tissue. (**C**), (**D**) metastatic UM patient liver tissue. The metastatic UM in the liver shows strong red staining that indicates CXCR4 expression throughout melanoma cells.

CXCR4 expression in metastatic uveal melanoma mouse models was validated by immunohistochemical staining as well. Metastatic uveal melanoma mouse models derived from M20-09-196, M20-07-070, and 92.1 cells were established by protocol introduced in chapter 2.9.2. FACS results show that the CXCR4 expression level in M20-09-196, M20-07-070, and 92.1 are high, medium, and low. Metastatic mouse models establish with these three UM cell lines. Both the primary tumor tissue and the metastases in the liver were stained with CXCR4 antibody, and immune reactive score (IRS) was analyzed.

CXCR4 IHC staining of mouse tissue shows that, in the primary uveal melanoma tumor, the CXCR4 expression level is consistent with the seeding cell lines. M20-09-196, M20-07-070, and 92.1 mouse primary uveal melanoma tissue staining exhibited high, medium, and low CXCR4 expression level, respectively. However, the CXCR4 IHC staining of liver metastases exclusively shows high CXCR4 expression level (Figure 5.5 and Figure 5.6).

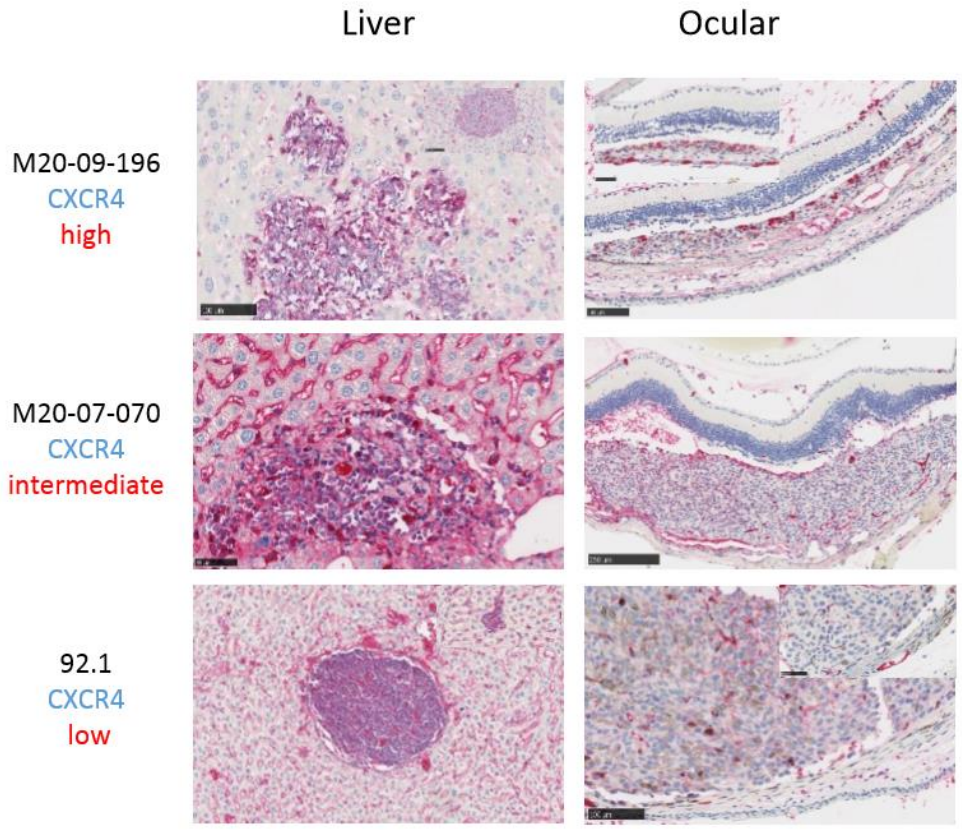

Figure 5.5 Immunohistochemical staining of CXCR4 in metastatic mouse models. Immunohistochemical staining of CXCR4 in metastatic mouse models M20-09-196, M20-07-070 and 92.1. Primary ocular uveal melanoma tissue and uveal melanoma metastases in the liver were stained with CXCR4. CXCR4 expression level is low, medium, and high for 92.1, M20-07-070 and M20-09-196 respectively in the primary tumor. CXCR4 expression level in metastases in the liver is high in three mouse models. (Data from Dr. Hua Yang).

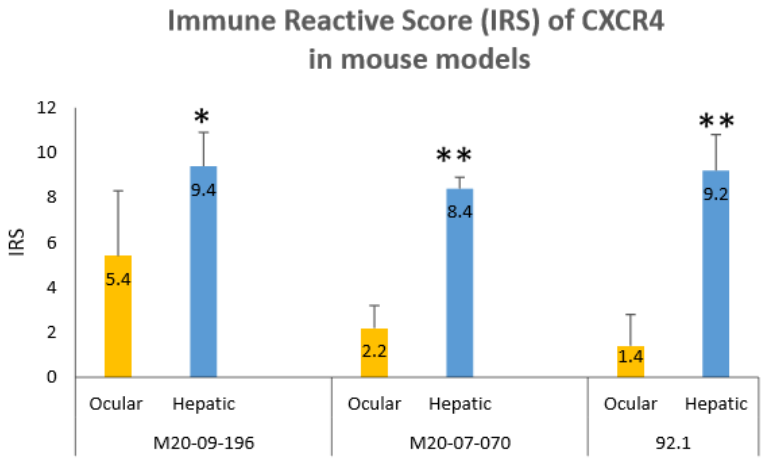

Figure 5.6 The immune reactive score (IRS) of CXCR4 in mouse models.
Immune reactive score of CXCR4 in mouse models M20-09-196, M20-07-070, and 92.1 were analyzed. In primary ocular UM, the IRS for M20-09-196, M20-07-070 and 92.1 are 5.4, 2.2 and 1.4 respectively. When UM metastasis to liver, the liver metastases exhibited elevated IRS regardless of the IRS of primary UM. (Data from Dr. Hua Yang)

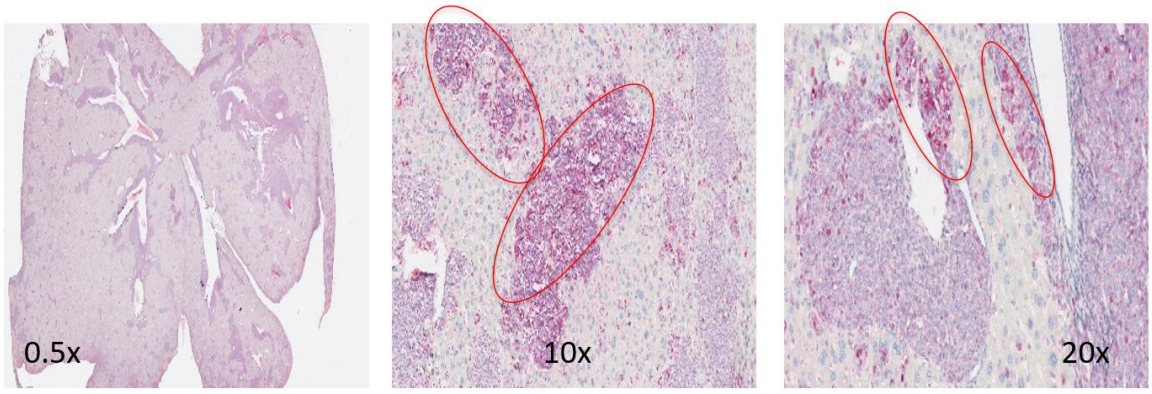

Figure 5.7 CXCR4 IHC staining of M20-09-196 mouse liver.
Metastatic uveal melanoma mouse model M20-09-196 has high CXCR4 expression level in the UM liver metastases regions, indicated by the red color staining, CXCR4 antibody is ab124824.

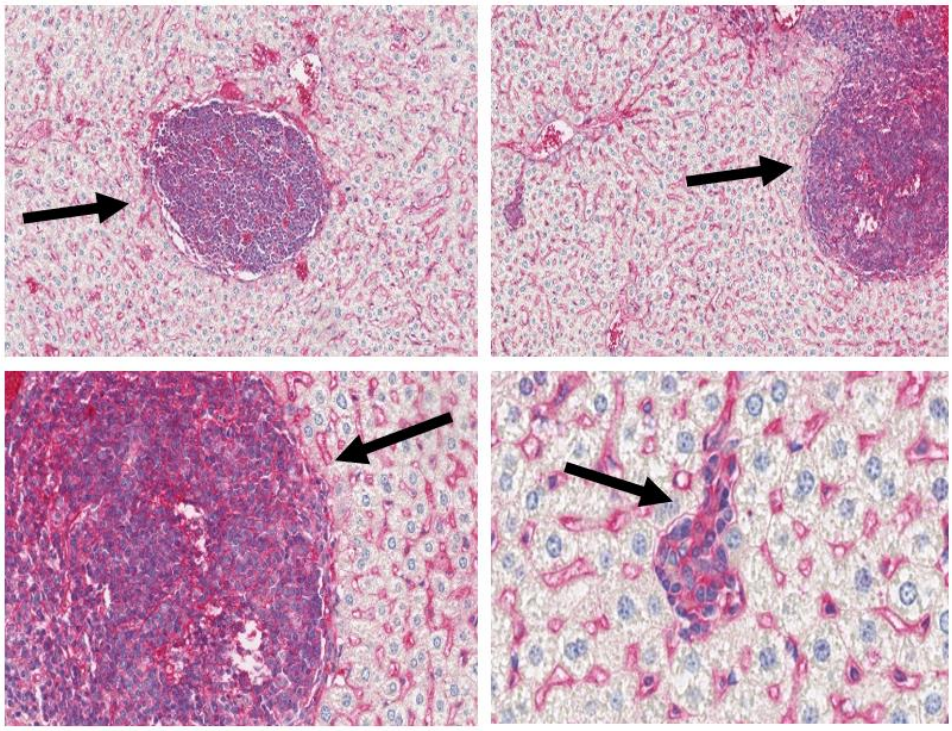

Figure 5.8 CXCR4 IHC staining of metastatic uveal melanoma mouse model 92.1.
Uveal melanoma mouse model developed by 92.1 melanoma cells has liver uveal melanoma metastases and high CXCR4 expression of liver metastases, indicated by red color and arrow.

5.2.4 ProCA32.CXCR4 targeting study

5.2.4.1 Immunofluorescence staining to study the CXCR4 targeting of ProCA32.CXCR4

CXCR4 expression cell line M290 was selected to study CXCR4 targeting capability of ProCA32.CXCR4 by immunofluorescence staining (Figure 5.9). 5 μM of fluorescein labeled ProCA32.CXCR4 was used to incubate the fixed Mel290 UM cells for one hour at 37 °C. Then washed gently by TBST buffer for three times. DAPI was used to stain the cell nucleus. The same concentration of fluorescein labeled ProCA32 was incubated with Mel290 with the same protocol as a control. After wash, ProCA32.CXCR4 incubated Mel290 cells shows green fluorescence,

whereas the control cells do not. The targeting capability of ProCA32.CXCR4 is proved by the immunofluorescent staining of Mel290.

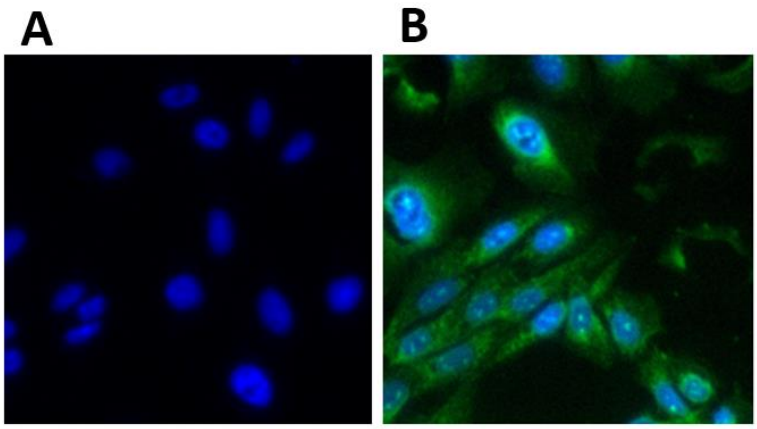

Figure 5.9 Immunofluorescence staining of Mel 290 cells.
CXCR4 targeting property of ProCA32.CXCR4 was studied with immunofluorescence staining of Mel290. (**A**) Mel 290 cells incubated with fluorescein-labeled non-targeted ProCA32 only shows blue color nucleus staining (DAPI). (**B**) Mel 290 cells incubated with fluorescein labeled ProCA32.CXCR4 shows green color staining on the cell surface.

Double staining of ProCA32.CXCR4 and chemokine receptor 4 are expected to reveal the spatial colocalization of ProCA32.CXCR4-CXCR4 interaction. Mel290 cells are fixed and incubated with 5 μM of fluorescein labeled ProCA32.CXCR4 at 37°C for one hour, then chemokine receptor 4 was stained by primary antibody and secondary fluorescence antibody following a standard protocol described in chapter 2. Double staining of ProCA32.CXCR4 and CXCR4 confirmed that ProCA32.CXCR4 bound to CXCR4 with a high spatial correlation (Pearson's r value = 0.82) (Figure 5.10)

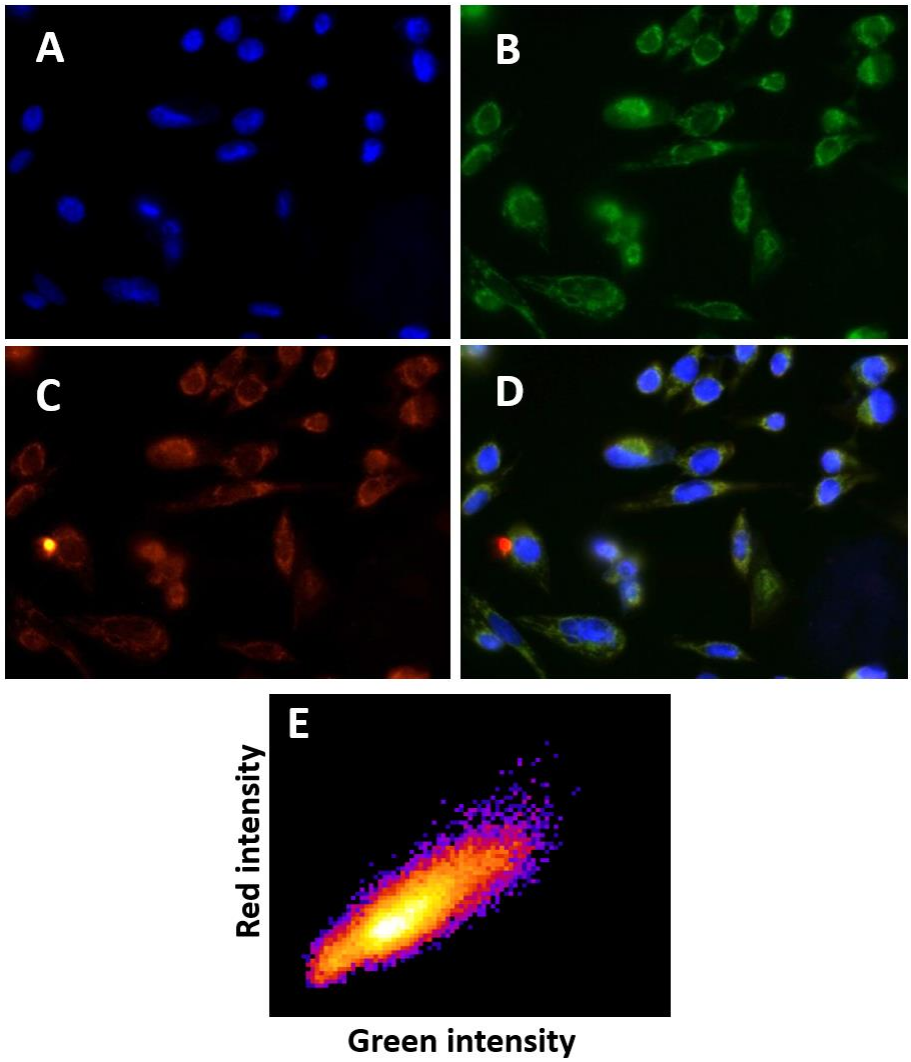

Figure 5.10 Immunofluorescence staining of Mel 290 cells and spatial colocalization with CXCR4 receptors.

Fluorescence staining with Mel290 to study the CXCR4 binding effect of ProCA32.CXCR4. (**A**) Blue fluorescence is nucleus staining with DAPI. (**B**) Green fluorescence shows fluorescein labeled ProCA32.CXCR4. (**C**) Red fluorescence staining indicates CXCR4 receptors on the cell membrane. (**D**) Overlay of blue, red, and green fluorescence of nucleus, CXCR4, and ProCA32.CXCR4. ProCA32.CXCR4 has good spatial colocalization with CXCR4; Pearson's r is 0.82.

5.2.4.2 Quantification of CXCR4 binding affinity with indirect ELISA

A modified enzyme-linked immunosorbent assay (ELISA) was carried out to quantify the CXCR4 binding affinity of ProCA32.CXCR4. It followed the steps shown in Figure 5.11.

Different concentration of ProCA32.CXCR4 (from 0 nM to 10000 Nm, 16 points in total) was added to the wells in 96-well plates that coated with Mel290 cell lysate for incubation. The absorbance of each well increases as ProCA32.CXCR4 concentration increase. By plotting the data with Prism with one to one binding model, the K_d value of ProCA32.CXCR4 bind to CXCR4 receptor is calculated.

The enzyme-linked immunosorbent assay relies on the interaction between epitope and antibody to measure the concentration of an analyte in solution. The absorbance of each well reflects the quantity of ProCA32.CXCR4. The ELISA distinguishes the specific binding and non-specific binding of all elements in the solution through a serial of binding processes to a solid surface, normally a 96-well microplate material in polystyrene. There are many variants of ELISA designed for different application, but all of them depend on the basic components of coating, blocking, probing, and signal measurement.

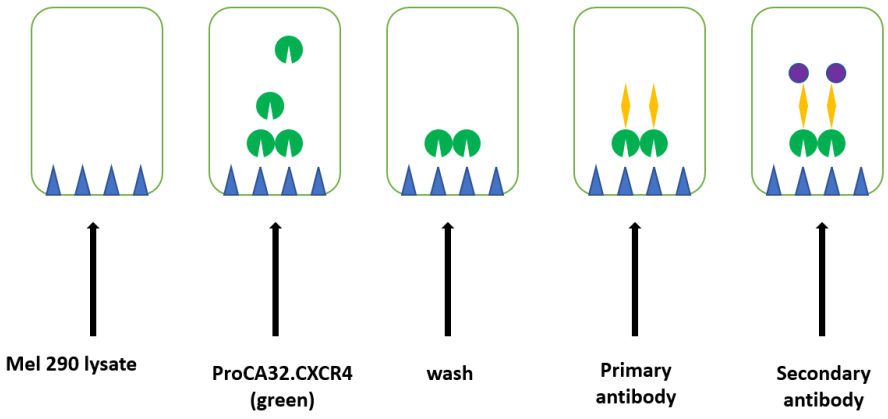

Figure 5.11 Illustration of ELISA protocols.
Indirect ELISA follows the steps of coating of CXCR4, incubate ProCA32.CXCR4 with coated plates, wash, primary antibody incubation, and secondary antibody incubation.

The coating of ELISA usually depends on the passive absorption of analytes, including proteins, peptides, hormones, and antigens to a polystyrene microplate surface. Most proteins can be attached to the polystyrene in carbonate/bicarbonate buffer (pH 9.6), and the transparent polystyrene facilitates the following colorimetric signal measurement. In typical procedure designed to detect an antigen in a protein mixture solution, the antigen immobilization is achieved either by direct coating the protein mixture to the 96-well microplate or through antibody absorbed to a microplate that can capture the specific antigen. The antibody coated on the microplate to capture the antigen called "capture antibody," it helps more specific capture antigen and immobilizes on the plate instead of coating all protein elements form mixture solution by direct coating.

Plate blocking is another important step in the ELISA experiment. Blocking buffer, such as BSA, nonfat dry milk, is usually rich in protein and occupy the unsaturated surface of the plate with irrelevant protein. The blocking step of ELISA helps prevent non-specific binding, reduce ELISA background signal and stable proteins absorbed to the microplates with better interaction.

ProCA32.CXCR4 shows μM range binding affinity to the CXCR4 receptor. PEGylation slightly affected the binding affinity. The CXCR4 binding affinity for ProCA32.CXCR4 is 0.39 ± 0.02 μM and 1.69 ± 0.28 μM for cysteine PEGylated ProCA32.CXCR4. The binding curve indicated a 1:1 binding stoichiometry, and the CXCR4 receptor number per Mel290 cell is $1.2 \pm 0.1 \times 10^6$.

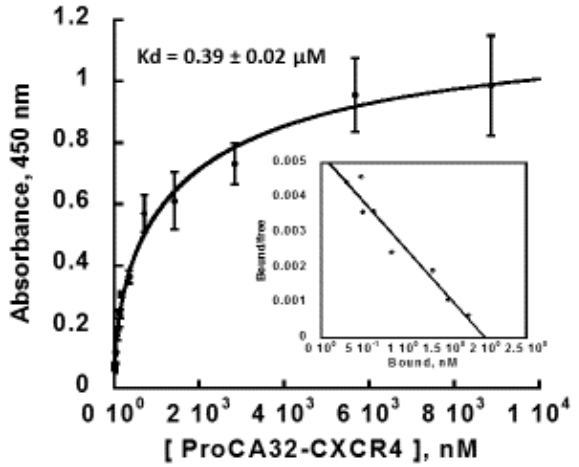

Figure 5.12 CXCR4 targeting study of ProCA32.CXCR4.
CXCR4 targeting capability of ProCA32.CXCR4 is determined by indirect ELISA. The dissociation constant of ProCA32.CXCR4 binds to CXCR4 is 0.39 ± 0.02 µM.

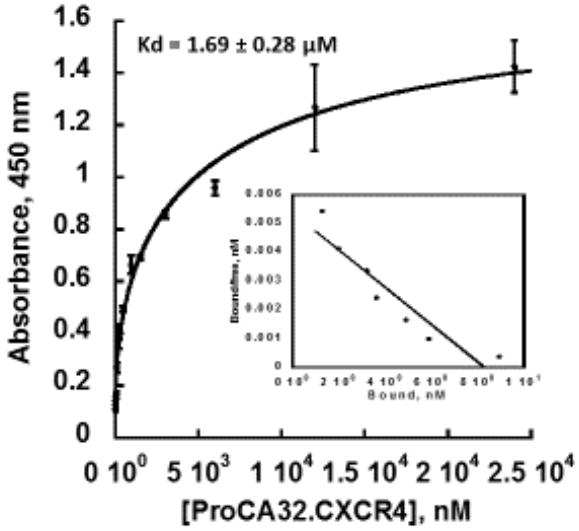

Figure 5.13 CXCR4 targeting study of Cys-ProCA32.CXCR4.
CXCR4 targeting capability of Cys-ProCA32.CXCR4 is determined by indirect ELISA. The dissociation constant of ProCA32.CXCR4 binds to CXCR4 is 1.69 ± 0.28 µM.

5.3 Conclusion and summary

CXCR4 is widely expressed in cancer cells and plays an important role in mediating organ-specific metastasis. Cancers metastasis to lung, liver, and bone marrow, express an

elevated level of CXCR4, such as breast cancer and pancreatic cancer. Uveal melanoma exhibits the liver-specific metastasis pattern and the intrinsic SDF-1α expression in liver is thought to be the reason for liver-specific metastasis of uveal melanoma.

The expression of CXCR4 in uveal melanoma is controversial. Scientists reported different results regarding the CXCR4 expression in uveal melanoma, both primary tumor and metastases. Most of the researchers conclude CXCR4 is expressed in both primary and metastases of uveal melanoma and is a risk factor for poor prognosis. CXCR4 blockage treatment inhibits tumor growth and metastasis.

We studied the CXCR4 expression using uveal melanoma cell lines, patient tissues and metastatic mouse models, and evaluated the CXCR4 expression level *in vitro* and *in vivo*. The cell lines study with FACS assay demonstrated that CXCR4 expressed across different uveal melanoma cell lines, the expression level varies. CXCR4 immunohistochemical staining with uveal melanoma patient tissues displays high positive staining rate in uveal melanoma tissues. Metastatic mouse models tissue analysis exhibits that CXCR4 expression elevated in the uveal melanoma metastases in the liver.

The targeting study of ProCA32.CXCR4 is carried out by immunofluorescent staining and ELISA. ProCA32.CXCR4 is verified to bind to CXCR4 with an excellent spatial colocalization (Pearson's r is 0.82), and the binding affinity is quantified to be 0.39 ± 0.02 μM and 1.69 ± 0.28 μM for non-PEGylated ProCA32.CXCR4 and ProCA32.CXCR4 with cysteine PEGylation. The PEGylation affects the binding affinity but not to a significant extent.

In summary, CXCR4 overexpressed in uveal melanoma, especially uveal melanoma metastases in the liver and is a useful imaging biomarker candidate for detecting liver metastases.

ProCA32.CXCR4 is validated to have CXCR4 targeting capability with both immunofluorescences staining assay and enzyme-linked immune absorbent assay.

6 APPLICATION OF PROCA32.CXCR4 FOR EARLY DETECTION AND CHARACTERIZATION OF UVEAL MELANOMA AND OVARIAN CANCER

6.1 Introduction

6.1.1 CXCR4 in uveal melanoma

Uveal melanoma (UM) is the most common primary intraocular malignancy. Approximately 50% of UM patients will develop metastases (175). Uveal melanoma metastasizes to the liver in ~93% of patients who have metastases and results in death in almost all cases due to lack of effective treatments (176). Through histological analysis of postmortem patient samples, UM liver metastases can be classified into three stages based on size (i.e., diameter): stage 1 (≤50 μm in diameter), stage 2 (51–500 μm in diameter), or stage 3 (>500 μm in diameter) (186). Pathologically, UM hepatic metastases primarily have two growth patterns: infiltrative or nodular. The infiltrative pattern occurs when circulating metastatic UM cells lodge in the sinusoidal space and eventually replace the hepatic lobule. The nodular pattern metastases, however, originate in the periportal area. UM cells co-opt the portal vein, and when the tumor grows, it exhibits angiogenesis and effaces the adjacent hepatocytes (187).

There are major barriers facing clinicians in UM management, such as the lack of non-invasive and sensitive imaging methods for metastases, and the resistance of UM to traditional systemic chemotherapies (188, 189). Contrast-enhanced CT is a widely used modality for screening for hepatic metastases (190); however, it has limited capacity regarding liver lesion characterization (191). 2-18F-fluoro-2-deoxy-D-glucose (^{18}FDG) positron emission

tomography/computed tomography (PET/CT) can locate the “hot-spot” for characterization of liver metastases, but the radiation-dosimetry and the comparatively low specificity are things for concern (192).

MRI is a preferred clinical imaging modality for the assessment and characterization of liver malignancy since it does not use ionizing radiation, and has high soft tissue penetration providing morphological, anatomical, and functional information. Dynamic-enhanced MRI, with liver-specific contrast agents, is widely used for liver lesion characterization. However, the sensitivity and specificity of clinical MRI are low for lesions less than 1 cm (193). Also, MRI with the administration of clinically-approved contrast agents cannot differentiate the different growth patterns of UM metastases in the liver (194). Previous studies have demonstrated that molecular imaging of corresponding biomarker expression, such as HER2, improves detection sensitivity for cancers (195). However, diagnostic biomarkers for imaging UM liver metastases have not yet been established until today. Therefore, there is a pressing unmet medical need to develop MRI contrast agents for early detection and follow-up of liver metastases, especially for high-risk patients.

CXCR4 plays a crucial role in cell migration and cancer metastasis to several organs such as liver, bone marrow, and lung that have the intrinsically high concentration of its natural ligand CXCL12 (140, 151, 152). A CXCR4 antagonist, Plerixafor (Mozobil®, AMD3100), is approved by the FDA for stem cell mobilization. Another ongoing study is focused on the effect of another CXCR4 antagonist, X4P-001, on T-cell infiltration in human metastatic melanoma (196). CXCR4 expression has been proposed as a prognostic factor and a potential therapeutic target. Elevated expression of CXCR4 has been reported in several uveal melanoma cell line studies (197, 198). In addition, blocking CXCR4 gene expression by transfection with CXCR4 siRNA has been found to inhibit invasive properties of uveal melanoma cells exposed to soluble factors produced by

human livers (140). Taken together, we hypothesize that CXCR4 will be a potential biomarker with treatment implications for imaging UM metastases in the liver.

6.2 Results

6.2.1 Detection of uveal melanoma using molecular dynamic contrast imaging

6.2.1.1 Molecular dynamic contrast imaging of ProCA32.CXCR4

A liver implanted uveal melanoma mouse model, generated with CXCR4 expression melanoma cell line, Mel290, was used to evaluate and validate the *in vivo* molecular imaging capability of ProCA32.CXCR4 at 4.7 T. Molecular dynamic contrast imaging (MDCI) was performed to display implanted uveal melanoma in mouse liver by the administration of Cys-ProCA32.CXCR4 via intravenous tail injection, followed by the acquisition of T_1-weighted gradient echo MRI as a function of time. The non-targeted contrast agent, ProCA32, was used as a control. The melanoma tumor regions exhibited different enhancement patterns between mice with ProCA32 and Cys-ProCA32.CXCR4 injection. In Mel290 mice with ProCA32 injection, the tumor MRI signal intensity increased at 12 min and 50 min post-injection and decreased after 3 hours of injection **(**Figure 6.1**,** Figure 6.2**)**. However, the tumor MRI signal intensity in the Mel290 mice with Cys-ProCA32.CXCR4 injection gradually increased to a maximum at 22 h post-injection, and then began to decrease due to excretion **(**Figure 6.1, Figure 6.2**)**. The time plot of melanoma tumor signal-noise-ratio (SNR) change followed by Cys-ProCA32.CXCR4 injection showed that melanoma tumors SNR increased over 40% at 22 hours post-injection when compared with pre-injection, whereas SNR of tumor region in the Mel290 mice with ProCA32 injection showed a mild increase (10%) right after injection (12 min) then washed out at 3 hours post-injection (Figure 6.2 B). On the other hand, MR images of Mel290 mice with Cys-

ProCA32.CXCR4 and ProCA32 injection exhibited similar patterns of SNR changes in the liver regions over time (Figure 6.2 C). The liver SNR of both mice with Cys-ProCA32.CXCR4 and ProCA32 injection increased drastically right after injection and up to 3 hours, the percentage increase of SNR is around 45% at 3 hours post-injection when compared with pre-injection. Such enhancement at the liver region gradually decreased due to elimination. Cys-ProCA32.CXCR4 can target and well distribute to the Mel290 mice tumor tissue. The MR images of the tumor region in Mel290 mice with ProCA32.CXCR4 injection showed that the tumor rim enhanced at early time points after injection and penetrated the center along with the time (Figure 6.2 A, D).

The MRI images follow the ProCA32.CXCR4 dynamically change along with time depend on the expression level of CXCR4. Tumor tissues with high expression of CXCR4 exhibited delayed enhancement than the normal liver tissue since the kinetic targeting to CXCR4 and showed the peak of intensity enhancement around 24 hours after injection. The normal liver tissue, however, shows the peak of signal noise ratio enhancement at 3 hours after injection for the biodistribution of ProCA32.CXCR4 to the liver along with time. This dynamic enhancement of ProCA32.CXCR4 is a combined result of blood circulation and CXCR4 targeting and allowing the differentiation of CXCR4 high expression tissue from the CXCR4 low expression tissue.

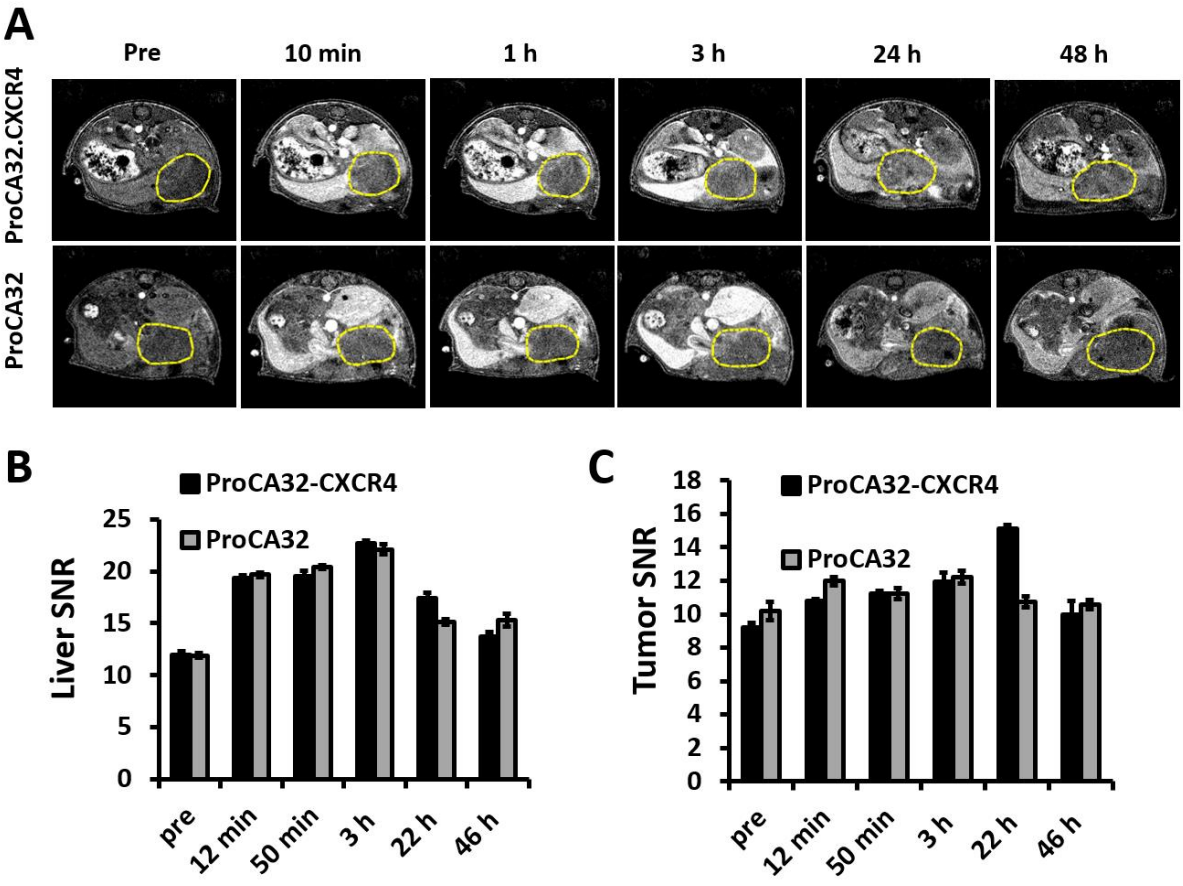

Figure 6.1 T1 weighted MR images of Mel290 with ProCA32 and ProCA32.CXCR4 injection and the signal-noise ratio of liver and tumor regions.

(**A**) T1 weighted MR images of Mel 290 uveal melanoma mice with ProCA32.CXCR4 injection (upper row) and ProCA32 injection (lower row) at different time points. Yellow circle regions are tumor region in the liver. (**B**) Quantification analysis of liver SNR change before and after ProCA32.CXCR4 and ProCA32 injection at different time points. (**C**) Quantification analysis of the SNR changes of Mel 290 mice tumor region before and after injection of ProCA32.CXCR4 and ProCA32 at different time points. For the Mel 290 mice with ProCA32.CXCR4 and ProCA32 injection, liver intensity change has the similar pattern after administration of ProCA32 and ProCA32.CXCR4. With both contrast agent intravenous bolus administration, liver SNR increases right after (10 min) and keep increasing up to 3 hours, after 3 hours, the SNR decrease. The tumor SNR of mice with ProCA32.CXCR4 administration keeps increase after injection up to 22 hours and the tumor SNR of ProCA32 mice and ProCA32.CXCR4 mice have significant differences which showing the CXCR4 targeting effect of ProCA32.CXCR4.

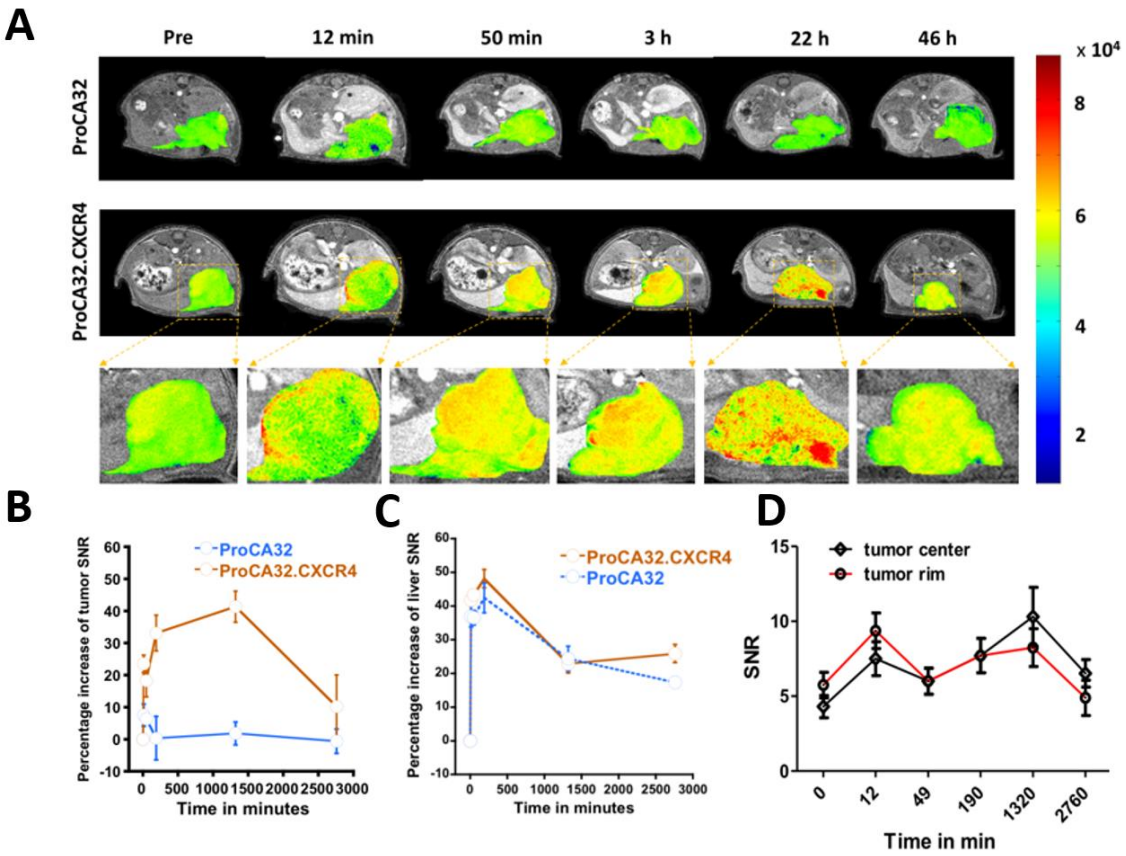

Figure 6.2 Progressive MR imaging of liver implanted melanoma mice M290 with an injection of ProCA32.CXCR4.

(A) T1 weighted gradient echo MR images of control mice (with the injection of non-targeted agent ProCA32) and mice with ProCA32.CXCR4 injection. MRI was scanned before, and after injection at different time points until 48 hours, the tumor is represented by the color region in MR images. (B) The percentage increase of SNR of melanoma tumor at different time points shows the dynamic binding process of ProCA32.CXCR4. Mice with ProCA32.CXCR4 injection showed gradual increase intensity in melanoma tumor region up to 24 hours, showing the CXCR4 targeting effect and intensity washed out at 48 hours (further time points not acquired). (C) Time plot of Liver SNR percentage increase following ProCA32 and ProCA32.CXCR4 injection. The liver SNR of both ProCA32 injected mice and ProAC32.CXCR4 injected mice shows a similar pattern of the SNR time plot, liver intensity drastically increases up to 3 hours after injection of both contrast agents and going down after 3 hours. (D) Time plot of tumor rim and tumor center SNR change of mice with ProCA32.CXCR4 injection. ProCA32.CXCR4 exhibits good tumor penetration, at early time points (12 min) following injection of ProCA32.CXCR4, tumor rim SNR increased, the intensity in the center of the tumor going up until 24 hours after injection, from (A) can see the tumor region with ProCA32.CXCR4 injection shows well distributed and heterogeneity enhancement.

6.2.1.2 Histology analysis and in vivo targeting of ProCA32.CXCR4

The immunofluorescence staining of Cys-ProCA32.CXCR4 administrated, Mel290 mouse tumor tissue showed strong and broadly distributed red immunofluorescence (Figure 6.3). In contrast, red fluorescence staining was not observed at the tumor tissues of the Mel290 mice with ProCA32 injection. Gd^{3+} content analysis using ICP-OES indicated that the tumor tissue of Mel290 mice with ProCA32.CXCR4 injection exhibited significantly higher Gd^{3+} content than tumor tissue of Mel290 mice with the ProCA32 injection (Figure 6.4). These results further validated the CXCR4 targeting capability of ProCA32.CXCR4 *in vivo* with excellent tumor permeability.

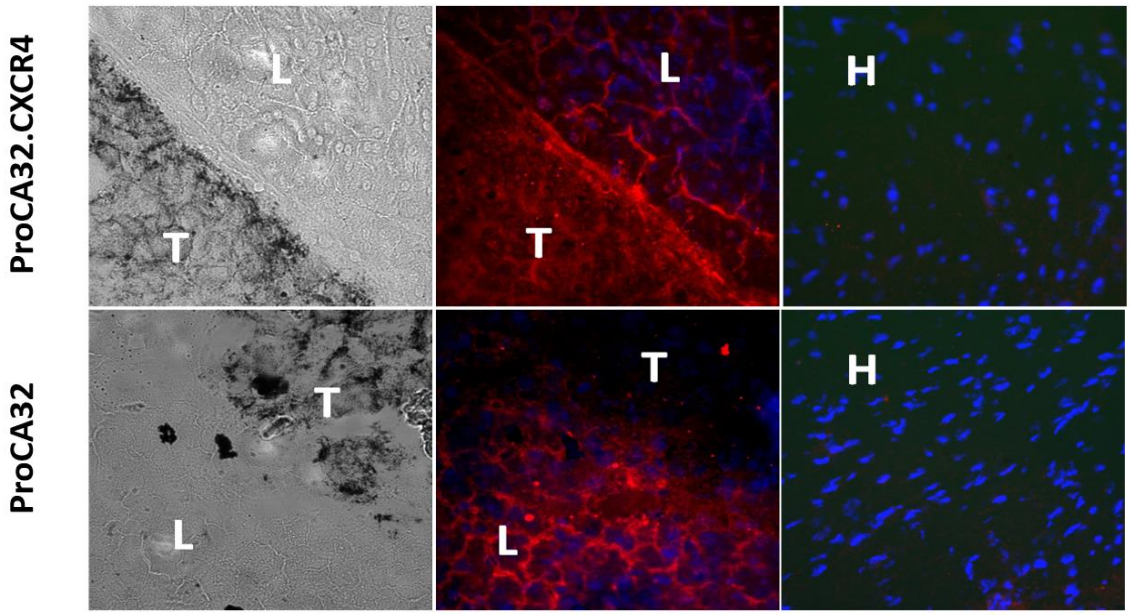

Figure 6.3 Immunofluorescence staining of ProCAs on Mel 290 mouse tissues.
Mouse liver and tumor tissue stained with immunofluorescence for ProCA32 antibody. Mel290 mouse livers with ProCA32.CXCR4 and ProCA32 injection are stained with primary rabbit antibody against ProCA32 and fluorescence secondary antibody. The nucleus is stained with DAPI. Melanoma in the liver shows melanin (black color) in the bright field and red fluorescence staining recognize the presence of ProCA32/ProCA32.CXCR4. For the Mel290 mouse with ProCA32.CXCR4 injection (upper row), the tumor region shows well spread red fluorescence color, which indicates the presence of ProCA32.CXCR4 at the tumor tissue. For the Mel290 mouse with ProCA32 injection (lower row), tumor regions exhibit no red fluorescence signal, only the

DAPI staining shows. Heart tissue is negative control; heart from both mice showed no presence of red fluorescence.

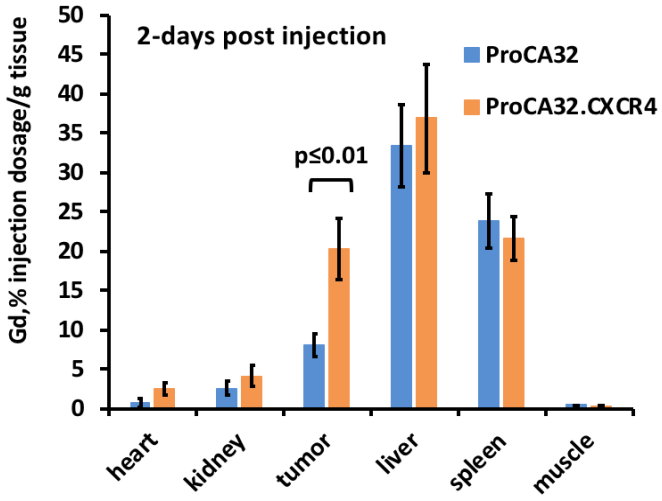

Figure 6.4 Biodistribution study of Mel290 mice with contrast agents injection.
Mel290 mouse tissues were collected and analyzed by ICP-OES after 2 days injection of contrast agent ProCA32.CXCR4 and ProCA32. Mel290 mouse tissues, including heart, kidney, tumor, liver, spleen, and muscle, were analyzed. The gadolinium content in heart, kidney, liver, spleen, and muscle showed no significant difference between mouse with ProCA32.CXCR4 injection and mouse with ProCA32 injection. The tumor of Mel290 mouse with ProCA32.CXCR4 injection has a significantly high amount of gadolinium when compared with the tumor of Mel290 mouse with ProCA32 injection, which demonstrated the *in vivo* affinity of ProCA32.CXCR4 to the CXCR4 high expression of tumor tissue.

6.2.2 Detection of uveal melanoma metastases in the liver with ProCA32.CXCR4

We demonstrated the unique imaging capability of ProCA32.CXCR4 for detection of liver metastases, improving the current detection limit, and enabling nodular pattern detection in metastatic M20-09-196 mice at 7.0 T. The early detection of UM metastases in the liver of M20-09-196 mice can be achieved using either Cys-ProCA32.CXCR4 or Lys-ProCA32.CXCR4. Liver micrometastases ranging from 0.01 mm^2 to 0.08 mm^2, which are “invisible” using Eovist or non-targeted ProCA32 (Figure 6.6, Figure 6.7), were detected with spin echo acquisition and fast spin echo acquisition following tail vein injection of 0.025mmol/kg Cys-ProCA32.CXCR4 (Figure

6.5). Following the same imaging protocol, a mouse model with Lys-ProCA32.CXCR4 injection, in place of Cys-ProCA32.CXCR4, exhibited metastases enhancement on post-injection as well (Figure 6.9). Both the Cys-ProCA32.CXCR4 and Lys-ProCA32.CXCR4 can enhance the small metastatic lesions in the liver. Targeting effect shows at 48 hours after administration.

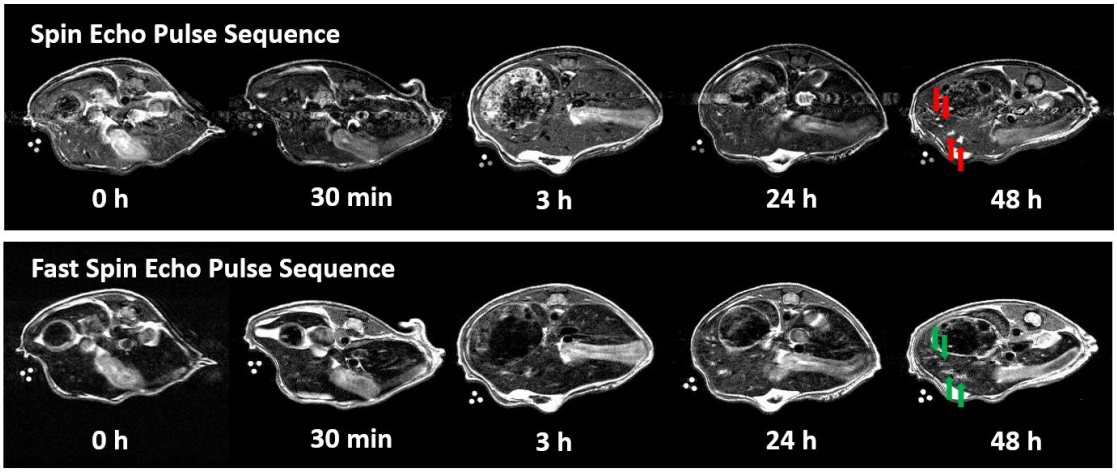

Figure 6.5 T_1 weighted, and T_2 weighted MRI scanning imaging at different time points after Cys-ProCA32.CXCR4 injection.

The first row shows the T_1 weighted MR images after Cys-ProCA32.CXCR4 injection. The red arrows pointed to the metastases brighten up after injection of contrast agent. The second row shows the T_2 weighted images; the green arrows pointed to the enhanced metastases after contrast agent injection.

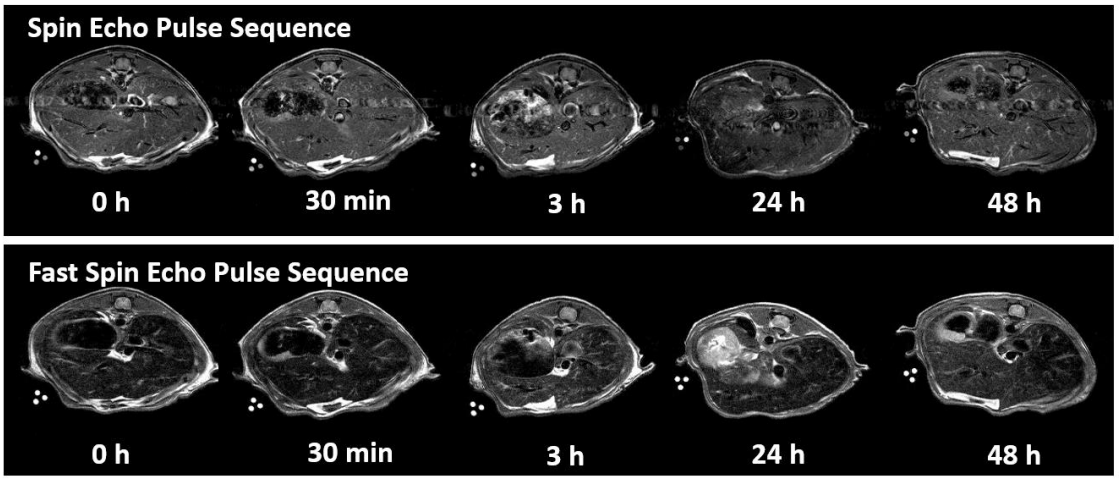

Figure 6.6 MRI imaging of Lysine-PEGylated ProCA32 injected mouse.

T_1 weighted MR images and T_2 weighted MR images were collected before and after the injection of lysine PEGylated ProCA32. T_1 weighted MR images and T_2 weighted MR images are collected by spin echo pulse sequence and fast spin echo pulse sequence, respectively. No metastasis lesion was observed after the administration of ProCA32 on both T_1 and T_2 weighted images.

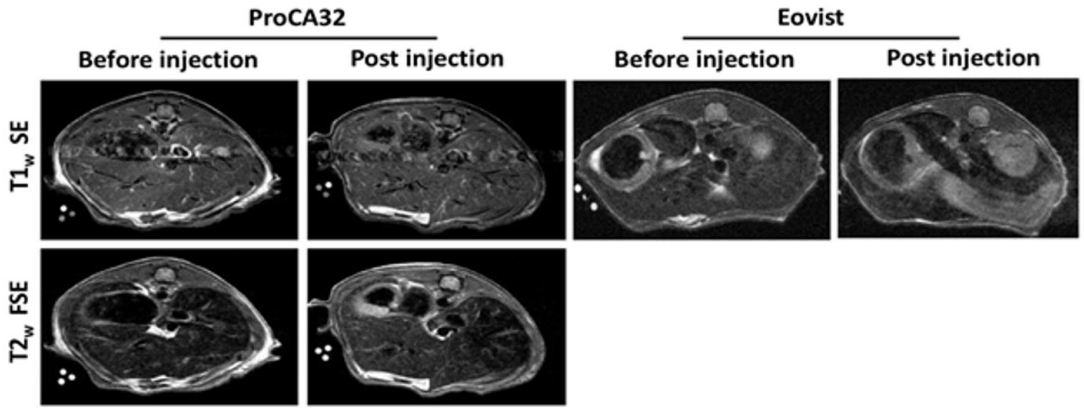

Figure 6.7 MR images of metastatic UM mice M20-09-196 before and after injection of ProCA32 and Eovist.

T1 weighted spin echo and T2 weighted fast spin echo MR images of M20-09-196 mice before and after injection of ProCA32 (left) and Eovist (right). After 48 hours of ProCA32 injection, no lesion enhanced on MR images. 30 min after injection of Eovist, no lesion enhanced on MR images as well.

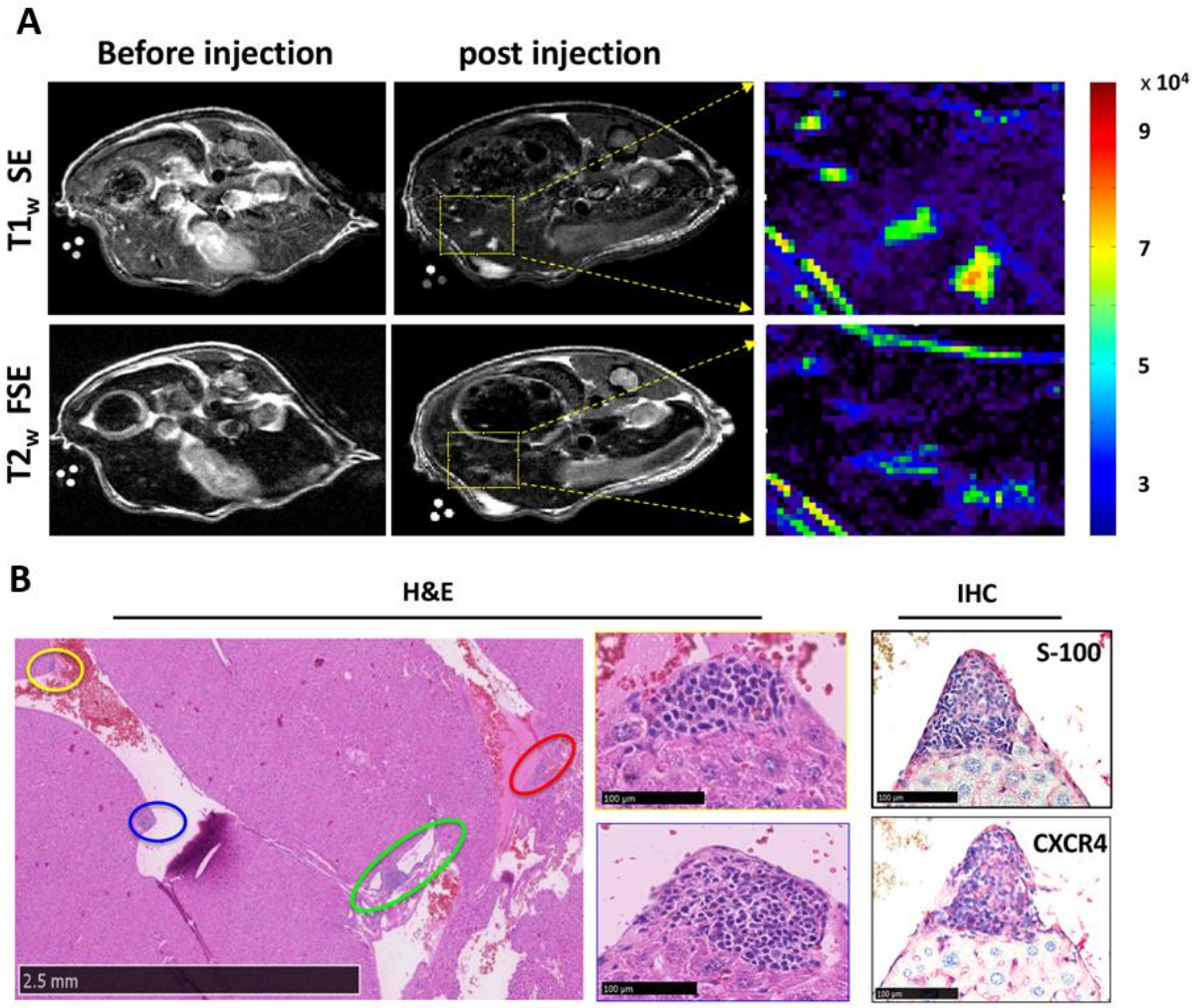

Figure 6.8 MR images of metastatic UM mice M20-09-196 and histological correlation. (**A**) T1 weighted spin echo and T2 weighted fast spin echo MR images of M20-09-196 before and 48 hours after Cys-ProCA32.CXCR4 injection. At 48 hours after injection, both T1 weighted and T2 weighted MR images showed four lesions light up when compared with before injection, the colormap is the zoom-in view of the yellow rectangular region. (**B**) H&E and IHC staining of M20-09-196 liver with UM metastases. H&E staining shows four metastasis lesions, highlighted by different color circles, that exhibit a similar location as the metastases in MR images. Higher magnification images show the growth pattern of metastases to be the nodular pattern. S100 immunohistochemical staining confirms the lesions are metastatic UM. CXCR4 immunohistological staining confirms the CXCR4 expression on UM metastases.

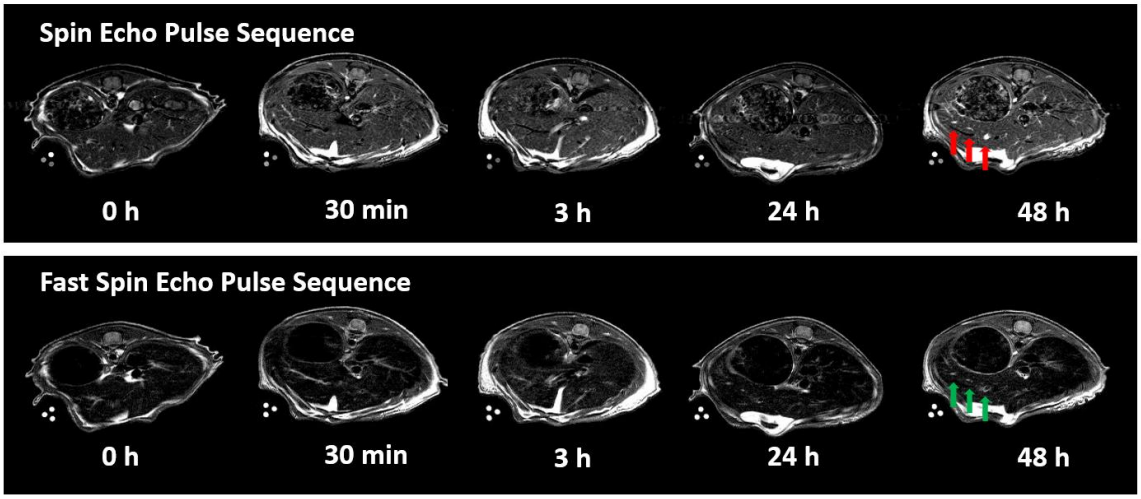

Figure 6.9 T_1 weighted and T_2 weighted MR images at different time points after Lys-ProCA32.CXCR4 injection.

The first row shows the T_1 weighted MRI images after Lys-ProCA32.CXCR4 injection. The red arrows pointed to the metastases brighten up after injection of contrast agent. The second row shows the T_2 weighted images; the green arrows pointed to the enhanced metastases after contrast agent injection.

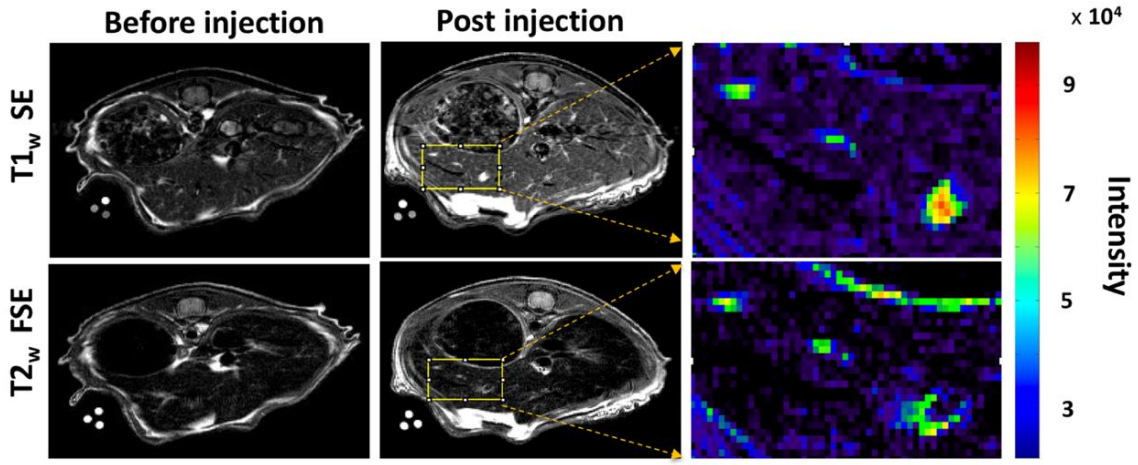

Figure 6.10 MR images of metastatic UM mice M20-09-196 before and after injection of Lys-ProCA32.CXCR4.

T1 weighted spin echo and T2 weighted fast spin echo MR images of M20-09-196 mice before and after injection of Lys-ProCA32.CXCR4. 48 hours post-injection of Lys-ProCA32.CXCR4, there are three lesions lighten up on both T1 and T2 weighted MR images. Color map shows the zoom-in view of the metastases.

These small liver lesions, detected by MRI with Cys-ProCA32.CXCR4, were further verified by detailed H&E staining analysis, and were found to be exclusively nodular growth pattern (labeled by the yellow, blue, red, and green circle) (Figure 6.8 B). The inter-lesion distances and diameters of lesions on MR images correlated well with the corresponding measurements in H&E staining of tissue sections (y=1.09x + 0.08) (Figure 6.12). The statistical analysis showed that MR images could readily differentiate the tumor from the healthy liver, with an AUC of 0.84 (Figure 6.12). IHC staining of S100 further confirmed the lesions to be metastatic melanoma, and IHC staining of CXCR4 verified the CXCR4 expression on metastatic melanoma (Figure 6.8).

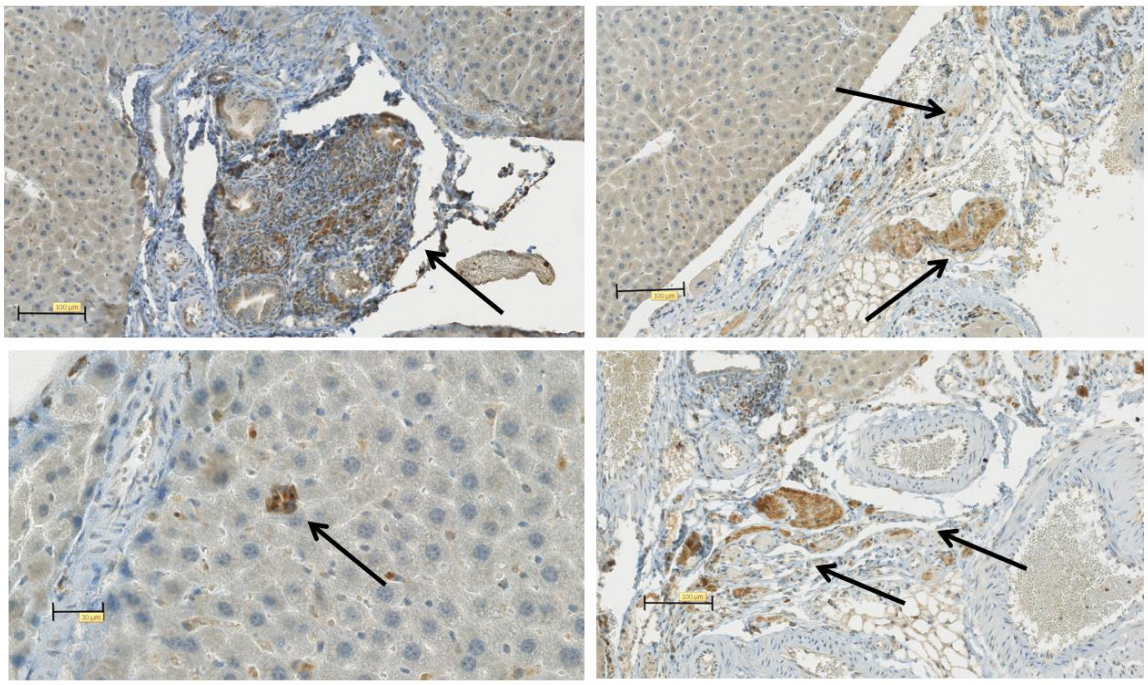

Figure 6.11 Immunohistological study of M20 mouse liver tissue using Mouse anti-human CXCR4 (ab189048).

The brown color staining region on liver indicates the CXCR4 expression. CXCR4 has a high expression on metastatic melanoma cells, scale bar, 200 µM.

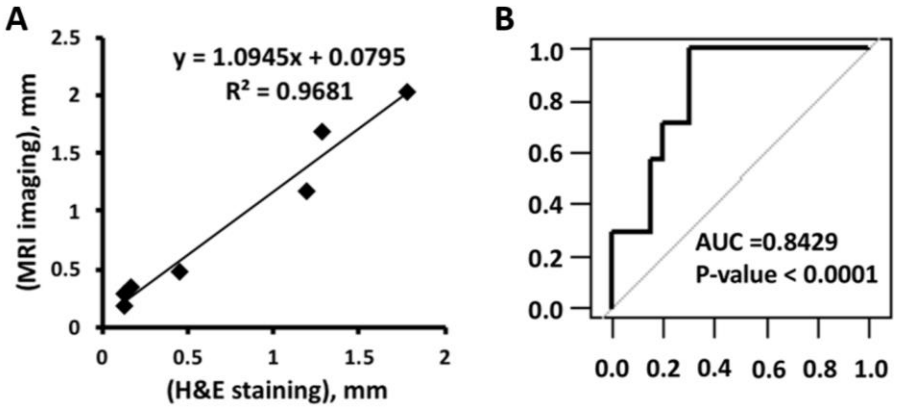

Figure 6.12 Statistics analysis of M20-09-196 mouse with Cys-ProCA32.CXCR4 injection. (**A**) The measurement of distances between the metastases and diameters of the metastases in the MR images correlates well with the H&E histological staining (y=1.09x + 0.08). (**B**) The stastistical analysis shows ProCA32.CXCR4 provides diagnosis validation for melanoma metastases in liver, AUC = 0.8429, P-value < 0.0001. Analysis based on 11 metastases found on MR images.

6.2.3 Validation of the in vivo CXCR4 targeting capability of ProCA32.CXCR4 by receptor blocking experiment

We validated the in vivo CXCR4 targeting capability of Cys-ProCA32.CXCR4 by receptor blocking experiment. A subcutaneous uveal melanoma (UM) murine model was developed to demonstrate that UM tumor signal intensity enhancement following Cys-ProCA32.CXCR4 administration could be blocked by first administering the CXCR4 blocking reagent. (Figure 6.14. A). The blocking reagent was administrated to subcutaneous uveal melanoma model prior to imaging, following the protocol illustrated in Figure 6.13.

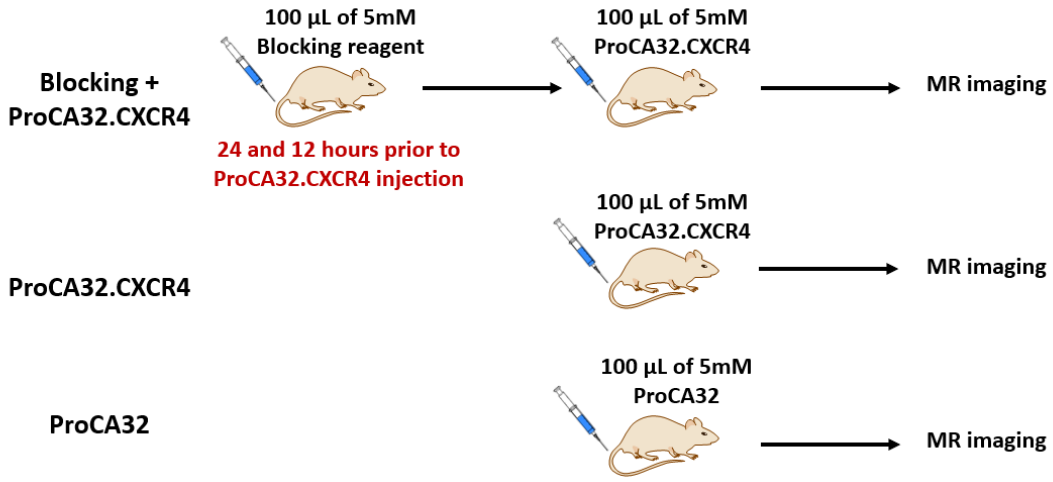

Figure 6.13 The protocol of blocking reagent administration.

We specifically constructed a CXCR4 blocking reagent by fusing the CXCR4-targeting moiety (LGASWHRPDKFCLGYQKRPLP) of ProCA32.CXCR4 to the C-terminal of the GST tag to ensure proper blocking. Injection of the non-targeted Lys-ProCA32 only resulted in initial SNR enhancement at 3 h post-administration due to blood pool distribution. This enhancement returned to baseline at 24 h. In contrast, injection of Cys-ProCA32.CXCR4 resulted in maximum SNR enhancement at 24 h post-injection and returned to the baseline at 48 h. Prior injection of CXCR4 receptor blocking reagent specifically eliminated the enhancement at 24 h by Cys-ProCA32.CXCR4 but retained the 3 h initial enhancement due to blood pool effect. (Figure 6.14 B, C, Figure 6.15) These results indicated that ProCA32.CXCR4 can specifically bind to the CXCR4 receptor over-expressed on the tumors and enables molecular targeting MR imaging.

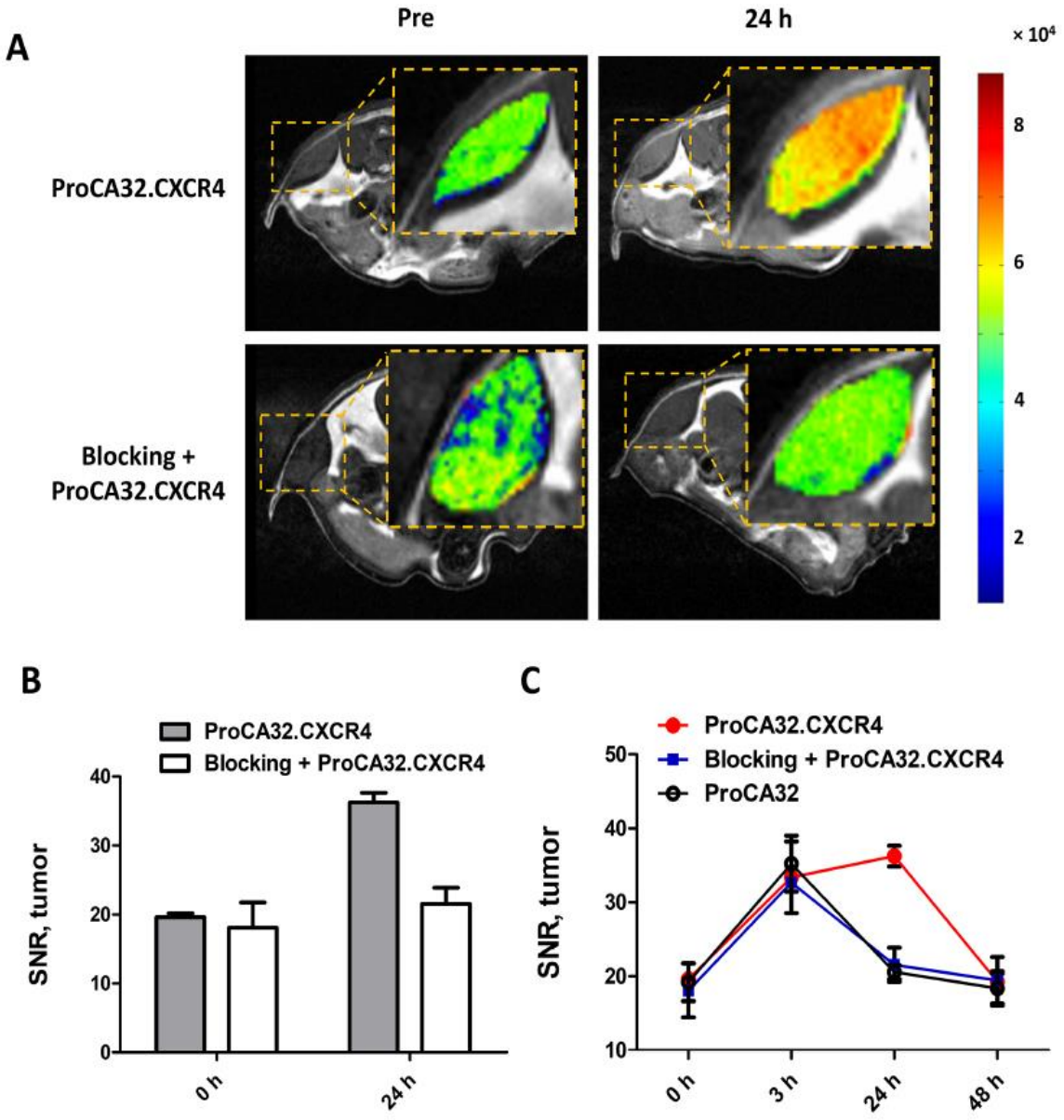

Figure 6.14 Validating CXCR4 binding specificity by receptor blocking study.
(**A**) Comparison of subcutaneous UM tumor intensity change on T1-weighted MR images following administration of Cys-ProCA32.CXCR4 with and without prior administration of blocking reagent; subcutaneous UM tumors are represented by color region. Tumor from UM mice that received Cys-ProCA32.CXCR4 injection showed a significant increase in MRI signal intensity after Cys-ProCA32.CXCR4 administration. This enhancement could be blocked by first administrating the CXCR4 receptor blocking reagent. (**B**) Comparison of UM tumor SNR change following administration of Cys-ProCA32.CXCR4 and blocking reagent + Cys-ProCA32.CXCR4. For the mice that received Cys-ProCA32.CXCR4 injection, the SNR of UM tumor significantly increased at 24 h after Cys-ProCA32.CXCR4 administration. This enhancement was blocked by first administrating a blocking reagent. As seen with the mice that received the blocking reagent and then the Cys-ProCA32.CXCR4 injection, the SNR of UM tumor was significantly lower in

comparison with the UM tumor SNR of the mice with Cys-ProCA32.CXCR4 administration. (**C**). UM tumor SNR change following administration of Cys-ProCA32.CXCR4, blocking reagent + Cys-ProCA32.CXCR4 and Lys-ProCA32. At 3 h after administration, mice from all three groups showed SNR increase. At 24 h, mice with blocking reagent + Cys-ProCA32.CXCR4 administration and mice with Lys-ProCA32 administration showed an SNR wash out; while mice that received Cys-ProCA32.CXCR4 exhibited further SNR increases compared with 3 h. At 48 hours, mice that received blocking reagent + Lys-ProCA32.CXCR4 and mice that received Lys-ProCA32 administration exhibited further SNR further decrease. Mice that received Cys-ProCA32.CXCR4 administration showed SNR wash out in comparison with 24 h.

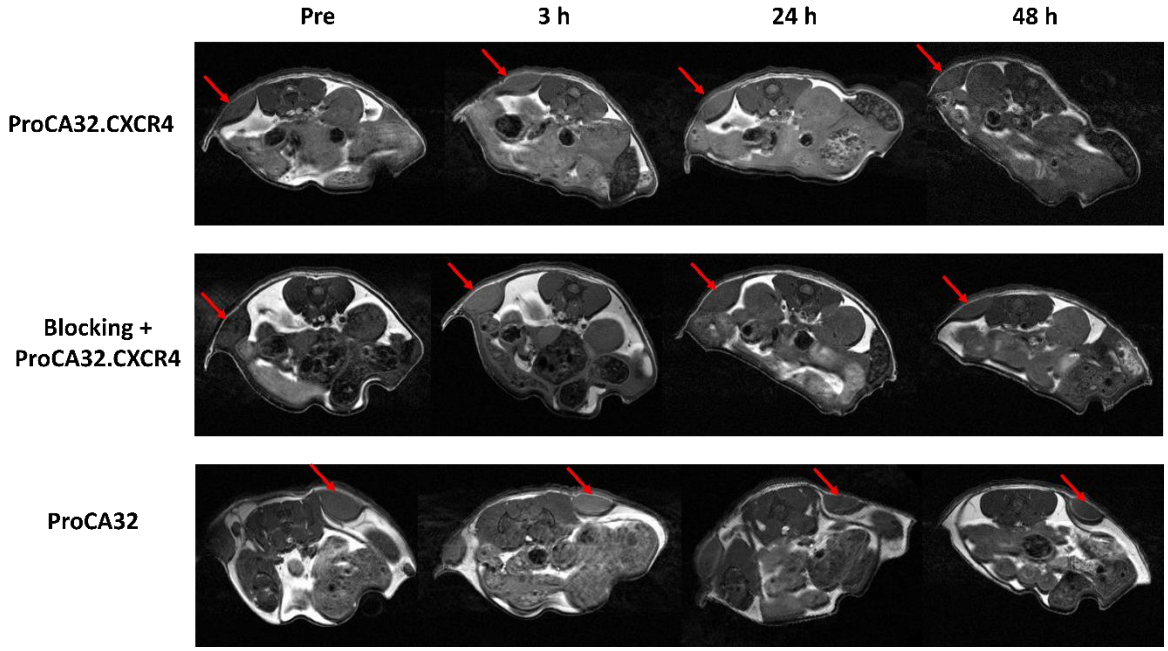

Figure 6.15 MR images of subcutaneous UM mice before and after administration of Cys-ProCA32.CXCR4, blocking reagent + Lys-ProCA32.CXCR4 and Lys-ProCA32.
T1-weighted MR images of xenografted mice with subcutaneous UM tumors before and after administration of Cys-ProCA32.CXCR4, blocking reagent + Cys-ProCA32.CXCR4 and Lys-ProCA32; imaging time points include pre-injection, 3 h, 24 h, and 48 h post-injection. Tumors are identified by red arrows. Three groups of mice exhibited tumor signal intensity increases at 3 h after injection of contrast agents. Mice that received the injection of Cys-ProCA32.CXCR4 presented further tumor signal enhancement at 24 h after injection, and signal intensity then washed out at 48 h. CXCR4 blocking reagent pre-treated mice and Lys-ProCA32 administration showed signal washout at 24 h and further decreases at 48 h.

6.2.4 Detection of liver metastases in SKOV3 orthotopic ovarian cancer mouse model

Orthotropic human ovarian cancer xenograft model was established by Dr. Lily Yang in a protocol detailed described in chapter 2.9.3. SKOV3 cells are stably transfected with firefly

luciferase. Followed the injection of luciferase substrate (D-luciferase, free acid), bioluminescence images showed the tumor enhancement around the ovary region. Tissues collected 20 minutes after injection of luciferase substrate showed metastases in spleen, liver, lung, and kidney (Figure 6.16)

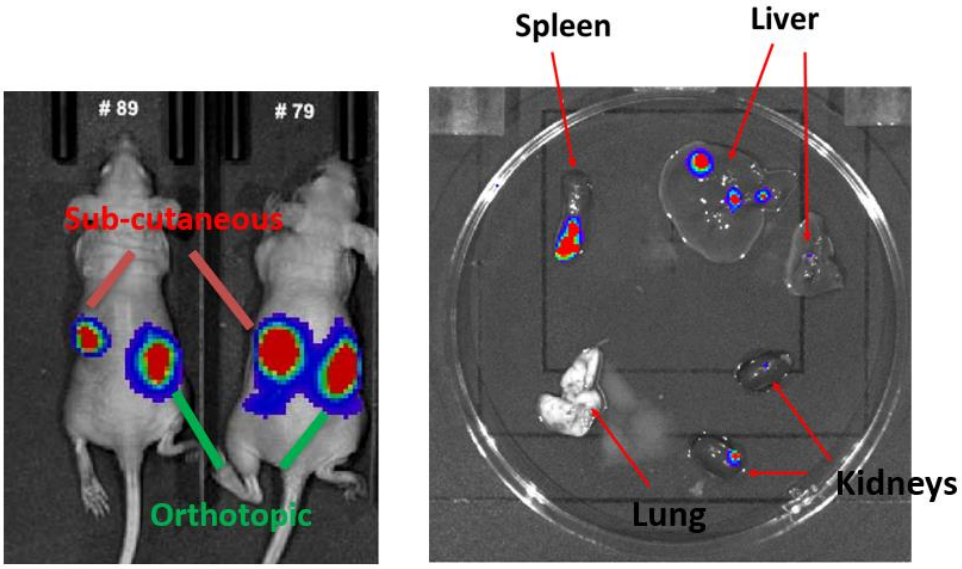

Figure 6.16 Bioluminescence images of orthotopic ovarian tumors and metastases. Bioluminescence images of SKOV3 ovarian cancer mice show the subcutaneous and orthotopic tumors. Organs, including spleen, liver, lung, and kidney, have metastasis lesion. (Data from Dr. Jingjuan Qiao)

T1 and T2 weighted MR images of SKOV3 ovarian cancer mice were collected with gradient echo acquisition and fast spin echo acquisition respectively at 4.7 T. T1 weighted MR images of SKOV3 mice show the liver enhancement followed by the administration of ProCA32.CXCR4 up to three hours, and the liver intensity started to wash out after three hours of injection. The tumor metastases have SNR enhancement, which exhibited the same pattern observed in Mel290 mice (Figure 6.18). The signal-noise ratio of metastases in the liver increased after administration of ProCA32.CXCR4 gradually and reach to the highest SNR at 24 hours after injection. Moreover, the SNR started to wash out after 24 hours after injection. However, owing

to the higher liver enhancement in 4.7 T than in 7.0 T, metastases, in contrast, exhibited darker lesions when compared with the rest of liver tissues.

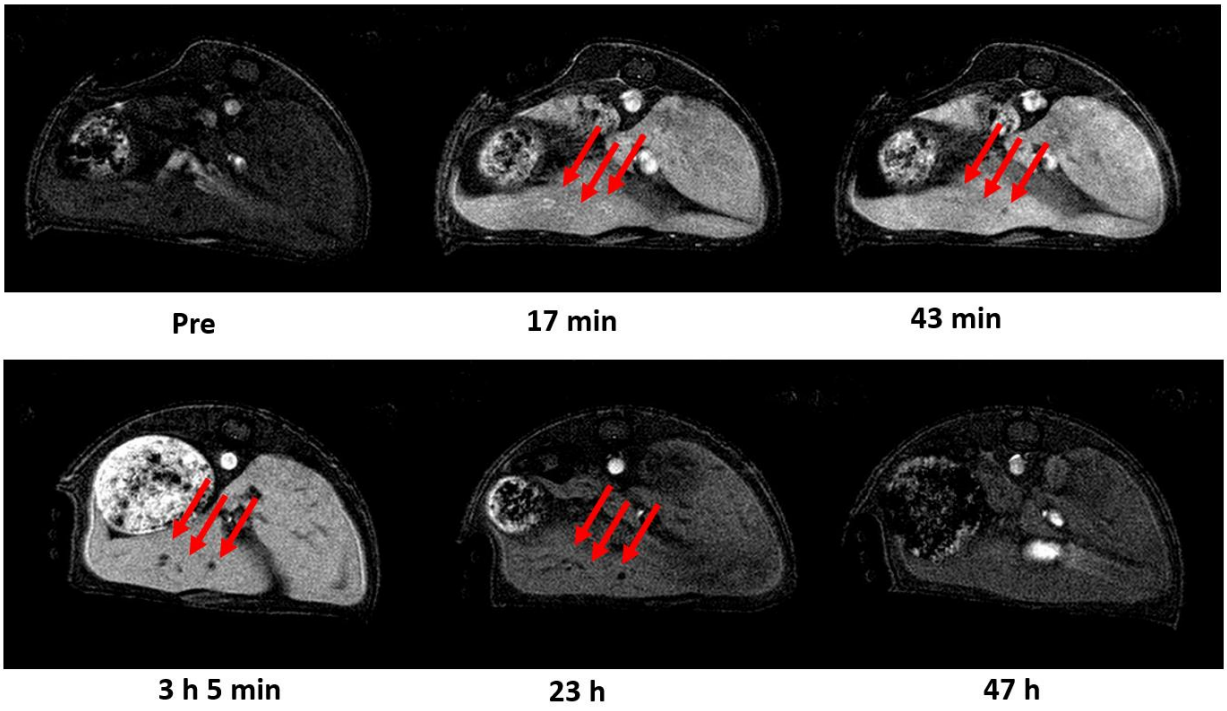

Figure 6.17 T_1 weighted MR images (gradient echo) of SKOV3 orthotopic mice model with ProCA32.CXCR4 injection.

T_1 weighted MR images of SKOV3 mice collected before and after the injection of ProCA32.CXCR4. Metastatic tumor lesions (pointed by red arrows) shows strong contrast with liver tissue and can be distinguished after the administration of ProCA32.CXCR4.

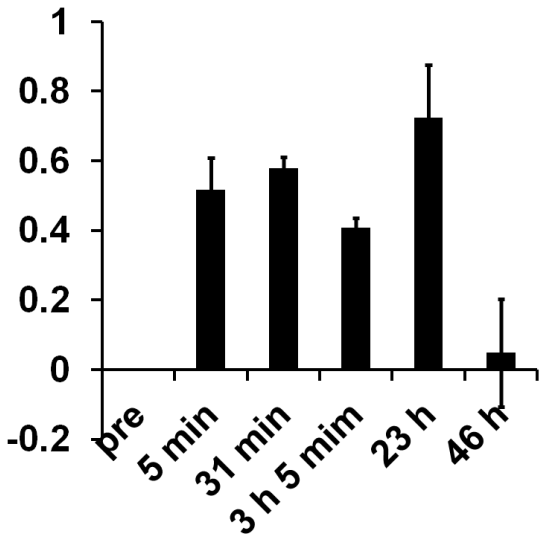

Figure 6.18 The intensity percentage increase of tumor region in SKOV3 mice model after ProCA32.CXCR4 injection.

6.3 Conclusion and discussion

The liver is a common site for cancer metastasis. UM almost exclusively metastasizes to the liver. The mechanism of the liver-specific metastases is not well known yet. Based on the findings that liver cells produce some chemoattractants (i.e., CXCL12) (199) and elevated expression of CXCR4 in several UM cell line studies (197, 200), one hypothesis is tumor cells that are overly express CXCR4 hijack the CXCR4/CXCL12 axis during the metastatic process and spread to the liver (140, 151, 152). CXCR4 is proposed to be a prognostic marker in acute myelogenous leukemia, breast cancers, colorectal cancers, and melanoma (99, 197, 201, 202). Thus, the development of imaging agents for CXCR4 may be highly informative regarding cancer diagnosis and prognosis.

By demonstrating elevated CXCR4 expression levels in UM patient liver metastases, UM cell lines, as well as metastatic UM mouse models, we validated the diagnostic value of CXCR4 as an imaging biomarker in UM. Multiple attempts have been made towards to develop CXCR4

molecular imaging agents over the years using different imaging technologies including SPECT, PET, and near-infrared imaging (203-205). MRI has the advantage of being able to provide high spatial resolution imaging without ionizing radiation and depth limitation. However, limited by the sensitivity of current MRI contrast agents and the low local concentration of receptors on the tumor cell surfaces (50), the application of MRI in molecular imaging is very challenging. We developed a CXCR4 targeted MRI contrast agent ProCA32.CXCR4 that exhibited 8 to 10 times increase in both r_1 and r_2 relaxivities over clinical GBCAs and enabled sensitive MRI detection of CXCR4. We have applied a metastatic UM mouse model M20-09-196, with small metastases in the liver, to demonstrate the imaging capacity of ProCA32.CXCR4. MR imaging following ProCA32.CXCR4 administration is able to detect UM micro-metastases in mouse livers as small as $0.1mm^2$, which is a significant improvement in the detection limit of MRI for liver lesions (193). Several factors contributed to the robust detection of micro-metastases at the early stages. First, CXCR4 targeting enabled ProCA32.CXCR4 accumulation at metastases sites. Secondly, high relaxivities of ProCA32.CXCR4 significantly improved the sensitivity of MR imaging. Compared with small molecule chelator, ProCA32.CXCR4 has secondary coordination shell and optimized rotational correlation time, which contributes to the relaxivities improvement (206).

Furthermore, both high r_1 and r_2 of ProCA32.CXCR4 doubled the confidence and avoided artifacts of detection by applying both T_1 and T_2 weighted acquisition. Another challenge in imaging UM metastases in the liver is to identify pathological growth patterns of metastases with MR imaging (194). MR images of M20-09-196 mice following administration of ProCA32.CXCR4 exclusively enhanced nodular growth pattern metastases. This enhancement might be caused by the CXCR4 expression difference of metastases with different growth patterns.

Administration of ProCA32.CXCR4 achieved detection of liver metastases using MDCI by MRI. In UM mouse model Mel290, the intensity changes over time exhibited different patterns in liver metastases than in the adjacent liver. Tumor region intensity steadily increased up to 24 hours after ProCA32.CXCR4 injection due to *in vivo* dynamic binding to CXCR4, followed by a slow wash out after 24 hours to 48 hours. However, tumor region intensity showed a small transient increase (at 12 min) right after ProCA32 injection due to *in vivo* distribution and wash out after 3 hours.

On the other hand, the liver region in both mice injected with ProCA32.CXCR4 and ProCA32 showed similar enhancement patterns over time. This unique property of ProCA32.CXCR4 provides a possibility of acquiring MDCI using MRI. MDCI provides an additional avenue to non-invasively differentiating tumors from healthy livers taking advantage of biomarker binding capability. Besides, ProCA32.CXCR4 has excellent tumor permeability, which is different from some nanoparticles or chelator-based targeting contrast agent that mostly enhance the tumor boundary (207). This allows for mapping heterogeneous CXCR4 expression inside the tumor. This property may facilitate monitoring of CXCR4 expression changes through the tumor tissue during progression and treatment.

The relatively long half-life of ProCA32.CXCR4 makes the best imaging time for optimized tumor enhancement around 24 to 48 hours after injection, which might be one limitation for clinical usage. We are in the process of optimizing PEG modification of ProCA32.CXCR4 to tune the PK/PD properties. Another concern would be ProCA32.CXCR4 nonspecific interactions with CXCR4 expressed on normal cells (i.e., immune-related cells). Further studies should be done to evaluate ProCA32.CXCR4 carefully before it can be taken to clinical application.

6.4 Summary

In this study, we verified that CXCR4 is a diagnostic imaging biomarker by its elevated expression level in liver metastases in UM patients, UM cell lines, and mouse models. Additionally, we have successfully designed a CXCR4-targeted, protein-based contrast agent, ProCA32.CXCR4, which can detect UM hepatic metastases as small as 0.1mm2. The detected liver micrometastases were further validated by histological analysis, which is well-correlated with MR images. Our results indicate that ProCA32.CXCR4 enables precision MRI capable of defining molecular signatures for identifying metastases.

In summary, we report results validating our hypothesis that CXCR4 is a diagnostic imaging biomarker for liver metastases using UM patient samples, UM cell lines, and animal models. Additionally, we successfully designed a CXCR4-targeting, protein-based contrast agent, ProCA32.CXCR4, for early detection of UM hepatic metastases. The detected liver micrometastases were validated by histological analysis and correlated well with MR images. Our results indicate that this contrast agent can enable precision MRI (pMRI) capable of defining molecular signatures for identifying metastases, and possibly for treatment stratification.

7 PRECLINICAL APPLICATIONS OF PROCA32.CXCR4 FOR DETECTION OF FIBROSIS AND HCC AND MONITORING TREATMENT EFFECT

7.1 Introduction

7.1.1 Hepatocellular carcinoma

Hepatocellular carcinoma (HCC) is the most common primary liver malignancy with increasing new cases (208, 209). Statistics show that: from 2011 to 2015, the liver cancer death rate rose 2.7% every year in female patients and 1.6% for male patients (1). Chronic liver diseases, including hepatitis B (210, 211), hepatitis C (211), alcoholic and non-alcoholic fatty liver (212)

and cirrhosis are the major risk factors for the HCC. Inflammation and fibrosis are two major phytological processes in HCC development. Chronic hepatitis caused by HBV and HCB combination infection significantly increases the risk of HCC development. HBC can lead to HCC even without the involvement of fibrosis (213). However, HCC progressed from HCV infection almost exclusively established on the cirrhotic liver (214).

7.1.2 Current state-of-art for HCC detection and surveillance monitoring

Since 2001, imaging-based diagnosis of HCC has been established to replace the biopsy-based diagnosis, and HCC diagnosis can be established based on imaging combined with laboratory tests (215). The HCC diagnosis at a late stage has a poor prognosis for the limit options of treatments. The early detection of HCC is of significant importance because of surgical resection yields similar or even better outcome than orthotopic liver transplantation, which solved the problem of the long waiting list, the high expense of transplantation and give patients better prognosis (216).

Different scientific associations and societies have developed slightly inconsistence imaging-based diagnostic systems and algorithm (Figure 7.2) for hepatocellular carcinoma. The imaging-based diagnostic systems have evolved because of the advance of understanding about HCC imaging features. The systems are developed for patients with a high risk of developing HCC for screening and surveillance. The first line for screening patients with high risk usually combines ultrasound with serum test screening of biomarkers (including alpha-fetoprotein (AFP), protein induced by vitamin K absence) according to the Japan Society of Hepatology (217). With people shows positive results on the screening test, dynamic CT/ MRI are recommended for imaging diagnosis and staging. The imaging features of HCC including arterial phase hyperenhancement, wash out appearance, corona enhancement, capsule appearance, etc. (215, 217) The typical

vascular pattern of HCC lesions are well agreed on including the hyper-enhancement in the arterial phase and hypo-enhancement (washout) appearance in the venous phase. The wash in and wash out features are caused by the blood supply difference of HCC lesions and healthy liver, which lead to the wash-in of contrast agents differently. The HCC lesions primarily have blood supply from the artery, so it has hyper-enhancement on arterial phase.

A comprehensive review of guidelines including the Asian Pacific Association for the Study of the Liver (APASL), Japanese Society of Hepatology (JSH), American Association for the Study of Liver Diseases (AASLD), and the European Association for the Study of the Liver (EASL) summarized the difference and similarity across the guidelines from those major scientific societies (218-221). Tumor size is the primary concern to assess HCC according to the AASLD and EASL. The JSH and APASL emphasize more on the vascular imaging pattern of HCC lesion. There is a slight difference between the societies regarding the choice of imaging contrast media as well, JSN advocates the liver-specific contrast agent, whereas the AASLD and EASL accept exclusively extracellular MRI contrast agents. The contrast agents for HCC detection can be majorly divided into extracellular agents and post-vascular phase agents (Figure 7.1). Most used extracellular vascular contrast agents for CT, MRI and contrast-enhanced US (CEUS) are iodine contrast agent, gadolinium-based small chelators and Sonovue respectively. The post vascular phase agents can be classified into two groups: Kupffer-specific contrast agents and hepatocyte-specific contrast agents. Sonazoid has very stable Kupffer-specific enhance around 20 min after injection. Gadolinium contrast agents for MRI, Primovist, and Multihance have the benefit of showing the regular vascular pattern on imaging right after injection and later hepatocyte-specific enhancement after being uptake by hepatocytes starts from 4 to 5 min after injection. A systematic review carried out to compare the sensitivity of MRI and multidetector CT shows that MR imaging

has higher per-lesion sensitivity (80%) than CT (68%) and recommended for diagnosis of HCC in the chronic liver disease patients (222).

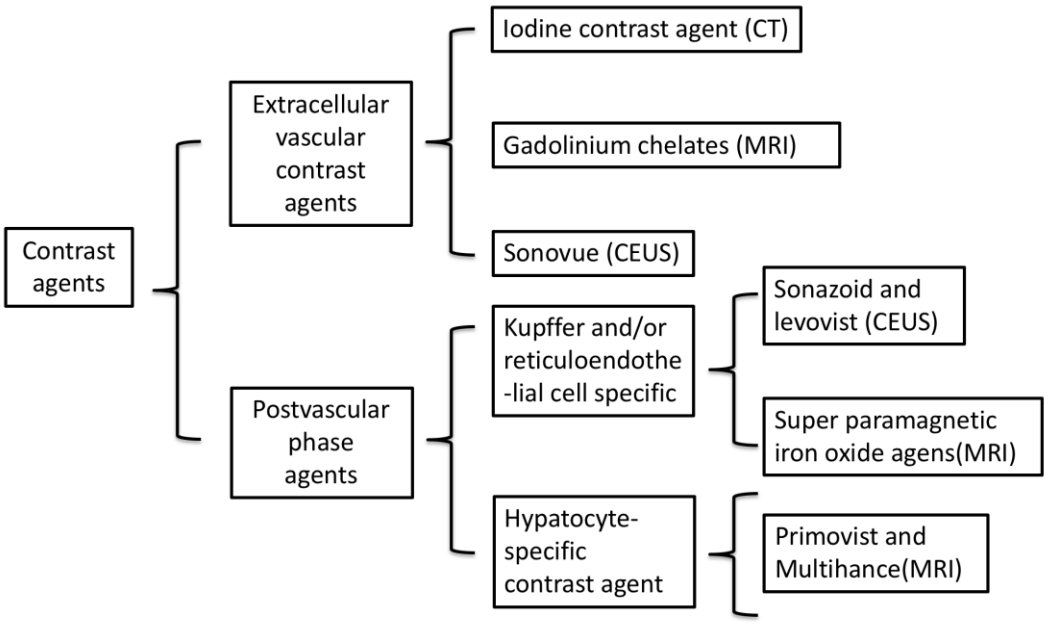

Figure 7.1 Summary of contrast agents currently used for HCC diagnosis across different imaging modalities.

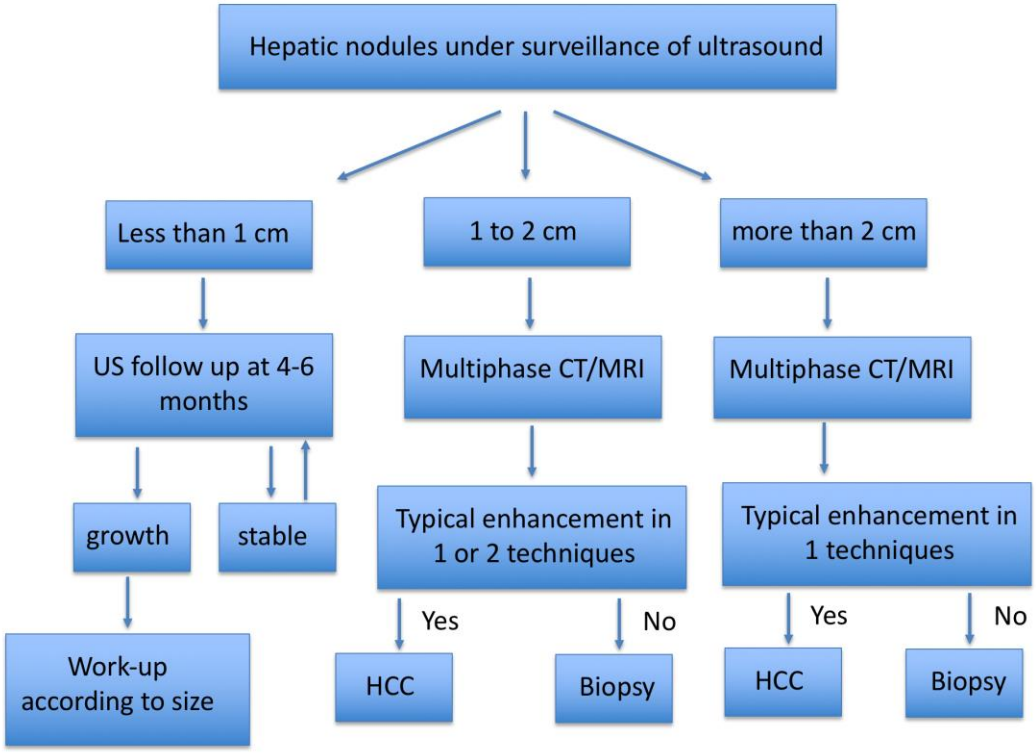

Figure 7.2 The algorism of establishing HCC diagnoses according to the European Association for the Study of the Liver (EASL). Figure adapted from (223).

The differentiation of HCC from other liver nodules including high-grade dysplasia, benign hypervascular liver lesions, and malignant hypervascular liver lesions are of significant importance because the lesions listed above have hypervascular structure and similar vascular phase enhancement with HCC. Especially for the early stage of HCC lesions which has not formed enough artery blood supply, which might not show typical vascular enhancement patterns (218).

7.1.3 Treatment options for HCC

Orthotopic liver transplantation yield the best outcome for HCC patients who are eligible. HCC patients met Milan criteria had a significantly better prognosis, and longer survival time, the five-year survival rate for patients treated with local tumor destruction, resection, and orthotopic liver transplantation is 37.6%, 55.5% and 77.2% respectively (224).

The poor prognosis of HCC and lack of effective treatments make seeking for new diagnostic and therapeutic approaches an unmet and urgent medical need. Sorafenib is an oral multi-kinase inhibitor that targets the Raf kinases, vascular endothelial growth factor receptor (VEGFR), and platelet-derived growth factor receptor (PDGFR) tyrosine kinases for anti-tumor and anti-angiogenesis effects. It demonstrated beneficial for overall survival (225). Most HCC patients have gone through cirrhosis, followed by inflammation, this process is mediated by chemokines (225). As a result, the role of chemokines in HCC development and the potential in targeted therapies has raised the interest of research in the related field. CCL20-CCR6 mediate the MAPK phosphorylation and affect the HCC progression (226).

CXCR4-CXCL12 axis is involving in cell migration and immune-cell recruitment. CXCR4 was found to have elevated expression in cirrhotic liver inflammatory foci (227). CXCR4 has multiple functions in the liver inflammation prior to liver cirrhosis and HCC, hepatocytes over-express CXCL12 following liver injury (228). We hypothesis there will be CXCR4 overexpression in HCC and it can be a potential biomarker for treatment stratification, and drug treatment effect monitoring.

7.2 Results

7.2.1 Pathology analysis of DEN-induced HCC

Mice with a C57BL/6 genetic background were used to develop DEN induced the HCC mouse model. All animal experiments performed in this study complied with an animal protocol reviewed and approved by the Institutional Animal Care and Use Committee (IACUC) at Georgia State University.

Detailed material and method see chapter 2.9.4. Three DEN-induced HCC mice with different treatment and one normal mouse as control were used for monitoring and comparing the CXCR4 expression level change using MRI scanning with one bolus tail vein injection of ProCA32.CXCR4 (0.025mmol/kg).

DEN induced HCC mice were treated with four different combination treatments. One group of animals treated with saline buffer, one group of animals treated with Doxorubicin, one treated with Doxorubicin and ProAgio (229). Mice from different groups were selected for MRI imaging to monitoring and comparing the treatment effects of different combination. All mice for MRI imaging were injected with one bolus dosage of ProCA32.CXCR4 through the tail vein. MRI scanning of the liver region of mice was collected before, 3 hours, 24 hours and 48 hours after contrast agent injection (Doxorubicin treated mouse and HCC mouse treated with a combination of Doxorubicin and ProAgio deceased after 24 hours and 48 hours scanning not collected). Right after imaging, mice were euthanized. Organs and tissues, including liver, heart, spleen, kidney, brain, tail, and muscle, were collected. The mice livers were measured and weighted, one small piece of liver from each mouse was reserved for ICP-OES analysis, the rest was fixed with 10% neutral buffered formalin for 3-7 days and embedded with paraffin for further histology analysis.

DEN-induced HCC mice liver is cirrhotic and enlarged, as seen in Figure 7.3, HCC weight is heavier and texture harder than the normal liver. Unifocal, multifocal tumor formed in the liver, color paler than normal liver tissue. There is no observable difference after Doxorubicin treatment and Doxorubicin and ProAgio combination treatment.

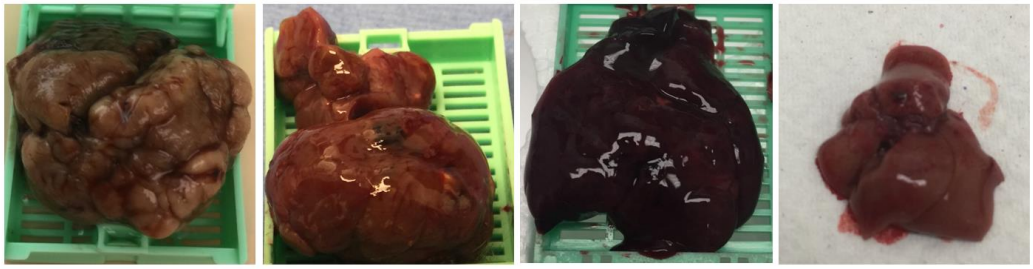

Figure 7.3 Comparison of normal mouse liver and HCC mouse liver with different treatment.

7.2.2 MRI images of HCC mice

7.2.2.1 Normal control mouse

DEN-induced HCC mice with buffer, Doxorubicin, and Doxorubicin combined with ProAgio treatment were selected for MRI imaging. Normal mouse with ProCA32.CXCR4 injection is imaged with the same protocol as control. Dosage of ProCA32.CXCR4 injection is 0.025mmol/kg, MRI images collected before the injection of ProCA32.CXCR4 and 3 hours, 24 hours, 48 hours after injection. T_1 weighted images, T_2 weighted images, T_1 mapping, and T_2 mapping were collected at each time points. 12 to 16 slides of MRI images were collected for each mouse with 1mm thickness, no gap. Detailed parameter for imaging collection sees chapter 2.10.

Normal mouse with ProCA32.CXCR4 injection shows a similar pattern as observed before for liver imaging. On both T_1 weighted and T_2 weighted imaging, the signal-noise ratio enhancement after injection showed a consistent pattern (Figure 7.4). T_1 weighted MRI imaging shows an SNR increase after 3 hours injection of ProCA32.CXCR4 and SNR washed out at 24 hours and 48 hours after contrast agent administration. T_2 weighted MRI imaging shows SNR

decreased after 3 hours of ProCA32.CXCR4 administration and SNR recover at 24 hours and 48 hours after contrast agent administration.

T_1 mapping of the mouse liver shows the liver t_1 time change before and after ProCA32.CXCR4 injection (Figure 7.5). Before ProCA32.CXCR4 injection, the liver t_1 time is 618.0 ms, at 3 hours after ProCA32.CXCR4 administration, the liver t_1 decrease to 484.3 ms. Along with the washout of contrast agent, t_1 time of liver increased at 24 hours and 48 hours, to 523.7 ms and 558.3 ms respectively.

T_2 mapping MRI scanning shows the quantitative representation of the t_2 time of the liver (Figure 7.6), the mean t2 time of liver before ProCA32.CXCR4 administration is 39.0 ms, it decreased to 35.0 at 3 hours after contrast agent administration, after 24 hours and 48 hours administration of ProCA32.CXCR4, the mean value of t2 time of liver goes back to 33.0 ms and 37.0 ms respectively along with the concentration of ProCA32.CXCR4 in liver washed out.

The signal enhancement of the whole liver is homogenous. In normal mouse, ProCA32.CXCR4 distributed to the liver through blood flow and caused signal intensity change, and the enhancement reached a peak at 3 hours and washed out along with ProCA32.CXCR4 wash out. The enhancement pattern of the normal mouse with ProCA32.CXCR4 injection is consistent on T_1 weighted, T_2 weighted, T_1 mapping, and T_2 mapping acquisition, which shows the distribution of ProCA32.CXCR4 in the liver after injection. ProCA32.CXCR4 distributed to the liver after tail vein injection, and the concentration reaches to the peak and 3 hours after and wash out ever since. As a result, the normal mouse with ProCA32.CXCR4 injection shows T1 signal enhancement, T2 signal decrease at 3 hours after injection, t1 and t2 time shortening at 3 hours after injection when compared with pre-scan and the change goes back at 24 hours and 48 hours after injection along with the washout of ProCA32.CXCR4.

The H&E staining of the normal liver shows the regular structure of mouse liver, liver lobule well- structured and hepatocytes lays in line with each other and form sinusoidal lining cells form sinusoidal space.

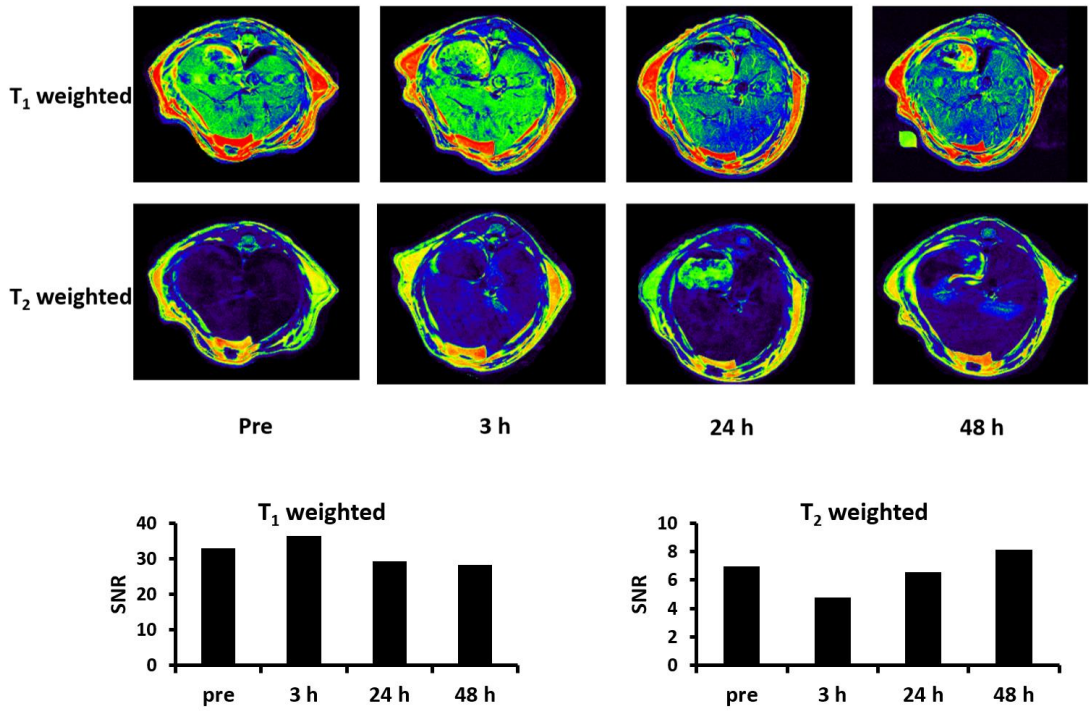

Figure 7.4 T_1, T_2 weighted MRI images and SNR of the normal mouse at different time points following ProCA32.CXCR4 injection.

Normal mouse with ProCA32.CXCR4 injection shows hyper signal intensity enhancement on T_1 weighted MRI images, and hypo signal intensity enhancement on T2 weighted MRI images after administration of ProCA32.CXCR4. The quantitative analysis of SNR shows consistent enhancement pattern followed ProCA32.CXCR4 injection. On T_1 weighted acquisition, SNR increases at 3 hours after injection of contrast agent and wash out at 24 hours and 48 hours after injection. On T_2 weighted acquisition, SNR decreases at 3 hours after contrast agent injection and come back at 24 hours and 48 hours after injection.

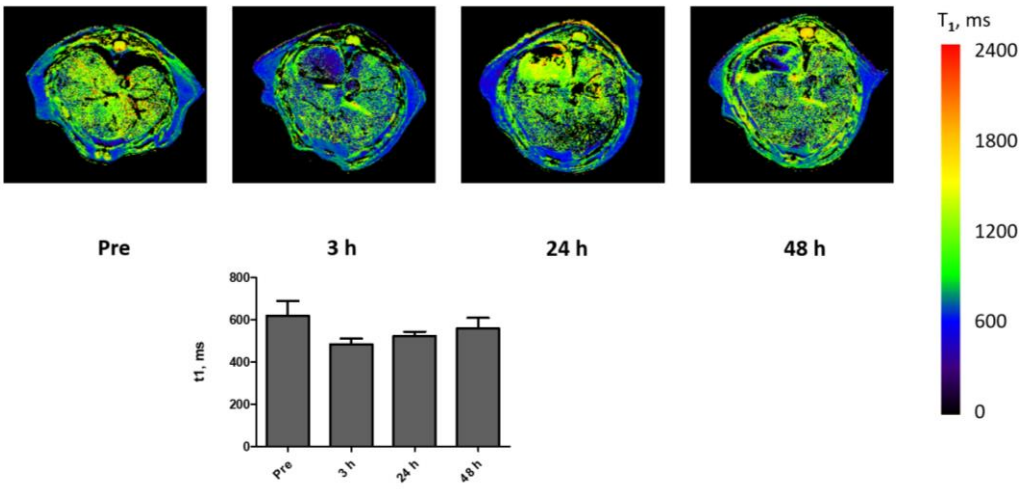

Figure 7.5 T_1 mapping MRI images and t_1 time of normal mouse at different time points follow ProCA32.CXCR4 injection.

T_1 mapping of normal mouse follows the injection of ProCA32.CXCR4 shows the t_1 time of liver decrease at 3 hours after injection of ProCA32.CXCR4 and goes back after 24 hours and 48 hours after injection.

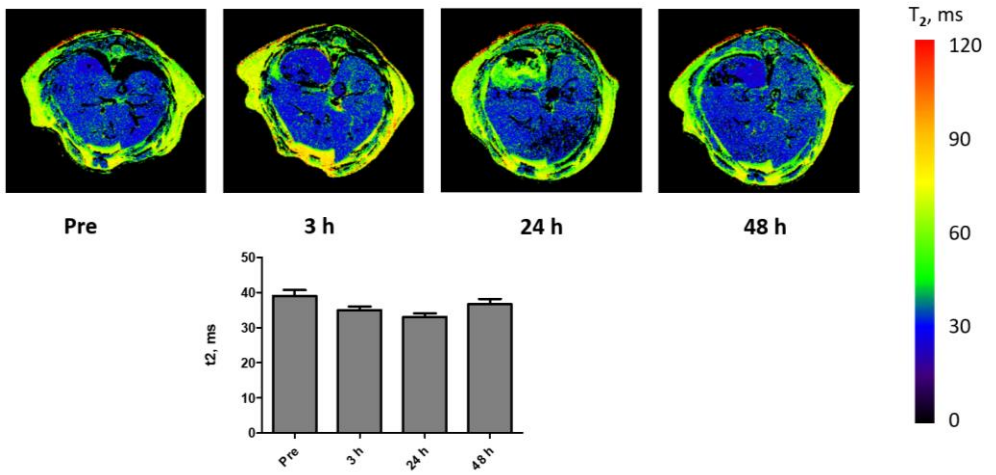

Figure 7.6 T_2 mapping MRI images and t_2 time of normal mouse at different time points follow ProCA32.CXCR4 injection.

T2 mapping of normal mouse follows the injection of ProCA32.CXCR4 shows the t2 time of liver decrease at 3 hours and 24 hours after injection of ProCA32.CXCR4 and goes back at 48 hours after injection.

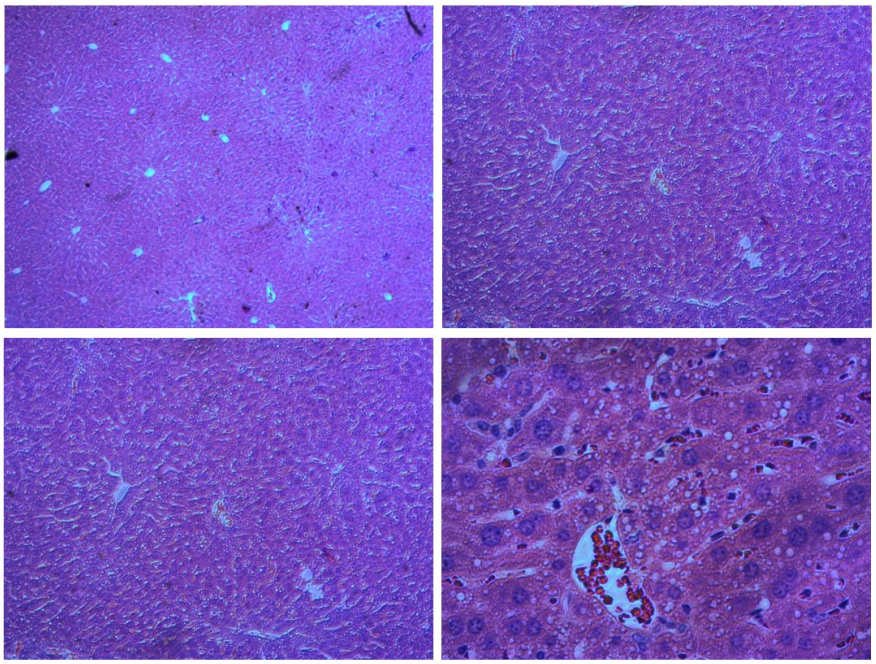

Figure 7.7 H&E staining of normal mouse liver.

Buffer treated HCC mouse has enlarged and cirrhotic liver with tumor forming in the liver (Figure 7.3), the MRI images of buffer treated HCC mouse shows the tumor nodule forming in the left part of liver on both T_1 weighted and T_2 weighted images (Figure 7.8, Figure 7.9 red circle regions). The pre-scanning of T_1 and T_2 weighted MRI images shows the left part of the liver has 10 – 20 HCC tumor nodules with a diameter of 0.5 to 3 mm. The HCC tumor nodules show hyperintensity in T_2 weighted imaging because of the intrinsic higher t_2 time of tumors. The quantitative analysis of SNR of HCC tumor nodules is based on the data of the tumors in the red circle. The SNR analysis of tumors on T_1 weighted imaging clearly shows HCC tumor has slightly higher SNR than normal liver (Figure 7.4), the HCC tumor SNR on T_1 weighted images is 34.7 whereas the normal mouse SNR is 31.3. The SNR of HCC tumors on T_2 weighted images is significantly higher than normal liver SNR; the normal liver SNR is 7.1. However, the HCC tumor

T_2 SNR is 46.8. The dramatic difference in SNR enables the HCC tumor distinguishing on T_2 weighted images.

Interestingly, after the injection of ProCA32.CXCR4, the HCC tumors intensity significantly enhanced when compared with pre-scanning on T_1 weighted images. The tumor SNR keep increasing up to 24 hours. Quantitative analysis of SNR on pre and after contrast agent administration T_1 weighted images (Figure 7.8) shows that at 3 hours after administration of ProCA32.CXCR4, the SNR of HCC tumors increase from 34.7 to 63.8, and SNR continuing increasing at 24 hours to 81.1 and wash out since then. At 48 hours after ProCA32.CXCR4 administration, the SNR goes back to 48.1.

The T_1 weighted imaging SNR change pattern at different time points after ProCA32.CXCR4 administration in buffer treated HCC mouse is different from the normal mouse and consistent with the SNR change pattern of uveal melanoma mouse with ProCA32.CXCR4 injection. For the mice carry CXCR4 high expression tumors (both uveal melanoma and HCC), the T_1 weighted SNR increase after the administration of CXCR4 targeted contrast agent ProCA32.CXCR4 up to 24 hours, and SNR wash out after that. For buffer treated HCC mouse, the SNR at 24 hours after injection is one time higher when compared with before injection (Figure 7.8), however, the uveal melanoma SNR is around 50% more than pre-scan (Figure 6.1). It indicates that the interaction of ProCA32.CXCR4 with CXCR4 *in vivo* are similar in uveal melanoma mouse models and HCC mouse model. HCC tumors might have higher CXCR4 expression levels than uveal melanoma, so it has higher SNR enhance than uveal melanoma. The T_1 mapping result is consistent with the T_1 weighted images and further proved the CXCR4 molecular imaging is achieved by administration of ProCA32.CXCR4. T_1 mapping of buffer treated HCC mouse (Figure 7.10) shows that the t_1 time of HCC tumor is intrinsically longer than

liver, the t1 time for HCC tumor is 1590 ms, after the administration of ProCA32.CXCR4, the t_1 time is shortening to 1401 ms at 3 hours and 1355 ms at 24 hours and goes back to 1588 at 48 hours. The T2 mapping of the same animal (Figure 7.12) shows the similar change pattern as T1 mapping, the t_2 time of HCC tumors is 93.7 ms, which is higher than the t2 time (39 ms) of the normal liver. After administration of ProCA32.CXCR4, the t_2 time is shortening up to 24 hours, t_2 time of HCC tumor is 74.3 ms at 3 hours and 66.0 ms at 24 hours and goes back to 84.3 ms at 48 hours.

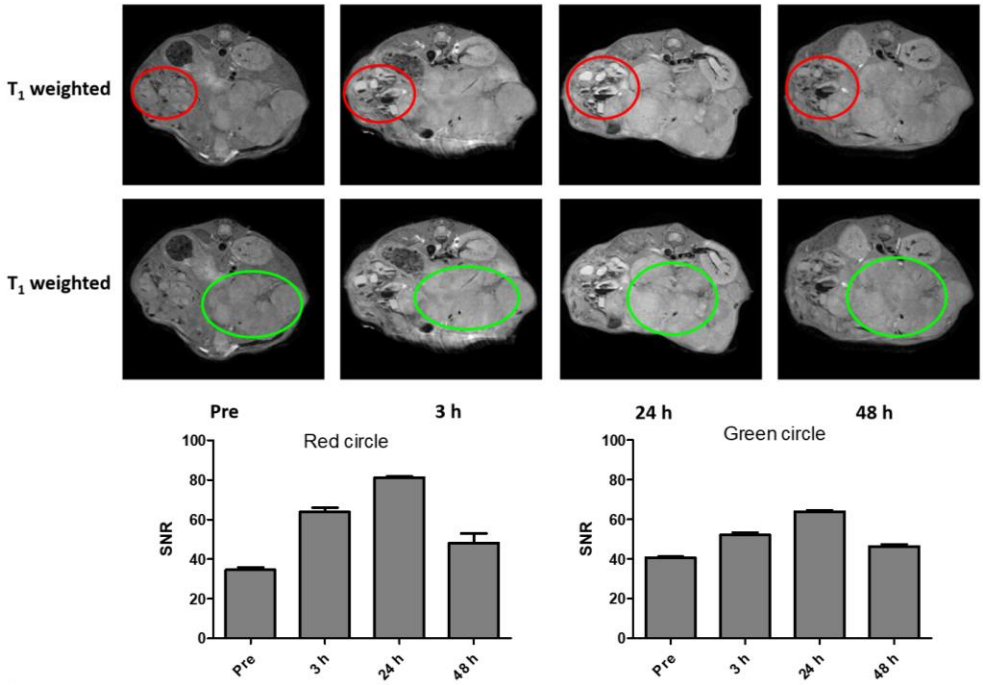

Figure 7.8 T_1 weighted MRI images and SNR comparison of buffer treated HCC mouse at different time points following ProCA32.CXCR4 injection.

T_1 weighted MR images of buffer treated HCC mouse shows increase SNR on T_1 weighted images on pre-scan. Red circle regions represent tumor nodules with high CXCR4 expression, after the injection of ProCA32.CXCR4, HCC tumor nodules with high CXCR4 expression exhibit enhancement up to 24 hours, at 24 hours, the SNR of tumor nodules is two times higher than the pre-scan SNR. At 48 hours, the SNR decreases. Green circle regions represent tumor nodules with low CXCR4 expression. For tumor nodules with low CXCR4 expression, the SNR enhancement is lower than tumor nodules with high CXCR4 expression.

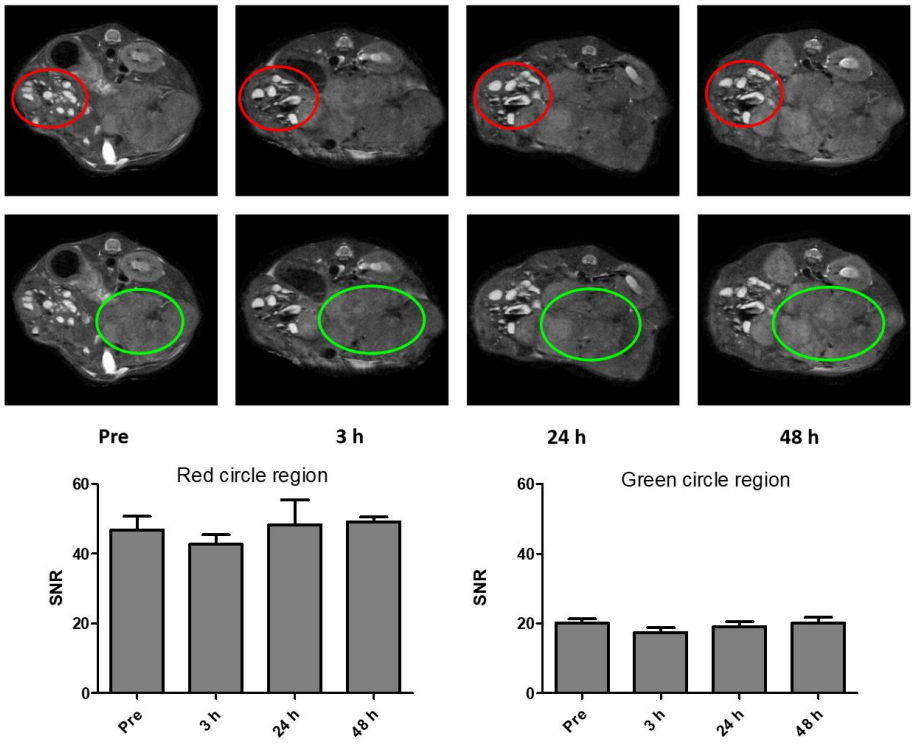

Figure 7.9 T_2 weighted MRI images and SNR comparison of buffer treated HCC mouse at different time points follow ProCA32.CXCR4 injection.

T_2 weighted MR images of buffer treated HCC mouse shows the tumor nodules circled by red circle exhibit higher SNR. Tumor nodules circled by the red circle shows about double of the value of SNR when compare with the rest part of the liver (represented by the green circled regions). After the injection of ProCA32.CXCR4, the SNR of tumors decreases at 3 hours after injection and goes back afterward. The green circled liver region has slightly decreased after the injection of ProCA32.CXCR4.

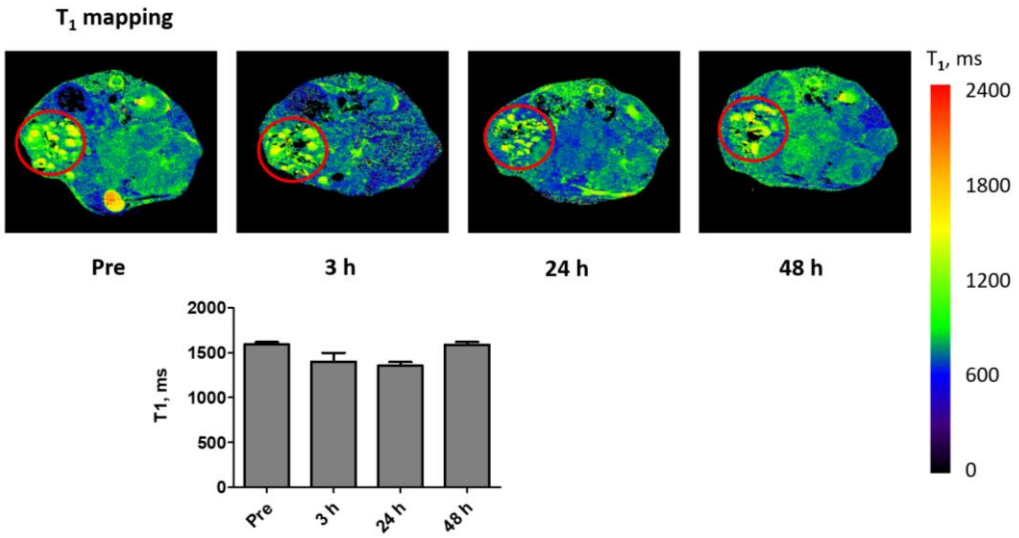

Figure 7.10 T_1 mapping MRI images and t_1 time of tumor nodules of buffer treated HCC mouse at different time points following ProCA32.CXCR4 injection.

T_1 mapping of buffer treated HCC mouse to analysis the t_1 time of tumor nodules (represented by red circled regions). The t1 time of tumor nodules on pre-scan is 1590 ms, after the administration of ProCA32.CXCR4, the t_1 time is shortening to 1401 ms at 3 hours and 1355 ms at 24 hours and goes back to 1588 at 48 hours. T1 mapping results of buffer treated HCC mouse is consistent with T1 weighted images.

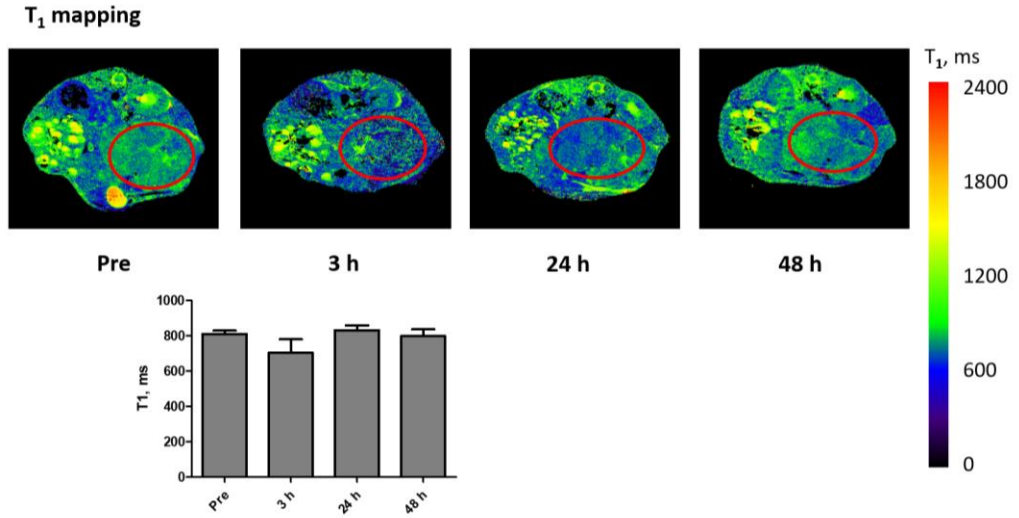

Figure 7.11 T_1 mapping MRI images and t_1 time of other regions of buffer treated HCC mouse at different time points follow ProCA32.CXCR4 injection.

T_1 mapping of buffer treated HCC mouse to analysis the t_1 time of regions other than tumor nodules (represented by red circled regions). The t_1 time of 809.3 ms, after the injection of ProCA32.CXCR4, t_1 time of the same region decreases to 703.0 at 3 hours after injection and goes back to 797.5 ms at 48 hours after ProCA32.CXCR4 injection.

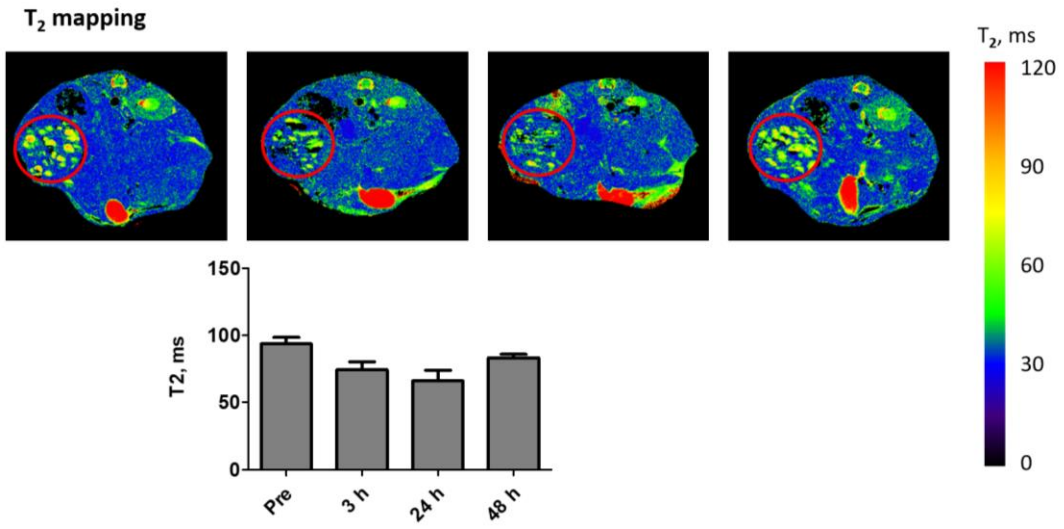

Figure 7.12 T_2 mapping MRI images and t_2 time of buffer treated HCC mouse tumor nodules at different time points following ProCA32.CXCR4 injection.

T_2 mapping of buffer treated HCC mouse to analysis the t_2 time of tumor nodules (represented by red circled regions). T2 mapping of the buffer treated HCC mouse shows the similar change pattern of CXCR4 high expression nodules as T_1 mapping, the t_2 time of HCC tumors on before injection scan is 93.7 ms, which is higher than the t2 time (39.0 ms) of the normal liver. After administration of ProCA32.CXCR4, the t_2 time is shortening up to 24 hours, t_2 time of HCC tumor is 74.3 ms at 3 hours and 66.0 ms at 24 hours and goes back to 84.3 ms at 48 hours.

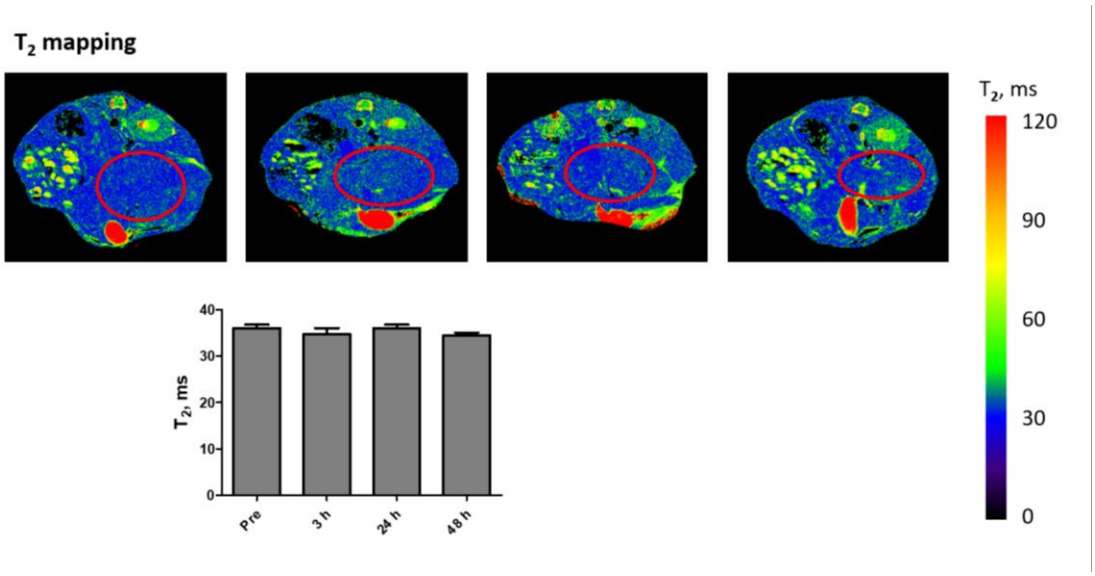

Figure 7.13 T_2 mapping MRI images and t_2 time of buffer treated HCC mouse other regions than tumor nodules at different time points following ProCA32.CXCR4 injection.

T2 mapping of buffer treated HCC mouse to analyze the t2 time of other regions than CXCR4 high expression nodules. The t2 time of the other region than tumor region of buffer treated HCC mouse (represented by the red circle region) shows the t2 time of red circle region slightly decreases at 3 hours after injection of ProCA32.CXCR4 and goes back afterwards.

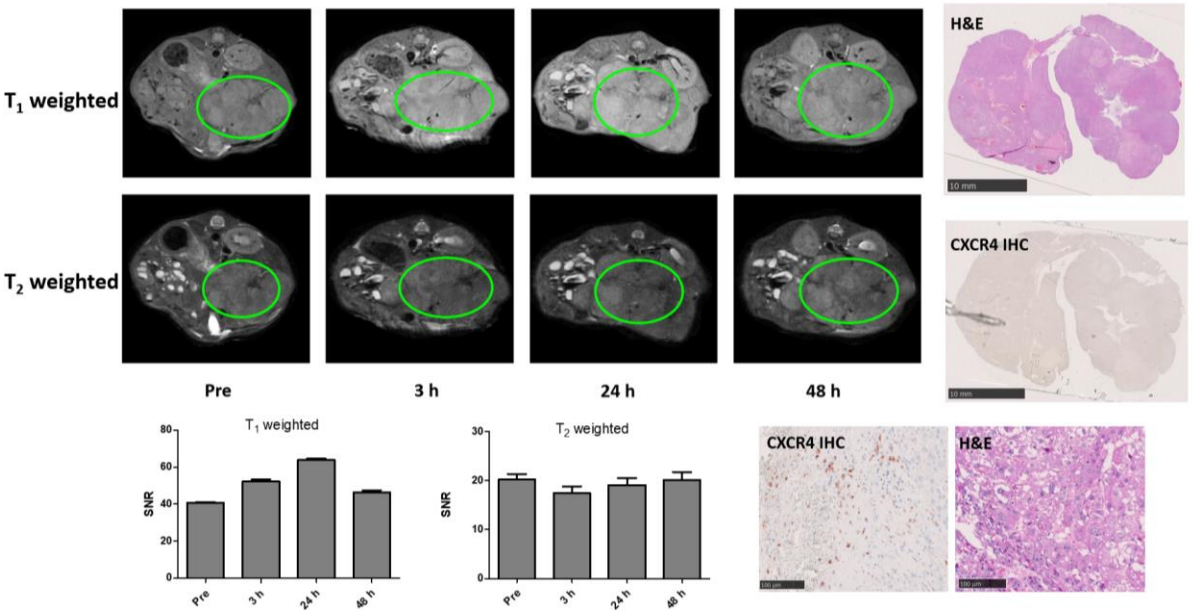

Figure 7.14 Correlation of MR images and histological results of buffer treated HCC mouse.

Histological correlation of buffer treated HCC mouse liver with both T_1 and T_2 weighted MR images.

Doxorubicin treated HCC mouse has distinctly different MRI imaging results than the buffer treated HCC mouse, the T_1 weighted images (Figure 7.15) of Doxorubicin treated mouse shows the signal decrease in both liver and tumor region when compare with pre-scan. The T_1 SNR slightly decrease at 3 hours after administration of ProCA32.CXCR4 and goes back at 24 hours. The T_2 SNR decrease at 3 hours after administration of ProCA32.CXCR4 and further decrease at 24 hours. The t_1 and t_2 time of the HCC tumor treated with Doxorubicin decreased at 3 hours after administration and went back at 24 hours (Figure 7.17, Figure 7.18). The t_1 time of HCC mouse treated with Doxorubicin is 1474 ms on the pre-scan and decrease to 1293 ms at 3 hours after ProCA32.CXCR4 injection. At 24 hours after administration of ProCA32.CXCR4, the

t_1 time of HCC tumor goes back to 1429 ms. The t_2 time of Doxorubicin treated HCC mouse tumor is 92.3 ms before the administration of ProCA32.CXCR4 and decrease to 75.7 ms at 3 hours after injection, at 24 hours, the t_2 goes back to 93.7 ms. The t_1 and t_2 time of Doxorubicin treated HCC tumor is similar with buffer treated HCC tumor, but the dynamic change of the t1 and t2 time is different which is caused by the CXCR4 expression change with Doxorubicin treatment.

The results proved that, for the HCC tumor treated with buffer and Doxorubicin, it is difficult to conclude the treatment effect, since the SNR on T1 weighted, T2 weighted images are similar with two different treatments. The T1 mapping and T2 mapping gave the results of t1 and t2 time of HCC tumor, which is similar as well for the buffer treated mice, and Doxorubicin treated mice. The MRI imaging without administration cannot provide enough information for treatment effect evaluation. With the administration of CXRC4 targeted contrast agent ProCA32.CXCR4, however, we can have further information regarding the molecular signature of HCC tumor change followed by different treatments. For the HCC mouse treated with buffer, tumor intensity and t_1 time significantly enhanced after ProCA32.CXCR4 was introduced, which enabled by the CXCR4 binding of ProCA32.CXCR4 and achieving of CXCR4 molecular imaging using MRI.

On the contrary, HCC mouse with Doxorubicin treatment did not show this change. For the reason that, after chemotherapy, CXCR4 level decreased before visible tumor size shrinking and tumor number decreased can be observed. It is enabling early assessment of treatment effect before any anatomical structure change can be detected. Treatment effect assessment and monitoring is another important application of molecular imaging using MRI. With the advantage of non-radiation exposure to MRI scanning, patients can be repeatedly assessed for treatment

follow-up. Molecular imaging provides information on a molecular level; such incidences happen ahead of macroscopic changes can be observed.

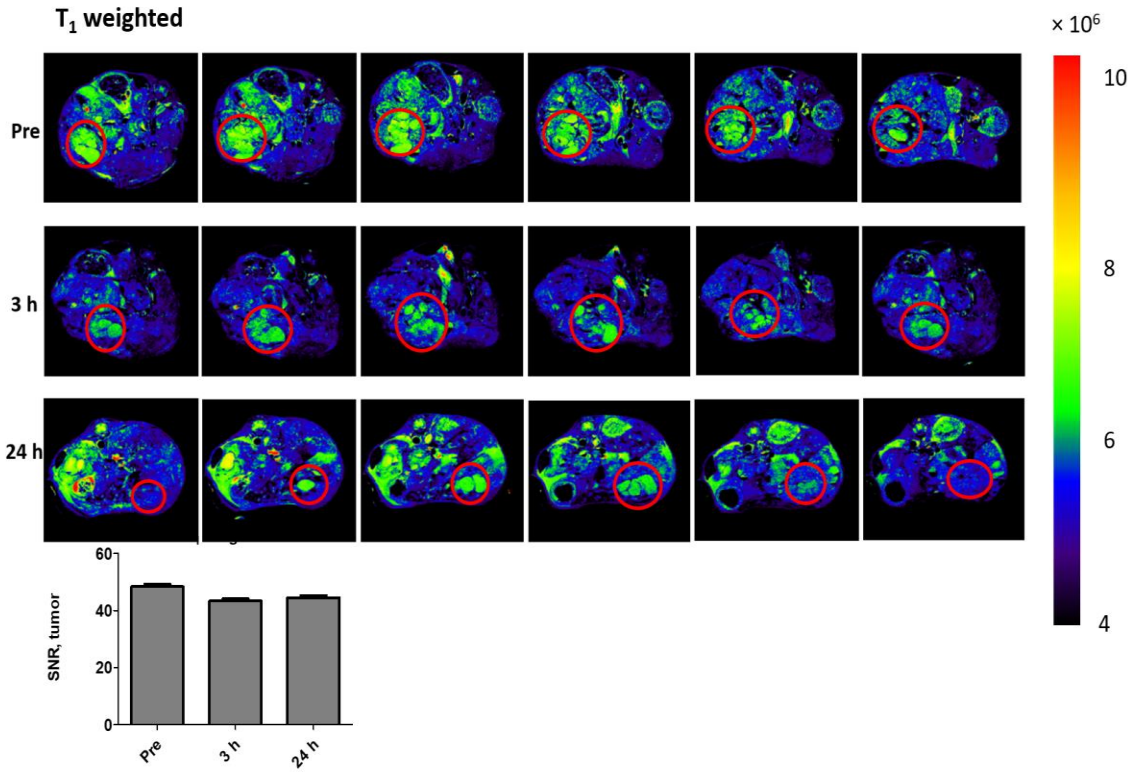

Figure 7.15 T_1 weighted images of Doxorubicin treated HCC mouse.
Six continuous T_1 weighted MRI images of Doxorubicin treated HCC mouse at before, 3 hours and 24 hours after the injection of ProCA32.CXCR4. Red circle regions represent the HCC region from which the SNR was analyzed. The SNR of tumor nodules of Doxorubicin treated HCC mouse shows a decrease after 3 hours injection of ProCA32.CXCR4 and goes back at 24 hours after injection of ProCA32.CXCR4.

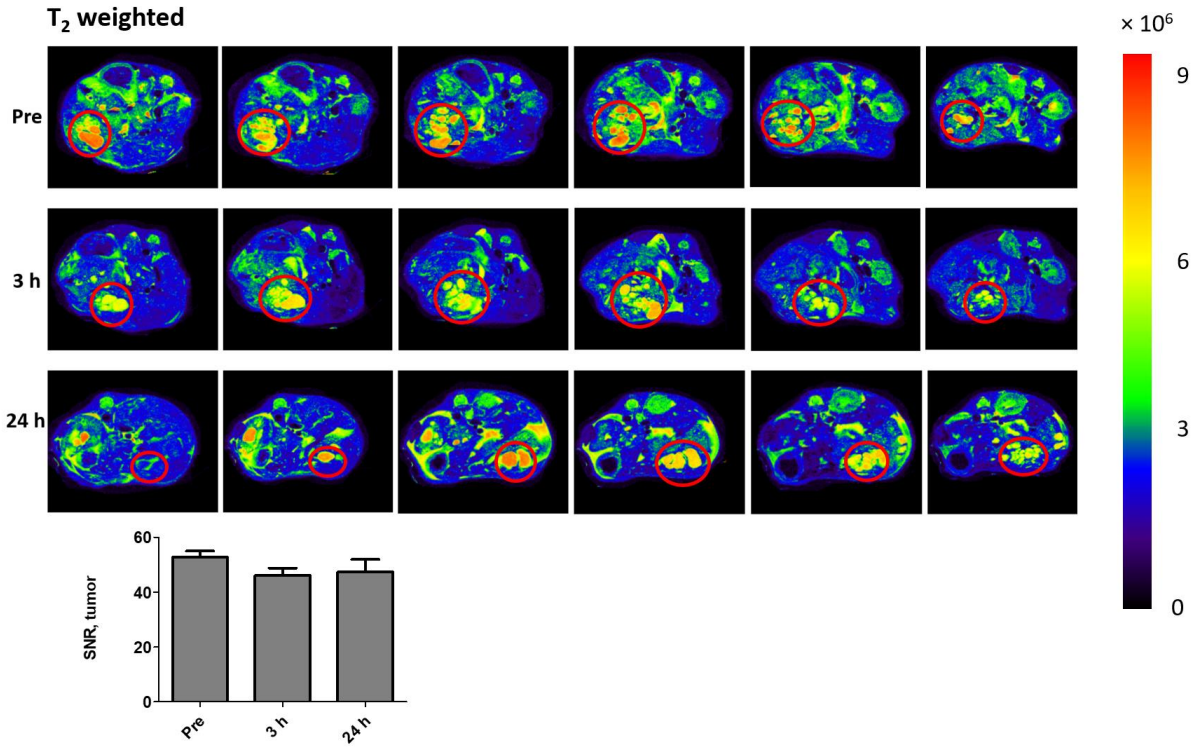

Figure 7.16 T_2 weighted MRI images of Doxorubicin treated HCC mouse.
Six continuous T_2 weighted MRI imaged of Doxorubicin treated HCC mouse at pre-injection, 3 hours and 24 hours after injection of ProCA32.CXCR4. The red circle regions represent the tumor regions selected for SNR analysis. T_2 weighted images of Doxorubicin treated HCC mouse shows SNR decrease at 3 hours after the injection of ProCA32.CXCR4 and SNR go back at 24 hours after injection of ProCA32.CXCR4.

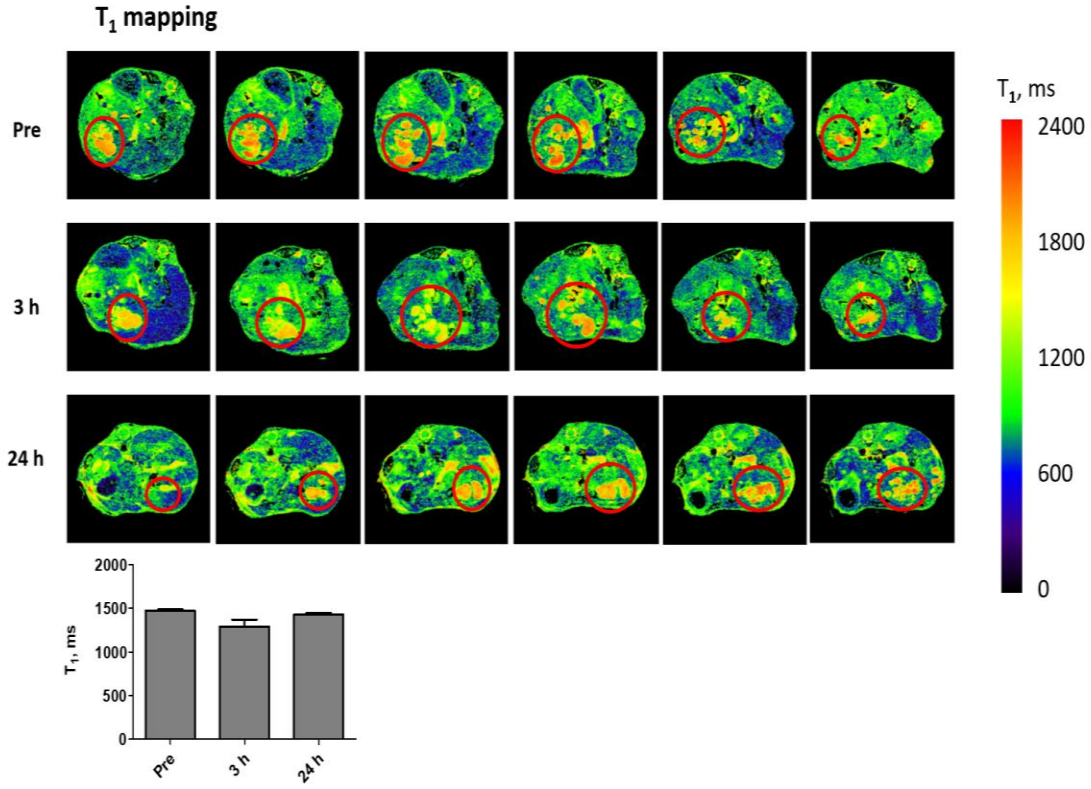

Figure 7.17 T1 mapping MRI images of Doxorubicin treated HCC mouse.
Six continuous slides of T_1 mapping of Doxorubicin treated HCC mouse at different time points following ProCA32.CXCR4 injection. T_1 time analysis based on the regions circle by red circles. T_1 time of the tumor nodules of Doxorubicin treated HCC mouse shows the t_1 time decrease followed the administration of ProCA32.CXCR4. The t_1 time of tumor nodules before ProCA32.CXCR4 injection is 1474.0 ms, at 3 hours after injection, the t_1 time decreases to 1293.0 ms and at 24 hours goes back to 1429.0 ms. The t1 time results are not consistent with the T1 weighted images of the same animal. T1 mapping is a more precise way to represent the tissue relaxation rate change followed the administration of contrast agents.

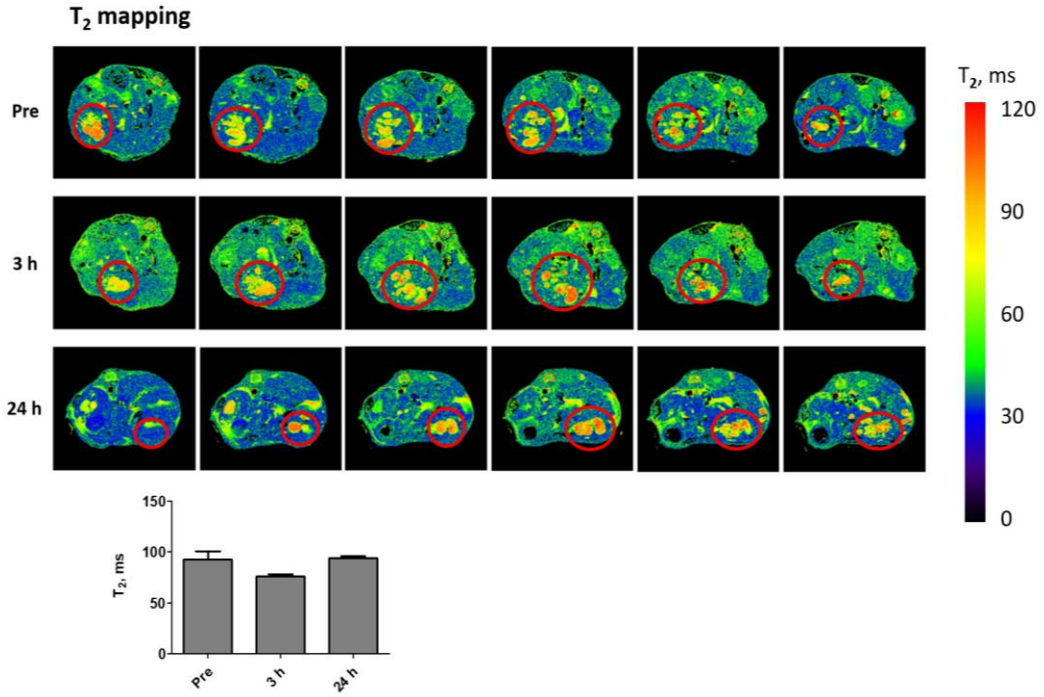

Figure 7.18 T_2 mapping MRI images and t_2 time of Doxorubicin treated HCC mouse at different time points following ProCA32.CXCR4 injection.

Six continuous slides of T_2 mapping of Doxorubicin treated HCC mouse at different time points following ProCA32.CXCR4 injection. T_2 time analysis based on the regions circle by red circles. T_2 time of tumor nodules of Doxorubicin treated HCC mouse decrease to 75.7 ms at 3 hours after the administration of ProCA32.CXCR4. T_2 time of tumor nodules on pre-scan is 92.3 ms at 24 hours after ProCA32.CXCR4 administration, the t_2 time goes back to 93.7 ms. The t_2 time change pattern of Doxorubicin treated HCC mouse is consistent with the T_2 weighted images and T_1 mapping results of the same animal.

The HCC mouse receiving combination treatment of Doxorubicin and ProAgio is different from HCC mouse with buffer treatment and HCC mouse with Doxorubicin treatment. The HCC mouse with a combination treatment of Doxorubicin and ProAgio shows no tumor nodules when compare with other treatment groups. The middle region of the liver (Figure 7.19, red circle region) has slightly higher intensity when compare with the rest, which is the fibrotic/ cirrhotic liver tissue.

The SNR analysis of this region shows no significant difference after injection of ProCA32.CXCR4. On the T_1 mapping and T_2 mapping (Figure 7.20, Figure 7.21), the cirrhotic region remained unchanged after the administration of ProCA32.CXCR4. This is a very interesting

finding because the cirrhotic region from buffer treated HCC behaves differently on MRI images followed by the same contrast agent administration. The buffered treated HCC mouse has signal enhancement after injection of ProCA32.CXCR4 but the combination treatment HCC mouse cirrhotic liver seems has ProCA32.CXCR4 delivery difference because no significant enhancement observed followed the contrast agent injection. This phenomenon might be related to the neovascular forming, followed by the ProAgio treatment. The newly formed vascular is not connecting to the existing vascular structure so ProCA32.CXCR4 is not able to deliver to the ProAgio treated mouse liver. This is causing hypo enhancement after the ProCA32.CXCR4 administration. On top of ProAgio, the Doxorubicin treatment reduced the CXCR4 expression level, which leads to the reduce of enhancement based on CXCR4 molecular imaging. Overall, due to the new vascular forming effect of ProAgio and CXCR4 expression reduction followed by

Doxorubicin treatment, the combination treatment mouse shows dim enhancement followed the administration of ProCA32.CXCR4.

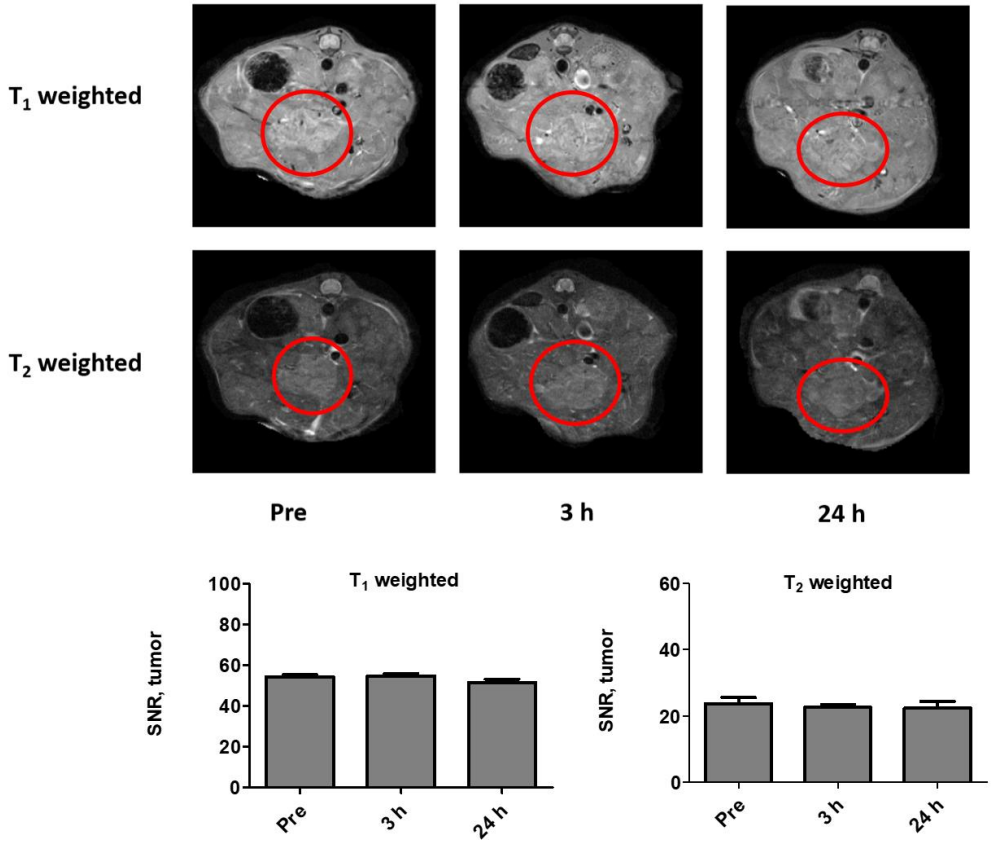

Figure 7.19 T_1, T_2 weighted MRI images and SNR of Doxorubicin and ProAgio treated HCC mouse at different time points following ProCA32.CXCR4 injection.

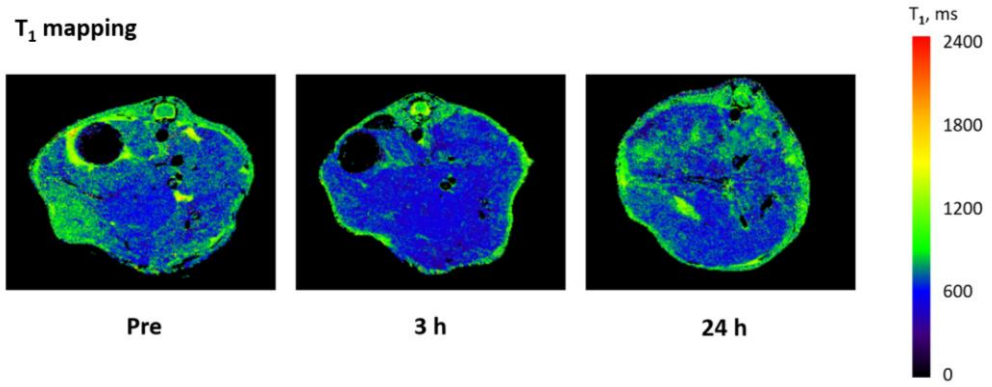

Figure 7.20 T_1 mapping MRI images and t_1 time of Doxorubicin and ProAgio treated HCC mouse at different time points follow ProCA32.CXCR4 injection.

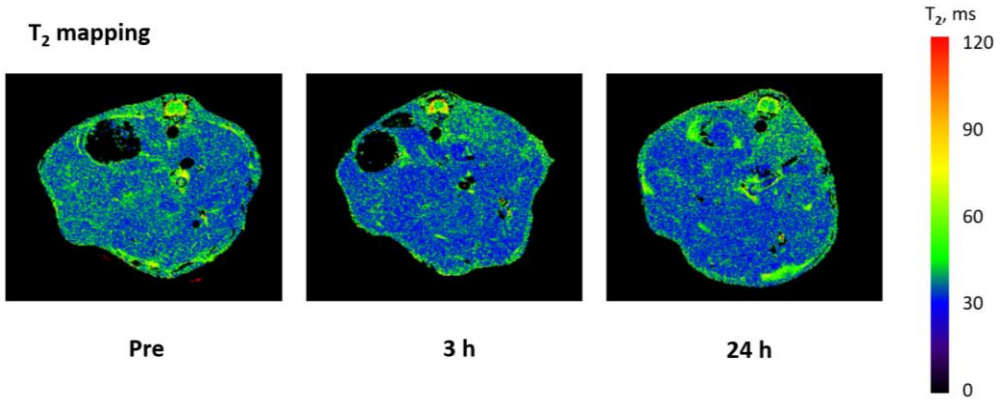

Figure 7.21 T_2 mapping MRI images and t_2 time of Doxorubicin and ProAgio treated HCC mouse at different time points following ProCA32.CXCR4 injection.

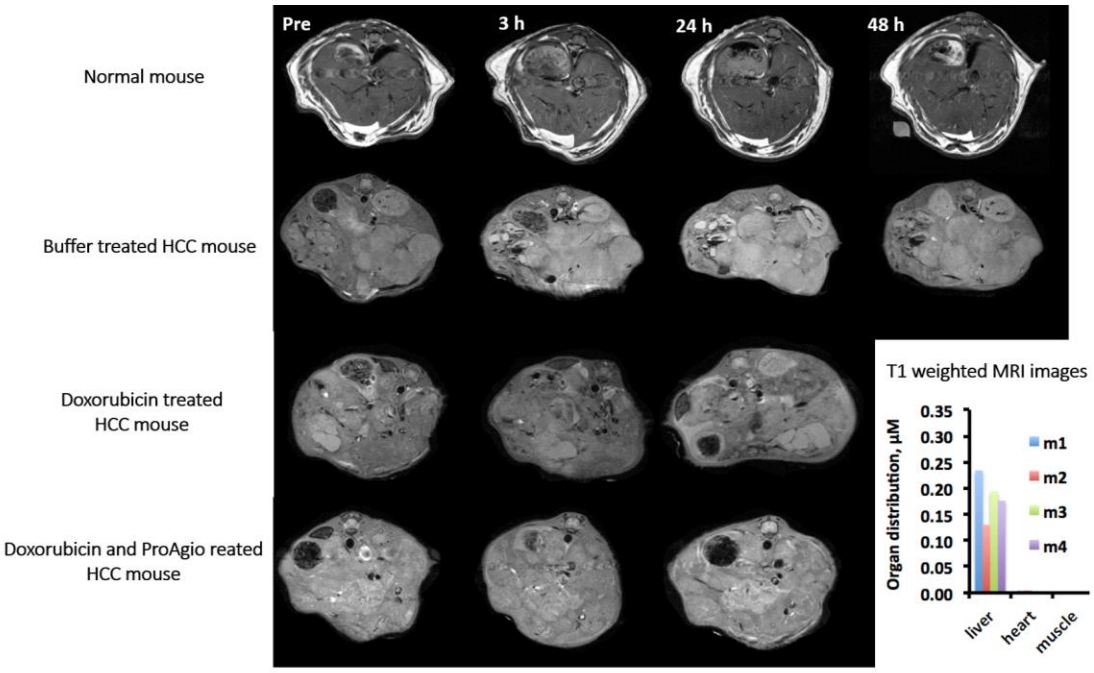

Figure 7.22 T_1 weighted images before and after injection of ProCA32.CXCR4 of HCC mice with different treatment.

Comparison of T_1 weighted images of HCC mouse with different treatment, before and after different time points of ProCA32.CXCR4 administration. Buffer treated HCC mouse shows a significant enhancement of whole liver regions, CXCR4 high expression nodules enhanced more than the rest region of liver, indicating the CXCR4 targeting effect at 24 hours after the injection of ProA32.CXCR4, which is consistent with the MR imaging results from other animal models, including uveal melanoma mouse model. Normal mouse and HCC mouse with other treatment do not show the CXCR4 targeted enhancement. ICP-OES to analysis the gadolinium content of tumor tissues confirmed the CXCR4 targeting effect of ProA32.CXCR4 and consistent with the MR images enhancement.

7.3 Discussion and conclusion

HCC is a primary liver malignancy with poor prognosis and a prevalent healthcare concern for society. Advance in imaging diagnosis already make HCC diagnosis establish based on imaging the reality. Improvement in diagnosis algorithm successfully improved the percentage of HCC patient surveillance and early detection. The introduce of Milan criteria for screening liver transplantation candidates significantly improve the success rate for HCC patients qualified for orthotopic liver transplantation. With all the advances in HCC surveillance and management, new

approaches for early detection and treatment effect evaluation using clinical imaging remains an unmet medical need.

Chemokines are considered to play an important role in HCC development for their roles in cell migration, inflammation, and immune cell recruitment. These incidences usually happen before cirrhosis forming, and chronic viral infection is a major etiology for HCC. Researchers have found that the CXCR4-CXCL12 axis involved in chronic viral hepatitis transition to liver cirrhosis and HCC. As a result, imaging targeting CXCR4 can be a new approach for HCC detection and related treatment effect monitoring.

With DEN induced HCC mouse model, we observed the elevated CXCR4 expression level, which proved by the hyperintensity T_1 weighted imaging followed by CXCR4 targeting MRI contrast agent PrOCA32.CXCR4. Owing to the high relaxivities of ProCA32.CXCR4, CXCR4 molecular imaging has been achieved in HCC tumor mice and showed elevated CXCR4 expression level in HCC mouse tumor. T_1 mapping and T_2 mapping of the same mouse has consistent result demonstrating the targeting effect at a longer time after injection of ProCA32.CXCR4 (24 hours). Within difference HCC tumor nodules, there is inconsistency regarding tumor tissue t_1 and t_2 time. However, the longitude analysis of tissue relaxation time along time points shows consistent tendency change based on CXCR4 expression level difference. For HCC mouse with buffer treatment, it has higher CXCR4 expression levels, which lead to a delayed time point after injection enhancement owing to the dynamic CXCR4 binding process. For HCC mouse with Doxorubicin treatment, it does not exhibit the same pattern of contrast enhancement at different time points, which is a result of CXCR4 level difference and molecular dynamic contrast enhancement property alteration.

Doxorubicin has limited treatment effect on HCC patients, the liver appearance of Doxorubicin treated HCC mouse has no significant improvement when compared with buffer treated HCC mouse. Interestingly, the CXCR4 molecular imaging shows the molecular dynamic enhancement property difference between the treated HCC mice and untreated ones. ICP-OES analysis of gadolinium content in HCC tumor gives the consistent result that after doxorubicin treatment, HCC tumor has lower gadolinium content when compared with the control. It is the evidence that Doxorubicin might affect the CXCR4-CXCL12 axis but no significant improvement in tumor size shrinking, etc.

CXCR4 is potentially a target for HCC treatment drug development, and CXCR4 imaging can be used for monitoring the treatment effect. ProCA32.CXCR4 achieved first CXCR4 molecular imaging to assess biomarker expression in HCC in our knowledge and is a potential tool for related treatment effect monitoring and assessment.

8 MULTICOLOR MRI BY DUAL CONTRAST ENHANCEMENT IMAGING AND INTEGRIN $\alpha_v\beta_3$ TARGETED CONTRAST AGENT

8.1 Introduction

8.1.1 Mn^{2+} based MRI contrast agents

The report of NSF and gadolinium-associated brain deposition bring about the development of safer alternative of gadolinium-based contrast agents. One approach is to replace Gd^{3+} with other paramagnetic metal ions that relax the water proton efficiently. Non-lanthanide metals have been investigated for their potential to be MRI contrast agent as alternative of gadolinium. Manganese is undoubtedly an attractive candidate for low toxicity. Unlike gadolinium, manganese is a physiologically present metal that serves as co-factor of a series of enzyme and essential to maintaining human health. Study regarding the toxicity assessment of

manganese demonstrated it as a low toxic substance (230). Although Mn^{2+} possess fewer unpaired electrons (five) when compared with gadolinium (seven), it still provides decent positive enhancement on MR imaging.

The only Mn^{2+} based contrast agent that had been proved for clinical usage was mangafodipir trisodium (Mn-DPDP), marketed under the tradename of Teslascan® in 1990. Mn-DPDP has similar T1 relaxivity (2.8 $mM^{-1}\cdot s^{-1}$) with gadolinium diethylenetriaminepentaacetic acid (4.5 $mM^{-1}\cdot s^{-1}$) in aqueous solution. However, in liver relaxivity of Mn-DPDP is 21.7 $mM^{-1}\cdot s^{-1}$, which is significantly higher than gadolinium-based contrast agents (231). Mn-DPDP does not have inner sphere water molecule and shows slow transmetallation with endogenous metal ions such as Ca^{2+}, Zn^{2+}, etc. The released manganese is uptake by hepatocytes and shows high relaxivity in liver tissue. However, due to the low sales, and concern about toxicity, Mn-DPDP withdrawn from the United States in 2003 and Europe in 2010.

Thermostability and inertness to transmetallation have to be taken into consideration when design manganese-based MRI contrast agents. Cu^{2+} and Zn^{2+} usually have a higher affinity to given ligand than Mn^{2+} in general. Ca^{2+} and Mg^{2+} have lower affinity but are present in higher concentration physiologically. Thus, although Mn^{2+} is less toxic than Gd^{3+}, the high amount of manganese exposure can still cause adverse neurological effects and Parkinson-like symptoms (232).

8.1.2 Multicolor MR imaging with dual contrast agents

Flask et al. recently reported that in the presence of two MRI contrast agents A and B, the T_1 and T_2 relaxation could be described by the following equations:

$$\frac{1}{T_1} = \frac{1}{T_{1\,pre}} + r_{1A} \times [A] + r_{1B} \times [B]$$

Equation 8.1

$$\frac{1}{T_2} = \frac{1}{T_{2\,pre}} + r_{2A} \times [A] + r_{2B} \times [B]$$

Equation 8.2

where [A] is the concentration of imaging agent A; T_{1pre} and T_{2pre} are the pre-contrast T_1 and T_2 relaxation times; T_1 and T_2 are the post-contrast T_1 and T_2 relaxation times; r_{1A} and r_{2A} are the relaxivities of contrast agent A; [B] is the concentration of contrast agent B, and r_{1B} and r_{2B} are the relaxivities of contrast agent B.

Based on these equations, we hypothesis that if T1pre, T2pre, T1, and T2 are measured before and after simultaneous injection of two different contrast agents with known relaxivities, [A] and [B] can be calculated by equation 5.1 and 5.2. Assuming these two different contrast agents have preferred sensitivity to longitudinal and transverse relaxation parameter, respectively. (e.g., a Gd^{3+}-based T_1 agent and an Mn^{2+}-based T_2 agent). The recently developed Magnetic Resonance Fingerprinting (MRF) methodology simultaneously generate inherently co-registered T_1 and T_2 relaxation time maps using a unique acquisition and quantification strategy that combines a prior acquisition parameter variation with a dictionary-based pattern matching algorithm.

Optimized MRF acquisition obtains quantitative T_1 and T_2 maps in 10–50 seconds per imaging slice, providing the possibility to dynamically generate quantitative maps of these two important MRI parameters simultaneously.

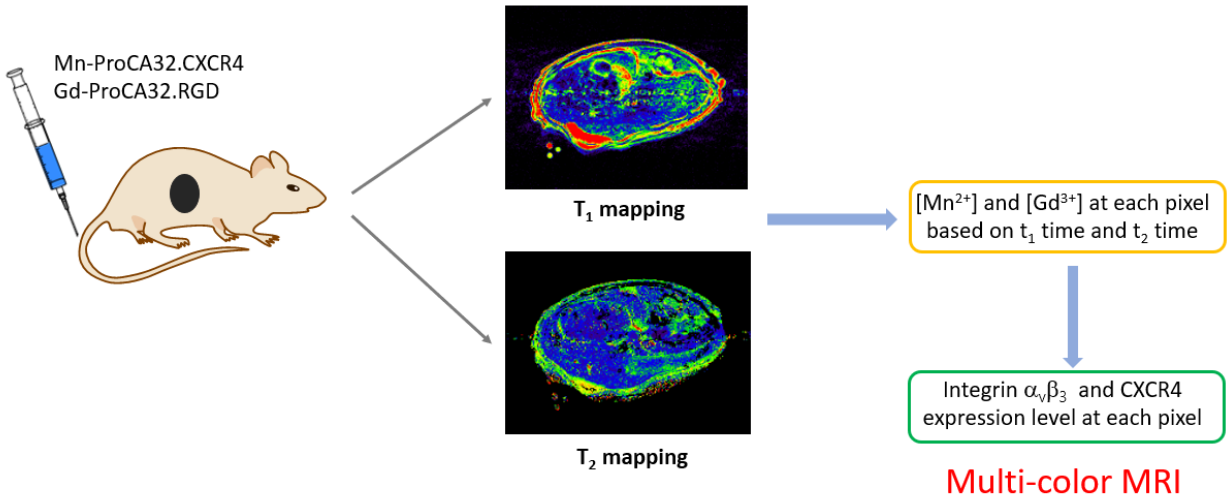

Figure 8.1 The workflow of multicolor MRI with dual contrast agent.

Based on our platform of developing protein-based contrast agents with different paramagnetic metals, and our achievement in targeted ProCAs, we reasoned that Multi-color protein MRI contrast agents targeted to biomarkers could be developed by designing several types of paramagnetic metal-binding sites into our developed ProCAs. We can further develop multi-color pMRI using multi-contrast Magnetic Resonance Fingerprinting (MRF) methodology (MC-MRF) to investigating the tumor microenvironment.

8.1.3 Integrin $\alpha_v\beta_3$

Integrins are one of the best-understood cell adhesion receptors. Integrins mediate cell adhesion, transmit a signal between the extracellular ligand with cytoplasmic domain and triggering intracellular signal pathways (233). The initial understanding of integrins' function is a cellular linkage between cells to extracellular matrix (ECM) proteins. A common integrin recognition motif shared by various extracellular matrix protein is the RGD peptide sequence (234). Integrins also mediate cell-cell adhesion with a more restricted recognition. The DXSXS

motif from the metal ion-dependent adhesion site (MIDAS) is proved to be critically important for RGD sequence binding (235), and the mutation in that site can affect ligand binding (236).

Integrin family consists of more than 24 integrins and each of them formed by a non-covalent association of two different subunits α and β. Integrins always form a heterodimer. 18 α and 8 β subunits assort with each other and form 24 distinct integrins (233) (Figure 8.2**Error! Reference source not found.**). Integrins involved in cell attachment, migration, angiogenesis and cancer formation, etc.

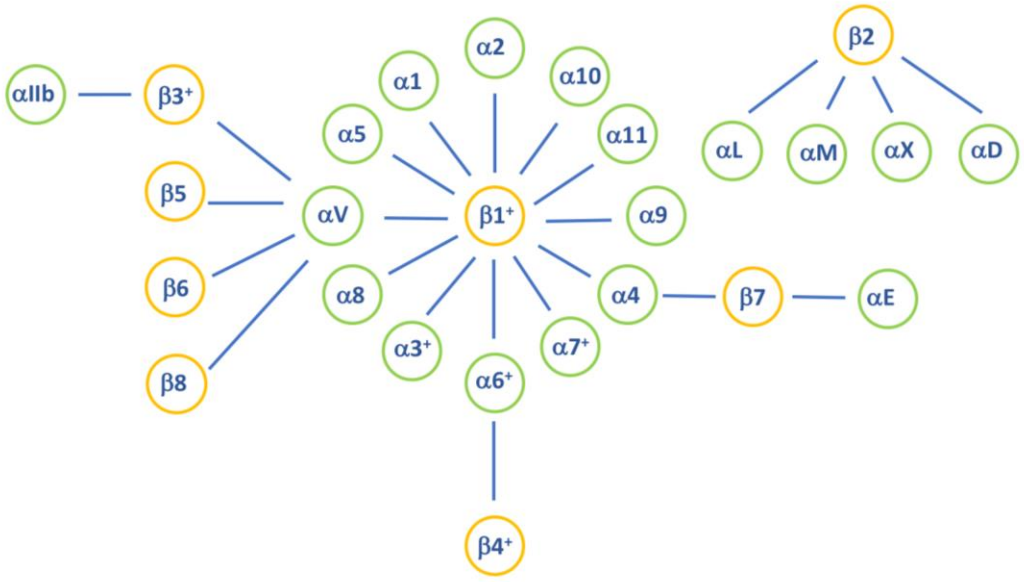

Figure 8.2 Integrin receptors.
Figure adapted from reference (233).

Angiogenesis is crucial in tumor progression. Tumor growth will be mostly limited if no neovascular formed (237). The angiogenesis can turn on the dormant tumor cell switch, promote tumor invasion, and metastasis. ECM structure degradation facilitates tumor cell invasion. As an essential cell adhesion molecule and adhesion mediator of the cell to ECM, integrins play an extremely important role in cancer development. Among a wide range of integrins, $\alpha_v\beta_3$ is the most important one in angiogenesis (238). Even more notably, $\alpha_v\beta_3$ presents on activated

endothelial cells and newly form vascular but absent on normal vasculature and resting endothelial cells. A study of wound healing revealed that $\alpha_v\beta_3$ is highly expressed on blood vessels in granulation tissue but not normal skin (238). Taken together, $\alpha_v\beta_3$ is a suitable biomarker for assessing the angiogenesis in tumors.

Breast cancer is the second most diagnosed cancer in women in the United States. Biomarker HER2 (human epidermal growth factor receptor) is a well-recognized biomarker for breast cancer staging and diagnosis and a successful example of the biomarker in cancer diagnosis and therapy. Integrin $\alpha_v\beta_3$ is related to angiogenesis and proposed as a prognostic factor for breast cancer. One study demonstrated the functional role of integrin $\alpha_v\beta_3$ in breast cancer and the association with the invasiveness of breast cancer (239); administration of monoclonal antibodies LM609 blocks the breast cancer growth and angiogenesis. As a result, $\alpha_v\beta_3$ targeted imaging can potential evaluate the angiogenesis of breast tumor and predict the invasively of breast tumor.

Attempts have been made towards $\alpha_v\beta_3$ targeted molecular imaging. An ^{18}F labeled RDG dimer peptide with PEG_4 linker has successfully achieved $\alpha_v\beta_3$ specific enhancement using PET imaging (240). A radiolabeled RGD peptide ^{99m}Tc-NC100692, which can target $\alpha_v\beta_3$ was demonstrated to enable enhancement of breast cancer malignant lesions (241). We propose a protein-based contrast agent contain the repetition of RGD sequence for $\alpha_v\beta_3$ can serve as an MRI contrast agent and imaging integrin $\alpha_v\beta_3$ non-invasively with no involvement of radiation.

8.2 Results

8.2.1 Relaxivities measurement of Mn^{2+} based ProCA32.CXCR4

The relaxivity of manganese ProCA32.CXCR4 was measured in a similar protocol as gadolinium ProCA32.CXCR4. Bivalent manganese ions and ProCA32.CXCR4 was loaded in a

2:1 ratio and both longitudinal and transverse relaxivity were measured with 1.4 T relaxometer and 7.0 T Bruker scanner. Mn-ProCA32.CXCR4 exhibits both high r_1 and r_2 relaxivities. In 1.4 T, the r_1 equals to 60.0 $mM^{-1}s^{-1}$ and r_2 equals to 133.2 $mM^{-1}s^{-1}$ (Figure 8.3). In 7.0 T, the r_1 equals to 11.9 $mM^{-1}s^{-1}$ and r_2 equals to 142.8 $mM^{-1}s^{-1}$.

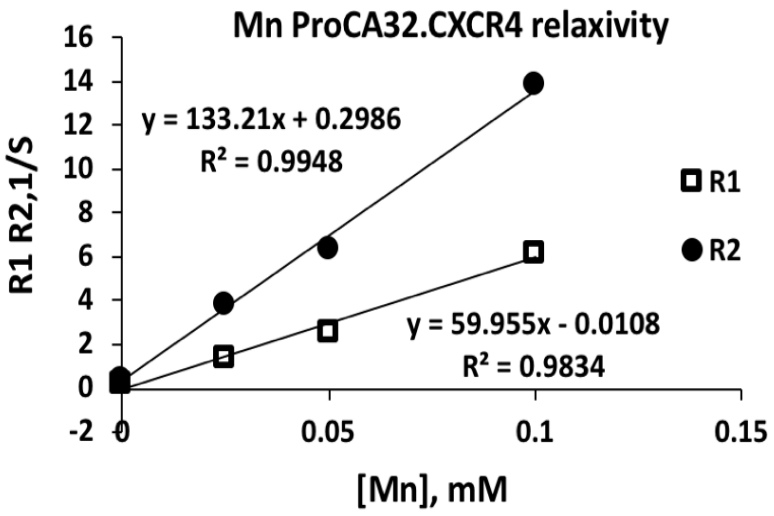

Figure 8.3 Relaxivities measurement of Mn-ProCA32.CXCR4 in 1.4 T.
The longitudinal and transverse relaxivity of Mn-ProCA32.CXCR4 was assessed with 1.4 T relaxometer. Mn^{2+} and ProCA32.CXCR4 loaded in 2:1 ratio. The r_1 equals to 60.0 $mM^{-1}s^{-1}$ and r_2 equals to 133.0 $mM^{-1}s^{-1}$. Measurements are done in buffer consists of 50 mM HEPES, 100 mM NaCl at pH 7.2, 37°C.

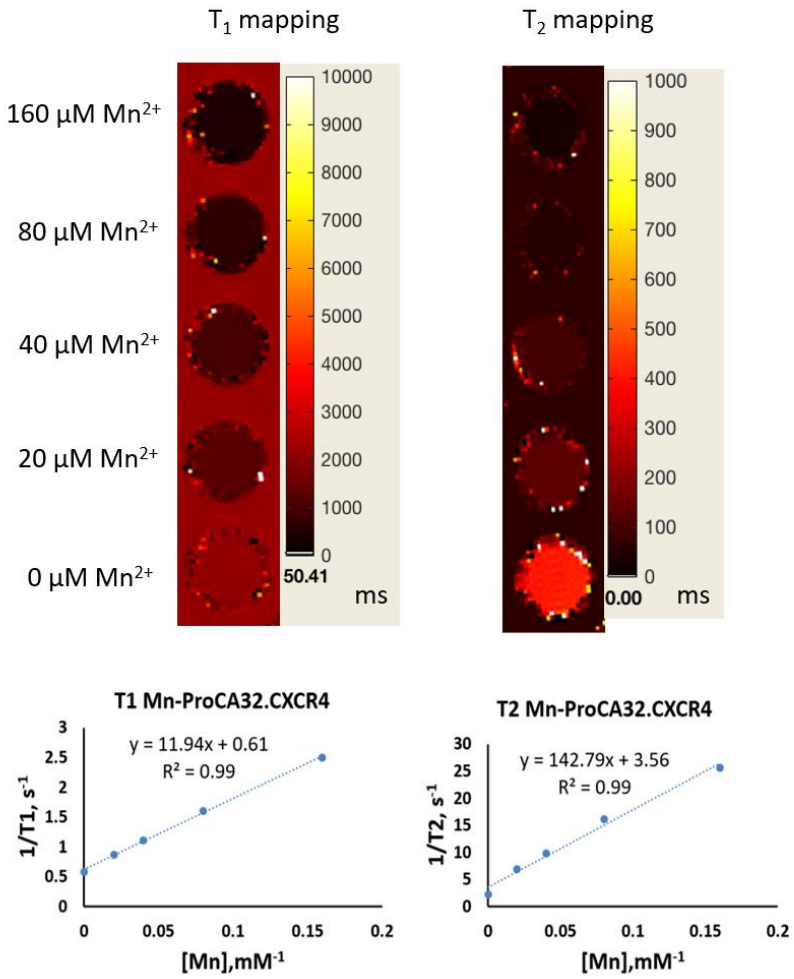

Figure 8.4 Relaxivities measurement of Mn-ProCA32.CXCR4 with 7.0 T Bruker scanner. The longitudinal and transverse relaxivity of Mn-ProCA32.CXCR4 was assessed with a 7.0 T Bruker scanner. The r_1 equals to 11.94 $mM^{-1}s^{-1}$ and r_2 equals to 142.79 $mM^{-1}s^{-1}$Measurements are done in buffer consists 50 mM HEPES, 100 mM NaCl at pH 7.2, 37°C.

The relaxation time of contrast agents' solution has a linear relationship with their relaxivities in the according magnetic field and the intrinsic relaxation time of buffer.

$$\frac{1}{T_1} = \frac{1}{T_{1\,buffer}} + r_1 \times [C]$$

Equation 8.3

$$\frac{1}{T_2} = \frac{1}{T_{2\,buffer}} + r_2 \times [C]$$

Equation 8.4

T_1, T_2 is the relaxation time of contrast agent solution, $T_{1\,\text{buffer}}$ and $T_{2\,\text{buffer}}$ are the relaxation time of buffer only. [*C*] is the concentration of contrast agent, r_1 and r_2 are the relaxivities of contrast agent.

Based on the linear relationship of relaxation time and contrast agent concentration, Christian E. Anderson et al. proposed a linear model for systems contains two contrast agents (242), the solution contains two contrast agents A and B, the relaxation time of solution is contributed by both contrast agents' relaxivities. (Equation 8.1, 8.2)

The concentration of two contrast agents can be estimated based on the longitudinal relaxation time and transverse relaxation time of solution system that contains two contrast agents if the relaxivities of contrast agents are known. (Figure 8.5) C, D shows that the estimated concentration of contrast agents and the known concentration of contrast agents has functional linear correlations.

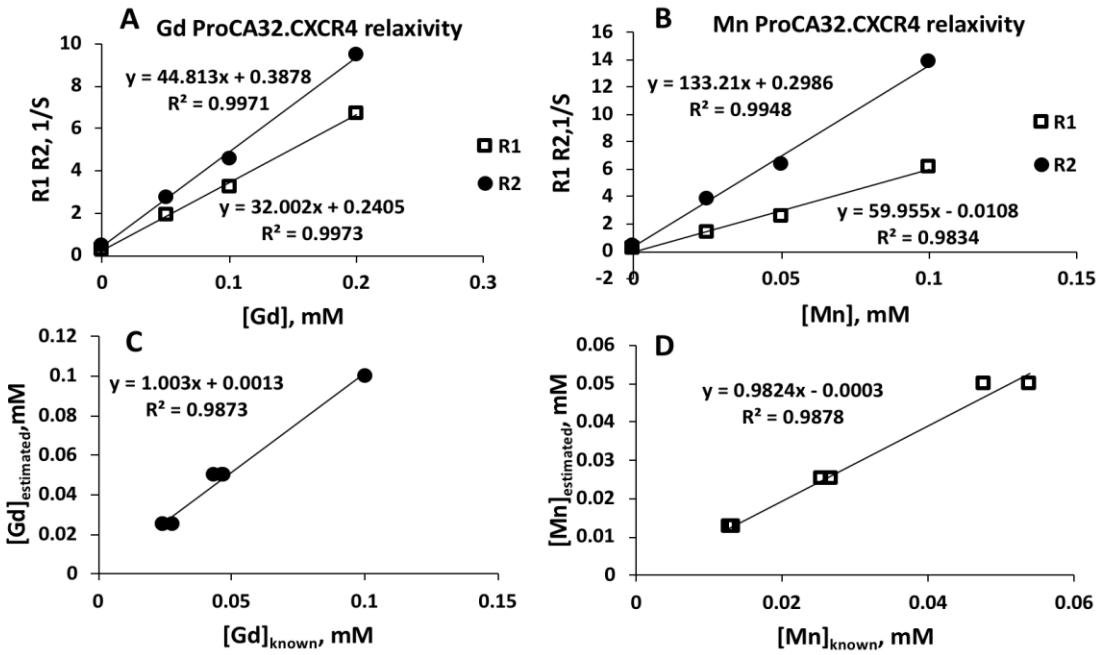

Figure 8.5 Determine the concentration contrast agents from relaxivities measurement, 1.4 T.

(**A**), (**B**). Relaxivities measurement of both Gd-ProCA32.CXCR4 and Mn-ProCA32.CXCR4 under 1.4 T. (**C**), (**D**). Correlation of known concentration and estimated concentration of Gd-ProCA32.CXCR4 and Mn-ProCA32.CXCR4 respectively.

8.2.2 Mn^{2+} binding affinity measurement of hProCA32.collagen1

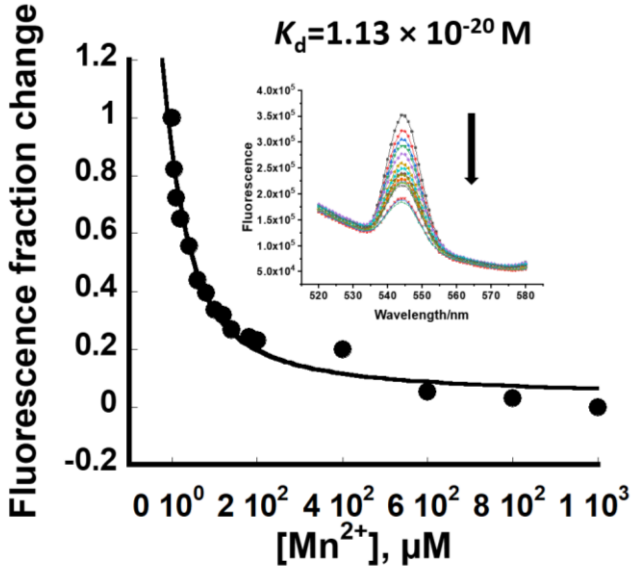

Figure 8.6 Determine the manganese binding affinity of hProCA32.collagen1.

The Manganese binding affinity of protein contrast agent is pivotally significant. By an Mn^{2+}-Tb^{3+} competition assay described in chapter 2.4.5, the K_d of Mn^{2+} binds to hProCA32.collagen1 was calculated to be 1.13×10^{-20} M (Figure 8.6).

8.2.3 Expression, purification, and characterization of ProCA32.RGD for integrin $\alpha_V\beta_3$ imaging

ProCA32.RGD was designed base on ProCA32, with the four repetitions of RDG sequence at the C terminus for Integrin $\alpha_v\beta_3$ binding. ProCA32.RGD sequence and structure are showed in Figure 8.7. ProCA32.RGD is bacterially expressed, purified follow the similar protocol of ProCA32.CXCR4 expression and purification. ProCA32.RGD expressed with competent cell *BL21 (DE3) pLysS* strain. After the 0.5 mM isopropyl β-D-1-thiogalactopyranoside induce expression, the ProCA32.RGD was successfully expressed (Figure 8.8. A).

After the expression by competent cell, the cell pellet was collected and ProCA32.RGD purification was carried out, followed the established protocol of purification described in chapter 2.2.3. Briefly, followed the overnight expression after IPTG induction, cell pellet is collected by centrifuge and resuspended in PBS buffer. Cells were broken with sonication; the supernatant was collected after centrifuge. Supernatant then boiled, incubated with streptomycin and dialyzed in 10 mM HEPES buffer for overnight. Ion exchange column was used to separate ProCA32.RGD with impurities and finish the purification of ProCA32.RGD (Figure 8.8.C).

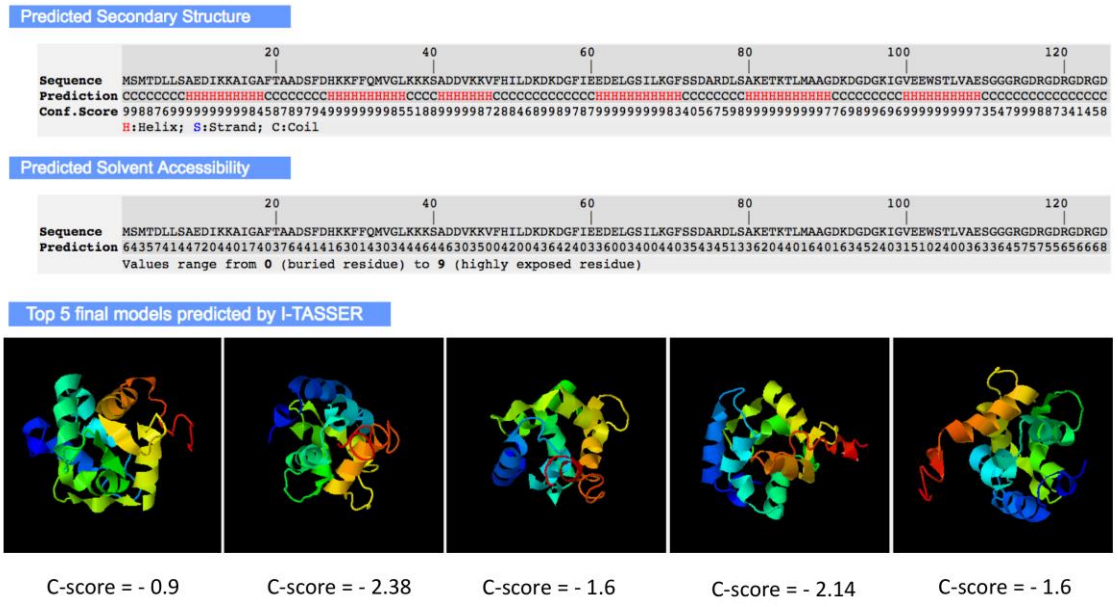

Figure 8.7 Predicted secondary structure, solvent accessibility, and models of ProCA32.RGD.

Prediction of secondary structure, solvent accessibility, and final models using I-TASSER (158). C-score is the confidence of protein model predicted by I-TASSER, which is typically in the range of [-5,2], where the higher value of C-score corresponding higher confidence of the prediction.

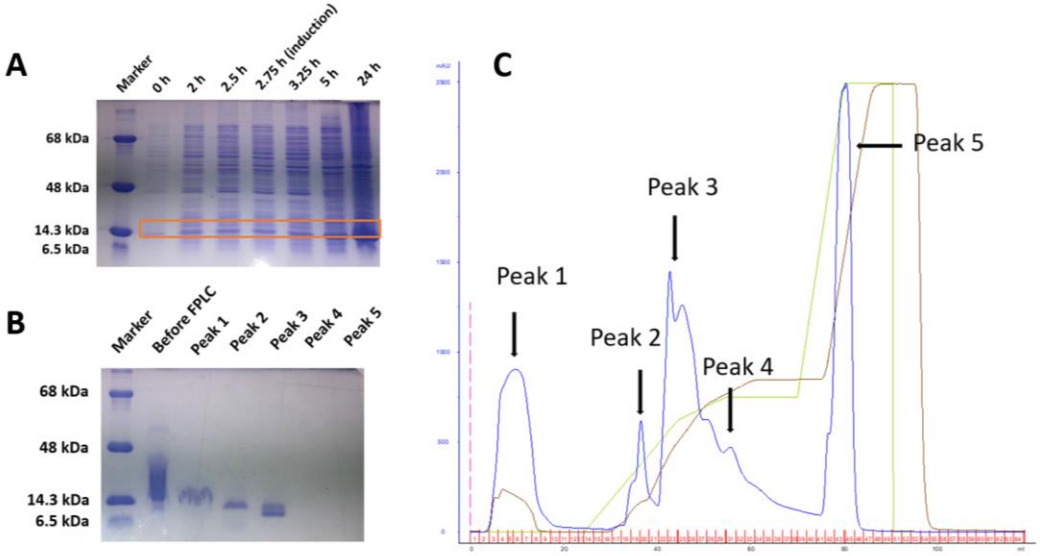

Figure 8.8 Expression and purification of ProCA32.RGD.

(**A**), (**B**) ProCA32.RGD expression and purification SDS-PAGE with Coomassie blue staining. (**A**) Cell pellet samples after different time of ProCA32.RGD expression is collected and analyzed with Coomassie blue staining, after the induction with IPTG, ProCA32.RGD was expressed,

orange box highlighted the ProCA32.RGD bands. (**C**) The FPLC spectrum of ProCA32.RGD, samples eluted from different peaks were analyzed by SDS-PAGE (**B**).

8.2.4 Relaxivities and metal-binding affinity measurement of ProCA32.RGD

Longitudinal relaxivity and transverse relaxivity of ProCA32.RGD was measured with 1.4 T relaxometer followed the standard protocol described in chapter 2.3. Different concentration of ProCA32.RGD (from 0 μM to 40 μM) were prepared in 50 mM HEPES, 100 mM NaCl, PH 7.2; in a loading ratio with gadolinium of 1:2. The longitudinal relaxivity of ProCA32.RGD is 29.2 $mM^{-1}s^{-1}$ and the transverse relaxivity of ProCA32.RGD is 40.7 $mM^{-1}s^{-1}$ under 1.4 T magnetic field (Figure 8.9). The relaxivities of ProCA32.RGD is consistent with the values of ProCA32 and ProCA32.CXCR4. All protein-based contrast agents mentioned above exhibited both high r_1 and r_2 relaxivity and enable the robust contrast enhancement in MR imaging.

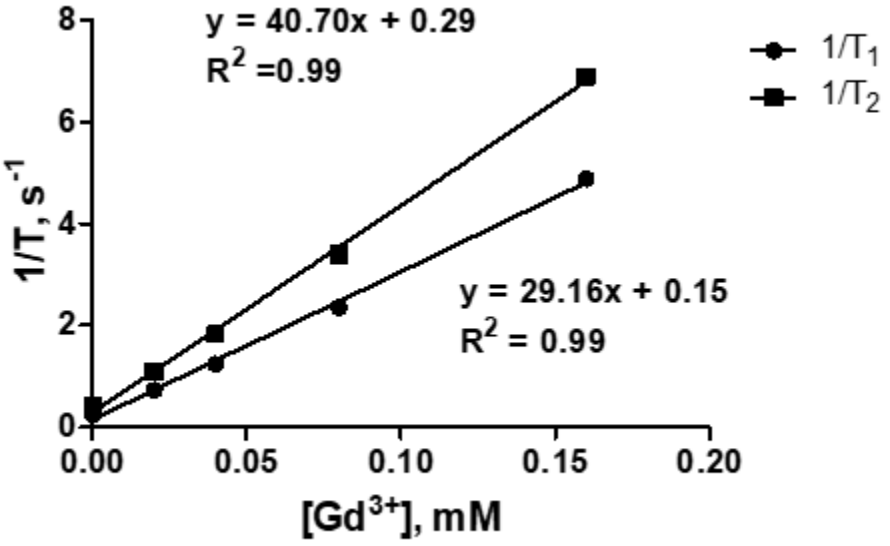

Figure 8.9 Relaxivity measurement of ProCA32.RGD.
Relaxivity assessment of ProCA32.RGD with 60 MHz relaxometer. At 1.4 T, r_1 of ProCA32.CXCR4 is 29.2 mM^{-1} s^{-1}, r_2 of ProCA32.CXCR4 is 40.7 mM^{-1} s^{-1}.

The metal-binding affinity of ProCA32.RGD was measured following the protocol described in chapter 2.4. The metal binding affinity of ProCA32.RGD to Ca^{2+}, Zn^{2+}, Tb^{3+} and Gd^{3+} were summarized in Table 8.1 Summary of the metal-binding affinity of ProCA32.RGD.. ProCA32.RGD presents high affinity to Tb^{3+}, Gd^{3+} and excellent selectivity of Gd^{3+} over Ca^{2+} and Zn^{2+}. The high metal binding affinity and good selectivity of Gd^{3+} over physiologically present metals such as Zn^{2+} and Ca^{2+} of ProCA32.RGD provided the foundation to be a contrast agent with robust imaging capacity.

Table 8.1 Summary of the metal-binding affinity of ProCA32.RGD.

Contrast agent	ProCA32.RGD
K_d (Ca^{2+}) (M)	$1.55 \pm 0.1 \times 10^{-8}$
K_d (Zn^{2+}) (M)	$1.4 \pm 1 \times 10^{-6}$
K_d (Tb^{3+}) (M)	$2.3 \pm 0.2 \times 10^{-21}$
K_d (Gd^{3+}) (M)	$3.4 \pm 0.76 \times 10^{-21}$

Data from Dr. Yueshuang Leng.

8.2.5 Integrin $\alpha_v\beta_3$ targeting study of ProCA32.RGD

ProCA32.RGD was designed as Integrin $\alpha_v\beta_3$ targeting contrast agent for integrin $\alpha_v\beta_3$ targeted molecular MR imaging application. The integrin $\alpha_v\beta_3$ targeting capability of ProCA32.RGD was assessed by immunofluorescence staining and cell attachment assay. Immunofluorescence staining of ProCA32.RGD was carried out with human umbilical vein endothelial cells (HUVECs). HUVECs have high expression level of $\alpha_v\beta_3$. With same concentration incubation (5 μM) of ProCA32 and ProCA32.RGD, HUVECs with non-targeted contrast agent ProCA32 incubation shows no fluorescence on the cell surface and HUVECs with

integrin $\alpha_v\beta_3$ targeted contrast agent ProCA32.RGD incubation show strong red fluorescence on the cell surface. Which proved that ProCA32.RGD interacts and targets integrin $\alpha_v\beta_3$.

Cell attachment experiment was carried out to test the specific binding of ProCA32.RGD to integrin $\alpha_v\beta_3$. There are over 28 different kinds of integrins in the big integrin family. The specific binding of ProCA32.RGD to integrin $\alpha_v\beta_3$ will facilitate integrin $\alpha_v\beta_3$ specific imaging. Chinese hamster ovary (CHO) cells transfected with different kinds of integrins, including $\alpha_v\beta_3$, $\alpha_{IIb}\beta_3$, $\alpha_v\beta_5$, and $\alpha_v\beta_6$ were used for cell attachment study. Results of cell attachment study (Figure 8.10) show that CHO cells with integrin $\alpha_v\beta_3$ expression has a significantly higher attachment to ProCA32.RGD than CHO cells expresses no integrin and other integrins including $\alpha_v\beta_3$, $\alpha_{IIb}\beta_3$, $\alpha_v\beta_5$, and $\alpha_v\beta_6$. Cell attachment study demonstrated the specific targeting of ProCA32.RGD to integrin $\alpha_v\beta_3$.

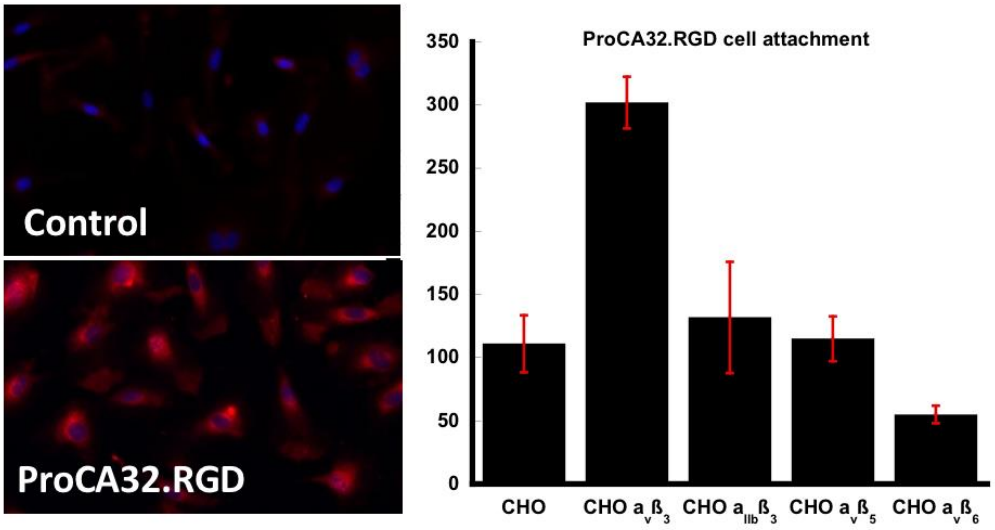

Figure 8.10 Integrin $\alpha_v\beta_3$ targeting study of ProCA32.RGD.
HUVEC cell with integrin $\alpha_v\beta_3$ expression was used for immunofluorescence staining to test the integrin $\alpha_v\beta_3$ targeting capability of ProCA32.RGD. HUVEC cells with ProCA32 incubation (control) shows rare red color fluorescence on the cell surface. HUVEC cells with ProCA32.RGD incubation exhibit strong fluorescence staining on the cell surface that indicates the presence of

ProCA32.RGD. CHO cells with different transfection of integrins ($\alpha_v\beta_3$, $\alpha_{IIb}\beta_3$, $\alpha_v\beta_5$, $\alpha_v\beta_6$) were incubated with ProCA32.RGD to test the specific binding of ProCA32.RGD. CHO cell with $\alpha_v\beta_3$ expression shows significantly higher cell attachment than CHO cell with other integrins expression and control.

8.2.6 Application of ProCA32.RGD for breast cancer and metastases detection

Orthotopic breast cancer mouse model derived from the 4T1*luc* cell was used for testing the imaging capability of ProCA32.CXCR4. The 4T1 cell was stably transfected with firefly luciferases and an aliquot of 5×10^4 cells injected orthotopically in the mouse breasts. Orthotopic breast tumors formed after 10 to 14 days of the injection of 4T1*luc* cells.

Before MR imaging, 4T1*luc* mice were injected with luciferase substrate (D-luciferin, Free Acid, ThermoFisher) and imaged by a bioluminescence system to visualize the location of tumor and potential metastases formed. After 10 min of D-luciferin injection, 4T1*luc* mice start to show the bioluminescence enhancement around the breast, mouse located in the right side shows enhancement gradually around kidneys, indicating there are potentially kidney metastases forming in that mouse. Bioluminescence imaging was taken every five minutes after 10 min; the highest luminescence enhancement showed around 25 to 30 min after injection of luciferase substrate (Figure 8.11).

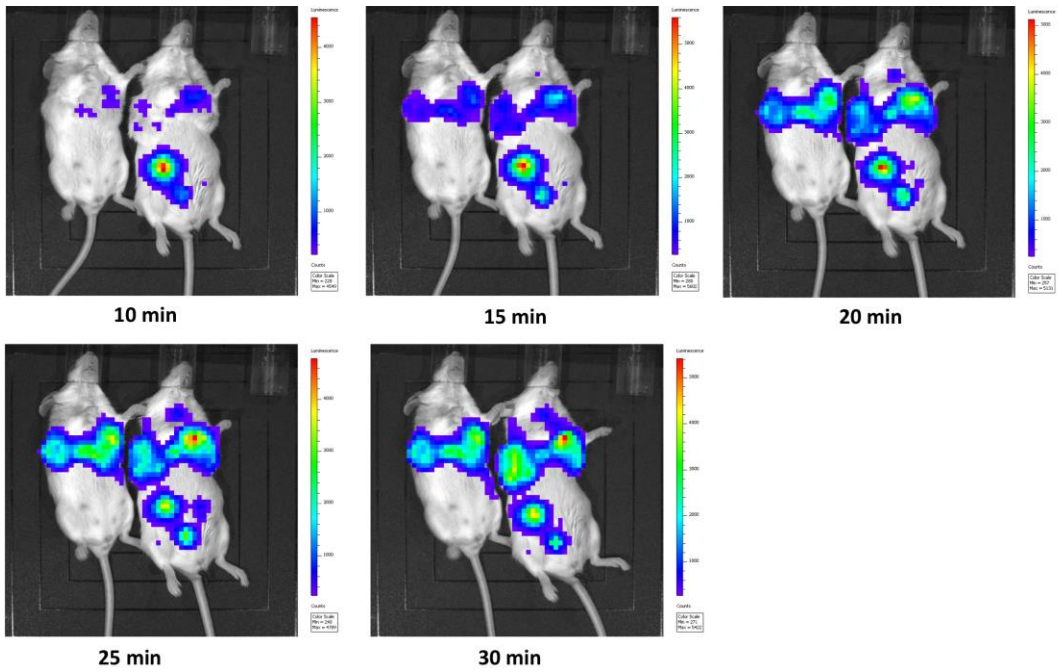

Figure 8.11 Bioluminescence imaging of 4T1*luc* mouse model.
Bioluminescence imaging of 4T1*luc* breast cancer mice after different time of injection of luciferase substrate (D-luciferin, Free Acid, ThermoFisher).

T_1 weighted, T_2 weighted, and T_2 mapping images of 4T1*luc* mice were collected by 7.0 T Bruker scanner (Figure 8.12, Figure 8.13). The signal-noise ratio analysis of tumor on T_1 weighted images shows that: before injection of ProCA32.RGD, the SNR of the tumor is 14.3, similar to the liver SNR; after the injection of ProCA32.RGD, the SNR of the tumor keep increasing up to 50 min after injection. At 24 hours after injection of ProCA32.RGD, the SNR decreases to a similar level to the pre-scanning.

ProCA32.RGD has both high r_1 and high r_2 values; the T_2 weighted images shows a similar enhancement pattern as T_1 weighted images. After the injection of ProCA32.RGD, the SNR on T_2 weighted image decrease when compared with pre-scan. SNR of the tumor on T2 weighted images keep decreasing up to 40 min after injection and after 24 hours, the contrast effect washed out, and the tumor SNR recovered back to the pre-scan level.

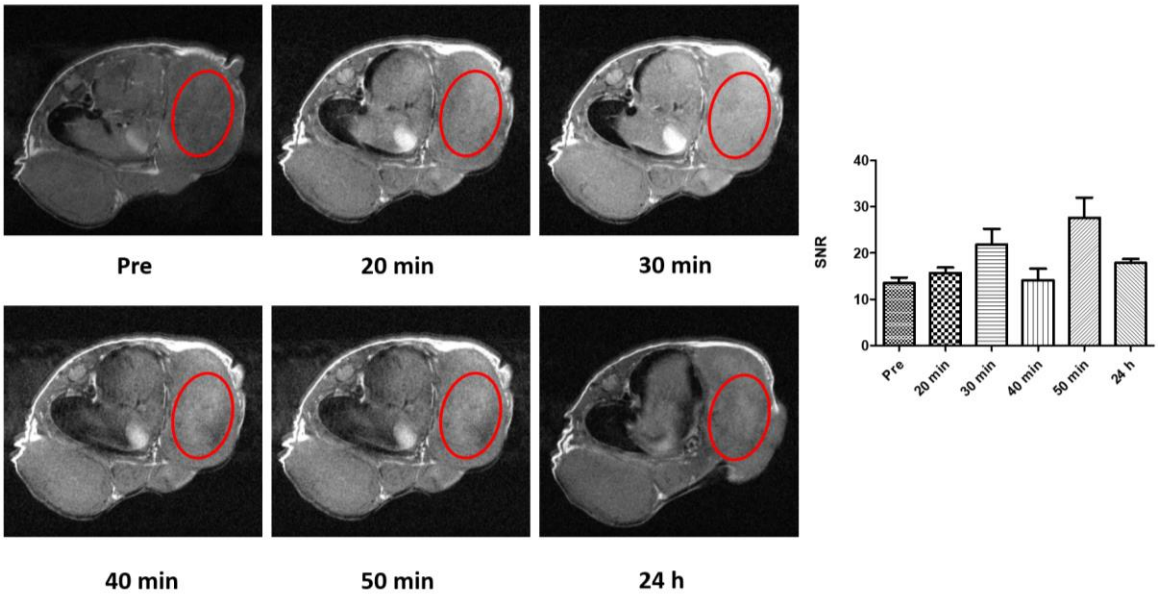

Figure 8.12 T_1 weighted MR images of 4T1*luc* breast cancer mouse.
T_1 weighted MR images of 4T1*luc* breast cancer mice were collected before and 20, 30, 40, 50 min and 24 hours after injection of ProCA32.RGD. SNR of breast tumors (represented by red circled regions) increase after the administration of ProCA32.RGD, the enhancement keeps accumulating up to 50 min. The SNR decreased after 24 hours of administration.

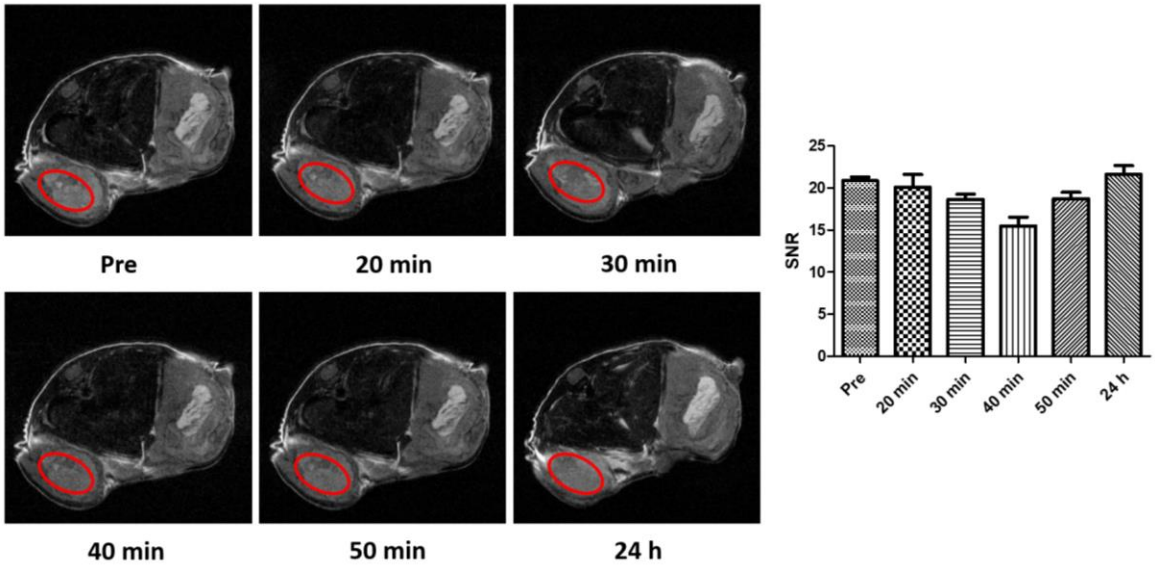

Figure 8.13 T_2 weighted MR images of 4T1*luc* breast cancer mouse.
T_2 weighted MR images of 4T1*luc* breast cancer mouse were collected before and after 20, 30, 40, 50 min and 24 hours after the administration of ProCA32.RGD. SNR of T_2 weighted MR images (represented by red circled regions) was keep decrease up to 50 min after ProCA32.RGD administration and washed out after 24 hours after administration.

8.3 Conclusion and discussion

In this chapter, we discussed the potential application of protein-based contrast agents platform technique using other magnetic metals than gadolinium. We investigated the manganese-based contrast agent specifically using CXCR4 targeted protein contrast agent ProCA32.CXCR4.

The relaxivities (both r_1 and r_2) of ProCA32.CXCR4 under 1.4 T and 7.0 T magnetic field are investigated, respectively. The r_1 of Mn-ProCA32.CXCR4 equals to 60.0 $mM^{-1}s^{-1}$ and r_2 equals to 133.2 $mM^{-1}s^{-1}$ at 1.4 T. The r_1 and r_2 of Mn-ProCA32.CXCR4 are 11.9 $mM^{-1}s^{-1}$ and 142.8 $mM^{-1}s^{-1}$, respectively. Manganese based protein contrast agent shows both high r_1 and r_2 relaxivities under 1.4 T. At 7.0 T, the r_1 decreased when compared with 1.4 T, but r_2 is highly reserved. As oppose to Gd-ProCA32.CXCR4, Mn-ProCA32.CXCR4 has a dominant effect on transverse relaxivity than longitudinal relaxivity. The r_1 / r_2 of Gd-ProCA32.CXCR4 and Mn-ProCA32.CXCR4 are different and suitable for application of multicolor MR imaging *in vivo.* Besides the relaxivity advantage of Mn^{2+} based protein contrast agents, we proved that the binding affinity of Mn^{2+} to hProCA32.collagen1 is strong enough to prevent potential Mn^{2+} associated toxicity.

The correlation of estimated contrast agents' concentration calculated using equation 5.1 and 5.2 and relaxation time measurement of Gd-ProCA32.CXCR4 and Mn-ProCA32.CXCR4 mixture with the known concentration of Gd-ProCA32.CXCR4 and Mn-ProCA32.CXCR4 has a linear relationship. It is the *in vitro* validation of MRF and dual contrast agent application. Further, *in vivo* experiment, including initial liver perfusion and live animal study are needed to be performed to establish the MRF approach with protein contrast agent platform technique.

Integrin $\alpha_v\beta_3$ targeted contrast agent ProCA32.RGD was developed and characterized. ProCA32.RGD has high relaxivities (r1 = 29.2 mM^{-1} s^{-1}, r2 = 40.7 mM^{-1} s^{-1}, 1.4 T), high metal

binding affinity and good metal selectivity over physiologically present metal ions such as Zn^{2+} and Ca^{2+}.

The imaging capacity of ProCA32.RGD was tested in 4T1*luc* breast cancer mice. Non-PEGylated ProCA32.RGD was used for animal experiment. Since the molecular weight of the non-PEGylated contrast agent is smaller than the PEGylated one. The corresponding pharmacokinetics and pharmacodynamics properties are expected to be different from the PEGylated agents. MR images acquired before and 20 min, 30 min, 40 min, 50 min, and 24 hours after injection. SNR of breast tumor significantly increased after administration of ProCA32.RGD, at 50 min after injection, the enhancement of intensity reaches the peak and washout effect observed at 24 hours after injection. Similar patterns observed on T2 weighted MR images, SNR decrease after administration of ProCA32.RGD up to 50 min after injection and the wash out effect and SNR increase observed after.

Application of ProCA32.RGD in breast cancer detection is an initiative of studying *in vivo* application of integrin $\alpha_v\beta_3$ targeted contrast agent. Non-PEGylated ProCA32.RGD was used in the animal experiment and successfully enhance tumor for the first time. Non-PEGylated ProCA32.RGD enhance the tumor at earlier points. However, the enhancement pattern of PEGylated and non-PEGylated ProCA32.RGD need to be compared, and pharmacokinetics difference of these two agents need to be studied before a solid conclusion can be reached.

9 SIGNIFICANCE AND FUTURE DIRECTION

Molecular imaging is aiming at revealing the molecular and cellular level information regarding diseases in a non-invasive way. The development of technology enables achieving molecular imaging through a variety of imaging platforms. PET and SPECT are the imaging

modalities that researchers focused on most to achieve molecular imaging for their high sensitivity. Most of the achievement of molecular imaging has been done with nuclear medicine approaches involving radiation.

The standard care of cancers has been evolved and improved over the past decades and primarily improved the life quality of cancer patients as well as extended the survival life span of cancer patients. A considerable effort has been made toward the development of novel therapeutic approaches for cancers. This brings the medical needs of advanced imaging techniques for characterization of diseased region repeatedly and safely for cancer early diagnosis and during the follow up of disease progression. Therefore, MRI becomes an attractive alternative approach for the non-radiation involvement and no-depth limitation.

The biggest challenge to achieve molecular MRI is the relatively low sensitivity of current contrast agents for clinical usage. The average r_1 value of gadolinium-based contrast agents is between 3-5 $mM^{-1}s^{-1}$. As a result, in order to achieve molecular imaging of biomarkers using contrast agents with such relaxivity requires the local concentration of contrast agents to be mM range. However, the concern of the toxicity of gadolinium-based contrast agents restrained the high dosage applications. How to balance the dosage of gadolinium contrast agents to maximize imaging capacity and minimize toxicity remains a difficulty in gadolinium contrast agents' development. Another challenge of achieving molecular imaging is lacking contrast agents with biomarker targeting capability. The development of biomarker targeting contrast agent with improved relaxivities is expected to resolve the problem.

Taken safety, enhance capacity together, the good strategy of designing MRI contrast agents for molecular imaging of specific biomarkers should consider improving the relaxivity, gadolinium binding affinity, and metal selectivity over physiologically existing metals. Besides,

constructing a structure that targeting keys biomarkers plays an essential role in disease development is a necessity of achieving biomarker molecular MRI.

The criteria for screening a good biomarker for molecular imaging should include location, disease relevance, therapeutic value. More specifically, biomarkers located at extracellular compartment are easier to access; the biomarkers can predict the cancer progression with their expression level and help the staging of cancer are of better disease relevance; the biomarkers are therapeutic targets and responsive to treatment have better therapeutic value. In this dissertation, we first verified CXCR4 as a good biomarker for uveal melanoma detection. Our rationale of study CXCR4 based on following facts: CXCR4 is by far the most common chemokine receptor expressed by cancers and over 23 different kinds of cancers express CXCR4; CXCR4-CXCL12 axis directs the cancer metastasis; CXCR4 considered as an adverse prognostic factor and therapeutic targets for cancer-related therapies. Based on the fact that uveal melanoma almost exclusively metastases to the liver, we studied the CXCR4 expression with cell line, tissue, and mice models. The role of CXCR4 in uveal melanoma development and the value of CXCR4 in uveal melanoma is controversial according to the previous researches from different groups. We evaluated the CXCR4 expression levels of different metastatic uveal melanoma cells and metastases UM in patients' livers. CXCR4 is generally over-expressed throughout the cell lines and UM metastases in livers. Metastatic mouse model study shows the CXCR4 expression levels of UM metastases in liver elevated even the primary UM in the eye are of low to medium CXCR4 expression. These results validated the high expression level of CXCR4 in UM metastases in the liver, and CXCR4 is a potential biomarker for UM metastases imaging. The overexpression of CXCR4 is observed in UM metastases. We are the first to systematically studied and established a biomarker to trace and image the UM metastases in the liver. In the future, the pathological role

of CXCR4 in UM metastases will be further studied and investigated. Multiple cancer immunotherapies target CXCR4 are under investigation and proved to be beneficial for UM metastases management. The CXCR4 molecular imaging will be beneficial for treatment planning and effect monitoring of UM patients with liver metastases involvement.

CXCR4 imaging agents that able to detect cancers are previously reported by researchers. Most of them are PET or SPECT agents. We are devoting in develop CXCR4 targeted MRI contrast agent to achieve CXCR4 molecular imaging without radiation and better safety profile. We successfully developed the CXCR4 targeted contrast agent ProCA32.CXCR4 for molecular imaging with MRI. ProCA32.CXCR4 is expressed and purified with high yield. The metal binding affinities, relaxivities, thermokinetic stability, transmetallation, and toxicity of ProCA32.CXCR4 are extensively studied and evaluated. ProCA32.CXCR4 has high gadolinium binding affinity, good metal selectivity over physiologically present metal ions such as calcium and zinc. The good gadolinium binding affinity and metal selectivity make ProCA32.CXCR4 a safe contrast agent for translational usage. ProCA32.CXCR4 possess bulkier structure than the small chelator contrast agents and inner-sphere water and outer sphere water that boost the relaxivities. Taken together, ProCA32.CXCR4 is a safe MRI contrast agent with significantly improved relaxivity. CXCR4 targeting capability of ProCA32.CXCR4 is proved by immunofluorescence cell lines study and indirect ELISA. ProCA32.CXCR4 possess significantly improved relaxivities and CXCR4 targeting capability, which enables imaging the small uveal melanoma metastases in mice livers and showing heterogeneity enhancement of UM tumor lesions owing to the good permeability. CXCR4 molecular imaging with ProCA32.CXCR4 significantly improved the current detection limit for liver lesions (1-2 cm). With ProCA32.CXCR4 administration, metastatic UM lesions range from 0.01 mm^2 to 0.08 mm^2 were enhanced and detected.

Administration of ProCA32.CXCR4 achieved detection of liver metastases using molecular dynamic contrast imaging by MRI. In the Mel290 murine model, intensity changes over time exhibited different patterns in liver metastases than in adjacent liver tissue. Tumor region intensity steadily increased up to 24 h after ProCA32.CXCR4 injection due to *in vivo* dynamic binding to CXCR4, followed by a slow wash out after 24 h to 48 h. We measured a transient increase (at 12 min) immediately after ProCA32 injection due to *in vivo* distribution, with subsequent wash out after 3 h. Similar enhancement patterns were observed in the liver regions of mice injected with both ProCA32.CXCR4 and ProCA32. This unique property of ProCA32.CXCR4 provides a possibility of acquiring molecular dynamic contrast imaging using MRI. MDCI provides an additional avenue to non-invasively differentiate tumors from healthy livers by taking advantage of biomarker binding capabilities. In this study, we also demonstrated ProCA32.CXCR4 exhibits excellent tumor permeability, which is very different from most nanoparticles or chelator-based targeting contrast agents that mostly enhance the tumor boundary. This property allows for mapping heterogeneous CXCR4 expression inside the tumor and may facilitate monitoring of changes in CXCR4 expression through the tumor tissue during progression and treatment.

The CXCR4 molecular imaging with MRI is successfully achieved with UM mice models. In the future, ProCA32.CXCR4 is planned to be tested in the larger animals such as canine and primate to verify the imaging capability and study the dosage upscale for human translational usage. Pharmacokinetics study of ProCA32.CXCR4 is initiated and ProCA32.CXCR4 has a relatively longer half-life and correspondingly longer imaging window. We are going to try different modification/ PEGylation of ProCA32.CXCR4 to tune the PK/PD properties and tease out the best way for post-expression modification protein-based MRI contrast agents. Currently,

we are using lysine PEGylation (multiple sites) and cysteine PEGylation (single site) for ProCA32.CXCR4 modification. Both lysine-PEGylated and cysteine-PEGylated ProCA32.CXCR4 showed good imaging capability. Cysteine-PEGylated ProCA32.CXCR4 is preferred for now because the site-specific property and homogenous PEGylated product meet the industrial standard better. Other PEGylation approach for protein contrast agent modification is ongoing. N-terminus PEGylation can be another approach for ProCA32.CXCR4 modification.

Besides the successful application of ProA32.CXCR4 in UM liver metastases detection. We expanded our study on ProCA32.CXCR4 to the detection of primary liver cancer and treatment effect monitoring. HCC is the most common primary liver cancer, and the development of HCC is through a serious of biomedical incidences. Chronic liver diseases are major risk factors of HCC, and the surveillance of chronic liver diseases including viral infection, alcoholic and non-alcoholic fatty liver is highly suggested to monitoring the disease progresses. We tested the imaging capability of ProCA32.CXCR4 in detecting HCC with a chemical-induced murine model monitored the CXCR4 expression level changes followed by different treatment groups. The HCC in the murine model is detected by the administration of ProCA32.CXCR4 and the CXCR4 molecular imaging by ProCA32.CXCR4 can assess the CXCR4 expression level changes. Thus, the CXCR4 molecular imaging by ProCA32.CXCR4 can not only achieve cancer and metastases detection in uveal melanoma but also HCC. The value of CXCR4 molecular imaging has been proved in cancer detection and cancer treatment monitoring.

The tumor microenvironment is a complex environment supporting and facilitating tumor growth. Angiogenesis and fibrosis are played critical roles in the development of cancers. We developed contrast agents targeting other biomarkers such as collagen and integrin $\alpha_v\beta_3$ for cancer microenvironment imaging. We assessed the Non-PEGylated ProCA32.RGD in a breast cancer

murine model and the imaging property proved to be dynamic. We observed that the SNR of tumor regions increase to almost double within a one-hour time frame followed the ProCA32.RGD administration. This result suggesting the earlier time points followed contrast agent administration might of great imaging value. Instead of tracing longer time points after injection as we did with PEGylated protein contrast agents, it could be another option to use non-PEGylated protein-based contrast agents if the stability, solubility, and toxicity been thoroughly studied and verified. Thus, one future direction of the protein contrast agent development will be assessing the influence of different PEGylation on PK/PD property.

Protein-based MRI contrast agents are platform technique that highly transferable to design and engineer versatile contrast agents. By engineering different targeting peptide into ProCAs, we can design contrast agents targeting different biomarkers. CXCR4, HER2, EGFR, PSMA, and collagen targeted contrast agent has been developed and well-studied. Other contrast agents that targeting biomolecules that play an important role can be designed and develop in future research. For example, checkpoints biomarkers such as PDL-1 can be good biomarker or imaging in the future study.

Owing to the safety concern of gadolinium-based contrast agents, MRI contrast agents use other paramagnetic metals such as manganese have been studied as an alternative of gadolinium. Manganese is physiologically existing and possesses relatively high relaxivity. Mn-DPDP is a manganese-based contrast agent approved in clinical usage for liver imaging. We explored the possibility of developing a manganese-based protein MRI contrast agent in this dissertation. Mn^{2+}-ProCA32.CXCR4 was proved to be possess high relaxivity (r_1 = 11.94 $mM^{-1}s^{-1}$, r_2 = 142.79 $mM^{-1}s^{-1}$, 7.0 T), even higher than Gd^{3+}-ProCA32.CXCR4. The binding affinity of Mn^{2+} with hProCA32.collagen1 was measured with competition assay and calculated as 1.13×10^{-20} M. To

compare the gadolinium-based ProCA32.CXCR4 and manganese-based ProCA32.CXCR4, Gd-ProCA32.CXCR4 has better r_1 property and Mn-ProCA32.CXCR4 has better r_2 property. These preliminary data of manganese-based protein contrast agent is promising. In the future, we plan to further characterize the manganese-based protein contrast agents and modify the metal binding pockets of scaffold protein to accommodate better for manganese contrast agents.

One of the most challenging tasks of molecular imaging is to differentiate different cell content. Take uveal melanoma imaging with ProCA32.CXCR4 as an example, CXCR4 has expressed on the uveal melanoma cells as well as the T lymphocytes. If we can differentiate CXCR4 from different cells, we can understand better the local tumor microenvironment. Protein-based MRI contrast agents with different paramagnetic metals provide the possibility of differentiating different biomarkers by quantitative assessment of concentrations of different contrast agents. As described in chapter 8, the local concentration of two contrast agents target different biomarkers can be calculated by the T_1 and T_2 relaxation time of the tissue. The technical obstacle is how to acquire the T_1 and T_2 mapping that provides the T_1 and T_2 relaxation times at the same time. The information must be collected in a time-sensitive assay that allows analyzing the T_1 and T_2 relaxation times of same region simultaneously to calculate the local concentration of different contrast agents corresponding to the biomarker distribution. Conventionally, collecting T_1 mapping and T_2 mapping is time-consuming procedure. This technical barrier can be overcome by magnetic resonance fingerprinting (MRF) approach. MRF acquisition is expected to collect both T_1 mapping and T_2 mapping with a time-resolved, dictionary-matching fashion. Taking advantage of MRF acquisition and protein contrast agents targeting different biomarkers that based on different paramagnetic metals, we are expected to subtype different cell population, quantify, and mapping the spatial distribution of different biomarkers.

REFERENCES

1. Siegel RL, Miller KD, Jemal A. Cancer statistics, 2018. CA Cancer J Clin. 2018;68(1):7-30.

2. Mortality in the United States. 2017.

3. Andreas Eger WM. Models of epithelial–mesenchymal transition. Drug Discovery Today: Disease Models. 2005;2(1):57-63.

4. Nguyen DX, Bos PD, Massague J. Metastasis: from dissemination to organ-specific colonization. Nature reviews Cancer. 2009;9(4):274-84.

5. Hirohashi S, Kanai Y. Cell adhesion system and human cancer morphogenesis. Cancer Sci. 2003;94(7):575-81.

6. Bujko M, Kober P, Mikula M, Ligaj M, Ostrowski J, Siedlecki JA. Expression changes of cell-cell adhesion-related genes in colorectal tumors. Oncol Lett. 2015;9(6):2463-70.

7. Cho EH, Wendel M, Luttgen M, Yoshioka C, Marrinucci D, Lazar D, et al. Characterization of circulating tumor cell aggregates identified in patients with epithelial tumors. Phys Biol. 2012;9(1):016001.

8. Carlsson A, Nair VS, Luttgen MS, Keu KV, Horng G, Vasanawala M, et al. Circulating tumor microemboli diagnostics for patients with non-small-cell lung cancer. J Thorac Oncol. 2014;9(8):1111-9.

9. Folkman J. What is the evidence that tumors are angiogenesis dependent? J Natl Cancer Inst. 1990;82(1):4-6.

10. Folkman J. Tumor angiogenesis: therapeutic implications. N Engl J Med. 1971;285(21):1182-6.

11. Whiteside TL. The tumor microenvironment and its role in promoting tumor growth. Oncogene. 2008;27(45):5904-12.

12. Hodi FS, O'Day SJ, McDermott DF, Weber RW, Sosman JA, Haanen JB, et al. Improved survival with ipilimumab in patients with metastatic melanoma. N Engl J Med. 2010;363(8):711-23.

13. Scher HI, Fizazi K, Saad F, Taplin ME, Sternberg CN, Miller K, et al. Increased survival with enzalutamide in prostate cancer after chemotherapy. N Engl J Med. 2012;367(13):1187-97.

14. Tevaarwerk AJ, Gray RJ, Schneider BP, Smith ML, Wagner LI, Fetting JH, et al. Survival in patients with metastatic recurrent breast cancer after adjuvant chemotherapy: little evidence of improvement over the past 30 years. Cancer. 2013;119(6):1140-8.

15. Bernards N, Creemers GJ, Nieuwenhuijzen GA, Bosscha K, Pruijt JF, Lemmens VE. No improvement in median survival for patients with metastatic gastric cancer despite increased use of chemotherapy. Ann Oncol. 2013;24(12):3056-60.

16. Worni M, Guller U, White RR, Castleberry AW, Pietrobon R, Cerny T, et al. Modest improvement in overall survival for patients with metastatic pancreatic cancer: a trend analysis using the surveillance, epidemiology, and end results registry from 1988 to 2008. Pancreas. 2013;42(7):1157-63.

17. Pysz MA, Gambhir SS, Willmann JK. Molecular imaging: current status and emerging strategies. Clin Radiol. 2010;65(7):500-16.

18. Massoud TF, Gambhir SS. Molecular imaging in living subjects: seeing fundamental biological processes in a new light. Genes Dev. 2003;17(5):545-80.

19. [Available from: https://www.cancerresearchuk.org/about-cancer/cancer-symptoms/why-is-early-diagnosis-important.

20. Perez EA, Barrios C, Eiermann W, Toi M, Im YH, Conte P, et al. Trastuzumab Emtansine With or Without Pertuzumab Versus Trastuzumab Plus Taxane for Human Epidermal Growth Factor Receptor 2-Positive, Advanced Breast Cancer: Primary Results From the Phase III MARIANNE Study. Journal of clinical oncology : official journal of the American Society of Clinical Oncology. 2017;35(2):141-8.

21. Shepherd FA, Rodrigues Pereira J, Ciuleanu T, Tan EH, Hirsh V, Thongprasert S, et al. Erlotinib in previously treated non-small-cell lung cancer. N Engl J Med. 2005;353(2):123-32.

22. Mankoff DA. A definition of molecular imaging. Journal of nuclear medicine : official publication, Society of Nuclear Medicine. 2007;48(6):18N, 21N.

23. Zhang X, Bloch S, Akers W, Achilefu S. Near-infrared molecular probes for in vivo imaging. Curr Protoc Cytom. 2012;Chapter 12:Unit12 27.

24. Biomarkers Definitions Working G. Biomarkers and surrogate endpoints: preferred definitions and conceptual framework. Clin Pharmacol Ther. 2001;69(3):89-95.

25. Romond EH, Perez EA, Bryant J, Suman VJ, Geyer CE, Jr., Davidson NE, et al. Trastuzumab plus adjuvant chemotherapy for operable HER2-positive breast cancer. N Engl J Med. 2005;353(16):1673-84.

26. Piccart-Gebhart MJ, Procter M, Leyland-Jones B, Goldhirsch A, Untch M, Smith I, et al. Trastuzumab after adjuvant chemotherapy in HER2-positive breast cancer. N Engl J Med. 2005;353(16):1659-72.

27. Van Cutsem E, Kohne CH, Hitre E, Zaluski J, Chang Chien CR, Makhson A, et al. Cetuximab and chemotherapy as initial treatment for metastatic colorectal cancer. N Engl J Med. 2009;360(14):1408-17.

28. Strijckmans K. The isochronous cyclotron: principles and recent developments. Comput Med Imaging Graph. 2001;25(2):69-78.

29. Townsend DW. Physical principles and technology of clinical PET imaging. Ann Acad Med Singapore. 2004;33(2):133-45.

30. F. Bloch WWH, and M. Packard. The Nuclear Induction Experiment. Phys Rev. 1946;70:474.

31. E. M. Purcell HCT, and R. V. Pound. Resonance Absorption by Nuclear Magnetic Moments in a Solid. Phys Rev. 1946.

32. Damadian R. Tumor detection by nuclear magnetic resonance. Science. 1971;171(3976):1151-3.

33. Mendonca-Dias MH, Gaggelli E, Lauterbur PC. Paramagnetic contrast agents in nuclear magnetic resonance medical imaging. Seminars in nuclear medicine. 1983;13(4):364-76.

34. Weinmann HJ, Brasch RC, Press WR, Wesbey GE. Characteristics of gadolinium-DTPA complex: a potential NMR contrast agent. AJR Am J Roentgenol. 1984;142(3):619-24.

35. Caravan P. Strategies for increasing the sensitivity of gadolinium based MRI contrast agents. Chemical Society reviews. 2006;35(6):512-23.

36. Tweedle MF. Physicochemical properties of gadoteridol and other magnetic resonance contrast agents. Invest Radiol. 1992;27 Suppl 1:S2-6.

37. Gandhi SN, Brown MA, Wong JG, Aguirre DA, Sirlin CB. MR contrast agents for liver imaging: what, when, how. Radiographics. 2006;26(6):1621-36.

38. Shokrollahi H. Contrast agents for MRI. Mater Sci Eng C Mater Biol Appl. 2013;33(8):4485-97.

39. Wendland MF. Applications of manganese-enhanced magnetic resonance imaging (MEMRI) to imaging of the heart. NMR Biomed. 2004;17(8):581-94.

40. Thuen M, Berry M, Pedersen TB, Goa PE, Summerfield M, Haraldseth O, et al. Manganese-enhanced MRI of the rat visual pathway: acute neural toxicity, contrast enhancement, axon resolution, axonal transport, and clearance of Mn(2+). Journal of magnetic resonance imaging : JMRI. 2008;28(4):855-65.

41. Caravan P, Ellison JJ, McMurry TJ, Lauffer RB. Gadolinium(III) Chelates as MRI Contrast Agents: Structure, Dynamics, and Applications. Chem Rev. 1999;99(9):2293-352.

42. Ramalho J, Ramalho M. Gadolinium Deposition and Chronic Toxicity. Magn Reson Imaging Clin N Am. 2017;25(4):765-78.

43. Huckle JE, Altun E, Jay M, Semelka RC. Gadolinium Deposition in Humans: When Did We Learn That Gadolinium Was Deposited In Vivo? Invest Radiol. 2016;51(4):236-40.

44. Port M, Idee JM, Medina C, Robic C, Sabatou M, Corot C. Efficiency, thermodynamic and kinetic stability of marketed gadolinium chelates and their possible clinical consequences: a critical review. Biometals. 2008;21(4):469-90.

45. Frenzel T, Lengsfeld P, Schirmer H, Hutter J, Weinmann HJ. Stability of gadolinium-based magnetic resonance imaging contrast agents in human serum at 37 degrees C. Invest Radiol. 2008;43(12):817-28.

46. Ramalho J, Semelka RC, Ramalho M, Nunes RH, AlObaidy M, Castillo M. Gadolinium-Based Contrast Agent Accumulation and Toxicity: An Update. AJNR Am J Neuroradiol. 2016;37(7):1192-8.

47. Shin W, Gu H, Yang Y. Fast high-resolution T1 mapping using inversion-recovery Look-Locker echo-planar imaging at steady state: optimization for accuracy and reliability. Magn Reson Med. 2009;61(4):899-906.

48. Wright PJ, Mougin OE, Totman JJ, Peters AM, Brookes MJ, Coxon R, et al. Water proton T1 measurements in brain tissue at 7, 3, and 1.5T using IR-EPI, IR-TSE, and MPRAGE: results and optimization. 2008;21(1):121.

49. Bazelaire CMJd, Duhamel GD, Rofsky NM, Alsop DC. MR Imaging Relaxation Times of Abdominal and Pelvic Tissues Measured in Vivo at 3.0 T: Preliminary Results. 2004;230(3):652-9.

50. Nunn AD, Linder KE, Tweedle MF. Can receptors be imaged with MRI agents? Q J Nucl Med. 1997;41(2):155-62.

51. Matsumura A, Shibata Y, Nakagawa K, Nose T. MRI contrast enhancement by Gd-DTPA-monoclonal antibody in 9L glioma rats. Acta Neurochir Suppl (Wien). 1994;60:356-8.

52. Shahbazi-Gahrouei D, Williams M, Rizvi S, Allen BJ. In vivo studies of Gd-DTPA-monoclonal antibody and gd-porphyrins: potential magnetic resonance imaging contrast agents for melanoma. Journal of magnetic resonance imaging : JMRI. 2001;14(2):169-74.

53. Sipkins DA, Cheresh DA, Kazemi MR, Nevin LM, Bednarski MD, Li KC. Detection of tumor angiogenesis in vivo by alphaVbeta3-targeted magnetic resonance imaging. Nature medicine. 1998;4(5):623-6.

54. Powell DH, Dhubhghaill OMN, Pubanz D, Helm L, Lebedev YS, Schlaepfer W, et al. Structural and Dynamic Parameters Obtained from 17O NMR, EPR, and NMRD Studies of Monomeric and Dimeric Gd3+ Complexes of Interest in Magnetic Resonance Imaging: An

Integrated and Theoretically Self-Consistent Approach1. Journal of the American Chemical Society. 1996;118(39):9333-46.

55. Casali C, Janier M, Canet E, Obadia JF, Benderbous S, Corot C, et al. Evaluation of Gd-DOTA-labeled dextran polymer as an intravascular MR contrast agent for myocardial perfusion. Acad Radiol. 1998;5 Suppl 1:S214-8.

56. Rohrer M, Bauer H, Mintorovitch J, Requardt M, Weinmann HJ. Comparison of magnetic properties of MRI contrast media solutions at different magnetic field strengths. Invest Radiol. 2005;40(11):715-24.

57. Port M, Corot C, Raynal I, Idee JM, Dencausse A, Lancelot E, et al. Physicochemical and biological evaluation of P792, a rapid-clearance blood-pool agent for magnetic resonance imaging. Invest Radiol. 2001;36(8):445-54.

58. Fulton DA, O'Halloran M, Parker D, Senanayake K, Botta M, Aime S. Efficient relaxivity enhancement in dendritic gadolinium complexes: effective motional coupling in medium molecular weight conjugates. Chemical communications. 2005(4):474-6.

59. Flacke S, Fischer S, Scott MJ, Fuhrhop RJ, Allen JS, McLean M, et al. Novel MRI contrast agent for molecular imaging of fibrin: implications for detecting vulnerable plaques. Circulation. 2001;104(11):1280-5.

60. Winter PM, Caruthers SD, Yu X, Song SK, Chen J, Miller B, et al. Improved molecular imaging contrast agent for detection of human thrombus. Magn Reson Med. 2003;50(2):411-6.

61. Jacques V, Dumas S, Sun WC, Troughton JS, Greenfield MT, Caravan P. High-relaxivity magnetic resonance imaging contrast agents. Part 2. Optimization of inner- and second-sphere relaxivity. Invest Radiol. 2010;45(10):613-24.

62. Xue S, Qiao J, Pu F, Cameron M, Yang JJ. Design of a novel class of protein-based magnetic resonance imaging contrast agents for the molecular imaging of cancer biomarkers. Wiley interdisciplinary reviews Nanomedicine and nanobiotechnology. 2013;5(2):163-79.

63. Xue S, Yang H, Qiao J, Pu F, Jiang J, Hubbard K, et al. Protein MRI contrast agent with unprecedented metal selectivity and sensitivity for liver cancer imaging. Proceedings of the National Academy of Sciences of the United States of America. 2015;112(21):6607-12.

64. Qiao J, Xue S, Pu F, White N, Jiang J, Liu ZR, et al. Molecular imaging of EGFR/HER2 cancer biomarkers by protein MRI contrast agents. Journal of biological inorganic chemistry : JBIC : a publication of the Society of Biological Inorganic Chemistry. 2014;19(2):259-70.

65. Pu F, Salarian M, Xue S, Qiao J, Feng J, Tan S, et al. Prostate-specific membrane antigen targeted protein contrast agents for molecular imaging of prostate cancer by MRI. Nanoscale. 2016.

66. Pu F, Qiao J, Xue S, Yang H, Patel A, Wei L, et al. GRPR-targeted Protein Contrast Agents for Molecular Imaging of Receptor Expression in Cancers by MRI. Scientific reports. 2015;5:16214.

67. Clore GM, Appella E, Yamada M, Matsushima K, Gronenborn AM. Three-dimensional structure of interleukin 8 in solution. Biochemistry. 1990;29(7):1689-96.

68. Griffith JW, Sokol CL, Luster AD. Chemokines and chemokine receptors: positioning cells for host defense and immunity. Annu Rev Immunol. 2014;32:659-702.

69. Baggiolini M, Dewald B, Moser B. Human chemokines: an update. Annu Rev Immunol. 1997;15:675-705.

70. Murphy PM. The molecular biology of leukocyte chemoattractant receptors. Annu Rev Immunol. 1994;12:593-633.

71. Bachelerie F, Ben-Baruch A, Burkhardt AM, Combadiere C, Farber JM, Graham GJ, et al. International Union of Basic and Clinical Pharmacology. [corrected]. LXXXIX. Update on the extended family of chemokine receptors and introducing a new nomenclature for atypical chemokine receptors. Pharmacol Rev. 2014;66(1):1-79.

72. Groom JR, Richmond J, Murooka TT, Sorensen EW, Sung JH, Bankert K, et al. CXCR3 chemokine receptor-ligand interactions in the lymph node optimize CD4+ T helper 1 cell differentiation. Immunity. 2012;37(6):1091-103.

73. Sarmiento J, Shumate C, Suetomi K, Ravindran A, Villegas L, Rajarathnam K, et al. Diverging mechanisms of activation of chemokine receptors revealed by novel chemokine agonists. PloS one. 2011;6(12):e27967.

74. Feng Y, Broder CC, Kennedy PE, Berger EA. HIV-1 entry cofactor: functional cDNA cloning of a seven-transmembrane, G protein-coupled receptor. Science. 1996;272(5263):872-7.

75. Burns JM, Summers BC, Wang Y, Melikian A, Berahovich R, Miao Z, et al. A novel chemokine receptor for SDF-1 and I-TAC involved in cell survival, cell adhesion, and tumor development. J Exp Med. 2006;203(9):2201-13.

76. Kucia M, Jankowski K, Reca R, Wysoczynski M, Bandura L, Allendorf DJ, et al. CXCR4-SDF-1 signalling, locomotion, chemotaxis and adhesion. J Mol Histol. 2004;35(3):233-45.

77. Yu L, Cecil J, Peng SB, Schrementi J, Kovacevic S, Paul D, et al. Identification and expression of novel isoforms of human stromal cell-derived factor 1. Gene. 2006;374:174-9.

78. Zlotnik A. New insights on the role of CXCR4 in cancer metastasis. The Journal of pathology. 2008;215(3):211-3.

79. Petit I, Jin D, Rafii S. The SDF-1-CXCR4 signaling pathway: a molecular hub modulating neo-angiogenesis. Trends Immunol. 2007;28(7):299-307.

80. Springer TA. Traffic signals on endothelium for lymphocyte recirculation and leukocyte emigration. Annu Rev Physiol. 1995;57:827-72.

81. Chatterjee S, Behnam Azad B, Nimmagadda S. The intricate role of CXCR4 in cancer. Adv Cancer Res. 2014;124:31-82.

82. Bleul CC, Fuhlbrigge RC, Casasnovas JM, Aiuti A, Springer TA. A highly efficacious lymphocyte chemoattractant, stromal cell-derived factor 1 (SDF-1). J Exp Med. 1996;184(3):1101-9.

83. Murdoch C, Monk PN, Finn A. Functional expression of chemokine receptor CXCR4 on human epithelial cells. Immunology. 1999;98(1):36-41.

84. Dwinell MB, Eckmann L, Leopard JD, Varki NM, Kagnoff MF. Chemokine receptor expression by human intestinal epithelial cells. Gastroenterology. 1999;117(2):359-67.

85. Salcedo R, Wasserman K, Young HA, Grimm MC, Howard OM, Anver MR, et al. Vascular endothelial growth factor and basic fibroblast growth factor induce expression of CXCR4 on human endothelial cells: In vivo neovascularization induced by stromal-derived factor-1alpha. Am J Pathol. 1999;154(4):1125-35.

86. Juremalm M HM, Olsson N, Harvima I, Nilsson K, Nillsson G. The chemokine receptor CXCR4 is expressed within the mast cell lineage and its ligand stromal cell-derived factor-1alpha acts as a mast cell chemotaxin. Eur J Immunol. 2000.

87. Zoeteweij JP, Blauvelt A. HIV-Dendritic cell interactions promote efficient viral infection of T cells. J Biomed Sci. 1998;5(4):253-9.

88. Viola A, Luster AD. Chemokines and their receptors: drug targets in immunity and inflammation. Annu Rev Pharmacol Toxicol. 2008;48:171-97.

89. Zou YR, Kottmann AH, Kuroda M, Taniuchi I, Littman DR. Function of the chemokine receptor CXCR4 in haematopoiesis and in cerebellar development. Nature. 1998;393(6685):595-9.

90. Balkwill F. Chemokine biology in cancer. Semin Immunol. 2003;15(1):49-55.

91. Balkwill F, Mantovani A. Inflammation and cancer: back to Virchow? Lancet. 2001;357(9255):539-45.

92. Murphy PM. Chemokines and the molecular basis of cancer metastasis. N Engl J Med. 2001;345(11):833-5.

93. Balkwill F. The significance of cancer cell expression of the chemokine receptor CXCR4. Semin Cancer Biol. 2004;14(3):171-9.

94. Xu TP, Shen H, Liu LX, Shu YQ. The impact of chemokine receptor CXCR4 on breast cancer prognosis: a meta-analysis. Cancer Epidemiol. 2013;37(5):725-31.

95. Hassan S, Ferrario C, Saragovi U, Quenneville L, Gaboury L, Baccarelli A, et al. The influence of tumor-host interactions in the stromal cell-derived factor-1/CXCR4 ligand/receptor axis in determining metastatic risk in breast cancer. Am J Pathol. 2009;175(1):66-73.

96. Kang H, Watkins G, Douglas-Jones A, Mansel RE, Jiang WG. The elevated level of CXCR4 is correlated with nodal metastasis of human breast cancer. Breast. 2005;14(5):360-7.

97. Zou W, Machelon V, Coulomb-L'Hermin A, Borvak J, Nome F, Isaeva T, et al. Stromal-derived factor-1 in human tumors recruits and alters the function of plasmacytoid precursor dendritic cells. Nature medicine. 2001;7(12):1339-46.

98. Scotton CJ, Wilson JL, Scott K, Stamp G, Wilbanks GD, Fricker S, et al. Multiple actions of the chemokine CXCL12 on epithelial tumor cells in human ovarian cancer. Cancer research. 2002;62(20):5930-8.

99. Spoo AC, Lubbert M, Wierda WG, Burger JA. CXCR4 is a prognostic marker in acute myelogenous leukemia. Blood. 2007;109(2):786-91.

100. Burger JA, Peled A. CXCR4 antagonists: targeting the microenvironment in leukemia and other cancers. Leukemia. 2009;23(1):43-52.

101. Nervi B, Ramirez P, Rettig MP, Uy GL, Holt MS, Ritchey JK, et al. Chemosensitization of acute myeloid leukemia (AML) following mobilization by the CXCR4 antagonist AMD3100. Blood. 2009;113(24):6206-14.

102. Zlotnik A. Involvement of chemokine receptors in organ-specific metastasis. Contrib Microbiol. 2006;13:191-9.

103. Muller A, Homey B, Soto H, Ge N, Catron D, Buchanan ME, et al. Involvement of chemokine receptors in breast cancer metastasis. Nature. 2001;410(6824):50-6.

104. Gladson CL, Welch DR. New insights into the role of CXCR4 in prostate cancer metastasis. Cancer Biol Ther. 2008;7(11):1849-51.

105. Darash-Yahana M, Pikarsky E, Abramovitch R, Zeira E, Pal B, Karplus R, et al. Role of high expression levels of CXCR4 in tumor growth, vascularization, and metastasis. FASEB J. 2004;18(11):1240-2.

106. Fernandis AZ, Cherla RP, Chernock RD, Ganju RK. CXCR4/CCR5 down-modulation and chemotaxis are regulated by the proteasome pathway. The Journal of biological chemistry. 2002;277(20):18111-7.

107. Sun YX SA, Jung Y, Wang J, Dai J, Wang J, Cook K, Osman NI, Koh-Paige AJ, Shim H, Pienta KJ, Keller ET, McCauley LK, Taichman RS. Skeletal localization and neutralization of the SDF-1(CXCL12)/CXCR4 axis blocks prostate cancer metastasis and growth in osseous sites in vivo. J Bone Miner Res. 2005.

108. Phillips RJ, Burdick MD, Lutz M, Belperio JA, Keane MP, Strieter RM. The stromal derived factor-1/CXCL12-CXC chemokine receptor 4 biological axis in non-small cell lung cancer metastases. Am J Respir Crit Care Med. 2003;167(12):1676-86.

109. Grande F, Giancotti G, Ioele G, Occhiuzzi MA, Garofalo A. An update on small molecules targeting CXCR4 as starting points for the development of anti-cancer therapeutics. European Journal of Medicinal Chemistry. 2017;139:519-30.

110. Dotto GP, Weinberg RA, Ariza A. Malignant transformation of mouse primary keratinocytes by Harvey sarcoma virus and its modulation by surrounding normal cells. Proceedings of the National Academy of Sciences of the United States of America. 1988;85(17):6389-93.

111. Orimo A, Gupta PB, Sgroi DC, Arenzana-Seisdedos F, Delaunay T, Naeem R, et al. Stromal fibroblasts present in invasive human breast carcinomas promote tumor growth and angiogenesis through elevated SDF-1/CXCL12 secretion. Cell. 2005;121(3):335-48.

112. Hartmann TN, Burger JA, Glodek A, Fujii N, Burger M. CXCR4 chemokine receptor and integrin signaling co-operate in mediating adhesion and chemoresistance in small cell lung cancer (SCLC) cells. Oncogene. 2005;24(27):4462-71.

113. Dehghani M, Kianpour S, Zangeneh A, Mostafavi-Pour Z. CXCL12 Modulates Prostate Cancer Cell Adhesion by Altering the Levels or Activities of beta1-Containing Integrins. Int J Cell Biol. 2014;2014:981750.

114. Salvucci O, Yao L, Villalba S, Sajewicz A, Pittaluga S, Tosato G. Regulation of endothelial cell branching morphogenesis by endogenous chemokine stromal-derived factor-1. Blood. 2002;99(8):2703-11.

115. Mirshahi F, Pourtau J, Li H, Muraine M, Trochon V, Legrand E, et al. SDF-1 activity on microvascular endothelial cells: consequences on angiogenesis in in vitro and in vivo models. Thromb Res. 2000;99(6):587-94.

116. Deshane J, Chen S, Caballero S, Grochot-Przeczek A, Was H, Li Calzi S, et al. Stromal cell-derived factor 1 promotes angiogenesis via a heme oxygenase 1-dependent mechanism. J Exp Med. 2007;204(3):605-18.

117. Martin SK, Dewar AL, Farrugia AN, Horvath N, Gronthos S, To LB, et al. Tumor angiogenesis is associated with plasma levels of stromal-derived factor-1alpha in patients with multiple myeloma. Clin Cancer Res. 2006;12(23):6973-7.

118. Barbero S, Bonavia R, Bajetto A, Porcile C, Pirani P, Ravetti JL, et al. Stromal cell-derived factor 1alpha stimulates human glioblastoma cell growth through the activation of both extracellular signal-regulated kinases 1/2 and Akt. Cancer research. 2003;63(8):1969-74.

119. Thoma G, Streiff MB, Kovarik J, Glickman F, Wagner T, Beerli C, et al. Orally bioavailable isothioureas block function of the chemokine receptor CXCR4 in vitro and in vivo. Journal of medicinal chemistry. 2008;51(24):7915-20.

120. Tamamura H, Hiramatsu K, Ueda S, Wang Z, Kusano S, Terakubo S, et al. Stereoselective synthesis of [L-Arg-L/D-3-(2-naphthyl)alanine]-type (E)-alkene dipeptide isosteres and its application to the synthesis and biological evaluation of pseudopeptide analogues of the CXCR4 antagonist FC131. Journal of medicinal chemistry. 2005;48(2):380-91.

121. Ueda S, Oishi S, Wang ZX, Araki T, Tamamura H, Cluzeau J, et al. Structure-activity relationships of cyclic peptide-based chemokine receptor CXCR4 antagonists: disclosing the importance of side-chain and backbone functionalities. Journal of medicinal chemistry. 2007;50(2):192-8.

122. Zachariassen ZG, Thiele S, Berg EA, Rasmussen P, Fossen T, Rosenkilde MM, et al. Design, synthesis, and biological evaluation of scaffold-based tripeptidomimetic antagonists for CXC chemokine receptor 4 (CXCR4). Bioorg Med Chem. 2014;22(17):4759-69.

123. Vitale RM, Gatti M, Carbone M, Barbieri F, Felicita V, Gavagnin M, et al. Minimalist hybrid ligand/receptor-based pharmacophore model for CXCR4 applied to a small-library of marine natural products led to the identification of phidianidine a as a new CXCR4 ligand exhibiting antagonist activity. ACS Chem Biol. 2013;8(12):2762-70.

124. Truax VM, Zhao H, Katzman BM, Prosser AR, Alcaraz AA, Saindane MT, et al. Discovery of tetrahydroisoquinoline-based CXCR4 antagonists. ACS Med Chem Lett. 2013;4(11):1025-30.

125. Debnath B, Xu S, Grande F, Garofalo A, Neamati N. Small molecule inhibitors of CXCR4. Theranostics. 2013;3(1):47-75.

126. Vinader V, Ahmet DS, Ahmed MS, Patterson LH, Afarinkia K. Discovery and computer aided potency optimization of a novel class of small molecule CXCR4 antagonists. PloS one. 2013;8(10):e78744.

127. Kircher M, Herhaus P, Schottelius M, Buck AK, Werner RA, Wester HJ, et al. CXCR4-directed theranostics in oncology and inflammation. Ann Nucl Med. 2018;32(8):503-11.

128. Weiss ID, Jacobson O, Kiesewetter DO, Jacobus JP, Szajek LP, Chen X, et al. Positron emission tomography imaging of tumors expressing the human chemokine receptor CXCR4 in mice with the use of 64Cu-AMD3100. Mol Imaging Biol. 2012;14(1):106-14.

129. Nimmagadda S, Pullambhatla M, Stone K, Green G, Bhujwalla ZM, Pomper MG. Molecular imaging of CXCR4 receptor expression in human cancer xenografts with [64Cu]AMD3100 positron emission tomography. Cancer research. 2010;70(10):3935-44.

130. Jacobson O, Weiss ID, Szajek L, Farber JM, Kiesewetter DO. 64Cu-AMD3100--a novel imaging agent for targeting chemokine receptor CXCR4. Bioorg Med Chem. 2009;17(4):1486-93.

131. Hartimath SV, Domanska UM, Walenkamp AM, Rudi AJOD, de Vries EF. [(9)(9)mTc]O(2)-AMD3100 as a SPECT tracer for CXCR4 receptor imaging. Nucl Med Biol. 2013;40(4):507-17.

132. De Silva RA, Peyre K, Pullambhatla M, Fox JJ, Pomper MG, Nimmagadda S. Imaging CXCR4 expression in human cancer xenografts: evaluation of monocyclam 64Cu-AMD3465. Journal of nuclear medicine : official publication, Society of Nuclear Medicine. 2011;52(6):986-93.

133. George GPC, Stevens E, Åberg O, Nguyen Q-D, Pisaneschi F, Spivey AC, et al. Preclinical evaluation of a CXCR4-specific 68Ga-labelled TN14003 derivative for cancer PET imaging. Bioorganic & Medicinal Chemistry. 2014;22(2):796-803.

134. Jacobson O, Weiss ID, Kiesewetter DO, Farber JM, Chen X. PET of tumor CXCR4 expression with 4-18F-T140. Journal of nuclear medicine : official publication, Society of Nuclear Medicine. 2010;51(11):1796-804.

135. Nishizawa K, Nishiyama H, Oishi S, Tanahara N, Kotani H, Mikami Y, et al. Fluorescent imaging of high-grade bladder cancer using a specific antagonist for chemokine receptor CXCR4. Int J Cancer. 2010;127(5):1180-7.

136. Gourni E, Demmer O, Schottelius M, D'Alessandria C, Schulz S, Dijkgraaf I, et al. PET of CXCR4 expression by a (68)Ga-labeled highly specific targeted contrast agent. Journal of nuclear medicine : official publication, Society of Nuclear Medicine. 2011;52(11):1803-10.

137. Li H AH, Niederkorn JY. Differential expression of chemokine receptors on uveal melanoma cells and their metastases. Invest Ophthalmol Vis Sci. 2008.

138. Kim J, Mori T, Chen SL, Amersi FF, Martinez SR, Kuo C, et al. Chemokine receptor CXCR4 expression in patients with melanoma and colorectal cancer liver metastases and the association with disease outcome. Ann Surg. 2006;244(1):113-20.

139. Dobner BC RA, Joussen AM, Englert S, Bechrakis NE. Expression of haematogenous and lymphogenous chemokine receptors and their ligands on uveal melanoma in association with liver metastasis. Acta Ophthalmol. 2012.

140. Li H, Yang W, Chen PW, Alizadeh H, Niederkorn JY. Inhibition of chemokine receptor expression on uveal melanomas by CXCR4 siRNA and its effect on uveal melanoma liver metastases. Invest Ophthalmol Vis Sci. 2009;50(12):5522-8.

141. Franco R, Botti G, Mascolo M, Loquercio G, Liguori G, Ilardi G, et al. "CXCR4-CXCL12 and VEGF correlate to uveal melanoma progression". Front Biosci (Elite Ed). 2010;2:13-21.

142. Schimanski CC, Bahre R, Gockel I, Muller A, Frerichs K, Horner V, et al. Dissemination of hepatocellular carcinoma is mediated via chemokine receptor CXCR4. Br J Cancer. 2006;95(2):210-7.

143. Li W, Gomez E, Zhang Z. Immunohistochemical expression of stromal cell-derived factor-1 (SDF-1) and CXCR4 ligand receptor system in hepatocellular carcinoma. J Exp Clin Cancer Res. 2007;26(4):527-33.

144. Chu H, Zhou H, Liu Y, Liu X, Hu Y, Zhang J. Functional expression of CXC chemokine recepter-4 mediates the secretion of matrix metalloproteinases from mouse hepatocarcinoma cell lines with different lymphatic metastasis ability. Int J Biochem Cell Biol. 2007;39(1):197-205.

145. Xiang ZL, Zeng ZC, Tang ZY, Fan J, Zhuang PY, Liang Y, et al. Chemokine receptor CXCR4 expression in hepatocellular carcinoma patients increases the risk of bone metastases and poor survival. BMC Cancer. 2009;9:176.

146. Chen Y, Huang Y, Reiberger T, Duyverman AM, Huang P, Samuel R, et al. Differential effects of sorafenib on liver versus tumor fibrosis mediated by stromal-derived factor 1 alpha/C-X-C receptor type 4 axis and myeloid differentiation antigen-positive myeloid cell infiltration in mice. Hepatology. 2014;59(4):1435-47.

147. Grynkiewicz G, Poenie M, Tsien RY. A new generation of Ca2+ indicators with greatly improved fluorescence properties. The Journal of biological chemistry. 1985;260(6):3440-50.

148. Horrocks WD, Sudnick DR. Lanthanide ion probes of structure in biology. Laser-induced luminescence decay constants provide a direct measure of the number of metal-coordinated water molecules. Journal of the American Chemical Society. 1979;101(2):334-40.

149. Laurent S, Vander Elst L, Henoumont C, Muller RN. How to measure the transmetallation of a gadolinium complex. Contrast Media Mol Imaging. 2010;5(6):305-8.

150. Satpathy M, Zielinski R, Lyakhov I, Yang L. Optical imaging of ovarian cancer using HER-2 affibody conjugated nanoparticles. Methods Mol Biol. 2015;1219:171-85.

151. Dobner BC, Riechardt AI, Joussen AM, Englert S, Bechrakis NE. Expression of haematogenous and lymphogenous chemokine receptors and their ligands on uveal melanoma in association with liver metastasis. Acta Ophthalmol. 2012;90(8):e638-44.

152. Ara T, Tokoyoda K, Okamoto R, Koni PA, Nagasawa T. The role of CXCL12 in the organ-specific process of artery formation. Blood. 2005;105(8):3155-61.

153. Kledal TN, Rosenkilde MM, Coulin F, Simmons G, Johnsen AH, Alouani S, et al. A broad-spectrum chemokine antagonist encoded by Kaposi's sarcoma-associated herpesvirus. Science. 1997;277(5332):1656-9.

154. Weber KS, Grone HJ, Rocken M, Klier C, Gu S, Wank R, et al. Selective recruitment of Th2-type cells and evasion from a cytotoxic immune response mediated by viral macrophage inhibitory protein-II. Eur J Immunol. 2001;31(8):2458-66.

155. Sozzani S, Luini W, Bianchi G, Allavena P, Wells TN, Napolitano M, et al. The viral chemokine macrophage inflammatory protein-II is a selective Th2 chemoattractant. Blood. 1998;92(11):4036-9.

156. Qin L, Kufareva I, Holden LG, Wang C, Zheng Y, Zhao C, et al. Structural biology. Crystal structure of the chemokine receptor CXCR4 in complex with a viral chemokine. Science. 2015;347(6226):1117-22.

157. Zhou N, Luo Z, Luo J, Hall JW, Huang Z. A novel peptide antagonist of CXCR4 derived from the N-terminus of viral chemokine vMIP-II. Biochemistry. 2000;39(13):3782-7.

158. Zhang Y. I-Tasser [Available from: https://zhanglab.ccmb.med.umich.edu/.

159. Cowper SE, Robin HS, Steinberg SM, Su LD, Gupta S, LeBoit PE. Scleromyxoedema-like cutaneous diseases in renal-dialysis patients. Lancet. 2000;356(9234):1000-1.

160. Cowper SE, Su LD, Bhawan J, Robin HS, LeBoit PE. Nephrogenic fibrosing dermopathy. Am J Dermatopathol. 2001;23(5):383-93.

161. Grobner T. Gadolinium--a specific trigger for the development of nephrogenic fibrosing dermopathy and nephrogenic systemic fibrosis? Nephrol Dial Transplant. 2006;21(4):1104-8.

162. Mendoza FA, Artlett CM, Sandorfi N, Latinis K, Piera-Velazquez S, Jimenez SA. Description of 12 cases of nephrogenic fibrosing dermopathy and review of the literature. Semin Arthritis Rheum. 2006;35(4):238-49.

163. Gilliet M, Cozzio A, Burg G, Nestle FO. Successful treatment of three cases of nephrogenic fibrosing dermopathy with extracorporeal photopheresis. Br J Dermatol. 2005;152(3):531-6.

164. Kanda T, Fukusato T, Matsuda M, Toyoda K, Oba H, Kotoku J, et al. Gadolinium-based Contrast Agent Accumulates in the Brain Even in Subjects without Severe Renal Dysfunction: Evaluation of Autopsy Brain Specimens with Inductively Coupled Plasma Mass Spectroscopy. Radiology. 2015;276(1):228-32.

165. Adin ME, Kleinberg L, Vaidya D, Zan E, Mirbagheri S, Yousem DM. Hyperintense Dentate Nuclei on T1-Weighted MRI: Relation to Repeat Gadolinium Administration. AJNR Am J Neuroradiol. 2015;36(10):1859-65.

166. Roccatagliata L, Vuolo L, Bonzano L, Pichiecchio A, Mancardi GL. Multiple sclerosis: hyperintense dentate nucleus on unenhanced T1-weighted MR images is associated with the secondary progressive subtype. Radiology. 2009;251(2):503-10.

167. McDonald RJ, McDonald JS, Kallmes DF, Jentoft ME, Murray DL, Thielen KR, et al. Intracranial Gadolinium Deposition after Contrast-enhanced MR Imaging. Radiology. 2015;275(3):772-82.

168. Thomsen HS. Nephrogenic systemic fibrosis: history and epidemiology. Radiol Clin North Am. 2009;47(5):827-31, vi.

169. Benet LZ, Zia-Amirhosseini P. Basic Principles of Pharmacokinetics. Toxicologic Pathology. 1995;23(2):115-23.

170. Li S-D, Huang L. Pharmacokinetics and Biodistribution of Nanoparticles. Molecular Pharmaceutics. 2008;5(4):496-504.

171. William DeW. Horrocks Jr. aDRS. Lanthanide ion probes of structure in biology. Laser-induced luminescence decay constants provide a direct measure of the number of metal-coordinated water molecules. Journal of the American Chemical Society. 1979.

172. Marckmann P, Skov L, Rossen K, Dupont A, Damholt MB, Heaf JG, et al. Nephrogenic systemic fibrosis: suspected causative role of gadodiamide used for contrast-enhanced magnetic resonance imaging. J Am Soc Nephrol. 2006;17(9):2359-62.

173. Staller P, Sulitkova J, Lisztwan J, Moch H, Oakeley EJ, Krek W. Chemokine receptor CXCR4 downregulated by von Hippel-Lindau tumour suppressor pVHL. Nature. 2003;425(6955):307-11.

174. Zhong W, Chen W, Zhang D, Sun J, Li Y, Zhang J, et al. CXCL12/CXCR4 axis plays pivotal roles in the organ-specific metastasis of pancreatic adenocarcinoma: A clinical study. Exp Ther Med. 2012;4(3):363-9.

175. Singh AD, Topham A. Incidence of uveal melanoma in the United States: 1973-1997. Ophthalmology. 2003;110(5):956-61.

176. Collaborative Ocular Melanoma Study G. Assessment of metastatic disease status at death in 435 patients with large choroidal melanoma in the Collaborative Ocular Melanoma Study (COMS): COMS report no. 15. Arch Ophthalmol. 2001;119(5):670-6.

177. Ariela Lifshits Miller AP, Jacob Pe'er, Shahar Frenkel. CXCR4 Expression In Primary And Metastatic Uveal Melanoma. Invest Ophthalmol Vis Sci. 2011;52(14).

178. van den Bosch T, Koopmans AE, Vaarwater J, van den Berg M, de Klein A, Verdijk RM. Chemokine Receptor CCR7 Expression Predicts Poor Outcome in Uveal Melanoma and Relates to Liver Metastasis Whereas Expression of CXCR4 Is Not of Clinical RelevanceCCR7 Predicts Poor Outcome in Uveal Melanoma. Investigative ophthalmology & visual science. 2013;54(12):7354-61.

179. H. E. Grossniklaus HY, K. Liu, Z. Liang, H. Shim. Human Uveal Melanoma Cells Express CXCR4 and a Synthetic Polypeptide CXCR4 Antagonist Decreases Hepatic Micrometastasis in Mouse Uveal Melanoma Model. Invest Ophthalmol Vis Sci. 2007;48(13).

180. Li H, Yang W, Chen PW, Alizadeh H, Niederkorn JY. Inhibition of Chemokine Receptor Expression on Uveal Melanomas by CXCR4 siRNA and Its Effect on Uveal Melanoma Liver Metastases. Investigative ophthalmology & visual science. 2009;50(12):5522-8.

181. Chiang YC, Chen CA, Chiang CJ, Hsu TH, Lin MC, You SL, et al. Trends in incidence and survival outcome of epithelial ovarian cancer: 30-year national population-based registry in Taiwan. J Gynecol Oncol. 2013;24(4):342-51.

182. Wong KH, Mang OW, Au KH, Law SC. Incidence, mortality, and survival trends of ovarian cancer in Hong Kong, 1997 to 2006: a population-based study. Hong Kong Med J. 2012;18(6):466-74.

183. Jiang Y-p, Wu X-h, Shi B, Wu W-x, Yin G-r. Expression of chemokine CXCL12 and its receptor CXCR4 in human epithelial ovarian cancer: An independent prognostic factor for tumor progression. Gynecologic Oncology. 2006;103(1):226-33.

184. Kajiyama H, Shibata K, Terauchi M, Ino K, Nawa A, Kikkawa F. Involvement of SDF-1alpha/CXCR4 axis in the enhanced peritoneal metastasis of epithelial ovarian carcinoma. Int J Cancer. 2008;122(1):91-9.

185. Li J, Jiang K, Qiu X, Li M, Hao Q, Wei L, et al. Overexpression of CXCR4 is significantly associated with cisplatin-based chemotherapy resistance and can be a prognostic factor in epithelial ovarian cancer. BMB Rep. 2014;47(1):33-8.

186. Grossniklaus HE. Progression of ocular melanoma metastasis to the liver: the 2012 Zimmerman lecture. JAMA ophthalmology. 2013;131(4):462-9.

187. Grossniklaus HE, Zhang Q, You S, McCarthy C, Heegaard S, Coupland SE. Metastatic ocular melanoma to the liver exhibits infiltrative and nodular growth patterns. Human pathology. 2016;57:165-75.

188. Pereira PR, Odashiro AN, Lim LA, Miyamoto C, Blanco PL, Odashiro M, et al. Current and emerging treatment options for uveal melanoma. Clin Ophthalmol. 2013;7:1669-82.

189. Carvajal RD, Sosman JA, Quevedo JF, Milhem MM, Joshua AM, Kudchadkar RR, et al. Effect of selumetinib vs chemotherapy on progression-free survival in uveal melanoma: a randomized clinical trial. JAMA. 2014;311(23):2397-405.

190. Hopper KD, Singapuri K, Finkel A. Body CT and oncologic imaging. Radiology. 2000;215(1):27-40.

191. Oudkerk M, Torres CG, Song B, Konig M, Grimm J, Fernandez-Cuadrado J, et al. Characterization of liver lesions with mangafodipir trisodium-enhanced MR imaging: multicenter study comparing MR and dual-phase spiral CT. Radiology. 2002;223(2):517-24.

192. Griffeth LK. Use of PET/CT scanning in cancer patients: technical and practical considerations. Proc (Bayl Univ Med Cent). 2005;18(4):321-30.

193. Becker-Weidman DJ, Kalb B, Sharma P, Kitajima HD, Lurie CR, Chen Z, et al. Hepatocellular carcinoma lesion characterization: single-institution clinical performance review of multiphase gadolinium-enhanced MR imaging--comparison to prior same-center results after MR systems improvements. Radiology. 2011;261(3):824-33.

194. Liao A, Mittal P, Lawson DH, Yang JJ, Szalai E, Grossniklaus HE. Radiologic and Histopathologic Correlation of Different Growth Patterns of Metastatic Uveal Melanoma to the Liver. Ophthalmology. 2018;125(4):597-605.

195. Qiao J, Li S, Wei L, Jiang J, Long R, Mao H, et al. HER2 targeted molecular MR imaging using a de novo designed protein contrast agent. PloS one. 2011;6(3):e18103.

196. Robert Andtbacka1 MY, Merrick Ross3,, Kenneth Grossman1 ET, Sarah, Blanchette4 LG, Yan Wang4, Mohammed, Milhem5, editors. X4P‐001, an orally bioavailable CXCR4 antagonist, increases T cell infiltration in
human metastatic melanoma. Society for Immunotherapy of Cancer (SITC) Annual Meeting; 2017; Maryland.

197. Scala S, Ottaiano A, Ascierto PA, Cavalli M, Simeone E, Giuliano P, et al. Expression of CXCR4 predicts poor prognosis in patients with malignant melanoma. Clin Cancer Res. 2005;11(5):1835-41.

198. Robledo MM, Bartolome RA, Longo N, Rodriguez-Frade JM, Mellado M, Longo I, et al. Expression of functional chemokine receptors CXCR3 and CXCR4 on human melanoma cells. The Journal of biological chemistry. 2001;276(48):45098-105.

199. Mendt M, Cardier JE. Stromal-derived factor-1 and its receptor, CXCR4, are constitutively expressed by mouse liver sinusoidal endothelial cells: implications for the

regulation of hematopoietic cell migration to the liver during extramedullary hematopoiesis. Stem Cells Dev. 2012;21(12):2142-51.

200. Scala S, Giuliano P, Ascierto PA, Ierano C, Franco R, Napolitano M, et al. Human melanoma metastases express functional CXCR4. Clin Cancer Res. 2006;12(8):2427-33.

201. Mirisola V, Zuccarino A, Bachmeier BE, Sormani MP, Falter J, Nerlich A, et al. CXCL12/SDF1 expression by breast cancers is an independent prognostic marker of disease-free and overall survival. Eur J Cancer. 2009;45(14):2579-87.

202. Ottaiano A, Franco R, Aiello Talamanca A, Liguori G, Tatangelo F, Delrio P, et al. Overexpression of both CXC chemokine receptor 4 and vascular endothelial growth factor proteins predicts early distant relapse in stage II-III colorectal cancer patients. Clin Cancer Res. 2006;12(9):2795-803.

203. Weiss ID, Jacobson O. Molecular imaging of chemokine receptor CXCR4. Theranostics. 2013;3(1):76-84.

204. Derlin T, Gueler F, Brasen JH, Schmitz J, Hartung D, Herrmann TR, et al. Integrating MRI and Chemokine Receptor CXCR4-Targeted PET for Detection of Leukocyte Infiltration in Complicated Urinary Tract Infections After Kidney Transplantation. Journal of nuclear medicine : official publication, Society of Nuclear Medicine. 2017;58(11):1831-7.

205. Guan G, Lu Y, Zhu X, Liu L, Chen J, Ma Q, et al. CXCR4-targeted near-infrared imaging allows detection of orthotopic and metastatic human osteosarcoma in a mouse model. Scientific reports. 2015;5:15244.

206. Xue S, Qiao J, Jiang J, Hubbard K, White N, Wei L, et al. Design of ProCAs (protein-based Gd(3+) MRI contrast agents) with high dose efficiency and capability for molecular imaging of cancer biomarkers. Medicinal research reviews. 2014;34(5):1070-99.

207. Zhou Z, Wu X, Kresak A, Griswold M, Lu ZR. Peptide targeted tripod macrocyclic Gd(III) chelates for cancer molecular MRI. Biomaterials. 2013;34(31):7683-93.

208. European Association for Study of L, European Organisation for R, Treatment of C. EASL-EORTC clinical practice guidelines: management of hepatocellular carcinoma. Eur J Cancer. 2012;48(5):599-641.

209. Ferlay J, Shin HR, Bray F, Forman D, Mathers C, Parkin DM. Estimates of worldwide burden of cancer in 2008: GLOBOCAN 2008. Int J Cancer. 2010;127(12):2893-917.

210. McMahon BJ. The natural history of chronic hepatitis B virus infection. Hepatology. 2009;49(5 Suppl):S45-55.

211. Hosaka T, Suzuki F, Kobayashi M, Seko Y, Kawamura Y, Sezaki H, et al. Long-term entecavir treatment reduces hepatocellular carcinoma incidence in patients with hepatitis B virus infection. Hepatology. 2013;58(1):98-107.

212. Marrero JA, Fontana RJ, Fu S, Conjeevaram HS, Su GL, Lok AS. Alcohol, tobacco and obesity are synergistic risk factors for hepatocellular carcinoma. Journal of hepatology. 2005;42(2):218-24.

213. Crissien AM, Frenette C. Current management of hepatocellular carcinoma. Gastroenterol Hepatol (N Y). 2014;10(3):153-61.

214. Asham EH, Kaseb A, Ghobrial RM. Management of hepatocellular carcinoma. Surg Clin North Am. 2013;93(6):1423-50.

215. Bruix J, Sherman M, Practice Guidelines Committee AAftSoLD. Management of hepatocellular carcinoma. Hepatology. 2005;42(5):1208-36.

216. Llovet JM, Fuster J, Bruix J. Intention-to-treat analysis of surgical treatment for early hepatocellular carcinoma: resection versus transplantation. Hepatology. 1999;30(6):1434-40.

217. Kudo M, Izumi N, Kokudo N, Matsui O, Sakamoto M, Nakashima O, et al. Management of hepatocellular carcinoma in Japan: Consensus-Based Clinical Practice Guidelines proposed by the Japan Society of Hepatology (JSH) 2010 updated version. Dig Dis. 2011;29(3):339-64.

218. Kudo M, Matsui O, Izumi N, Iijima H, Kadoya M, Imai Y, et al. JSH Consensus-Based Clinical Practice Guidelines for the Management of Hepatocellular Carcinoma: 2014 Update by the Liver Cancer Study Group of Japan. Liver Cancer. 2014;3(3-4):458-68.

219. European Association For The Study Of The L, European Organisation For R, Treatment Of C. EASL-EORTC clinical practice guidelines: management of hepatocellular carcinoma. Journal of hepatology. 2012;56(4):908-43.

220. Omata M, Lesmana LA, Tateishi R, Chen PJ, Lin SM, Yoshida H, et al. Asian Pacific Association for the Study of the Liver consensus recommendations on hepatocellular carcinoma. Hepatol Int. 2010;4(2):439-74.

221. Bota S, Piscaglia F, Marinelli S, Pecorelli A, Terzi E, Bolondi L. Comparison of international guidelines for noninvasive diagnosis of hepatocellular carcinoma. Liver Cancer. 2012;1(3-4):190-200.

222. Lee YJ, Lee JM, Lee JS, Lee HY, Park BH, Kim YH, et al. Hepatocellular carcinoma: diagnostic performance of multidetector CT and MR imaging-a systematic review and meta-analysis. Radiology. 2015;275(1):97-109.

223. Schraml C, Kaufmann S, Rempp H, Syha R, Ketelsen D, Notohamiprodjo M, et al. Imaging of HCC-Current State of the Art. Diagnostics (Basel). 2015;5(4):513-45.

224. Wong RJ, Devaki P, Nguyen L, Cheung R, Cho-Phan C, Nguyen MH. Increased long-term survival among patients with hepatocellular carcinoma after implementation of Model for End-stage Liver Disease score. Clin Gastroenterol Hepatol. 2014;12(9):1534-40 e1.

225. Furuse J. Sorafenib for the treatment of unresectable hepatocellular carcinoma. Biologics. 2008;2(4):779-88.

226. Fujii H, Itoh Y, Yamaguchi K, Yamauchi N, Harano Y, Nakajima T, et al. Chemokine CCL20 enhances the growth of HuH7 cells via phosphorylation of p44/42 MAPK in vitro. Biochem Biophys Res Commun. 2004;322(3):1052-8.

227. Wald O, Pappo O, Safadi R, Dagan-Berger M, Beider K, Wald H, et al. Involvement of the CXCL12/CXCR4 pathway in the advanced liver disease that is associated with hepatitis C virus or hepatitis B virus. Eur J Immunol. 2004;34(4):1164-74.

228. Zheng D, Oh SH, Jung Y, Petersen BE. Oval cell response in 2-acetylaminofluorene/partial hepatectomy rat is attenuated by short interfering RNA targeted to stromal cell-derived factor-1. Am J Pathol. 2006;169(6):2066-74.

229. Turaga RC, Yin L, Yang JJ, Lee H, Ivanov I, Yan C, et al. Rational design of a protein that binds integrin alphavbeta3 outside the ligand binding site. Nat Commun. 2016;7:11675.

230. Churin AA, Karpova GV, Fomina TI, Vetoshkina TV, Dubskaia T, Voronova OL, et al. [Preclinical toxicological evaluation of Pentamang and Mangascan]. Eksp Klin Farmakol. 2008;71(4):49-52.

231. Elizondo G, Fretz CJ, Stark DD, Rocklage SM, Quay SC, Worah D, et al. Preclinical evaluation of MnDPDP: new paramagnetic hepatobiliary contrast agent for MR imaging. Radiology. 1991;178(1):73-8.

232. Santamaria AB. Manganese exposure, essentiality & toxicity. Indian J Med Res. 2008;128(4):484-500.

233. Hynes RO. Integrins: bidirectional, allosteric signaling machines. Cell. 2002;110(6):673-87.

234. Ruoslahti E. RGD and other recognition sequences for integrins. Annu Rev Cell Dev Biol. 1996;12:697-715.

235. Bergelson JM, Hemler ME. Integrin-ligand binding. Do integrins use a 'MIDAS touch' to grasp an Asp? Curr Biol. 1995;5(6):615-7.

236. Bajt ML, Loftus JC. Mutation of a ligand binding domain of beta 3 integrin. Integral role of oxygenated residues in alpha IIb beta 3 (GPIIb-IIIa) receptor function. The Journal of biological chemistry. 1994;269(33):20913-9.

237. Folkman J. Seminars in Medicine of the Beth Israel Hospital, Boston. Clinical applications of research on angiogenesis. N Engl J Med. 1995;333(26):1757-63.

238. Brooks PC, Clark RA, Cheresh DA. Requirement of vascular integrin alpha v beta 3 for angiogenesis. Science. 1994;264(5158):569-71.

239. Brooks PC, Stromblad S, Klemke R, Visscher D, Sarkar FH, Cheresh DA. Antiintegrin alpha v beta 3 blocks human breast cancer growth and angiogenesis in human skin. J Clin Invest. 1995;96(4):1815-22.

240. Liu Z, Liu S, Wang F, Liu S, Chen X. Noninvasive imaging of tumor integrin expression using (18)F-labeled RGD dimer peptide with PEG (4) linkers. European journal of nuclear medicine and molecular imaging. 2009;36(8):1296-307.

241. Bach-Gansmo T, Danielsson R, Saracco A, Wilczek B, Bogsrud TV, Fangberget A, et al. Integrin receptor imaging of breast cancer: a proof-of-concept study to evaluate 99mTc-NC100692. Journal of nuclear medicine : official publication, Society of Nuclear Medicine. 2006;47(9):1434-9.

242. Anderson CE, Donnola SB, Jiang Y, Batesole J, Darrah R, Drumm ML, et al. Dual Contrast - Magnetic Resonance Fingerprinting (DC-MRF): A Platform for Simultaneous Quantification of Multiple MRI Contrast Agents. Scientific reports. 2017;7(1):8431.